Asteroseismology in the Red Clump: Mass Transfer and Merger Remnants through Mixed Modes

By

Walter Eduard van Rossem

A thesis submitted to
the University of Birmingham
for the degree of
DOCTOR OF PHILOSOPHY

Suns, Stars, and Exoplanets
School of Physics and Astronomy
College of Engineering and Physical Sciences
University of Birmingham
January 30, 2023

UNIVERSITY OF
BIRMINGHAM

University of Birmingham Research Archive

e-theses repository

This unpublished thesis/dissertation is copyright of the author and/or third parties. The intellectual property rights of the author or third parties in respect of this work are as defined by The Copyright Designs and Patents Act 1988 or as modified by any successor legislation.

Any use made of information contained in this thesis/dissertation must be in accordance with that legislation and must be properly acknowledged. Further distribution or reproduction in any format is prohibited without the permission of the copyright holder.

© Copyright WALTER E. VAN ROSSEM, 2023

All Rights Reserved

ABSTRACT

Asteroseismology enables the study of the interiors of stars through the detection and interpretation of their global oscillation modes. The high-quality observations by the *Kepler* space telescope of thousands of giant stars have opened the door to detailed investigations of their structures, facilitating numerous avenues of research that give key insights into stellar structure and evolution. In this context, a particularly exciting prospect offered by seismic constraints is to exploit the probing power of so-called mixed modes. Mixed modes are oscillation modes with both a pressure-mode and a gravity-mode character. Pressure-modes typically propagate in the envelope of a star, whilst gravity-modes do so in the dense radiative regions near the stellar core. The mixed-mode coupling coefficient describes how easily the two types of oscillations can transfer energy between them. The aim of this thesis is twofold. The first aim is to provide a better understanding of mixed-mode coupling in stars undergoing core-helium burning, as well as contributing to the interpretation of mixed-mode coupling in giant stars. The second aim is to search for candidate stars that have undergone mass transfer or mergers in their past. In this thesis stars are modelled using the stellar evolution code `MESA`, which enables the inherent complexity of stars to be simulated. Detailed evolutionary models enable stellar properties to be calculated precisely, and the physical relation between these properties to be investigated.The behaviour of model-predicted mixed-mode coupling coefficients in this thesis reproduces that of observed data, in particular its dependence with mass and metallicity. In both the red clump and red giant branch the mixed-mode coupling coefficient is anti-correlated with metallicity for both observed and modelled stars, with the dependence being of the order of -0.1 dex^{-1} in the red clump and -0.01 dex^{-1} in the red giant

branch. The modelled coupling coefficient depends on the oscillation frequency in both the red giant branch and the red clump of the order of $10^{-3}\mu\text{Hz}^{-1}$. In the red giant branch, this frequency dependence provides an avenue for detailed mapping of the evanescent zone. In the second part of this thesis parametric models are constructed using the stellar evolution code `MESA`, allowing for the approximation of mass transfer/merger models. Based on this approximation it is possible to study the effect of the helium core on various observational parameters such as period spacing, luminosity and coupling. From the 1029 stars in our sample of observations, two candidate stars, KIC4275220 and KIC6047033, are identified as candidates of objects which may have had non-standard evolutionary histories.

DEDICATION

I dedicate my thesis to my family:

My father Steven, who is my Sun,

My mother Okkie who put me in the Universe,

My brothers Duco and Max who orbit with me.

Thank you

ACKNOWLEDGMENTS

I would like to thank Andrea Miglio for his open-minded approach to our work and for his role as my thesis supervisor which he fulfilled with kindness and professionalism. I very much appreciated his drive and inspiring technical leadership to improve on the asteroseismic modelling. My gratitude also goes to Josefina Montalban for her push to be thorough and to get the most out of the modelling data and the high-quality detailed review that she did. Bill Chaplin as my formal supervisor for the second half of my PhD has been a rock for me to go to, he was always there despite all the other roles at the School that he manages. His thoughtfulness to me is much appreciated.

Over the last few years I have been fortunate to work together with several post graduate colleagues in Birmingham University. Thank you to Matt, Eddie, Alex, Alex, Emma, Vedad, Oli, Saniya, Martin, George, Emily, Thomas, Mat, Ben, Yasmin, Owen, and Alix for making the office such a nice and fun place to work during my time in Brum.

I would like to thank my brother Duco for the time we spent in splendid isolation during the pandemic and thank my brother Max for the opportunity to work on areas far away from stellar modelling. I would like to thank my parents Okkie and Steven for their love and support throughout my astrophysical journey. Finally, it wouldn't be asteroseismology without acknowledging a cat, Qapoes. For 20 years she was there to give me my dose of cat when visiting home.

Contents

List of Figures

Acronyms

CoRoT Convection, Rotation and planetary Transits. 1, 2, 64

GONG Global Oscillation Network Group. 1

TESS Transiting Exoplanet Survey Satellite. 1, 2, 64

AGB Asymptotic Giant Branch. viii, 7, 18, 90, 93, 94

CE Common Envelope. 7, 24

CEE Common Envelope Evolution. 7, 24

CHeB Core Helium-Burning. viii, 1, 2, 17, 88–90, 92, 94, 124, 150, 169

GA Galactic Archaeology. 1, 3, 5

GOLF Global Oscillation at Low Frequencies. 26, 37

HRD Hertzsprung-Russell Diagram. v, viii, 7, 9–11, 16, 17, 88–90, 141

HSE Hydrostatic Equilibrium. 7, 10

JWKB Jeffreys-Wentzel–Kramers–Brillouin. 26, 29, 34, 69–71

MG Merger. 7, 124

MS Main Sequence. vi, 7, 10, 14, 32, 33, 51, 114, 143

MT Mass Transfer. 7, 20, 124

MT/MG Mass Transfer/Merger. xi, 7, 124–126, 130, 136, 150, 163

MW Milky Way. 1–3, 5

PMS Pre-Main Sequence. 7, 10

PSD Power-Spectral Density. vi, 26, 37

RC Red Clump. ix, x, 3, 6, 7, 17, 65, 66, 77, 88, 90, 92, 93, 97, 99, 101–106, 108, 110, 114, 117, 121, 123, 129, 132, 141, 145, 150, 163, 166, 168, 172

RGB Red Giant Branch. vii, viii, x, 1, 2, 14, 16, 39, 40, 53, 65, 66, 68, 71, 72, 88, 92–94, 96, 97, 106, 108, 114, 117, 119, 123, 124, 131, 132, 166, 167, 171, 172

RGBb Red Giant Branch bump. vii, 7, 16, 40, 47, 68, 80, 92, 97, 98, 114, 117, 172

RL Roche Lobe. 7, 21

RLOF Roche Lobe Overflow. 7, 22

SGB Sub-Giant Branch. viii, 7, 12, 39, 74, 77, 92, 94, 114, 172

SLO Solar-Like Oscillations. 26, 36

SoHO Solar and Heliospheric Observatory. 26, 37

SSE Single Stellar Evolution. 7, 124, 130, 132, 136–138, 145, 150, 153, 156, 159, 163–165, 168–170

ZAMS Zero Age Main Sequence. 7, 10

Chapter One

Introduction

Stars make sound, the waves of which propagate inside the star. The oscillations created by these sounds waves are affected by the temperature and composition of different parts of the star. Asteroseismology enables the study of the stellar interior by observing oscillations and interpreting what they tell us about the internal structure of a star.

In the summers of 1960 and 1961, enormous systems of laterally moving material, measuring some 16,000km across, were observed on the surface of the Sun (Leighton 1960; Leighton et al. 1962). Some ten years later, Ulrich (1970) and Leibacher & Stein (1971) proved that these systems were acoustic standing waves. These publications were the start of the study of oscillations in the Sun and was called helioseismology, derived from the Greek word helios for Sun and seismos for quake. As oscillations propagate through the Sun, the internal structure of the Sun is reflected in the oscillation signals. When these oscillations are observed, it allows for the interior structure of the Sun to be studied. The internal rotation of the Sun as a function of radius (Duvall & Harvey 1984; Duvall et al. 1984) was determined through the inferences made from oscillations observed in the Sun. Later, using Global Oscillation Network Group (*GONG*) observations, Basu (1997) showed that the rotation profile of the Sun was also longitude dependent. Thompson et al. (2003),

and references therein, provide additional support for these observations. Christensen-Dalsgaard et al. (1991) were able to measure the depth of the Sun's convective envelope of approximately 0.287 $R_\odot$ using mode inversion with over 1600 p-modes, which are acoustic waves which propagate in the convective envelope. Given the proximity of the Sun to Earth, helioseismology can be done at high spatial resolution. The disc of the Sun can be resolved spatially as can standing waves on the surface of the Sun. For stars other than the Sun it is not possible to resolve oscillations on the stellar disc given their distances from Earth. The technique used for the study of the interior of stars other than the Sun is called asteroseismology. Similar to helioseismology, in asteroseismology oscillations can be measured as variations in brightness of the star. Oscillations can also be observed as variations in spectral line profiles. Based on these measurements, parameters such as radius, mass, age and some parts of the evolutionary phase of stars can be deduced. Additionally, these oscillations can also be used to probe the star's internal physics (e.g. Chaplin & Miglio 2013; Montalbán & Noels 2013; Mosser et al. 2014; Di Mauro 2016; Hekker & Christensen-Dalsgaard 2017 and references therein). High-quality observations are important if oscillations in stars are to provide useful information on the stellar properties. This can only be achieved through long, uninterrupted and dedicated observation periods with high-precision space telescopes such as *Kepler*, which was retired in 2018 after being in operation for over 9 years (Borucki et al. 2010; Howell et al. 2014). The space telescope Convection, Rotation and planetary Transits (*CoRoT*) also had asteroseismic information gathering as one of its primary objectives and was operational between 2006 and 2013 (Auvergne et al. 2009). The currently operational Transiting Exoplanet Survey Satellite (*TESS*), which started observations in 2018 (Ricker et al. 2015) has also been indispensable in the collection of stellar oscillation data. In 2023 only *TESS* is still observing and producing a wealth of data in which to look for oscillations to characterise stars (e.g. Hatt et al. 2023). These advancements in helioseismology and asteroseismology in combination with precise observations over the last 60 years have been instrumental in discovering and understanding the internal properties of stars.

Through asteroseismology it is possible to determine precise masses and radii of different types of stars. Asteroseismology also facilitates the investigation of properties of populations of stars, such as their precise age (e.g. Miglio et al. 2021). Knowing the precise age of giant stars in the Milky Way (MW) Galaxy allows these stars to be used as tracers of various galactic dynamic processes. One of the key advancements facilitated by asteroseismology is the ability to differentiate Red Giant Branch (RGB) stars from Red Clump (RC) stars through their period spacings (Bedding et al. 2011; Mosser et al. 2015; Hekker et al. 2018). The ability to differentiate between RGB stars and RC stars is crucial for the field of Galactic Archaeology (GA), which is the study of the formation history of the MW, as RC stars can serve as standard candles. This ability to serve as standard candles is possible as the luminosity of low-mass RC stars depends only weakly on mass and metallicity (Girardi 2016). This weak dependence on mass and metallicity allows for the RC to be used as a yard-stick to approximately 10 kpc (e.g. Bovy et al. 2014) in the MW. This method of measuring distance becomes more precise than Gaia parallaxes beyond around 3 kpc, and these distances have also been used to further refine *Gaia*'s ability to measure distances (Davies et al. 2017; Khan et al. 2019).

For any given star it is difficult to know from its surface properties alone whether it has had any binary interactions in its past, such as mass transfer to or from another star. Therefore, it is not straightforward to determine whether a star has undergone single-star evolution. A star appears older than it truly is if it is a more massive star which has lost mass. It appears as a lower-mass star in a more advanced stage of evolution which implies that it is older. Similarly, a lower-mass star which gains mass appears younger than its actual age because it appears as a more massive star in an earlier phase of evolution. This phenomenon was first studied in detail in the Algol system, and is called the "Algol paradox" (Pustylnik 1998, and references therein). The Algol system is a hierarchical triple system where an inner binary is orbited by a third star. The inner binary consists of a 3.2 $M_\odot$ main-sequence star and a 0.7 $M_\odot$ subgiant on a 2.87 day orbit (Baron et al. 2012). The tertiary star is a 1.5 $M_\odot$ main sequence star which orbits the inner

binary with a period of around 680 days (Baron et al. 2012). The inner binary is thought to have formed at approximately the same time as the tertiary star, and therefore it is expected that the more massive component is in a more advanced phase of evolution. However, the less massive star in the inner binary is a subgiant which contradicts the fact that massive stars evolve more quickly (e.g. Salaris & Cassisi 2005; Kippenhahn et al. 2013; Benacquista 2013). This contradiction leads to the "Algol paradox", of which the Algol system is the prototype. It is also possible that stars merge to form a single, more massive star. The Algol paradox illustrates the importance of being able to differentiate between stars which have undergone single stellar evolution and stars that have undergone more complex evolutionary interactions. If it is possible to differentiate between single stellar evolution and binary products, then this information can be used in stellar population studies. Tokovinin (2014a,b) shows that 46% of the almost 5000 F&G dwarfs within 67 pc from the Sun are not single stars and have one or more companions. Additionally, Moe & Di Stefano (2017) show that in general this is also true for stars with a similar mass to the Sun which have on average 0.50 ± 0.04 companions. To determine accurate ages of stars, the effects of mergers and mass transfer need to be accounted for in population studies (Miglio et al. 2021). In clusters it is relatively straightforward to observe these effects. A good example is the cluster NGC6791 where a population of under- and over-massive stars can be observed (e.g. Miglio et al. 2021). However, in field stars this approach is not possible as these stars do not have a cluster or other mono-age population to which they belong. Being able to identify stars which have had binary interaction in their past is important in galactic archaeology as knowing the accurate ages of stars is of crucial importance in this field of study.

Galactic archaeology is done mainly through the study of different stellar populations throughout the MW, as well as through the study of kinematic data of the stars from *Gaia* (Gaia Collaboration et al. 2016), and their elemental abundances (Matteucci 2021, and references therein). The composition of a field star alone can give an estimate of when a star was formed (e.g. Anders et al. 2023). However, deducing more is difficult as galactic mergers and dynamical processes such

as stellar migration and kinematic heating strongly influence the development of the MW Galaxy as these processes mix stars of different compositions and histories (Haywood 2008). Clusters, on the other hand, provide an alternative method with which to probe the galaxy. Stars in clusters are assumed to have formed from the same material and are assumed to have the same age. Modelling of these clusters, as well as of stars in these clusters gives insight into the evolution of the galaxy. The combination of GA and the ability of asteroseismology to give precise ages makes it possible to place constraints on the formation history of the MW (e.g. Noels et al. 2016; Chaplin et al. 2020; Matteucci 2021). Stars which may have had binary interactions in their past are the young α-rich metal-poor stars (Chiappini et al. 2015; Martig et al. 2015). These α-rich metal-poor stars are typically found in old populations of stars that are formed due to supernovae of massive stars. These supernovae enrich the galaxy with α-elements before low- and intermediate-mass stars enter their late phases of evolution which enrich the galaxy with metals (Matteucci 2001; Pagel 2009). One possible avenue for the formation of such α-rich stars is through binary mergers (Silva Aguirre et al. 2018). The two progenitors would be lower-mass stars with long lifetimes, and once the more massive component reaches a more advanced phase of evolution, the stars merge. The resulting star, a merger product, is a more massive star with a composition similar to the progenitors, which were low-mass and old. Stars with compositions and initial masses similar to the merger product have already died and therefore this merger product would appear younger than it is. The effects of multiplicity need to be taken into account as they are typically neglected during modelling of the formation and evolution of galaxies, even though these effects can significantly affect the evolution of galaxies (Rosdahl et al. 2018). Asteroseismology has advanced in spectacular fashion over the past decades. The wealth of observational data that has been and is being collected allows for the modelling of stars to be conducted in a very precise and quantified manner because the available observational data provide an excellent way to constrain the developed models. Based on these models, new fields for further asteroseismic research are opening up. In particular, RC stars are a great target for asteroseismic research. This thesis focuses on the use of asteroseismology to look for signs of previous binary interactions in stars exhibiting mixed modes (e.g. Rui & Fuller 2021;

Li et al. 2022). The behaviour of mixed-mode coupling of single stars and parametric models of mass transfer/merger remnants is compared to observations using stellar models. This comparison allows for inferences to be made on the near-core region of the observed stars and opens up the possibility to find candidates for stars which have undergone binary interactions in their past.

This thesis is structured as follows. In Chapter 2, I give an overview on the stellar evolution of low- and intermediate-mass stars, as well as an overview of binary stellar evolution. In Chapter 3, I explain the key components used in asteroseismology and how these can be used to infer the global properties of a star. In Chapter 4, the behaviour of mixed-mode coupling in the red clump is explored. In Chapter 5, the behaviour of mixed modes of parametric mass transfer/merger models during core helium-burning is explored. Finally, Chapter 6 concludes.

Chapter Two

Stellar evolution

The theory of Single Stellar Evolution (SSE) is now well established following over a century of research. Russell (1914) gives an overview of how stars were thought to evolve and Russell (1919) discusses the sources of stellar energy, and the "unknown store of energy of enormous magnitude" which was required to reconcile the probable age of the Sun. Shapley (1919) discusses the issue that with the known sources of energy at the time the Sun could only have radiated energy at the present rate for less than twenty million years through gravitational contraction. However, geological evidence around the same time showed that the age of Earth's crust was at least 1.1×10^9 years (Holmes 1915; Barrell 1917), resulting in a discrepancy in age of a factor of at least 200. It was postulated that the unknown source of energy could be from the fusion of hydrogen to helium (Eddington 1920). The mechanism of stellar energy was finally determined by Weizsäcker (1937, 1938); Bethe & Critchfield (1938); Bethe (1939). The different phases that stars go through during their evolution are now better understood (Salaris & Cassisi 2005; Kippenhahn et al. 2013; Benacquista 2013, and references therein). Stellar evolution calculations have progressed enormously over the past decades. Stellar evolution codes include more internal physics and more

accurate prescriptions for the internal physics (e.g. Paxton et al. 2011, 2013, 2015, 2018, 2019; Jermyn et al. 2022). Combining these improvements in modelling with increasing computational resources, made available by more powerful CPUs and increasing amounts of memory, will make the increasingly stringent requirements asked of stellar models tractable.

This chapter provides a short overview of the structure and evolution of stars in so far as relevant to this thesis. There are four equations fundamental to understanding the interior workings of stars. Together they are called the Equations of Stellar Structure. Key assumptions when using these equations are:

- The star is spherically symmetric.
- The star is not rotating.
- The star is in hydrostatic equilibrium.
- The star is in local thermodynamic equilibrium.
- The effect of magnetic fields is negligible.

In reality, these assumptions are not completely true. For example the Sun rotates approximately once every 25 days along its equator and rotates approximately once every 38 days near its poles (Schou et al. 1998). Another example that these assumptions are not completely true are sunspots, which are caused by magnetic fields (e.g. Solanki 2003). However, these five assumptions greatly simplify the study of the structure and evolution of stars.

The first equation of stellar structure is the mass continuity equation:

$$\frac{\mathrm{d}r}{\mathrm{d}m} = \frac{1}{4\pi r^2 \rho}, \tag{2.1}$$

where r is the radius of a spherical shell in the star, m is the mass contained within a sphere of radius r in the star (also called mass coordinate), and ρ is the density at m. The second equation is

the hydrostatic equilibrium equation:

$$\frac{\mathrm{d}P}{\mathrm{d}m} = -\frac{\mathrm{G}m}{4\pi r^4}, \tag{2.2}$$

where P is the pressure at m, and G is the gravitational constant. The third equation is the equation of conservation of energy:

$$\frac{\mathrm{d}l}{\mathrm{d}m} = \epsilon, \tag{2.3}$$

where l is the local luminosity of a shell with radius r, and ϵ is the energy generation rate. This energy generation rate depends on three components:

$$\epsilon = \epsilon_{\mathrm{nuc}} + \epsilon_{\mathrm{grav}} - \epsilon_{\nu}, \tag{2.4}$$

where ϵ_{nuc} is the nuclear energy generation rate. This is the sum of all energy released by nuclear reactions. ϵ_{grav} is the energy released during contractions or absorbed during expansion. ϵ_{ν} is the energy lost due to neutrinos. The fourth equation is that of energy transport:

$$\frac{\mathrm{d}T}{\mathrm{d}m} = -\frac{\mathrm{G}mT}{4\pi r^4 P}\nabla, \tag{2.5}$$

where T is temperature, and ∇ is the radiative or convective temperature gradient depending on how energy is transported in the star. The radiative temperature gradient and the adiabatic temperature gradient are defined as:

$$\nabla_{\mathrm{rad}} = \frac{3}{16\pi \mathrm{acG}}\frac{\kappa l P}{m T^4} \tag{2.6}$$

and

$$\nabla_{\mathrm{ad}} = \left(\frac{\partial \ln T}{\partial \ln P}\right)_S, \tag{2.7}$$

where a is the radiation density constant, c the speed of light, and κ the opacity at r.

In addition to these four equations that are fundamental to the understanding of the stellar interior, it is also essential to determine whether a region inside a star is stable against convection. There are two criteria which determine this and they are the Schwarzschild and Ledoux criteria (e.g. Gabriel et al. 2014). In the Schwarzschild criterion, a region is convective if $\nabla_{\mathrm{rad}} > \nabla_{\mathrm{ad}}$.

When this condition is satisfied, an upward moving parcel keeps rising as it becomes buoyant in its surrounding medium. Similarly, if displaced downwards, the parcel continues to sink. This process causes large scale motions inside the star, and is called convection. Convection efficiently transports energy outwards and well-mixes the regions where convection occurs. The second criterion, from Ledoux, incudes the stabilizing effect of a composition gradient in the inequality. In chemically homogeneous layers, the Ledoux criterion reduces to the Schwarzschild criterion. Therefore, if a star is radiative at r the temperature gradient ∇ is $\nabla_{\rm rad}$, whilst if it is fully convective the temperature gradient is $\nabla_{\rm ad}$. However, as this criteria for convection is local, parcels may cross this $\nabla = \nabla_{\rm ad} = \nabla_{\rm rad}$ boundary. The acceleration of the parcel becomes zero at the boundary, but the velocity might be non-zero. Therefore, the parcel may penetrate into the convectively stable radiative region beyond the boundary. This extra mixing beyond a convective zone boundary is called *overshooting* (e.g. Salaris & Cassisi 2005; Pedersen et al. 2018). When overshooting occurs below the convective envelope of a star it is also called *undershooting* (e.g. Khan et al. 2018).

2.1 Single stellar evolution

This thesis focuses on low- and intermediate-mass stars with masses between 0.8–3.0 $M_\odot$. This section briefly describes the evolutionary phases a typical 1 $M_\odot$ star goes through during its lifetime up to and including the early asymptotic giant branch. During these phases, stars can have internal structures which significantly differ from each other. To describe these evolutionary phases, a 1 $M_\odot$ star with Solar metallicity was modelled using the stellar evolution code Modules for Experiments in Stellar Astrophysics (`MESA`; Paxton et al. 2011, 2013, 2015, 2018, 2019; Jermyn et al. 2022). Figure 2.1 shows the track this modelled star takes in the Hertzsprung-Russell Diagram (HRD). The star in this section is modelled using `MESA` version 11701 and is a Solar analogue with $Z/X = 0.0178$ at the Solar age (Serenelli et al. 2009), exponential overshooting below the convective envelope with overshooting parameter $f_{\rm OV,CE} = 0.02$, and penetrative helium-core overshooting

with $\alpha_{\mathrm{He}} = 0.5$. Lines of constant radius are shown as grey dashed lines and the direction the modelled star moves in the HRD is shown by the arrows. The different phases the star goes through are described in Section 2.1.1. A more detailed description of the theory of stellar evolution can be found in textbooks such as Salaris & Cassisi (2005), Kippenhahn et al. (2013), and Benacquista (2013).

2.1.1 Evolutionary phases

The following sections will each briefly describe the phases of evolution a low-mass star goes through during its life from the pre-main sequence until it exhausts the helium in its core.

2.1.1.1 Pre-main sequence

Stellar evolution starts when a cold interstellar gas cloud collapses. When this happens the cloud fragments into smaller clumps. This fragmentation process continues and eventually these clumps form protostars and the evolution continues in hydrostatic equilibrium (HSE; e.g. Hayashi 1966; Salaris & Cassisi 2005). A protostar continues to contract isothermally until its core becomes optically thick and therefore opaque to radiation. Material from the interstellar gas cloud continues to accrete onto the protostar. As this accretion continues the core increases in temperature until it becomes hot enough to dissociate H_2 into H. Because of this dissociation the core contracts and heats up, eventually ionizing the hydrogen. Because of the increasing temperature throughout the contracting protostar, the photosphere also moves inwards. Once the photosphere becomes hot enough it blows away the gas cloud containing the protostar. Now the star becomes visible as a Pre-Main Sequence (PMS) star. When the central temperature reaches around 10^7 K, hydrogen ignites in the stellar core and starts to fuse hydrogen into helium (e.g. Salaris & Cassisi 2005). At this point, the star enters the Main Sequence (MS) as a Zero Age Main Sequence (ZAMS) star.

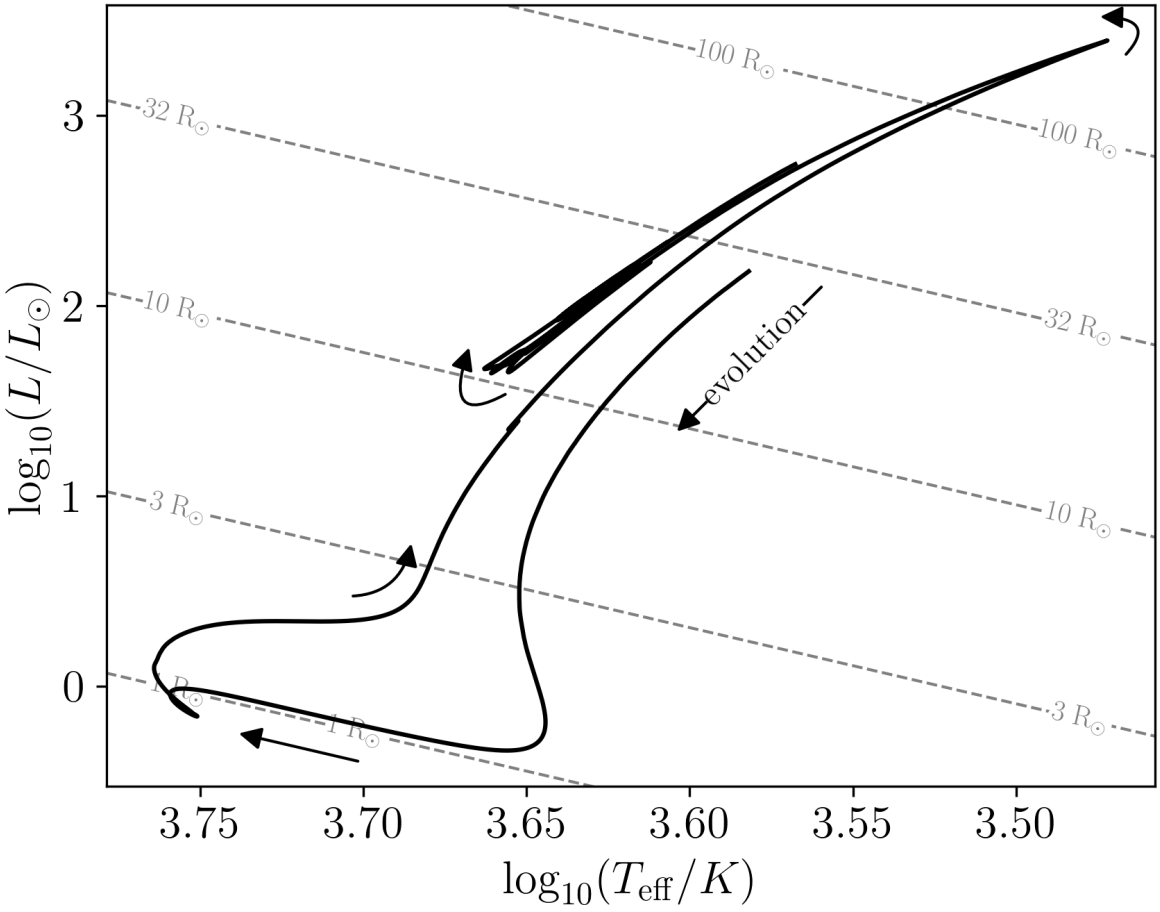

Figure 2.1: Hertzsprung-Russell diagram showing the path of a 1 $M_\odot$ Solar metallicity star modelled using `MESA`. Lines of constant radius are shown as grey dashed lines. The direction the star evolves is shown by the arrows.

The ZAMS can have multiple definitions, for example Paxton et al. (2011) define the ZAMS as the first point in time when the luminosity is equal to the total nuclear burning luminosity ($L = L_{\rm nuc}$). This is the definition used in this thesis.

2.1.1.2 Main sequence

Once hydrogen ignites in a stellar core it is on the MS. This evolutionary phase is the longest lasting of all phases, with a duration of around 11 Gyr for 1 $M_\odot$ stars (Salaris & Cassisi 2005). In stars with masses less than around 1.3 $M_\odot$ the core is radiative and the envelope is convective, whilst in stars with masses greater than around 1.3 $M_\odot$ the core is convective and envelope is radiative. Figure 2.2 shows a Kippenhahn diagram of a 1 $M_\odot$ star with Solar metallicity in the left panel, the composition profile of the star with central hydrogen mass fraction $X_{\rm C} = 0.38$ in the top right panel, and the track that the MS star makes in the HRD is shown in red in the bottom right panel. A Kippenhahn diagram shows how the internal stellar structure varies over time. Along the y-axis, the mass coordinate inside the star is shown and the x-axis shows the age of the star. The diagram also shows where in the star mixing occurs, as well as the net nuclear energy generation rate. Figure 2.2 shows the structure of a $1M_\odot$ star during the main sequence. The convective envelope is shown as the green //-hatched region along the top of the Kippenhahn diagram. In terms of mass, the convective envelope is quite small ($\simeq 0.02$ $M_\odot$). However, the convective envelope makes up almost a third of the stellar radius. The fact that the core is radiative is seen by the lack of green hatching. This means that fresh hydrogen is not mixed into the core. This causes a composition gradient to develop in the radiative region as the star burns hydrogen into helium. In stars with $M \leq 1.3$ $M_\odot$, hydrogen is burnt into helium mainly through the proton-proton (pp) chain (Bethe & Critchfield 1938; Burbidge et al. 1957; Cyburt et al. 2010). In higher-mass stars hydrogen is mainly burnt in a different process called the CNO-cycle (Salaris & Cassisi 2005, and references therein). Here, carbon, nitrogen, and oxygen act as catalysts for hydrogen-burning (Weizsäcker 1937, 1938; Bethe 1939; Cyburt et al. 2010). These processes, and hence the associated $\epsilon_{\rm nuc}$, are temperature

dependent with the pp-chain having a dependence of around T^4, and the CNO-cycle of around T^{18}. There is no mixing in the radiative core of low-mass stars and therefore, the centre of the star burns hydrogen faster than the outer layers of the hydrogen-burning zone in the core. This is because the temperature deeper in the core is higher, as seen by the darkening blue shading towards the bottom of the Kippenhahn diagram. When hydrogen is exhausted, a hydrogen-burning shell forms which continues to deposit helium onto the core. When the CNO-cycle starts to dominate at around $T \gtrsim 2 \times 10^7$ K (Salaris & Cassisi 2005), stars with these core temperatures form a convective core. This convective core efficiently mixes material, and the whole convective core then shares the same composition as the mixing timescale is much faster than the nuclear burning timescale. The main sequence ends when hydrogen has been exhausted in the centre and is called Terminal Age Main Sequence (TAMS). The definition used in this thesis for the TAMS is when the central hydrogen mass fraction $X_C = 10^{-3}$.

2.1.1.3 Sub-giant branch

During this phase stars transition to shell hydrogen-burning. In this thesis the Sub-Giant Branch (SGB) is defined as the phase of evolution immediately after TAMS ($X_C < 10^{-3}$) and ends when the convective envelope mass reaches 0.35 $M_\odot$. This results in the HRD track ending within approximately 0.01 dex of the base of the RGB in terms of effective temperature. During the SGB, the convective envelope extends further into the star. Figure 2.3 shows how the convective envelope (green hatching) begins to further extend into the star at around 11000 Myr. The transition to shell hydrogen-burning is shown by the net region with positive net nuclear energy generation (blue shading) moving away from the centre as the helium core grows. During this phase, the surface of the star cools and starts to expand in radius as its envelope becomes a significant fraction of its stellar mass. Stars with masses above approximately 2.2 $M_\odot$, traverse this region in the HRD quickly compared to lower-mass MS stars. This results in a dearth of observed stars between the MS and RGB in the HRD. This lack of observed stars is called the *Hertzsprung Gap* (Hoyle 1960;

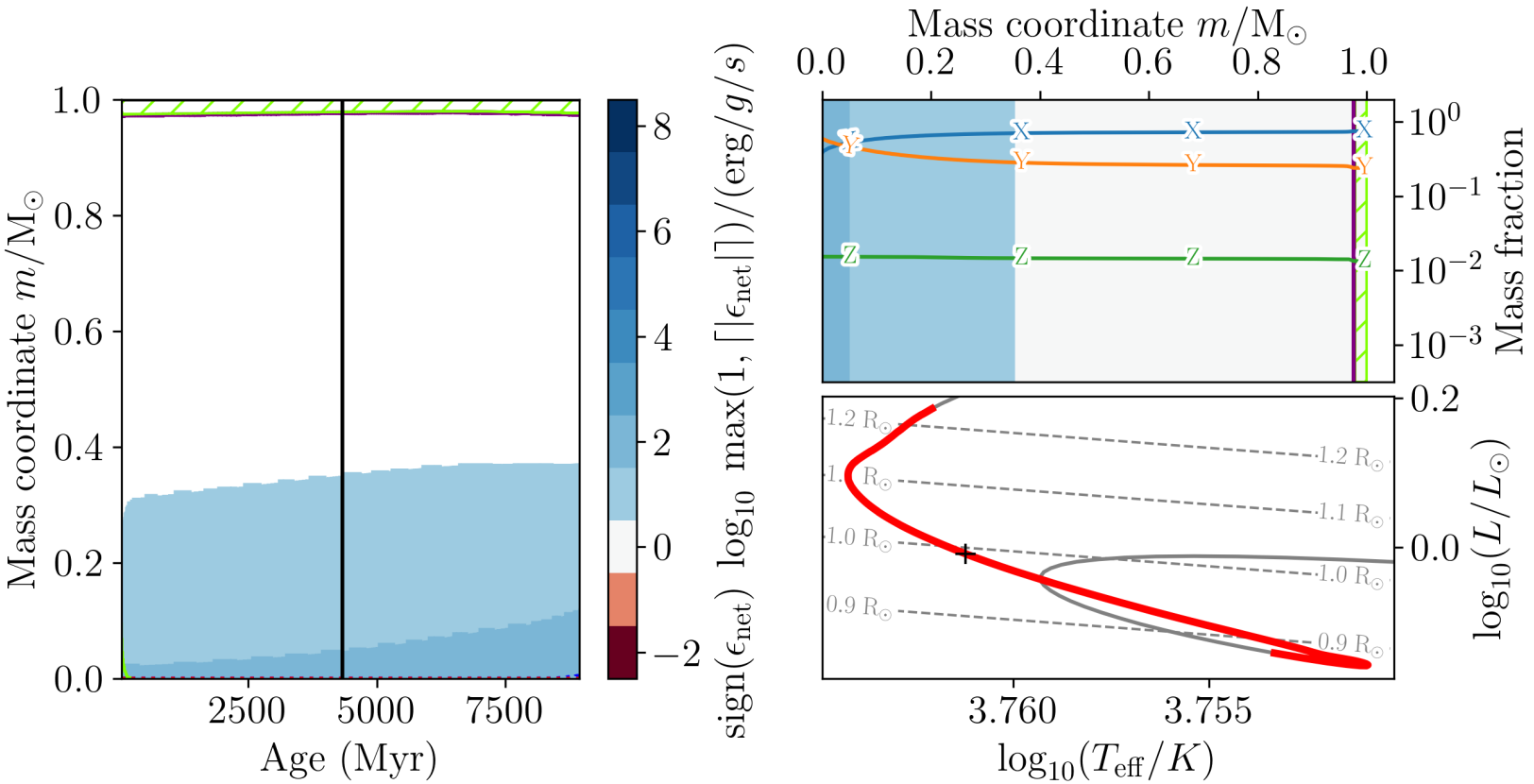

Figure 2.2: The left panel shows a Kippenhahn diagram of a $1M_\odot$ star with Solar metallicity on the MS. The vertical black line shows where the composition profile in the top right panel is taken and has a central hydrogen mass fraction $X_C = 0.38$. The mass coordinate is shown along the y-axis and age is shown along the x-axis. The green //-hatched region shows where convection takes place, the purple X-hatched region shows overshooting (which is difficult to see for the MS in this figure, but is clearer in later phases as shown in e.g. Figure 2.6), the blue shaded region shows net nuclear energy generation rate ($\epsilon_{\mathrm{net}} = \epsilon_{\mathrm{nuc}} - \epsilon_\nu$). If ϵ_{net} is negative the region is shaded red (e.g. Figure 2.7). The top right panel shows the hydrogen (X), helium (Y), and metal (Z) composition profile of the star as blue, orange, and green lines respectively. It also shows ϵ_{net} using the same colour scale as the left panel. The bottom right panel shows the HRD track of the evolutionary phase in red, the full track in grey, and the location at which the composition profile is taken as the black plus. Lines of constant radius are shown as dashed grey lines.

Salaris & Cassisi 2005).

2.1.1.4 Red giant branch

The hydrogen-burning shell continues to move outward in mass coordinate, and the helium core continues to become more massive as seen by the blue line on the Kippenhahn diagram in Figure 2.4. The star is now a RGB star. As the convective envelope increases in mass, it enters a region where the star has burnt hydrogen during the MS and SGB and mixes these hydrogen-burning products into the convective envelope which brings them to the surface. This mixing is shown by the bottom of the convective envelope reaching into the previously blue shaded region at a mass coordinate of around 0.4 $M_{\odot}$ in Figures 2.2 and 2.3 (Thomas 1967; Iben 1968; Salaris & Cassisi 2005). This is called the *First Dredge-up*. In low-mass stars, the core continues to contract until it becomes dense enough to be supported by electron degeneracy pressure (Schönberg & Chandrasekhar 1942). As the core becomes degenerate, pressure becomes independent of temperature. There is now no heat generation in the degenerate core. Neutrinos are, however, still able to escape, thereby removing energy from the core of the star. This results in cooling, which results in $\mathrm{d}l/\,\mathrm{d}m = \epsilon < 0$. This is seen as red shading in the bottom right corner in the Kippenhahn diagram in Figure 2.4. This means that there is a source of cooling in the core with the highest rate of cooling in the centre. This causes the hottest part of the star to be off-centre in the helium core (Thomas 1967; Salaris & Cassisi 2005). In intermediate-mass stars, the temperature and density are high enough for the helium core to stay non-degenerate when it contracts. Once the core has contracted enough, the intermediate-mass star starts to burn helium quiescently and does not ignite helium under degenerate conditions. At the tip of the RGB, helium ignites and is discussed further in Section 2.1.1.6.

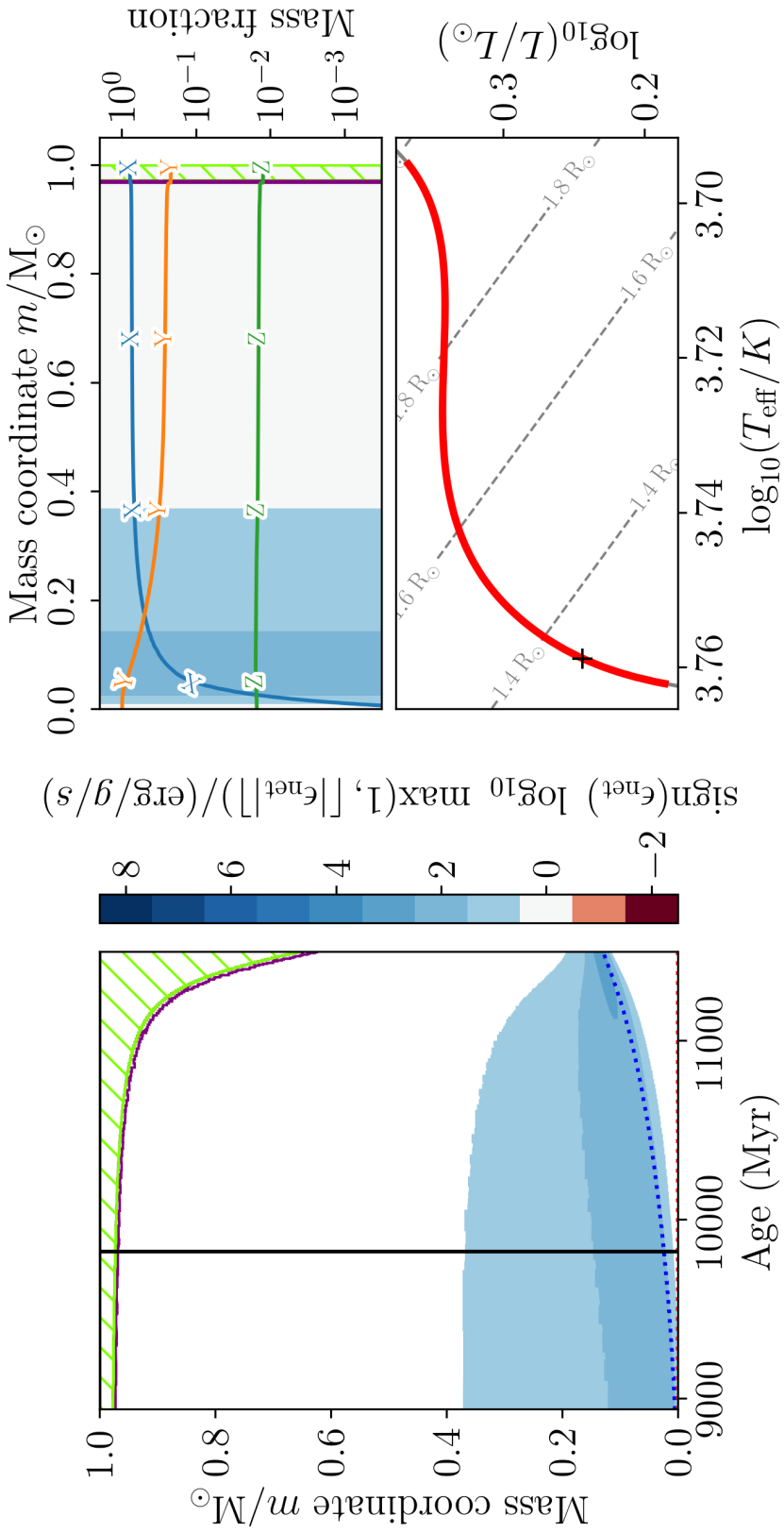

Figure 2.3: Same as Figure 2.2 but for a star in the SGB. The helium-core boundary is shown as the blue dotted line.

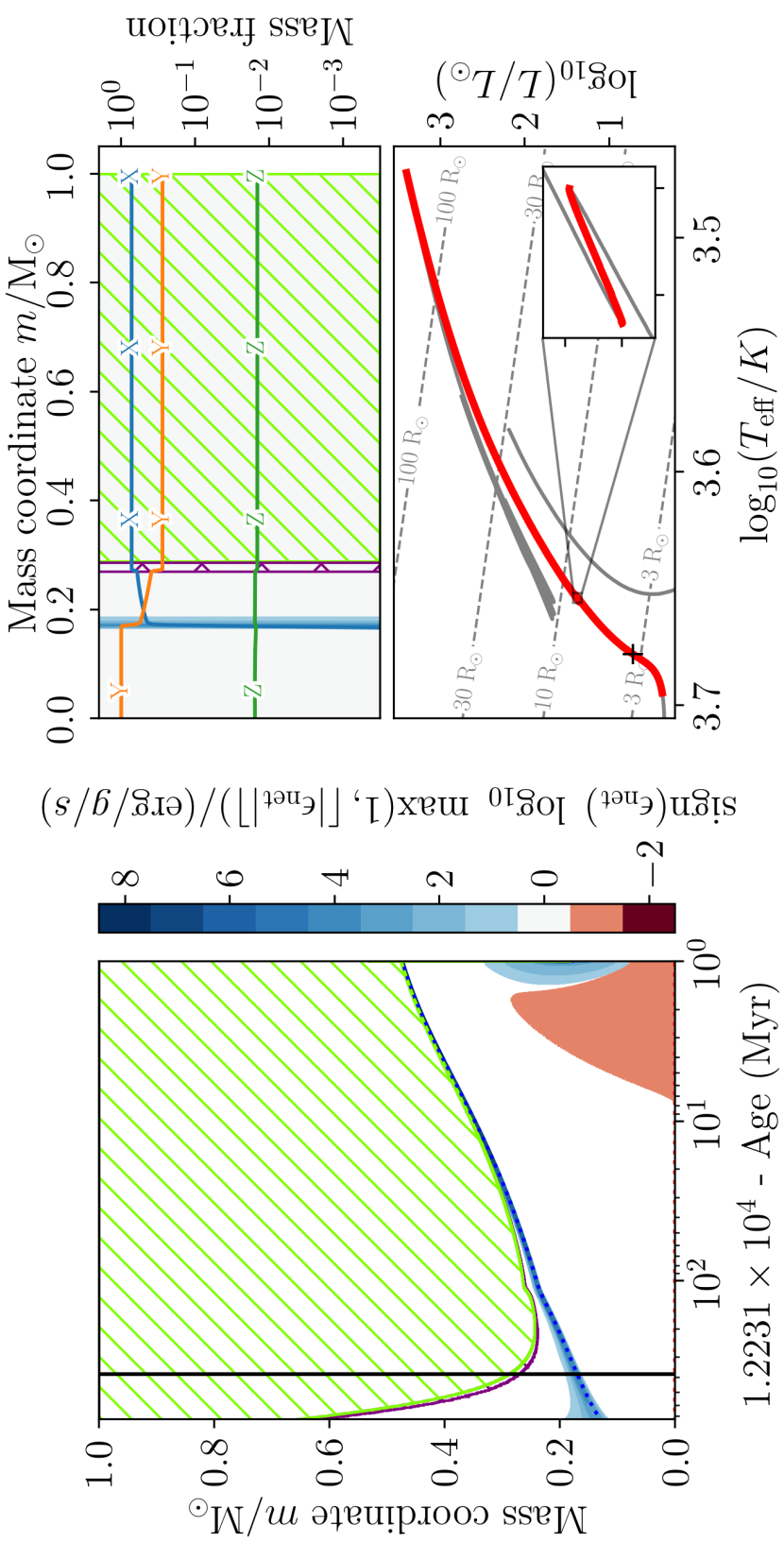

Figure 2.4: Same as Figure 2.3 but for a star in the RGB. The x-axis in the left panel is rescaled using $\tau_{\rm fin} - t$ with a logarithmic scale.

2.1.1.5 Red giant branch bump

Early in the RGB the track a star makes in the HRD reverses direction and descends slightly (around 0.05 dex in luminosity) before continuing to ascend the RGB. The star crosses the same location in the HRD three times as seen in the lower right inset in the bottom right panel of Figure 2.4. This means that in star clusters there is an excess of stars observed at this location. This pile up of stars is called the Red Giant Branch bump (RGBb), and was predicted by Thomas (1967); Iben (1967, 1968) and confirmed in the globular cluster 47 Tuc (King et al. 1985). The cause for this temporary reversal of the track in the HRD is that the hydrogen-burning shell encounters the change in composition left behind by the deepest extent of the convective envelope during first dredge-up (Thomas 1967; Iben 1967, 1968; Salaris et al. 2002; Khan et al. 2018). Once the hydrogen-burning shell has passed through this region of varying composition, the star continues up the RGB.

2.1.1.6 Helium flash

In stars with masses less than around $1.8 - 2.2$ $M_\odot$, when the helium-core mass reaches approximately 0.45–0.5 $M_\odot$ helium ignites off-centre (e.g. Girardi 1999). This is shown in the left panel of Figure 2.5 by the positive net nuclear energy generation rate (blue shaded region) starting at around 0.2 $M_\odot$. The precise mass of the helium core depends on metallicity, stellar mass, and input physics (Chiosi et al. 1992; Salaris et al. 2002, and references therein). The peak temperature is at a mass coordinate of around 0.2 $M_\odot$, which is where helium ignition starts. The process through which helium burns is the triple-α process whereby three α particles combine to form a carbon nucleus (Salpeter 1952; Cyburt et al. 2010). This triple-α process is extremely sensitive to temperature with a burn rate proportional to approximately T^{30-40}. Due to this extreme dependence on temperature, and the degeneracy of the core, helium-burning under these conditions is a run-away thermal process. The increase in temperature because of the energy release from helium burning

is not counterbalanced by an increase in pressure as the core is degenerate. The burning is only halted when the temperature of the core becomes high enough to lift the degeneracy. This process of runaway burning is known as the helium flash (e.g. Thomas 1967; Chiosi et al. 1992; Salaris & Cassisi 2005). The first and strongest flash reaches a peak helium-burning luminosity $L_{\rm He}$ of 10^{9-10} $L_{\odot}$. However, almost all of this energy is absorbed to lift the degeneracy in the core. After the first main helium flash, the core is still partly degenerate as the layers below the flash are not heated by it. This same process occurs repeatedly but each sub-flash is slightly closer to the centre until the whole helium core is no longer degenerate and quiescent Core Helium-Burning (CHeB) begins. Stars with masses greater than around 2.2 $M_{\odot}$ do not go through the helium flash process as their cores do not become degenerate before helium ignition.

2.1.1.7 Core helium-burning

Low-mass stars, with masses below around 1.8 $M_{\odot}$ ignite helium with approximately the same helium-core mass (around 0.45–0.5 $M_{\odot}$) because of the helium flash (Chiosi et al. 1992). As a result of helium-burning, a carbon-oxygen core forms inside the helium core. As a consequence of this almost constant helium-core mass these stars all occupy the same location in the HRD, even though the stars all have different total masses. This concentration of stars in the HRD is called the RC. The investigation in this thesis concentrates on this RC phase of stellar evolution. Stars which did not go through the helium flash are intermediate-mass stars and their helium-core mass is proportional to their total mass. These intermediate-mass stars have masses greater than around 2.2 $M_{\odot}$ (Chiosi et al. 1992; Girardi 1999; Salaris et al. 2002; Salaris & Cassisi 2005). In both low- and intermediate-mass stars the centre of the helium core is convective when quiescent core helium-burning is achieved. In low-mass stars there are still traces left of the helium flash and sub-flashes as shown in the composition profile in the top right panel of Figure 2.6. These traces can most easily be seen by the steps in the Z composition profile between m = 0.3 $M_{\odot}$ and m = 0.4 $M_{\odot}$ in the top right panel of Figure 2.6. These steps are left behind by the top of the convective zones of

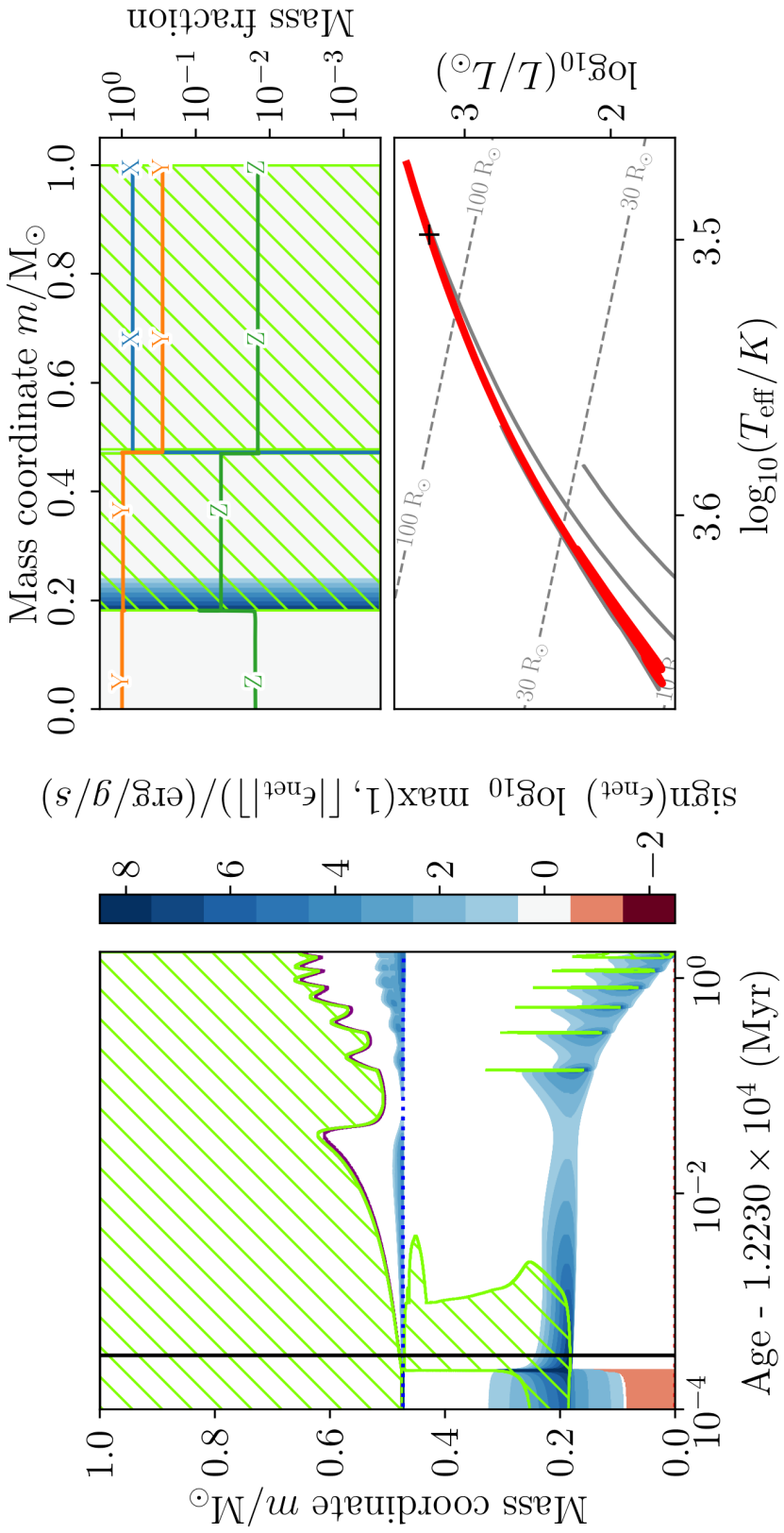

Figure 2.5: Same as Figure 2.3 but when undergoing the helium flash and sub-flashes.

the helium flash and sub-flashes. Chapters 5 and 6 discuss this evolutionary phase in more detail. In this thesis this phase is defined as having a convective helium-core and ends when the central helium mass fraction reaches $Y_C = 10^{-6}$.

2.1.1.8 Early asymptotic giant branch

The next phase in stellar evolution takes place after helium is exhausted in the core and a helium-burning shell forms around the carbon-oxygen core. In this thesis only the early-Asymptotic Giant Branch (AGB) is discussed as the evolutionary models are stopped in the early-AGB phase. As the star transitions from core helium-burning to shell helium-burning, there is a phase of micropulses (Mazzitelli & Dantona 1986). These micropulses, also called gravonuclear instabilities, are secular instabilities and are caused by a sharp change in composition at the carbon-oxygen core boundary. This sharp change in composition results in a thin-shell instability (Sweigart et al. 2000). These micropulses increase the width of the composition transition until quiescent shell helium burning can occur. Once quiescent shell helium-burning has been established, there is no longer a source of energy below it and the carbon-oxygen core cools. It is here that the simulation is stopped and further phases are not covered in this thesis. When the star loses its envelope it becomes a white dwarf (Salaris & Cassisi 2005). Neither the Asymptotic Giant Branch nor the white dwarf evolutionary phases are covered in this work.

2.1.2 MESA

Stellar structure and evolution models are essential tools to fulfil the research objectives of this work. The detailed stellar evolution code MESA allows for a broad range of astrophysical problems to be investigated. MESA has been utilised for more than a decade and has gone through numerous updates. In this thesis, MESA version 11701 is used.

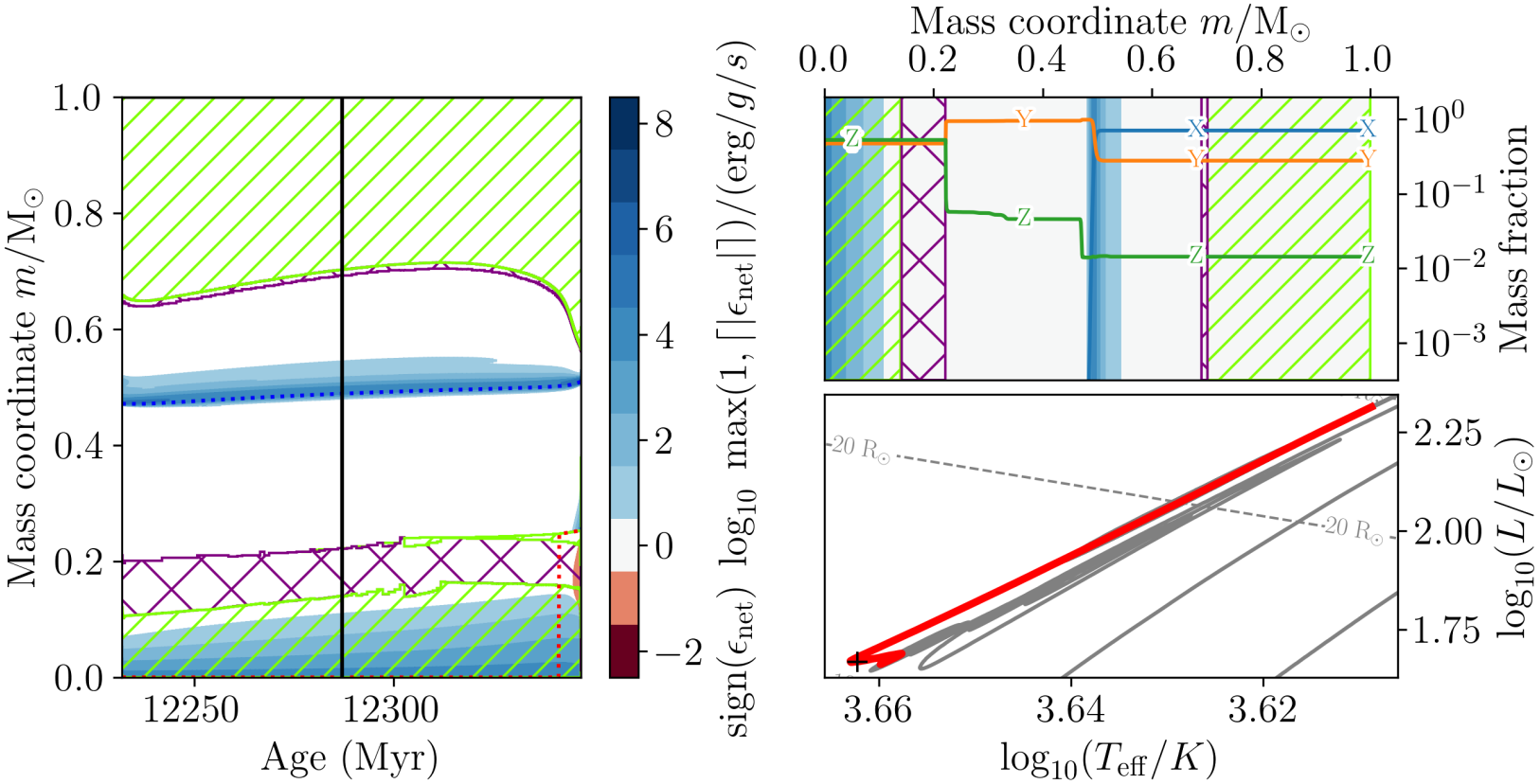

Figure 2.6: Same as Figure 2.3 but for a star undergoing core helium-burning. The carbon-oxygen-core boundary is shown by the red-dotted line.

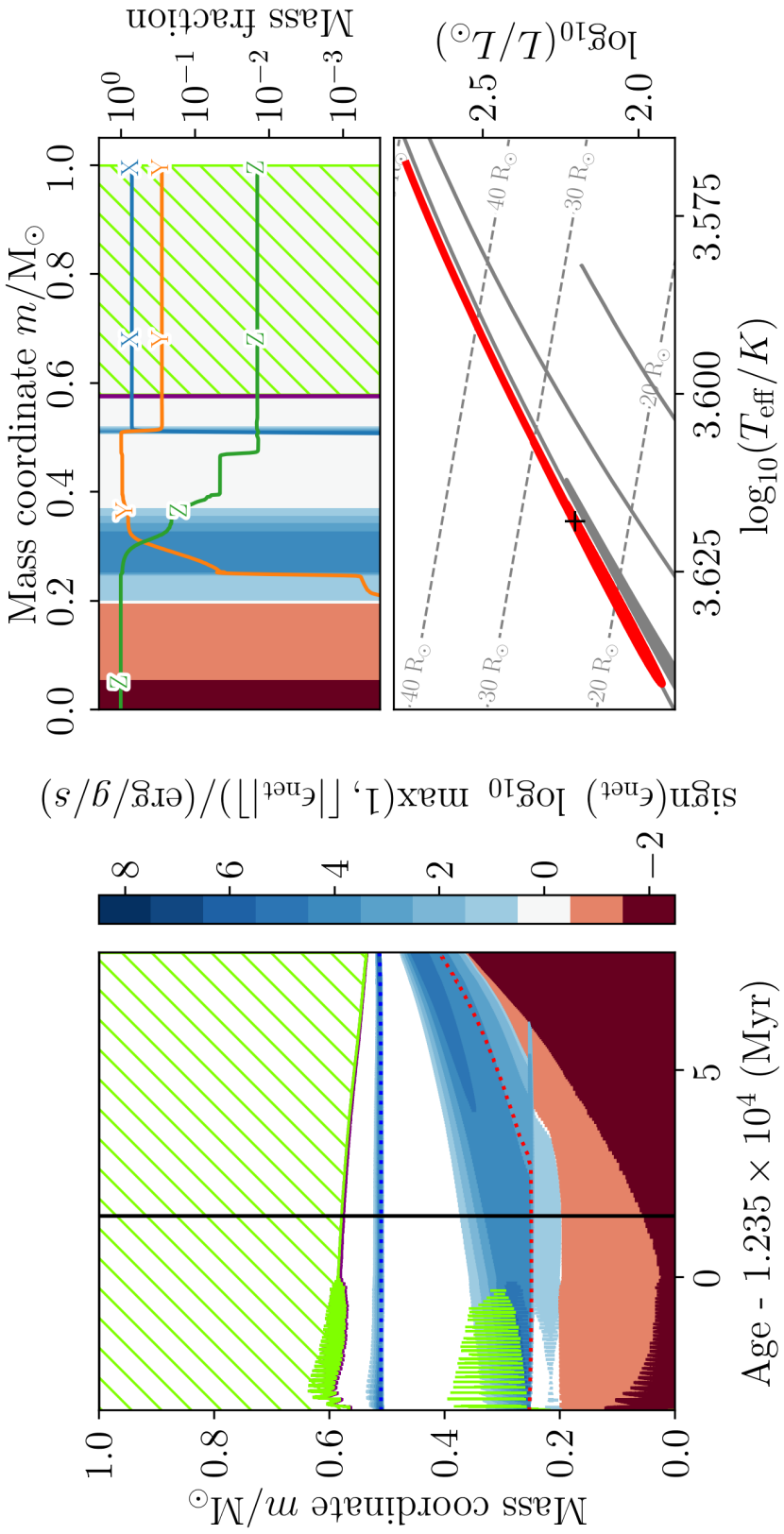

Figure 2.7: As Figure 2.6 but for a star early on the AGB.

The star module in MESA is a one-dimensional stellar evolution code. MESA star models stellar physics, structure, and evolution through advanced numerical methods. The functionality in MESA enables the modelling and exploration of a wide range of stellar masses and metallicities. With the numerical methods implemented, MESA star is able to simulate difficult evolutionary phases such as degenerate helium ignition (also called the helium flash and described in Section 2.1.1.6). In this work MESA models are used to analyse core helium-burning in the red clump.

MESA solves the full structure and composition equations simultaneously (Paxton et al. 2011). There are two main types of files output by MESA, they are the history file and the profile files. History files contain quantities such as stellar age, current mass, effective temperature, and a wide array of other quantities selected by the user. Similarly, profile files contain model properties in each zone from the surface to the centre of the star at a single time, such as temperature, density, pressure, composition, and a wide array of other quantities also selected by the user. In the models used in this thesis, the atmosphere of the modelled star is treated as part of its interior. This avoids the issue described by Jermyn et al. (2022) in Section 6.4 thereof, which states that when writing a profile file to disk for use with the stellar oscillation code gyre (Townsend & Teitler 2013; Townsend et al. 2018, and described in Section 3.5), the atmosphere is attached incorrectly as the reconstructed atmosphere is not in hydrostatic equilibrium. One of the key advantages of MESA is that it enables custom code to run through so-called hooks. These hooks are used to run my own additions inside MESA. In this thesis, whenever I refer to MESA, I refer to the star module.

To run MESA, a set of inlists needs to be supplied to it. These inlists define the inputs options MESA uses whilst running. These inputs determine the initial parameters of the star as well as the macro- and micro-physics used inside the star. In circumstances where the inlist options are insufficient to correctly model a problem, MESA provides a way to extend its capabilities. The run_star_extras file of MESA provides hooks which allow for custom code to be executed by MESA during a calculation.

2.2 Binary stellar evolution

The types of stars that are the focus of this thesis are low- and intermediate-mass stars which are in the CHeB phase of evolution. These stars can have had mass transfer or stellar mergers, and therefore an introduction to binary stellar evolution is required. Stars in the RC can have helium-core masses that do not correspond to the star's total mass if assuming single stellar evolution.

This section describes the main points of interest for binary stellar evolution. A more detailed overview is provided by e.g. Paczynski (1976); Langer (2012); Benacquista (2013); De Marco & Izzard (2017) and references therein. Pairs of stars that are gravitationally bound to each other are called binary stars. All binary systems consist of a primary and a secondary star, in which the more massive star is typically the primary one. Approximately half of stars in the mass range between $0.8M_{\odot}$ and $1.4M_{\odot}$ are actually binary, triple, or higher order systems of stars that are gravitationally bound (Tokovinin 2014a; Moe & Di Stefano 2017). There are also indications of the binary star fraction being metallicity dependent, with metal poor stars having a higher binary fraction (Gao et al. 2014, 2017; Majewski et al. 2017; Moe & Di Stefano 2017). Depending on their mass, their separation, and their evolutionary state, the two stars in a binary system interact with each other. These interactions can significantly alter the evolution and orbits of these binary stars. An example of such an interaction is Mass Transfer (MT) from one star in a binary system to the other. This mass transfer can happen for a variety of reasons. The simplest mass transfer mechanism is due to stellar wind which accretes mass from one on to the other star. Including the effect of binary evolution is difficult as there is great variability in the outcome of the modelling depending on the assumed initial conditions. For instance, a minor change in the initial separation of a binary system can either lead to the two stars merging or to both stars evolving as single stars.

If the stars in a binary system are 'close enough' they interact. The definition of 'close enough' depends on a few parameters such as the mass of each star, their separation, their evolutionary state, and their radii (e.g. Benacquista 2013). Eccentricity can also play a role, however

once a star ascends the giant branch their orbits circularize rapidly (e.g. Price-Whelan & Goodman 2018). One of the defining characteristics of a binary is the mass ratio $q_{\rm bin}$. It is defined as:

$$q_{\rm bin} = \frac{m_2}{m_1}, \tag{2.8}$$

where m_1 is the mass of the primary star, and m_2 the mass of the secondary star. To understand binary interactions, a definition of the Roche Lobe (RL) is required. The Roche lobe of a star in a binary system is the first shared equipotential surface in the corotating frame of reference (e.g. Paczyński 1971). Figure 2.8 shows a Roche lobe for a binary system with $q_{\rm bin} = 2$. The L_1, L_2, and L_3 Lagrange points are also shown in Figure 2.8. L_1 is where, in the corotating frame, a point feels no net force and the pull from the primary (m_1) and the secondary (m_2) stars are perfectly balanced. L_2 is on the opposite side of the secondary star, and this is the location where matter can most easily leave the binary system. The L_3 Lagrange point is on the opposite side of the primary point, L_1. The shape of the Roche lobe is determined by $q_{\rm bin}$ and is scaled by the orbital separation between the stars. Close to each star, the potential is dominated by gravity from that star. This causes the potential surface to be nearly spherical. Figure 2.8 also shows the potential in the orbital plane. The shape of the potential surface starts to be influenced by tidal effects, moving further from the star. At larger distances, the surface stretches towards the other star. The surface is also flattened along the line connecting the two stars because of the centrifugal forces present in the co-rotating frame. In practice, this means that if stars are much smaller than their Roche lobe and stay that way, they effectively evolve as if they were single stars. However, during their evolution, their radii increase significantly. If the radius increases to such an extent that it approaches the Roche lobe it is no longer spherically symmetric. As the Roche lobe is an inherently three-dimensional structure, an approximation to its volume can be made. Eggleton (1983) found that the volume of the RL can be approximated as a sphere with radius $R_{\rm L}$, which is defined as:

$$R_{\rm L} = a\frac{0.49q_{\rm bin}^{2/3}}{0.69q_{\rm bin}^{2/3} + \ln(1 + q_{\rm bin}^{1/3})}, \tag{2.9}$$

where a is the orbital separation and $q_{\rm bin}$ is the mass ratio. This approximation has an error of less than 1% over the full range of $q_{\rm bin}$.

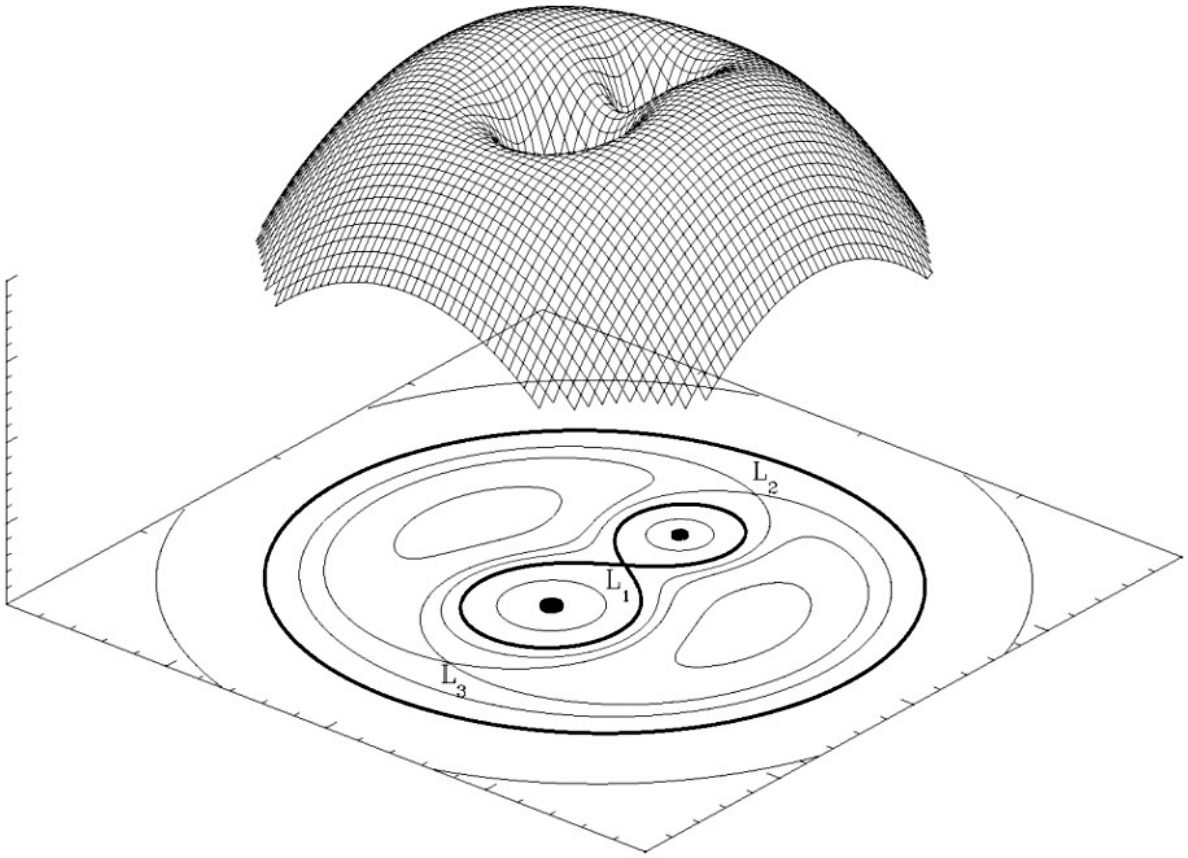

Figure 2.8: Potential surface for a binary with $q_{\rm bin} = 2$. Equipotentials are shown below the potential surface. The locations of L_1, L_2, and L_3 are also shown. The Roche lobe is shown as the thick black line making a figure-8 in the orbital plane containing the L_1 point. Figure from http://hemel.waarnemen.com/Informatie/Sterren/hoofdstuk6.html

If a star fills its Roche lobe it can overflow and transfer mass to its companion due to Roche Lobe Overflow (RLOF) through the L_1 point (e.g. Paczyński 1971; De Marco & Izzard 2017). This filling can occur due to stellar expansion during evolution, changes in the orbital separation, or changes in the mass ratio. During the mass transfer phase, the star that is losing mass is called the donor and the star gaining mass is the accretor. The primary star is not necessarily the accretor. Mass transfer can happen multiple times and in either direction, depending on the system. Mass transfer can also change the orbital separation between stars due to the conservation of angular momentum. This further affects the rate of mass transfer. As the donor star itself is losing mass, its radius also changes. Depending on whether the envelope is convective or radiative the radius either increases or decreases. The radius of a star with a convective envelope increases due to loss of mass. However, when a star has a radiative envelope, the radius decreases due to loss of mass. Main sequence stars with a convective envelope behave differently as for these stars the radius decreases when losing mass (Benacquista 2013). The stability of mass transfer depends on the relative rate of change of the stellar radius and the Roche lobe radius. If the Roche lobe radius grows faster (or shrinks more slowly) than the stellar radius due to mass transfer, then mass transfer is stable as changes in the star caused by mass transfer serve to reduce the mass transfer rate. This then becomes a self-limiting process. Mass transfer proceeds on a nuclear timescale as the evolution of the star drives the relative increase in stellar radius which in turn drives mass transfer. However, if the Roche lobe grows more slowly (or shrinks faster) than the stellar radius, a runaway scenario occurs, and the mass transfer becomes unstable. Three phases can be recognized in which mass transfer occurs. If the donor star is not degenerate, mass transfer can occur in each of these three phases (Thomas 1977; De Marco & Izzard 2017):

(A) while the star is burning hydrogen in its core (in the main sequence),

(B) when the star is burning hydrogen in a shell (in the subgiant branch, Hertzsprung gap, or red giant branch),

(C) or when the star is burning helium (in the asymptotic giant branch).

Mass transfer which occurs in one of these three phases is called case A, case B, or case C mass transfer respectively. If during the mass transfer the total mass of the system is conserved it is said to be conservative mass transfer. When mass is lost from the system, it is called non-conservative mass transfer (e.g. Benacquista 2013). There are two primary mechanisms for non-conservative mass transfer. The first mechanism occurs during dynamically unstable mass transfer. If the envelope of the donor grows beyond the Roche lobe radius, it can engulf the accretor and form a Common Envelope (CE). The second mechanism occurs if mass transfer is dynamically stable, and the mass loss rate of the donor is larger than the maximum accretion rate of the accretor. Material builds up around the accretor which eventually causes a common envelope to form. Once a common envelope has formed, Common Envelope Evolution (CEE) takes place. Mass can be removed from the common envelope by the orbital motion of the stars. The energy required to eject material comes from the orbital energy of the system. This extraction of energy from the orbit causes the orbital radius to decrease. This decrease in orbital separation may also increase the mass transfer rate of the donor. This could become a run-away process and cause the stars to eventually merge. Stars which merge in the main sequence due to case A mass transfer are called case A mergers. These types of mergers generally result in stars which closely follow the evolution of a more massive main sequence star as they have not yet had time to develop a helium core that can live through the merger process. Similarly, when the merger occurs during case B mass transfer it is called a case B merger. In case B mergers, the more massive component of the binary has a helium core which survives the merging process because of the stabilizing effect of the composition gradient at the helium-core boundary. However, the CEE and merging phases are not well understood as it is very complex to model the CEE and merging phases (Ivanova et al. 2013).

The types of stars that are the focus of this thesis are low- and intermediate-mass stars during their core helium-burning phases. These stars can only have had case A or case B mass

transfer or mergers. In case A stars, the large scale changes induced are difficult to infer as these stars behave as a main-sequence star with a higher initial mass and different composition from their initial composition. If such a star were found in a cluster, it is possible to see that it has an anomalous composition and a different age, compared to the rest of the cluster (e.g. Miglio et al. 2021). In case B mass transfer and mergers the helium core is well developed and insulated from mass gain or mass loss due to binary interactions. This means that it is possible for stars in the RC to have helium-core masses that do not correspond to the star's total mass.

Chapter Three

Asteroseismology

This chapter is an introduction to asteroseismology and I show some examples of numerically computed modes. Comprehensive coverage is provided in Aerts et al. (2010), the lecture notes by Christensen-Dalsgaard (2014)[1], or Basu & Chaplin (2018). With the advance of observational platforms, as discussed in Chapter 1, it is possible to have high-quality observations of stellar oscillations. This means high precision observations with multi-year baselines. The *Kepler* space telescope achieved this high-quality through four years of uninterrupted observations with better than 20 parts-per-million precision in magnitude (Borucki 2017). Stellar oscillations are characterised as pressure-mode oscillations (p-modes), gravity-mode oscillations (g-modes), a mixture between p-modes and g-modes called mixed-mode oscillations, and fundamental-mode oscillations (Christensen-Dalsgaard 2014). P-mode oscillations can be clearly observed in the Sun (e.g. Thompson et al. 2003) and are acoustic. The perturbations associated with these modes in the stellar interior are largely radial in nature. The pressure gradient is the restoring force for these oscillations which brings the system back into equilibrium. G-mode oscillations can be observed in many types of stars, for example γ-Dor and δ-Sct stars (e.g. Fitch 1976; Kaye et al. 1999; Aerts et al. 2010, and references therein). The perturbations associated with g-modes are largely hori-

[1] https://users-phys.au.dk/jcd/oscilnotes/ or https://web.archive.org/web/20221006160016/https://users-phys.au.dk/jcd/oscilnotes/Lecture_Notes_on_Stellar_Oscillations.pdf

zontal. They can only propagate in radiative regions inside stars as the restoring force for these oscillations is buoyancy. In a radiative zone, if a parcel of material is displaced downwards it experiences an upwards force due to its buoyancy in the more dense surrounding medium. It then overshoots into the less dense region above its equilibrium position and experiences a downwards force, thus repeating the cycle. However, if the parcel enters a convective region it continues its motion until it mixes with the surrounding medium. Fundamental modes are analogous to surface waves in deep water and will not be discussed further in this thesis but are included here for completeness.

This chapter is structured as follows. In Section 3.1 the wave equations are derived. Section 3.2 describes the basics of stellar oscillations. Section 3.3 describes solar-like oscillations. Section 3.4 discusses mixed modes. Finally, Section 3.5 describes numerically computed oscillation modes.

3.1 Stellar linear adiabatic oscillation equations

The study of oscillations in stars requires knowledge of the response of stellar structure to mechanical disturbances to that structure. As stars are comprised of self-gravitating fluids, the basic equations from hydrodynamics can be utilized to describe this response.

3.1.1 Basic equations

The equations which enable study of the response to mechanical disturbances are the mass continuity equation (conservation of mass), equations of motion (conservation of momentum), Poisson's equation for the gravitational field, and an equation to describe heat transport (conservation of energy). Assuming that the fluid is inviscid and gravity is the only force counterbalancing pressure

(Christensen-Dalsgaard 2014), the equations are:

$$\frac{\partial \rho}{\partial t} + \vec{\nabla} \cdot (\rho \vec{v}) = 0, \tag{3.1}$$

$$\rho \left(\frac{\partial}{\partial t} + \vec{v} \cdot \vec{\nabla} \right) \vec{v} = -\vec{\nabla} P + \rho \vec{\nabla} \Phi, \tag{3.2}$$

$$\nabla^2 \Phi = 4\pi G \rho, \tag{3.3}$$

where ρ is density, t is time, $\vec{v}$ is the velocity of a fluid element, P is pressure, and Φ the gravitational potential. Equations (2.1) and (3.1) are equivalent as the latter is the time derivative of the former. A fourth equation is required to link pressure and density. When assuming the motion of the fluid is adiabatic (Christensen-Dalsgaard 2014) the energy equation is:

$$\frac{\mathrm{d}P}{\mathrm{d}t} = \frac{\Gamma_1 P}{\rho} \frac{\mathrm{d}\rho}{\mathrm{d}t}, \tag{3.4}$$

where Γ_1 is the first adiabatic exponent defined by Chandrasekhar (1939) as:

$$\Gamma_1 = \left(\frac{\partial \ln P}{\partial \ln \rho} \right)_{\mathrm{ad}}, \tag{3.5}$$

and for a fully-ionized ideal gas $\Gamma_1 = 5/3$. Additionally, the energy equation is related to the sound speed by

$$c_{\mathrm{s}}^2 = \frac{\Gamma_1 P}{\rho}. \tag{3.6}$$

3.1.2 Perturbation analysis

Equations (3.1)–(3.4) form a set of non-linear, coupled differential equations which describe the behaviour of fluid in a star. This set of equations is difficult to solve and can only be solved analytically in special cases (e.g. Pekeris 1938; Owen 1957) through the use of polytropes. However, stellar oscillations can be treated as small perturbations around the equilibrium structure. For example, oscillations in the Sun cause variations in luminosity of order 10^{-6} and in velocity of order 1 m s^{-1}(Davies et al. 2014; Hale et al. 2016). Such small variations enable the oscillations to be treated as linear oscillations and allows for the use of first-order perturbation analysis.

In this perturbation analysis the equilibrium structure is assumed to be static. If an arbitrary physical quantity ψ (e.g. pressure, temperature, density, etc.) is perturbed there are two ways in which this can be represented: the Eulerian or Lagrangian form. The Eulerian perturbation is defined as the perturbation at a fixed location, and is denoted by the superscript '$\prime$'. The perturbed quantity ψ takes the form

$$\psi(\vec{r}, t) = \psi_0(\vec{r}) + \psi'(\vec{r}, t), \tag{3.7}$$

where $\vec{r}$ is the position vector from the origin, the subscript '0' denotes the equilibrium value, and $|\psi'/\psi| \ll 1$. The Lagrangian perturbation is defined as the perturbation to a specific fluid element, and is denoted by δ. The perturbed quantity takes the form

$$\psi(\vec{r}, t) = \psi_0(\vec{r}_0) + \delta\psi(\vec{r}_0, t). \tag{3.8}$$

The two forms of perturbation are related to each other by

$$\delta\psi(\vec{r}, t) = \psi(\vec{r}, t) + \vec{\xi} \cdot \vec{\nabla}\psi_0(r), \tag{3.9}$$

where

$$\vec{\xi} \equiv \vec{r} - \vec{r}_0. \tag{3.10}$$

The total time derivative of ψ is:

$$\frac{\mathrm{d}\psi}{\mathrm{d}t} = \frac{\partial\psi}{\partial t} + \vec{v} \cdot \vec{\nabla}\psi. \tag{3.11}$$

As the equilibrium structure is assumed to be static ($\vec{v}_0 = 0$), any velocity $\vec{v}$ is due to the perturbation. Therefore, the Lagrangian and Eulerian velocities are equal, and

$$\vec{v} = \frac{\mathrm{d}\vec{\xi}}{\mathrm{d}t} = \frac{\partial\vec{\xi}}{\partial t}. \tag{3.12}$$

Substituting the perturbed quantities (Equation 3.7) into Equations (3.1)–(3.4) and keeping only first-order terms gives the Eulerian linearized basic equations. This gives for the continuity equation:

$$\frac{\partial\rho'}{\partial t} + \vec{\nabla} \cdot \left(\rho_0 \frac{\partial\vec{\xi}}{\partial t}\right) = 0, \tag{3.13}$$

for the equations of motion:

$$\rho_0 \frac{\partial^2 \vec{\xi}}{\partial t^2} = -\vec{\nabla} P' + \rho_0 \vec{\nabla} \Phi' + \rho' \vec{\nabla} \Phi_0, \tag{3.14}$$

for the Poisson equation:

$$\nabla^2 \Phi' = 4\phi \mathrm{G} \rho', \tag{3.15}$$

and for the adiabatic energy equation:

$$P' + \vec{\xi} \cdot \vec{\nabla} P_0 = \frac{\Gamma_{1,0} P_0}{\rho_0} \left(\rho' + \vec{\xi} \cdot \vec{\nabla} \rho_0 \right). \tag{3.16}$$

The $\Gamma_{1,0} P_0 / \rho_0$ term only uses equilibrium quantities and therefore it is simply equal to the unperturbed sound speed

$$\frac{\Gamma_{1,0} P_0}{\rho_0} = c_{\mathrm{s},0}^2. \tag{3.17}$$

3.1.3 Stellar linear adiabatic oscillation equations

The linear adiabatic oscillation equations are obtained by rewriting Equations (3.13)–(3.15) in spherical polar coordinates with the origin at the centre of the star. In this system, r is the radial distance, θ the co-latitude (angle from the north pole), and ϕ the longitude. In this coordinate system, vector quantities can be split into a radial component and a horizontal (or angular) component. For example, the displacement $\vec{\xi}$ can be split into:

$$\vec{\xi} = \xi_r \hat{e}_r + \vec{\xi}_h, \tag{3.18}$$

where $\hat{e}_r$ is the radial unit vector.

Combining the continuity equation (Equation 3.13) with the horizontal divergence ($\vec{\nabla}_h \cdot$) of the equation of motion (Equation 3.14) and the fact that horizontal gradients of the equilibrium quantities are zero results in:

$$-\frac{\partial^2}{\partial t^2} \left[\rho' + \frac{1}{r^2} \frac{\partial}{\partial r} \left(r^2 \rho_0 \xi_r \right) \right] = \nabla_h^2 P' + \rho_0 \nabla_h^2 \Phi'. \tag{3.19}$$

Combining the radial component of the equation of motion with $\vec{\nabla}\Phi_0 = -g_0\hat{e}_r$ gives:

$$\rho_0 \frac{\partial^2 \xi_r}{\partial t^2} = -\frac{\partial P'}{\partial r} - \rho' g_0 - \rho_0 \frac{\partial \Phi'}{\partial r}. \tag{3.20}$$

Poisson's equation becomes:

$$\frac{1}{r^2}\frac{\partial}{\partial r}\left(r^2 \frac{\partial \Phi'}{\partial r}\right) + \nabla_h^2 \Phi' = 4\pi \mathrm{G}\rho'. \tag{3.21}$$

Finally, the adiabatic energy becomes:

$$\rho' = \frac{\rho_0}{\Gamma_{1,0} P_0} P' + \rho_0 \xi_r \left(\frac{1}{\Gamma_{1,0} P_0}\frac{\partial P_0}{\partial r} - \frac{1}{\rho_0}\frac{\partial \rho_0}{\partial r}\right). \tag{3.22}$$

In this set of equations the dependence on time appears only in the perturbed quantities, and derivatives with respect to θ or ϕ appear only in ∇_h^2. Therefore, solutions for the dependent variables can take the form:

$$\psi(r, \theta, \phi, t) = \psi'(r) Y_l^m(\theta, \phi) e^{-i\omega t}, \tag{3.23}$$

where $Y_l^m(\theta, \phi)$ is a spherical harmonic. Spherical harmonics are described by two numbers, namely the degree ℓ, and the azimuthal order m. The degree ℓ specifies the number of surface node lines, which is the total number of planes which slice through the Sun. The azimuthal order m specifies how many of these planes slice through the sphere along lines of longitude. Figure 3.1 shows these nodal planes for an $\ell = 6, m = 0$ and an $\ell = 6, m = 3$ mode. Spherical harmonics take the form

$$Y_l^m(\theta, \phi) = (-1)^m c_{lm} P_l^m(\cos\theta) e^{im\phi} \tag{3.24}$$

where c_{lm} is a normalization constant such that the integral of $|Y_l^m|^2$ over the unit sphere is unity and is given by

$$c_{lm}^2 = \frac{(2l+1)(\ell - m)!}{4\pi(\ell + m)!}, \tag{3.25}$$

P_l^m is an associated Legendre polynomial which for positive m takes the form of:

$$P_l^m(x) = \frac{(-1)^m}{2^\ell \ell!}\left(1 - x^2\right)^{m/2} \frac{\mathrm{d}^{\ell+m}}{\mathrm{d}x^{\ell+m}}\left(x^2 - 1\right)^\ell \tag{3.26}$$

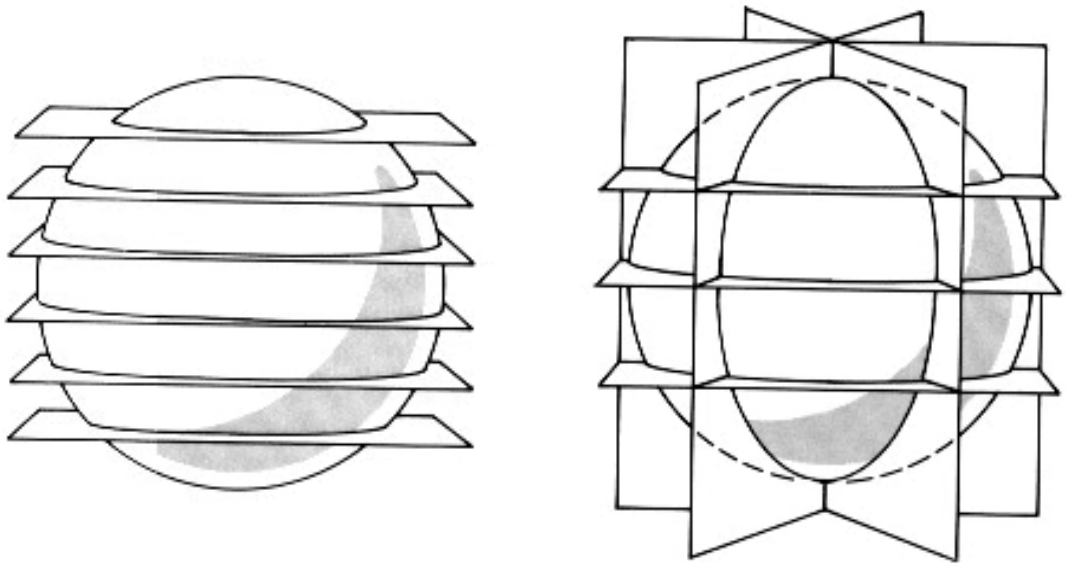

Figure 3.1: Nodal planes of the spherical harmonic with $\ell = 6$ and $m = 0$ in the left panel and with $\ell = 6$ and $m = 3$ in the right panel. Figure from Noyes (1990).

and for negative m:

$$P_l^{-m}(x) = (-1)^m \frac{(\ell - m)!}{(\ell + m)!} P_l^m(x). \tag{3.27}$$

Spherical harmonics also satisfy:

$$\nabla_h^2 Y_l^m(\theta, \phi) = -\frac{\ell(\ell + 1)}{r^2} Y_l^m(\theta, \phi). \tag{3.28}$$

Figure 3.2 shows how perturbations appear on the surface of a sphere according to various ℓ and m.

The radial dependence of the perturbation is found by solving the set of equations formed from Equations (3.19)–(3.21) and substituting ρ' with Equation (3.1.3) and then using Equation (3.23) for each perturbed quantity. Suppressing the 0-subscript for the equilibrium quantities results in:

$$\frac{\mathrm{d}\xi_r}{\mathrm{d}r} = -\left(\frac{2}{r} + \frac{1}{\Gamma_1 P}\frac{\mathrm{d}P}{\mathrm{d}r}\right)\xi_r + \frac{1}{\rho c_\mathrm{s}^2}\left(\frac{S_\ell^2}{\omega^2} - 1\right)P' - \frac{\ell(\ell + 1)}{\omega^2 r^2}\Phi', \tag{3.29}$$

$$\frac{\mathrm{d}P'}{\mathrm{d}r} = \rho\left(\omega^2 - N^2\right)\xi_r + \frac{1}{\Gamma_1 P}\frac{\mathrm{d}P}{\mathrm{d}r}P' + \rho\frac{\mathrm{d}\Phi'}{\mathrm{d}r}, \tag{3.30}$$

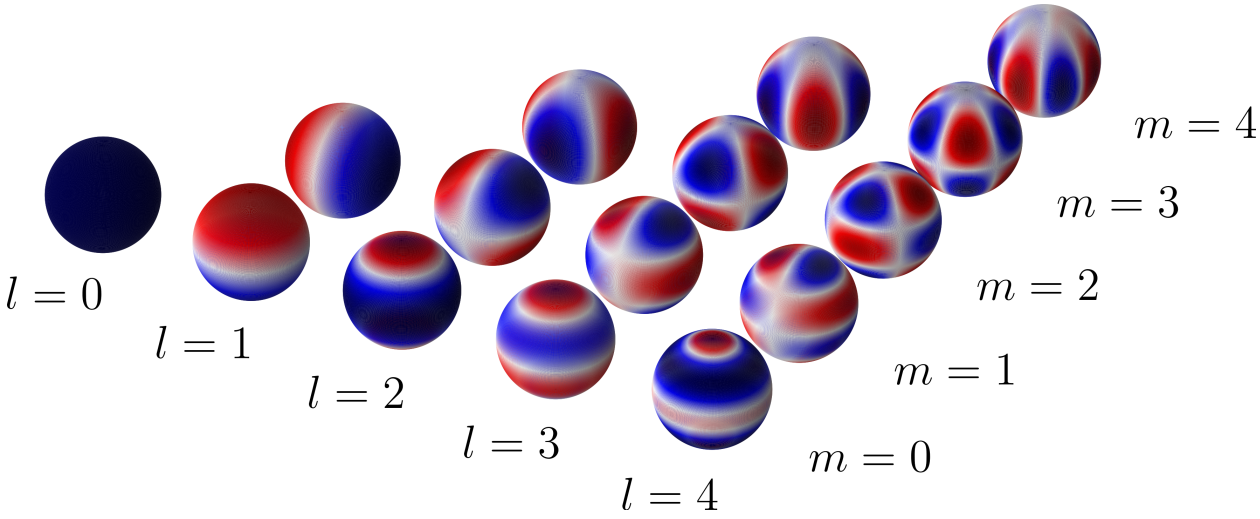

Figure 3.2: Spherical harmonics showing how oscillations perturb the surface for $\ell = 0, 1, 2, 3, 4$ and $0 \leq m \leq \ell$. Red shows the maximum positive displacement from equilibrium, blue the maximum negative displacement from equilibrium, and white is the equilibrium value. Based on Beck (2013).

and

$$\frac{1}{r^2}\frac{\mathrm{d}}{\mathrm{d}r}\left(r^2\frac{\mathrm{d}\Phi'}{\mathrm{d}r}\right) = -4\pi\mathrm{G}\left(\frac{P'}{c_\mathrm{s}^2} + \frac{\rho\xi_r}{g}N^2\right) + \frac{\ell(\ell+1)}{r^2}\Phi', \tag{3.31}$$

where S_ℓ is the Lamb frequency and is defined as:

$$S_\ell^2 = \frac{\ell(\ell+1)c_\mathrm{s}^2}{r^2}, \tag{3.32}$$

and is the reciprocal of the time scale of one horizontal wavelength divided by the local sound speed (Unno et al. 1989). N is the Brunt-Väisälä frequency and is defined as:

$$N^2 = g\left(\frac{1}{\Gamma_1}\frac{\mathrm{d}\ln P}{\mathrm{d}r} - \frac{\mathrm{d}\ln\rho}{\mathrm{d}r}\right). \tag{3.33}$$

It is the frequency at which a parcel of material oscillates when it is displaced from equilibrium (Christensen-Dalsgaard 2014). Equations (3.29)–(3.32) form a fourth-order system of differential equations with eigenvalue ω. Each eigenvalue is called a mode of oscillation and is indexed with n, called the radial order.

The mode inertia, $E_{n,\ell}$, is the fraction of mass of a star which is engaged in pulsation (Basu & Chaplin 2018). It is defined as:

$$E_{n,\ell} = \frac{4\pi \int_0^R \left(\xi_{r,n,\ell}(r)^2 + \ell(\ell+1)\xi_{h,n,\ell}(r)^2\right)\rho r^2 \, \mathrm{d}r}{M\left(\xi_{,n,\ell}(R)^2 + \ell(\ell+1)\xi_{h,n,\ell}(R)^2\right)}, \tag{3.34}$$

where R is the total radius of the star, and M the total mass of the star.

3.1.4 Boundary conditions

To solve the system of equations described in the previous section four boundary conditions are required. These boundary conditions are described in detail in Unno et al. (1989) or Christensen-Dalsgaard (2014). By expanding the equations near $r = 0$, it can be shown that for $\ell > 0$:

$$\xi_r \simeq \ell \xi_h \tag{3.35}$$

and

$$\frac{\mathrm{d}\Phi'}{\mathrm{d}r} \simeq \frac{\ell}{r}\Phi'. \tag{3.36}$$

Similarly, assuming a definite boundary at $r = R$ and assuming that the Lagrangian pressure perturbation vanishes at this surface results in:

$$\delta P = P' + \xi_r \frac{\mathrm{d}P}{\mathrm{d}r} = 0 \tag{3.37}$$

The final boundary condition is found by assuming that Φ' and its gradient are continuous at the surface, which results in:

$$\frac{\mathrm{d}\Phi'}{\mathrm{d}r} + \frac{\ell+1}{r}\Phi' = 0. \tag{3.38}$$

3.2 Approximate solutions to the wave equations: the 1st order asymptotic approximation

Non-radial, adiabatic oscillations in stars are determined by a fourth-order system of differential equations and associated boundary conditions, as shown by Equations (3.29)–(3.32) and Equations (3.35)–(3.38) respectively. Obtaining solutions for this system of equations is difficult, and to make analytical study tractable it is possible to reduce the equations to a system of second-order equations. This is done by ignoring the perturbation to the gravitational potential by setting $\Phi' = 0$. This is known as the Cowling approximation (Cowling 1941). The set of equations reduces to the single second order equation:

$$\frac{\mathrm{d}^2\xi_r}{\mathrm{d}r^2} = -K\xi_r, \tag{3.39}$$

where

$$K = \frac{\omega^2}{c_\mathrm{s}^2}\left(\frac{S_\ell^2}{\omega^2} - 1\right)\left(\frac{N^2}{\omega^2} - 1\right). \tag{3.40}$$

The solution oscillates as a function of r when $K > 0$ and is exponential when $K < 0$. Therefore, it is oscillatory when:

$$|\omega| > |N| \quad \text{and} \quad |\omega| > S_\ell, \tag{3.41}$$

or

$$|\omega| < |N| \quad \text{and} \quad |\omega| < S_\ell, \tag{3.42}$$

and is exponential (evanescent) when:

$$|N| < |\omega| < S_\ell, \tag{3.43}$$

or

$$S_\ell < |\omega| < |N|. \tag{3.44}$$

Depending on the structure of the star, there may be multiple regions (or cavities) where the mode oscillates. The zeros of the dispersion relation give the boundaries of these cavities, and are known

as turning points. The region where the mode oscillates is also known as the trapping region. There are two types of oscillating solutions, a high-frequency case (Equation 3.41) and a low-frequency case (Equation 3.42). These are called p-modes when the restoring force is pressure, and g-modes when the restoring force is buoyancy (Basu & Chaplin 2018). Figure 3.3 is a propagation diagram, which shows the behaviour of these characteristic frequencies in a 1 $M_\odot$ Solar metallicity star on the MS with central hydrogen mass fraction $X_C = 0.48$. P-mode propagation cavities are the regions where Equation (3.41) is satisfied and are shown for a 3100 μHz $\ell = 1$ p-mode and a 3500 μHz $\ell = 10$ p-mode as the black solid and black dot-dashed lines respectively. These two modes of similar frequency but different degree probe different regions of the star, due to the lower turning point of the $\ell = 10$ mode being less deep. Similarly, g-mode propagation cavities are the regions where Equation (3.42) is satisfied. The propagation cavity of a 60 μHz g-mode is shown in Figure 3.3 as the lower black dashed line. The cavity is independent of ℓ as there is no dependence on ℓ in the Brunt-Väisälä frequency. Mixed modes are modes which have both a p-like and a g-like component. A mixed mode with a frequency of approximately 200 μHz is shown in Figure 3.3 and at this frequency the mode has both a p-mode cavity (black solid line) and a g-mode cavity (black dashed line) separated by an evanescent zone (black dotted line). Mixed modes are briefly discussed in Section 3.4 and discussed in more detail in Chapter 4.

Acoustic oscillations which have a horizontal component encounter a temperature gradient as the wavefront travels through the stellar interior. The part of the wave that propagates deeper in the star is in a hotter region and therefore propagates in a region with a higher sound speed as $c_s \propto \sqrt{T}$. This causes the wave to refract away from the radial direction and undergo total internal reflection. A similar effect occurs with internal gravity waves, where the radial component encounters a gradient in N. These effects are shown in Figure 3.4 which shows the ray paths of two different acoustic waves in the left panel and the ray path of an internal gravity wave in the right panel. Modes of different frequencies travel through different regions of a star. This permits the structure of that star to be investigated in detail as the modes are sensitive to different parts of the

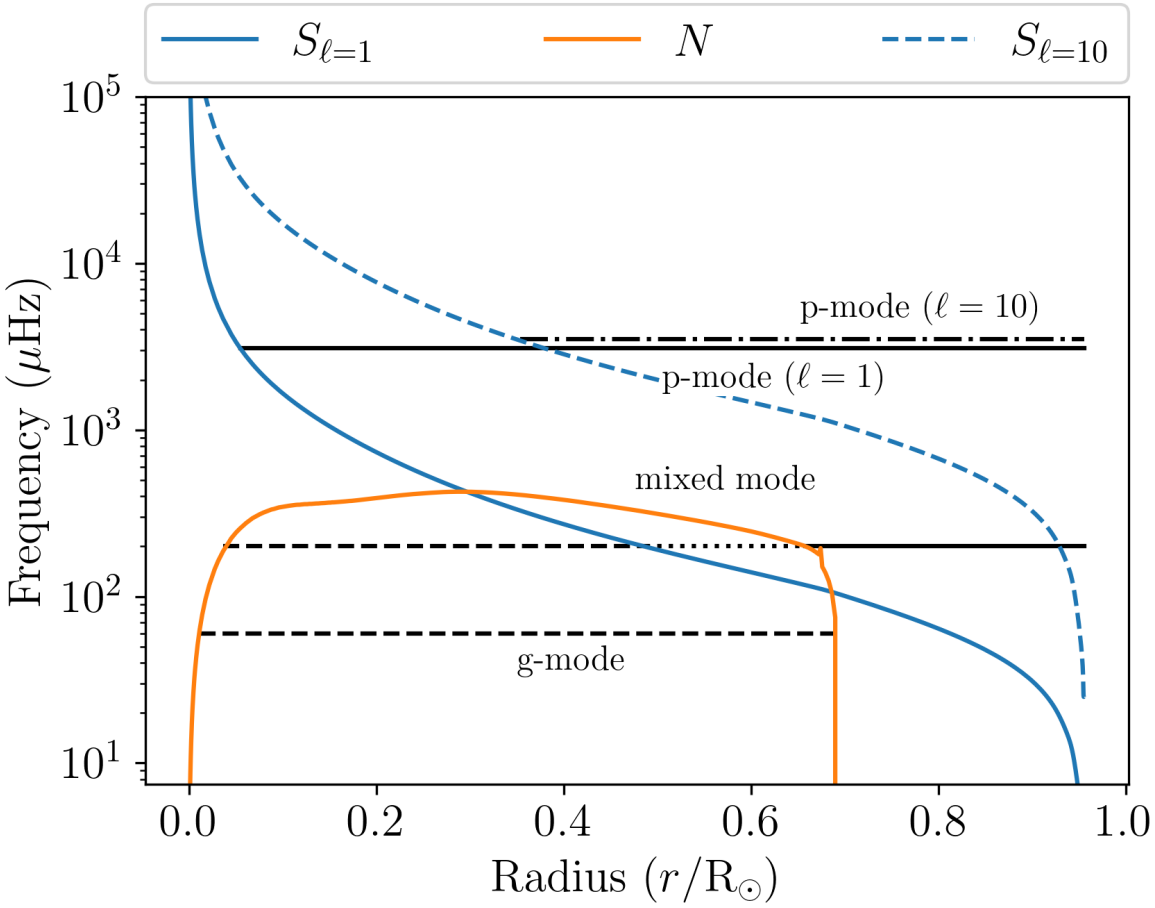

Figure 3.3: Propagation diagram of a 1 $\mathrm{M}_\odot$ solar-metallicity star on the MS with $X_\mathrm{C} = 0.48$. $S_{\ell=1}$ is shown as the solid blue line, $S_{\ell=10}$ as the dashed blue line, and N as the orange line. An $\ell = 1$ p-mode with a frequency of 3100 μHz is shown as the solid horizontal black line, an $\ell = 10$ p-mode with a frequency of 3500 μHz is shown as the dash-dotted black line. A g-mode with a frequency of 60 μHz is shown as the dashed black line. An $\ell = 1$ mixed mode with a frequency of 200 μHz is shown with a dashed black line in the g-like part, with a solid black line in the p-like part, and as a dotted black line in the evanescent zone.

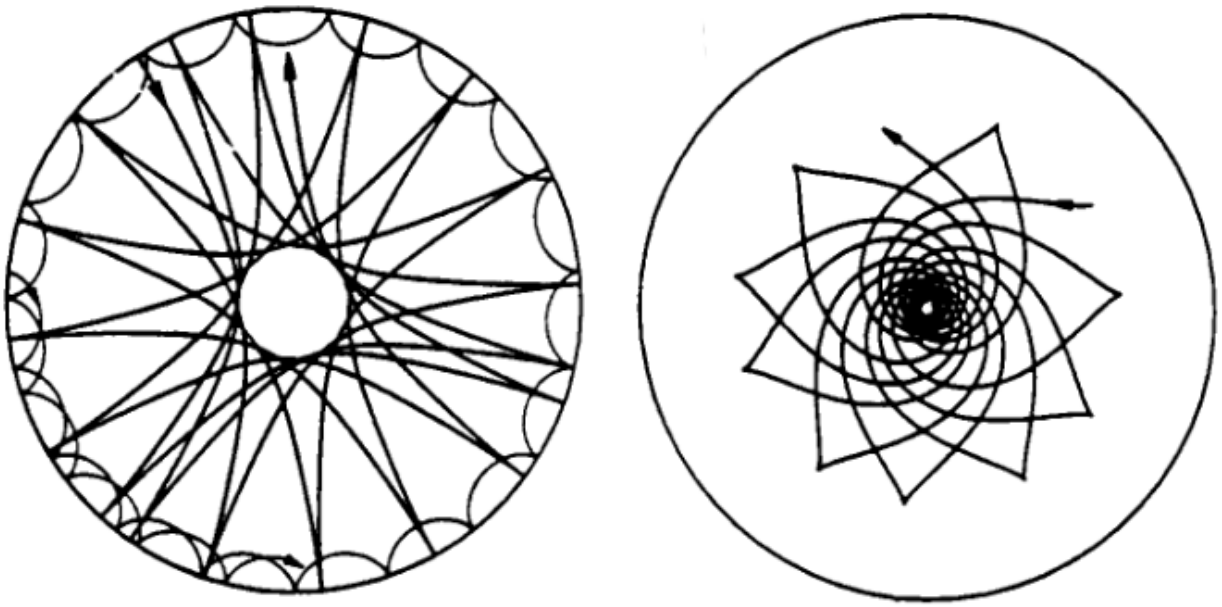

Figure 3.4: The left panel shows ray paths of two acoustic waves in the Sun, the deeply penetrating wave has $\ell = 2,\ n = 8$ and the shallow wave has $\ell = 100,\ n = 8$. The right panel shows the ray path of an internal gravity wave in the Sun with $\ell = 5,\ n = 10$. Figure from Gough et al. (1996).

internal structure of stars. For example, the sound speed inside the Sun has been calculated using this behaviour for 90% of its radius (Basu 1997; Thompson et al. 2003).

Modes with $|m| \geq 1$ are travelling waves. The azimuthal order also satisfies $|m| \leq \ell$, therefore for each mode there are $2l + 1$ possible values of m. Whether m is positive or negative depends on the direction in which the surface nodes move relative to stellar rotation. Modes which travel in the direction of rotation are called prograde modes and have positive m. Modes which travel against the direction of rotation are called retrograde modes and have negative m. In a spherically symmetric star, the frequencies of the $2l + 1$ modes are degenerate. This degeneracy is lifted when the star becomes asymmetric. Typical sources of this asymmetry are stellar rotation or magnetic fields. In the case of rotation, the frequency is split into multiple modes. Modes with positive m have frequencies slightly lower than the $m = 0$ mode, and the oscillations with negative m have frequencies slightly higher than the $m = 0$ mode. The strength of splitting depends on the

rotational frequency Ω and the resulting mode frequency ω_m becomes:

$$\omega_m = \omega_0 + m\Omega, \tag{3.45}$$

where ω_0 is the mode frequency of the $m = 0$ mode and $\Omega \ll \omega_0$.

Changes in brightness of a star is one of the ways in which oscillations are observed. However, only for the Sun do we have adequate resolution to directly image and resolve the surface spatially. This means that for other stars a different approach must be taken. When observing stars, they are at such a great distance that they are point sources. This means that the light which is observed is integrated over the stellar disk. Therefore, the light that is observed is the surface integral of the hot and cold regions from Figure 3.2. For modes with $\ell \geq 1$, there are both hot and cold spots, which are more and less bright respectively. When integrating over the stellar disc the strength of the signal is reduced. It is therefore impossible to directly observe the perturbations shown in Figure 3.2 in stars other than the Sun, and instead the integrated quantities over the stellar disk are observed. Figure 3.5 illustrates the relationship between the degree of a mode, ℓ, and the visibility of the mode (García & Ballot 2019) for a spherically symmetric star with and without limb darkening. As ℓ increases there are more bright and faint regions on the surface (Figure 3.2) which results in more destructive interference of the signal with itself.

3.2.1 P-modes

The cyclic frequency, $\nu_{n,\ell}$, of p-modes is determined by the sound speed in a stellar interior and is approximated by

$$\nu_{n,\ell} = \frac{\omega_{n\ell}}{2\pi} \simeq \Delta\nu\left(n + \frac{\ell}{2} + \epsilon\right), \tag{3.46}$$

where $\nu_{n,\ell}$ is the frequency of the mode with order n and degree ℓ, $\Delta\nu$ is the large frequency separation, and ϵ is a frequency dependent phase determined by near-surface conditions. The large

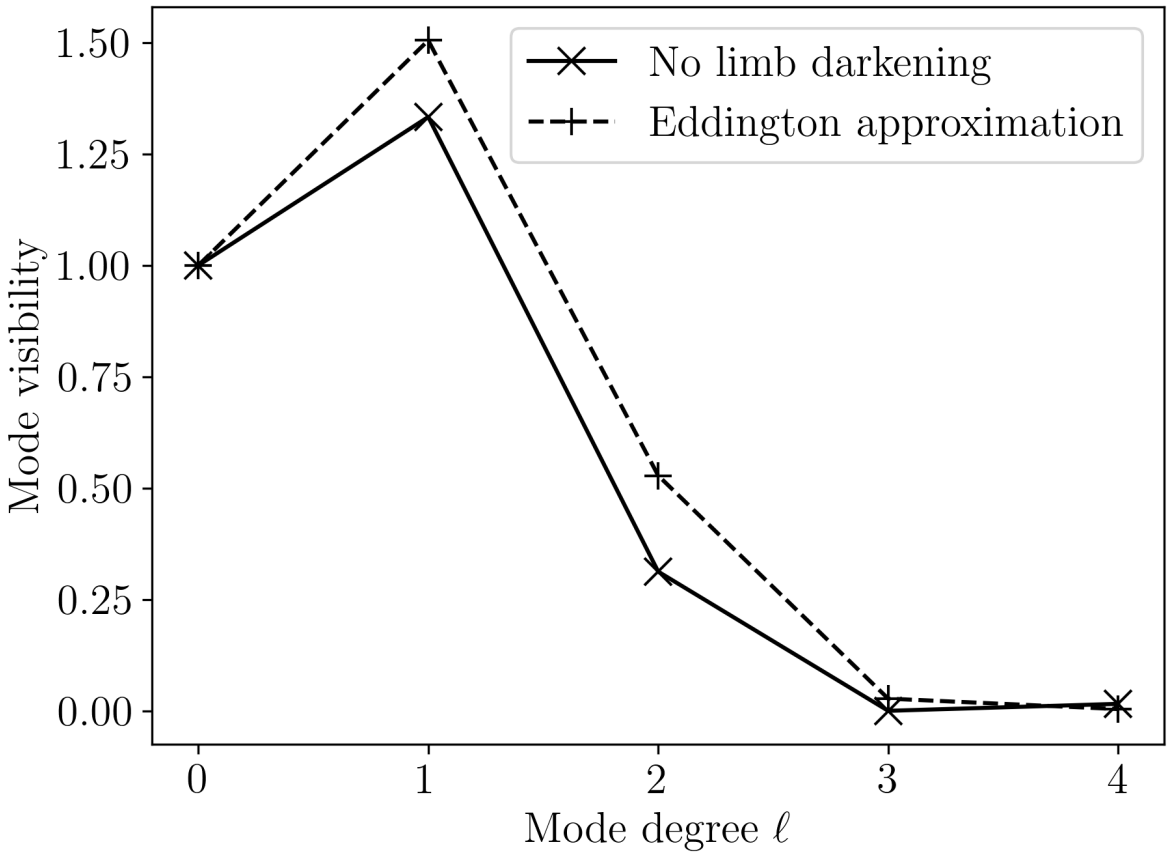

Figure 3.5: Mode visibility normalized to the $\ell = 0$ mode. The solid line with crosses shows the mode visibility without limb darkening and the dashed line with plusses shows the mode visibility with the Eddington approximation of limb darkening.

frequency separation, $\Delta\nu$, is defined as:

$$\Delta\nu = \left(2\int_0^R \frac{\mathrm{d}r}{c_\mathrm{s}}\right)^{-1}, \tag{3.47}$$

where R is the radius of the star and c_s is the sound speed in the interior of the star (Tassoul 1980, 1990). $\Delta\nu$ is the inverse of the travel time of a sound wave to travel from the surface of the star to the core and back to the surface. Therefore, $\Delta\nu$ depends strongly on R, the radius of a star, as well as on c_s, the sound speed. According to Equation (3.46), it is expected that

$$\nu_{n,\ell} \simeq \nu_{n-1,\ell+2}, \tag{3.48}$$

is almost degenerate, where modes with different n and ℓ have almost the same frequency. This results in the so-called small-frequency separation $\delta\nu$ (Christensen-Dalsgaard 2014), which is defined as:

$$\delta\nu_{n,\ell} = \nu_{n,\ell} - \nu_{n-1,\ell+2}. \tag{3.49}$$

Extending the Jeffreys-Wentzel–Kramers–Brillouin (JWKB) analysis to higher order (Tassoul 1980) allows for the variation of c_s in the core to be taken into account. This results in the following relation for $\nu_{n,\ell}$:

$$\nu_{n,\ell} = \frac{\omega_{n,\ell}}{2\pi} \simeq \Delta\nu\left(n + \frac{\ell}{2} + \epsilon\right) - (A\ell(\ell+1) - \delta)\frac{\Delta\nu^2}{\nu_{n,\ell}}, \tag{3.50}$$

where

$$A = \frac{1}{4\pi^2\Delta\nu}\left(\frac{c_\mathrm{s}(R)}{R} - \int_0^R \frac{1}{r}\frac{\mathrm{d}c_\mathrm{s}}{\mathrm{d}r}\,\mathrm{d}r\right). \tag{3.51}$$

Neglecting the $c_\mathrm{s}(R)/R$ term results in:

$$\delta\nu \propto \int_0^R \frac{1}{r}\frac{\mathrm{d}c_\mathrm{s}}{\mathrm{d}r}\,\mathrm{d}r. \tag{3.52}$$

In the central region of a main-sequence star, the change in c_s is mainly driven by the change in composition as hydrogen burns into helium whilst the temperature during hydrogen-burning remains relatively constant (e.g. Solanki 2003). This means that the increase in the mean molecular weight, μ, causes $\delta\nu$ to decrease with age as μ is related to the sound speed through

$$c_\mathrm{s}^2 = \frac{\Gamma_1 P}{\rho} \propto \frac{T}{\mu} \tag{3.53}$$

for an ideal gas.

3.2.2 G-modes

The low-frequency solutions (g-modes) which satisfy Equation (3.42) are better described when using their pulsation periods instead of their frequencies. This pulsation period, $P_{n,\ell}$, of high-order g-modes can be estimated using (Tassoul 1980):

$$P_{n,\ell} = \frac{\Pi_0}{\sqrt{\ell(\ell+1)}}\left(n + \epsilon_g\right), \tag{3.54}$$

where n is the order of the mode, ℓ the degree of the mode, ϵ_g the phase offset determined by the boundary conditions (Christensen-Dalsgaard 2014), and Π_0 is a characteristic period. Π_0 is defined as:

$$\Pi_0 = 2\pi^2 \left(\int \frac{N}{r}\, \mathrm{d}r \right)^{-1}. \tag{3.55}$$

Here, N is the Brunt-Väisälä frequency and r is the radius in the star. The integral is taken over the region where g-modes propagate. These modes are sensitive to the chemical stratification in stars. When assuming a fully ionized ideal gas, the Brunt-Väisälä frequency can be approximated by

$$N^2 \simeq \frac{g^2 \rho}{P}\left(\nabla_{\mathrm{ad}} - \nabla + \nabla_\mu\right), \tag{3.56}$$

where

$$\nabla_{\mathrm{ad}} = \left(\frac{\partial \ln T}{\partial \ln P}\right)_{\mathrm{ad}}, \quad \nabla = \frac{\mathrm{d}\ln T}{\mathrm{d}\ln P}, \quad \text{and} \quad \nabla_\mu = \frac{\mathrm{d}\ln \mu}{\mathrm{d}\ln P}, \tag{3.57}$$

are the adiabatic temperature gradient (∇_{ad}), the temperature gradient (∇), and the composition gradient (∇_μ). For a fully ionized gas the mean molecular mass μ can be approximated by

$$\mu \approx \left(2X + \frac{3}{4}Y + \frac{1}{2}Z\right)^{-1}. \tag{3.58}$$

The composition gradient can have more abrupt variations which cause observable features in modes. An example of this is the abrupt change in composition below the convective envelope after the first dredge-up (e.g. Jiang et al. 2022). The dependence of N^2 on the composition gradient can be seen in Equation (3.56). This dependence permits analysis of the composition gradient (∇_μ) using periods of g-modes.

Similar to p-modes, a period spacing $\Delta P_{n,\ell}$ can be defined as:

$$\Delta P_{n,\ell} = P_{n+1,\ell} - P_{n,\ell}. \tag{3.59}$$

This is the period difference between two modes of the same degree (ℓ), and consecutive radial order (n). Deviations from constant period spacing can provide information about the stratification of density or composition in stars (e.g. Miglio et al. 2008; Degroote et al. 2010). This is possible as period spacings depend on ∇_μ through N as shown in Equation (3.56). In the asymptotic limit (Tassoul 1980), period spacing is independent of n and therefore can be described as:

$$\Delta P_{n,\ell} = \frac{\Pi_0}{\sqrt{\ell(\ell+1)}}. \tag{3.60}$$

3.3 Solar-like oscillations

There are many different kinds of stars in which oscillations are observed (e.g. Christensen-Dalsgaard 2014). In this thesis stars which show Solar-Like Oscillations (SLO) are studied. As the name implies, they are oscillations that are excited and damped via the same mechanisms as in the Sun. The acoustic waves forming oscillations are stochastically driven and damped through turbulent convection in the outer layers of the envelope. This excitation mechanism applies to low-mass stars in the main sequence and low- and intermediate-mass stars in the RGB and later evolutionary stages, i.e. stars that have an outer convective envelope.

The typical signature of SLO is that of a Gaussian-shaped power excess in the Power-Spectral Density (PSD) of observed data. A PSD shows the distribution of power as a function of frequency. Figure 3.6 shows the PSD of the Sun using data from the Global Oscillation at Low Frequencies (GOLF) experiment onboard the Solar and Heliospheric Observatory (SoHO) mission (García et al. 2005). The inset shows the PSD from 3–3.18 mHz with the visible small and large frequency annotated. A comb-like pattern can be seen in the power-excess around 3.1 mHz. This

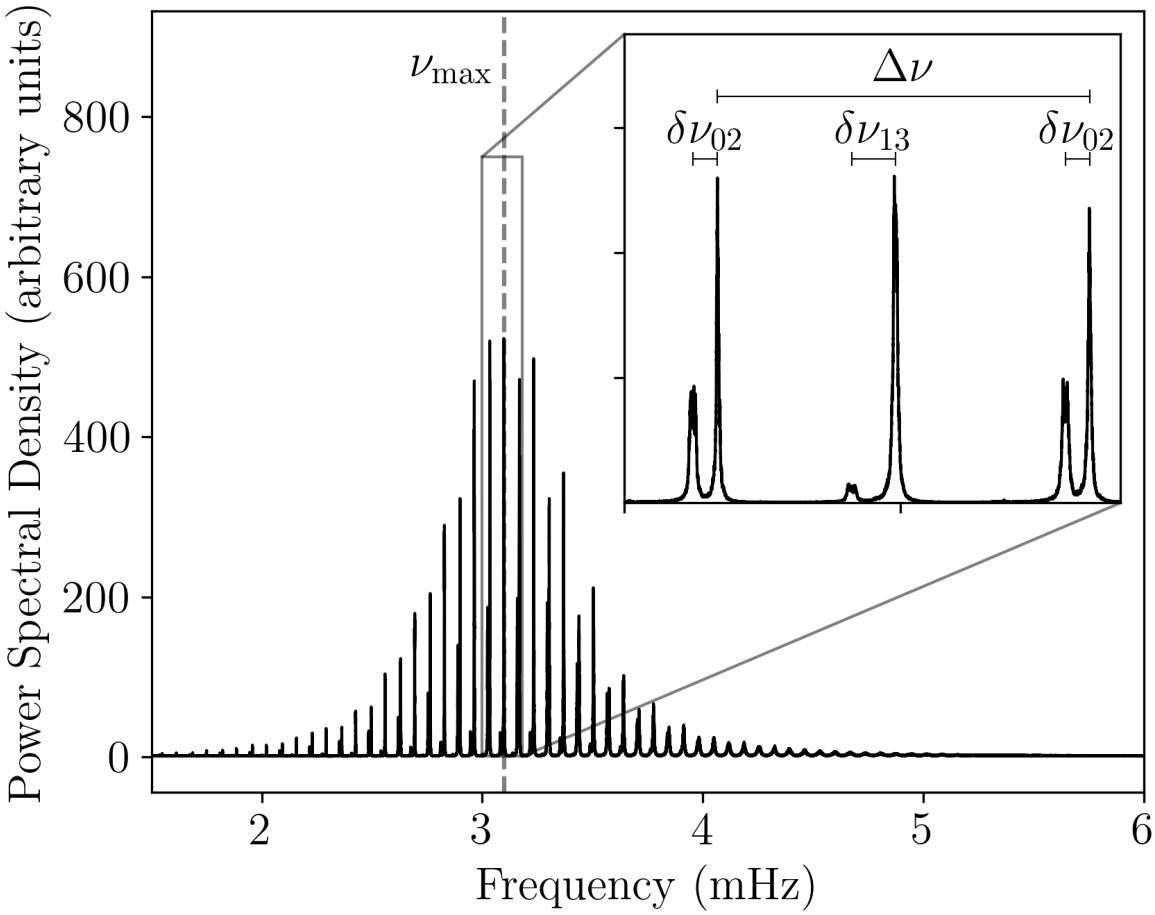

Figure 3.6: Smoothed PSD of the Sun using data from the *GOLF* experiment onboard the *SoHO* mission (García et al. 2005) showing a comb-like pattern of low-degree modes ($\ell \leq 3$). The frequency of maximum oscillation power $\nu_{\max}$ is shown as the grey vertical dashed line. The inset shows the PSD from 3–3.18 mHz and the large and small frequency separations $\Delta\nu$ and $\delta\nu$ are indicated.

frequency is called the frequency of maximum oscillation power $\nu_{\rm max}$, and is shown as the grey vertical dashed line. It has been shown by Brown et al. (1991) that:

$$\nu_{\rm max} \propto \nu_{\rm ac} \propto \frac{g}{\sqrt{T_{\rm eff}}} \propto \frac{M}{R^2\sqrt{T_{\rm eff}}}, \tag{3.61}$$

where $\nu_{\rm ac}$ is the acoustic cut-off frequency, g the surface gravity, $T_{\rm eff}$ the effective temperature, M the stellar mass, and R the stellar radius. However, this scaling between $\nu_{\rm max}$ and $\nu_{\rm ac}$ is empirical and the physical reason for it is still not fully understood. The width of this Gaussian-like power excess was estimated by Mosser et al. (2012) to follow the empirical relation:

$$\sigma = 0.66\ \nu_{\rm max}^{0.88}. \tag{3.62}$$

The average large frequency separation, $\langle\Delta\nu\rangle$, is a good approximation to $\Delta\nu$ in Equation (3.47). Ulrich (1986) showed that $\langle\Delta\nu\rangle$ scales with the square root of the star's mean density such that

$$\langle\Delta\nu_{n,\ell}\rangle \propto \sqrt{\langle\rho\rangle} \propto \sqrt{\frac{M}{R^3}}. \tag{3.63}$$

Equations (3.61) and (3.63) are known as the seismic scaling relations. They are fundamental to inferring global properties of stars. Scaling them by Solar values and combining them, results in the following equations:

$$\frac{M}{\rm M_\odot} \simeq \left(\frac{\langle\Delta\nu\rangle}{\Delta\nu_\odot}\right)^{-4}\left(\frac{\nu_{\rm max}}{\nu_{\rm max\odot}}\right)^{3}\left(\frac{T_{\rm eff}}{T_{\rm eff\odot}}\right)^{3/2}, \tag{3.64}$$

$$\frac{R}{\rm R_\odot} \simeq \left(\frac{\langle\Delta\nu\rangle}{\Delta\nu_\odot}\right)^{-2}\left(\frac{\nu_{\rm max}}{\nu_{\rm max\odot}}\right)\left(\frac{T_{\rm eff}}{T_{\rm eff\odot}}\right)^{1/2}. \tag{3.65}$$

If the luminosity of a star is known, through for example the *Gaia* mission (Gaia Collaboration et al. 2016), an alternate equation for mass can be defined using Equations (3.64) and (3.65) in combination with the Stefan-Boltzmann law $L \propto R^2T_{\rm eff}^4$. This results in the following equation:

$$M \simeq \left(\frac{L}{L_\odot}\right)\left(\frac{\nu_{\rm max}}{\nu_{\rm max\odot}}\right)\left(\frac{T_{\rm eff}}{T_{\rm eff\odot}}\right)^{-7/2}. \tag{3.66}$$

3.4 Mixed modes

In evolved stars, such as SGB and RGB stars, the density in the stellar centre increases as the core contracts and the envelope expands. This results in stronger buoyancy forces acting in the stellar interior. The stronger buoyancy forces in the post-MS phases cause the frequency range of g-modes to increase, whilst p-mode frequencies decrease due to the expansion of the stellar envelope, which causes $\nu_{\max}$ to decrease. This increase of g-mode frequencies and decrease of p-mode frequencies cause them to overlap. Modes in this overlapping frequency range behave as g-modes in the central region of the star and as p-modes in the envelope of the star. A mode with these mixed characteristics is called a mixed mode. As g-modes have only non-radial solutions ($\ell > 0$), mixed modes are only possible for non-radial modes.

Mixed modes have only relatively recently been detected (Carrier et al. 2005; Hekker et al. 2009; Bedding et al. 2010) in solar-like oscillators and the theoretical work on these modes was expanded by Takata (2016a,b). The work of Takata enables a semi-analytical approach to the study of mixed modes. A key requirement for research on mixed modes is to understand the coupling between the g-mode part and the p-mode part of the mixed mode. A brief explanation and derivation of the coupling between the g-mode part and the p-mode part of a mixed mode is given in Section 4.2.1. The full derivation is provided in Takata (2016a).

3.5 Numerically computed oscillation modes

Linking asteroseismic observations from space-based instruments such as *Kepler* and *TESS* to stellar evolutionary models requires a stellar oscillation code. A stellar oscillation code calculates the eigenfrequency spectrum of a given stellar model. The oscillation code `gyre` (Townsend & Teitler 2013; Townsend et al. 2018) has been utilized in this work to compute the eigenfrequency

spectra. Comparing a calculated spectrum from `gyre` to a measured one provides a quantifiable metric for evaluating a stellar model. `gyre` solves the stellar pulsation equations[2] (either adiabatic or non-adiabatic) by linearising the differential equations under the assumption that oscillations can be described by perturbations around an equilibrium state. The equilibrium state is defined by the input stellar model. Although `MESA` can compute some asymptotic seismic quantities, the combination of `MESA` and `gyre` is synergistic in that `gyre` allows us to characterise the seismic properties of `MESA` models more accurately than `MESA` by itself. This in turn, increases the precision of comparisons between models and observations.

In Equation (3.46), which represents the idealised homogenous case, it is expected that the frequencies at which a star oscillates are regularly spaced in frequency. An echelle diagram shows how modes at which a star oscillates can depart from regular spacing (Basu & Chaplin 2018). Echelle diagrams are typically created by plotting ν vs. ν mod $\Delta\nu$. Modes of the same degree ℓ show up as vertical ridges. Figure 3.7 shows a propagation diagram (left) and an echelle diagram (right) for a $1M_\odot$ star with [Fe/H] = -0.5 (top) and [Fe/H] = 0.25 (bottom) for modes around $\nu_{\max}$ calculated using `gyre`. In both models the diagrams show clear vertical ridges as only pure p-modes can propagate in the star. The two models are almost the same, with the [Fe/H] =-0.5 model having a $\Delta\nu$ which is 5% smaller, and therefore has a larger inferred radius since $\Delta\nu \propto \sqrt{\bar{\rho}}$. The small-frequency separation, $\delta\nu_{02}$ (Equation 3.49), is also visible as the offset between the $\ell = 0$ and $\ell = 2$ ridges. The $\delta\nu_{02}$ in the [Fe/H] =-0.5 model is larger than that of the [Fe/H] =0.25 model due to the temperature dependence of the sound speed, c_s. This small-frequency separation decreases as the star evolves along the MS and consumes hydrogen in its core.

Figure 3.8 shows the propagation diagram and echelle diagram in the left panels for a 1 $M_\odot$ immediately after the RGBb with [Fe/H] = -0.5. In the right panels the mode inertia (Equation 3.34) and period-spacing diagrams are shown. The mode inertia of mixed modes can vary greatly. Modes where the g-like component dominates have high inertia as the perturbations are largely in

[2] https://gyre.readthedocs.io/en/stable/ref-guide/osc-equations/dimless-form.html

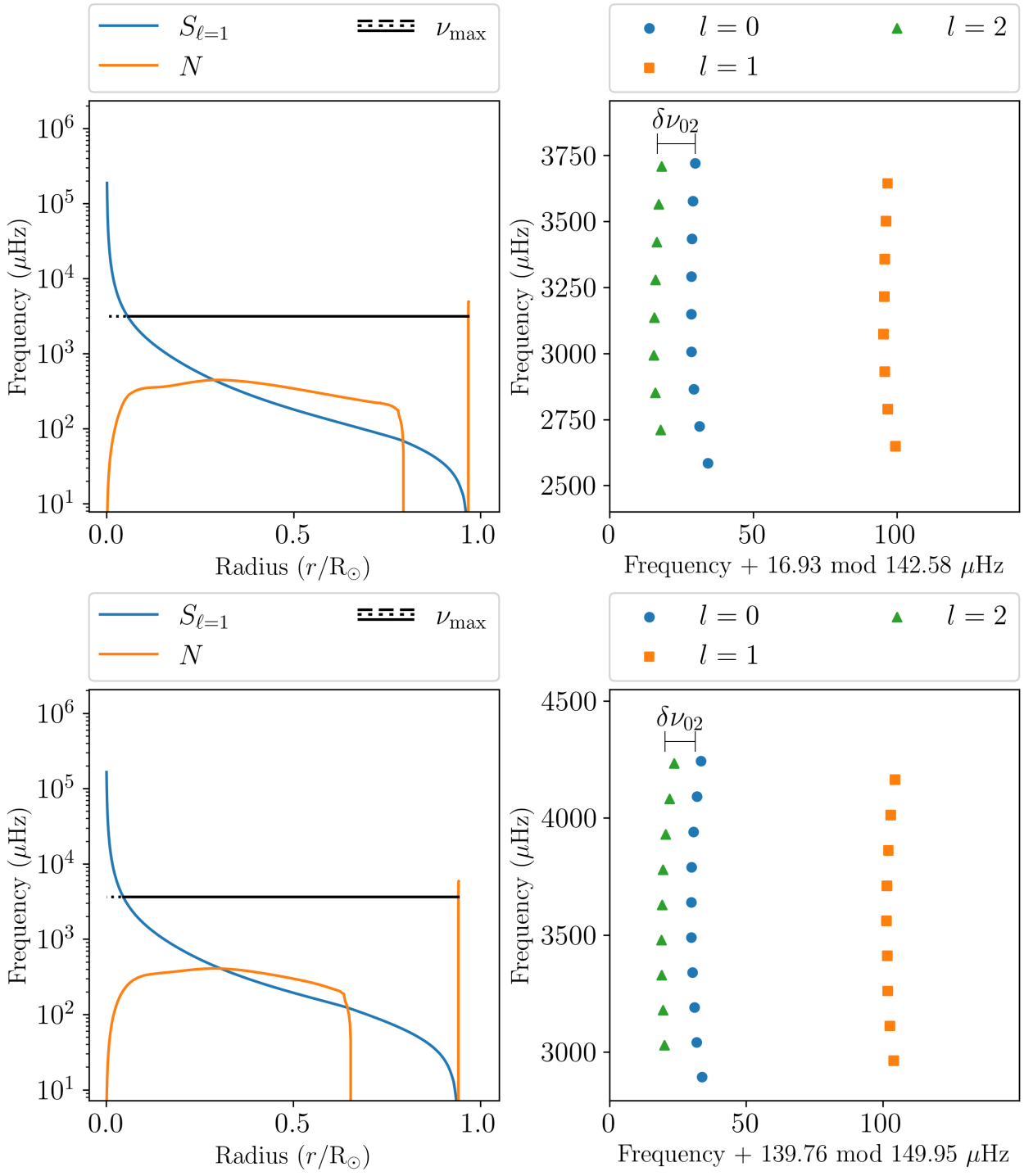

Figure 3.7: Propagation diagram (left) and echelle diagram (right) for a 1 $M_\odot$ star on the MS with [Fe/H] = -0.5 (top) and [Fe/H] = 0.25 (bottom).

the core, where the density is orders of magnitude higher than in the envelope, where the p-like component dominates. Modes with high inertia are difficult to excite and hence are less likely to be observable. The period-spacing diagram (bottom right panel of Figure 3.8) shows the difference in period between two consecutive modes of the same degree as a function of frequency. There are three main features visible in both the $\ell = 1$ and $\ell = 2$ modes. The first feature is the decline from 70 s to 62 s for the $\ell = 1$ modes, and from 40 s to 36 s for the $\ell = 2$ modes. This slight decline is due to the phase term ϵ_g in Equation (3.54). The second feature is the small periodic component in the amplitude of ΔP and E_l with an amplitude in ΔP of 2 s for the $\ell = 1$ modes and 0.4 s for the $\ell = 2$ modes. These variations in ΔP and E_l are due to glitches (relatively rapid changes in the structure compared to the local mode wavelength), which cause a variation in ΔP related to where in the star the glitch occurs. Finally, the third feature is the approximately evenly spaced dips in ΔP, which are caused by mixed modes. The dips also correspond to the dips in mode inertia as the modes with low inertia have a more p-like characteristic.

Figure 3.9 shows the same panels as Figure 3.8 but for a star in the RC with a central helium mass fraction Y_C of approximately 0.5. The general behaviour is similar to that of the RGB star but there are some key differences. The first is that the small oscillations in ΔP are more pronounced and are of order 50 s. For the $\ell = 1$ modes it is approximately 70 s, and for $\ell = 2$ modes it is approximately 40 s. Additionally, oscillations are also present in the mode inertias in combination with the sharp dips seen in the RGB. The mode inertias in the non-radial modes are also around a factor 100 smaller, indicating stronger mixed-mode coupling of modes compared to the RGB. Finally, the period spacing in this evolutionary phase is much larger than on the RGB, with typical ΔPs of 300–400 s compared to 50–100 s in the RGB.

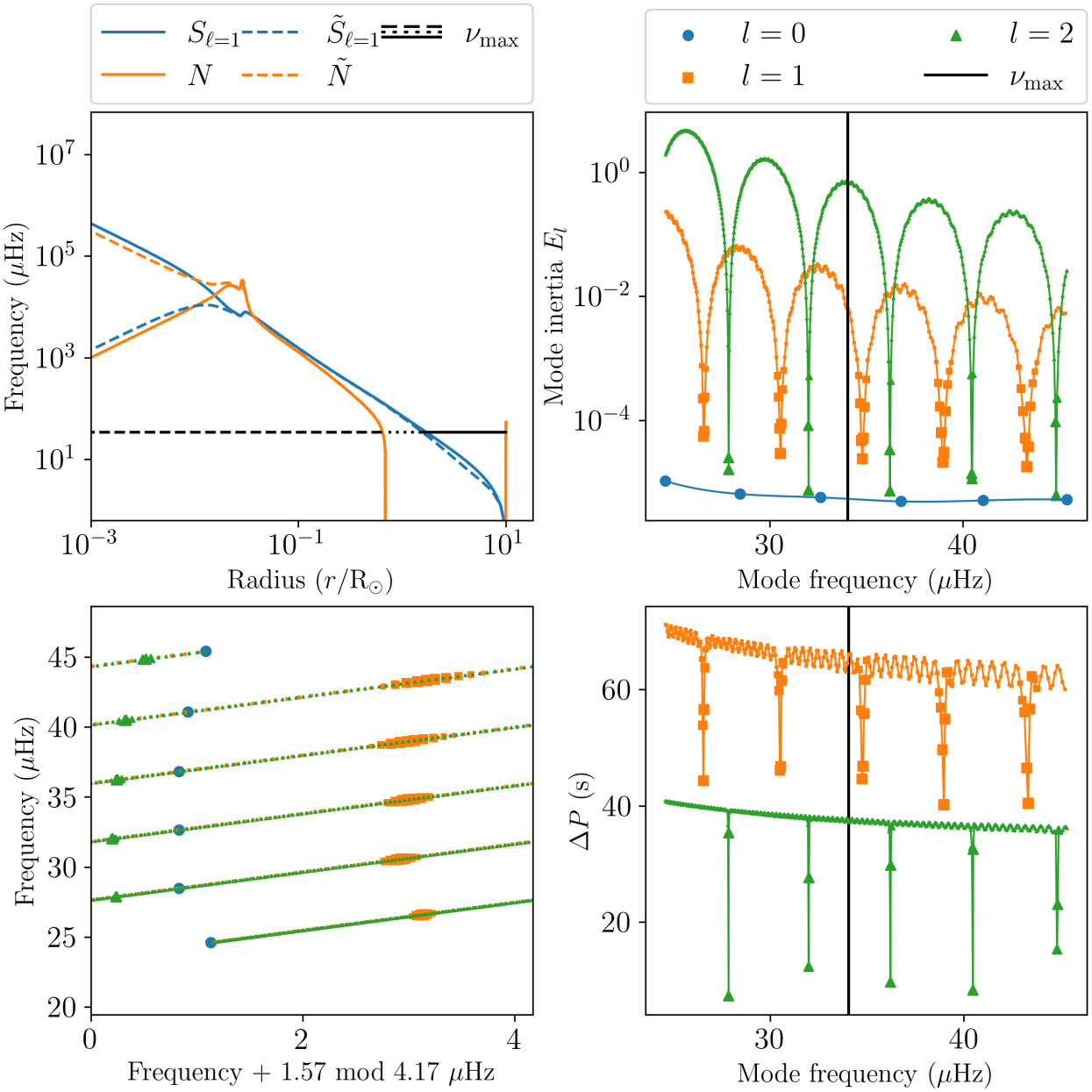

Figure 3.8: Propagation diagram (top left) and echelle diagram (bottom left) mode inertia (top right), and period-spacing diagram (bottom right) for a 1 $M_\odot$ Solar metallicity star in the RGB, immediately after the RGB bump with [Fe/H] = -0.5. The size of the markers in the echelle diagram, mode inertia diagram, and period-spacing diagrams increase with decreasing mode inertia.

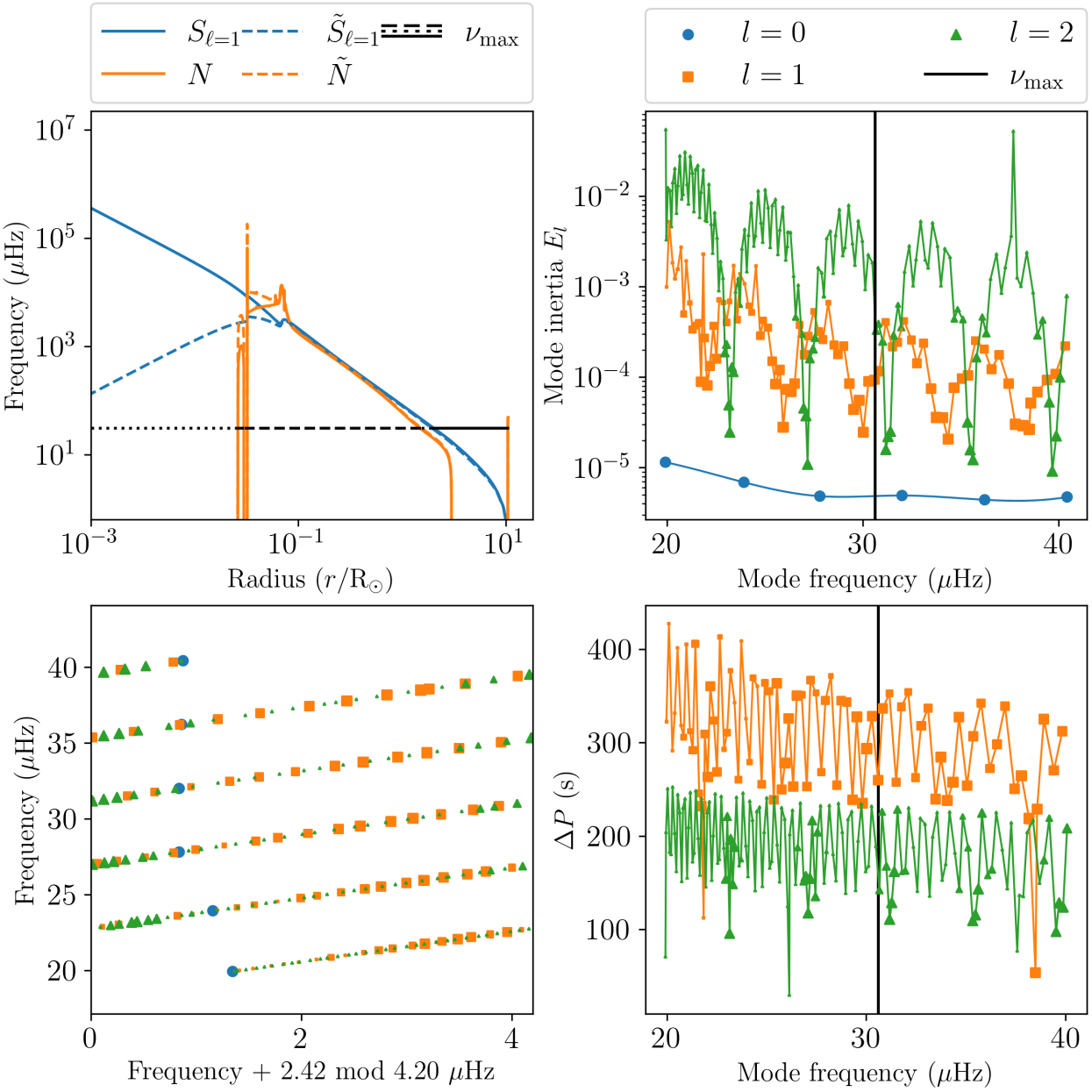

Figure 3.9: Same as Figure 3.8 but for a star in the RC with a central helium mass fraction of approximately 0.5.

Chapter Four

Mixed-mode coupling in the red clump: I. Standard single-star models

This chapter is a reformatted version of van Rossem et al. (in prep.) of which I am to be first author and will be submitted to A&A. I completed all the work, with detailed discussions with Andrea Miglio and Josefina Montalbán. This chapter explores the mixed-mode coupling in red clump stars using the mixed-mode coupling prescription by Takata (2016a). We investigate how sensitive the coupling is to changes in stellar structure due to different masses and metallicities. By implementing the Takata prescription in the detailed stellar evolution code `MESA`*, and running a grid of models, we explore the behaviour of the coupling coefficient whilst varying mass and metallicity.*

4.1 Introduction

Over the past decade space-based missions such as CoRoT (*Convection Rotation & Planetary Transits*; Auvergne et al. 2009), *Kepler*/K2 (Borucki et al. 2010; Howell et al. 2014), and now TESS (*Transiting Exoplanet Survey Satellite*; Ricker et al. 2015), have provided photometric time series

of sufficient precision and duration to enable the detection and precise characterization of stellar oscillations in different classes of stars. Particularly information-rich oscillation spectra have been detected in evolved stars showing solar-like oscillations. In the case of solar-like oscillations, the observed oscillation frequencies are typically described by a Gaussian-shaped power excess centred at the frequency of maximum oscillation power, $\nu_{\rm max}$ (Section 3.3). These oscillations can be used to illuminate the star's internal physics (e.g. Chaplin & Miglio 2013; Montalbán & Noels 2013; Mosser et al. 2014; Di Mauro 2016; Hekker & Christensen-Dalsgaard 2017 and references therein).

In MS stars solar-like oscillations are primarily p-modes. However, when stars leave the MS mixed modes exhibit both gravity- and pressure-like characteristics. Mixed modes are useful as they enable investigation of the deeper interior of the star due to their mixed characteristic. These mixed modes carry information on the structure of both the inner, dense radiative core (probed predominantly by g-modes) and the envelope (which largely determines the frequencies of p-modes). The detection of mixed modes in red-giant branch giants and red clump stars (Bedding et al. 2010; Mosser et al. 2011) has enabled the determination of the star's evolutionary stage (Bedding et al. 2011; Mosser et al. 2015; Hekker et al. 2018) based on the coupling of acoustic modes in the envelope of the star and gravity modes in the stellar interior. Also, inferences can be made on the rotation of stellar cores (Deheuvels & Michel 2011; Beck et al. 2012; Eggenberger et al. 2012; Gehan et al. 2018), the structure of the core, and near-core mixing (Bedding et al. 2011; Montalbán et al. 2013; Mosser et al. 2015; Bossini et al. 2015; Cunha et al. 2015; Deheuvels et al. 2016).

Two complementary approaches are available to explore and appraise the interior of stars. A numerical computational approach to simulate modes by solving the equations in Section 3.1 (e.g. using the stellar oscillation code `gyre` (Townsend & Teitler 2013; Townsend et al. 2018)) can be taken as well as a more analytical approach in which the properties of modes are approximated. This latter approach is taken in this work and these analytical approximations are fundamental

in revealing information from the modes. The coupling coefficient is an essential quantity in the study of mixed modes. It is a measure of how much energy can be transferred between the acoustic- and gravity-mode cavities, which is shown in the relative amplitudes of the mixed modes in the cavities. One limitation in the interpretation of this coupling is that the analytical description of the coupling developed by Unno et al. (1989) is only valid in the weak-coupling regime. Takata (2016a) developed a prescription for the strong-coupling regime, which allows an extension of the study of mixed-mode coupling to the RC. The first explorations of information contained in the strong-coupling regime have been reported but are still mainly limited to the RGB (e.g. Mosser et al. 2017, 2018; Hekker et al. 2018; Pinçon et al. 2020; Jiang et al. 2022).

In this work, we explore mixed-mode coupling in RC models and what the mixed-mode coupling coefficient can reveal about the interior of the star. We conduct this exploration driven by the question of whether this additional constraint on the interior can help us identify structures which are products of mass-transfer events arising from non-single stellar evolution. Current pipelines for inferences from asteroseismology typically assume single stellar evolution and ignore effects due to mass transfer processes that may have altered the initial mass of the star. AIMS (Rendle et al. 2019), for instance, uses a grid of single stellar evolution models and interpolates between them to infer stellar parameters. For single stars this process is well-founded, however, binary interactions can significantly change the structure of a star and therefore change their seismic appearance as well as their surface properties. Some RGB and RC stars have been found to have larger-than-expected masses among giants in the high-[α/Fe] population (e.g. Martig et al. 2015; Chiappini et al. 2015; Jofré et al. 2016; Izzard et al. 2018; Silva Aguirre et al. 2018; Miglio et al. 2021). In stellar clusters some RGB and RC stars are either under- or over-massive compared to the rest of the population (e.g. Handberg et al. 2017; Brogaard et al. 2021). Assuming single-star evolution, this could mean that these RGB and RC stars are older or younger respectively than the rest of the population. However, if the effects of binary interactions are considered, stars can transfer mass to each other and even merge. This mass transfer can cause them to appear

older if they lose mass (under-massive), or younger if they gain it (over-massive). Li et al. (2022) found 7 under-luminous helium-burning stars compared to single-star evolution counterparts, as well as 32 red giants with masses down to $0.5M_{\odot}$, which implies ages that are unattainable through single-star evolution. Similarly, Matteuzzi et al. (2023) found three helium burning stars with very high coupling coefficients, indicating that these stars likely have small hydrogen envelopes. This provides further evidence for non-standard stellar evolution. To investigate whether mixed-mode coupling can be used as a specific seismic signature of these non-standard products, we first need to understand which structural properties determine its value.

The following chapter is structured as follows. In Section 4.2 we review the analytical approximation of the coupling coefficient and discuss various cases and limitations encountered when estimating the coupling in the grid of models considered. In Section 4.3 we describe how the coupling coefficient depends on stellar properties. In Section 4.3.3 we compare the results of this dependence with observations. Finally, in Section 4.4 we discuss the implications of this work and conclude.

4.2 Method

4.2.1 Analytic approximations of the mixed-mode coupling coefficient

Non-radial adiabatic stellar oscillations are governed by a fourth-order system of differential equations (Chapter 3). To obtain approximate solutions or to understand the behaviour of non-radial waves in complex environments such as stellar interiors, one usually reduces that problem to one of second order which can then be studied using standard analytical techniques. Ignoring perturbations to the gravitational potential in the oscillation equations (Cowling approximation, Cowling 1941), allows approximate solutions to be developed. An asymptotic analysis of the resulting sys-

tem, assuming that the scale of variation of the equilibrium quantities is much longer than the wavelength of studied oscillation, leads to a wave equation with a dispersion relation:

$$k_r^2 \approx \frac{\omega^2}{c_s^2}\left(\frac{S_\ell^2}{\omega^2} - 1\right)\left(\frac{N^2}{\omega^2} - 1\right), \tag{4.1}$$

where k_r is the local radial wavenumber, c_s is the sound speed, and ω the angular oscillation frequency. This dispersion relation involves two characteristic frequencies, the Brunt-Väisälä frequency (N), and the Lamb frequency (S_ℓ). The zeros of this relation (also called turning points) define the internal boundaries of the oscillatory propagation regions ($k_r^2 > 0$) of the perturbation with respect to adjacent regions of evanescent propagation, ($k_r^2 < 0$). Figure 4.1 shows the propagation diagram of a perturbation with a frequency close to the typical frequency of stochastic oscillations in a red giant ($\omega \approx 2\pi\nu_{\max}$). As shown, this perturbation can, in principle, propagate as a g-character mode in the interior region (g-cavity where $\omega < N, S$), and as an acoustic (p-character) mode in the outer region (p-cavity where $\omega > N, S$). In fact, a wave in the g-cavity can tunnel through the turning point and reach the p-cavity with an amplitude high enough to be reactivated in that cavity and propagate as an acoustic wave. Shibahashi (1979) performed an asymptotic analysis of the 2$^{\text{nd}}$ order system for these mixed modes. The JWKB solution under the assumption of a large evanescent zone (large with respect to the wavenumber) of these mixed modes, leads to the resonance condition for mixed modes, which can be written as:

$$\cot\Theta_g \tan\Theta_p = q, \tag{4.2}$$

where Θ_g and Θ_p are the integrals of k_r in the p- and g-cavities respectively, together with the phase shifts induced by reflection at their boundaries. The parameter q, called the coupling coefficient, is related to the transmission (T) of wave energy through the evanescent zone between those cavities and can take a value between 0 and 1. Although first derived in the context of large evanescent zones, the resonance condition in Equation (4.2) is general, as has been proven by Takata (2016a), and q can be written as:

$$q = \frac{1 - \sqrt{1 - T^2}}{1 + \sqrt{1 - T^2}}. \tag{4.3}$$

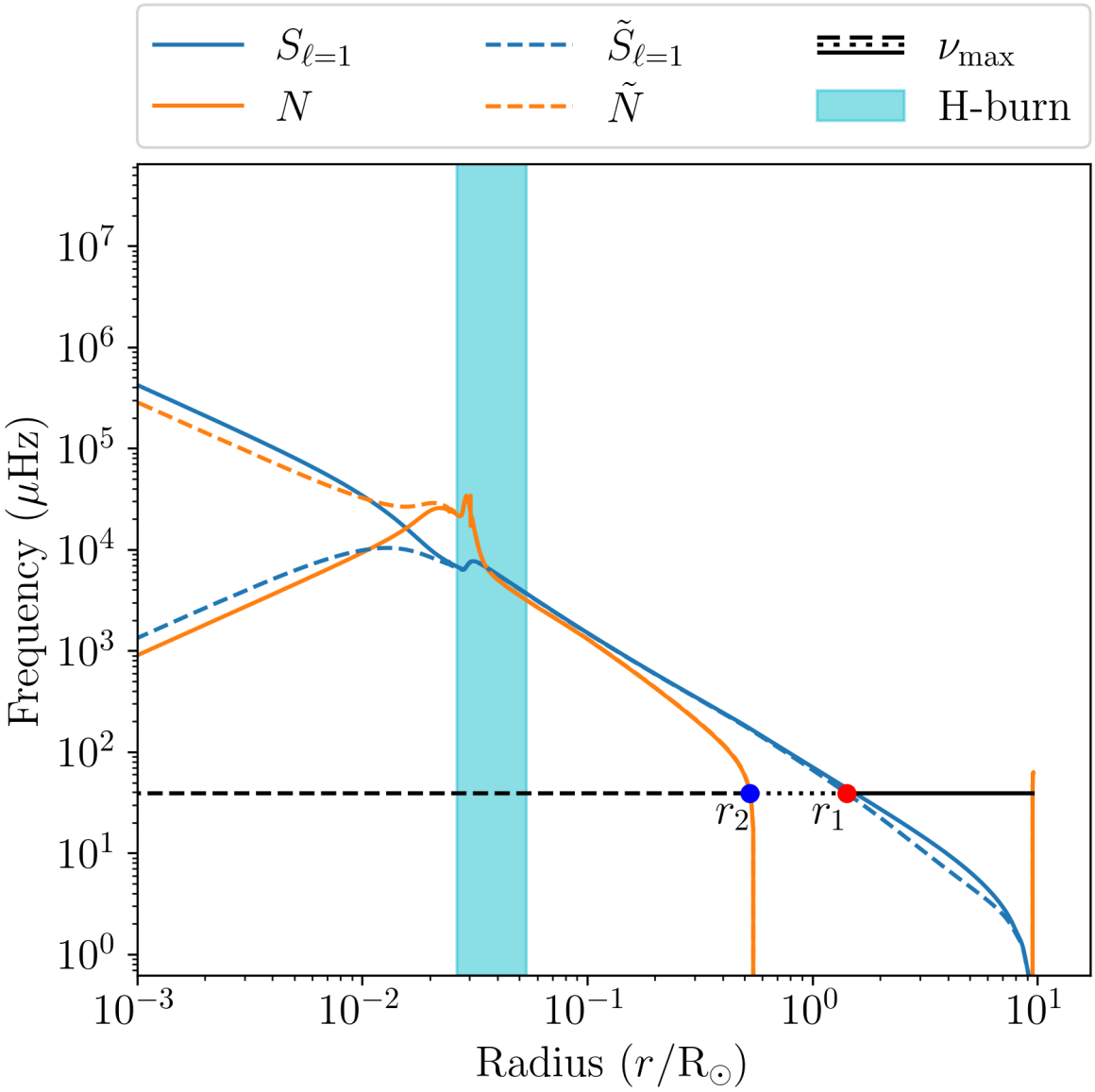

Figure 4.1: Propagation diagram of a $1M_\odot$ star in the RGB, just after the RGBb. The Lamb and Brunt-Väisälä frequencies are shown as the solid blue and orange lines respectively. Their reduced counterparts are shown as dashed blue and orange lines respectively. A mixed mode with a frequency of $\nu_{\max}$ is shown as a dashed black line in the g-like part, as a solid black line in the p-like part, and as a dotted black line in the evanescent zone. The boundaries of the evanescent zone, r_1 and r_2 are shown as red and blue dots respectively. The hydrogen-burning shell is shown as the cyan shaded region.

When $q << 1$, the wave is mainly trapped in one of the two cavities with properties close to those of pure p- or g-modes. As q increases, the energy of the wave is distributed amongst the two regions. The final frequency of the mixed mode and its dominant character depends not only on Θ_g and Θ_p, but also on the properties of the evanescent zone, through q.

In the framework of the large evanescent zone solved by Shibahashi (1979), which hereafter will be called the weak approximation, the weak-coupling coefficient is defined as:

$$q_w = \frac{1}{4}\exp(-2\int_{r_1}^{r_2}|k_r|dr) = \frac{1}{4}\exp(-2\pi X) \approx \frac{T^2}{4}, \tag{4.4}$$

with $X = 1/\pi \int_{r_1}^{r_2}|k_r|dr$, and r_1, r_2 being the limits of the evanescent zone. As can be seen from Equation (4.4), q_w can reach a maximum of 0.25, which is lower than the maximum coupling determined by fitting the asymptotic relation for mixed modes to *Kepler* observations of dipolar modes (e.g. Mosser et al. 2017).

The limitations of this coupling-coefficient prescription may be due to approximations made in its derivation: the Cowling approximation and the weak-coupling approximation. The Cowling approximation is not valid in the case of dipole modes, in particular dipole mixed p- and g-modes (e.g. appendix A.1 from Pinçon et al. 2020). The weak-coupling approximation is not valid due to the evolution of the central and mean density of stars after the end of central hydrogen-burning. There are phases where the turning points (r_1, r_2) are very close in terms of the oscillation wavenumber, which makes the weak-coupling approximation no longer valid.

Takata's work (Takata 2005, 2006, 2016a,b) has made it possible to study mixed dipole modes without using these approximations. Takata (2005, 2006) simplified the problem by a change of dependent variables, and identified a first integral specific to dipolar oscillations. This reduces the problem to a second-order system of ordinary differential equations while keeping the perturbation to the gravitational potential. On the other hand, Takata (2016a,b) performed an asymptotic analysis of the system and provides a JWKB solution for the dipole mixed modes in the case of a very narrow evanescent zone. The system of equations is similar in form to that obtained

using the Cowling approximation (Equation 3.39). Also, the equivalent dispersion relation has the same form as Equation (4.1), but with the critical frequencies replaced by the corresponding reduced characteristic frequencies:

$$\tilde{N} = \frac{N}{J} \tag{4.5}$$

and

$$\tilde{S} = JS_{\ell=1}, \tag{4.6}$$

where J includes the effects of perturbations to the gravitational potential, and is related to the density concentration through:

$$J = 1 - \frac{4\pi}{3}\frac{\rho r^3}{m} = 1 - \frac{\rho}{\langle\rho\rangle_r}, \tag{4.7}$$

where ρ is the local density, m the mass coordinate, and $\langle\rho\rangle_r$ the mean density of a sphere of radius r.

The terms P and Q appearing in the system of equations (Equations 16 and 17 of Takata 2016a) are now:

$$P = 2J\left(1 - \frac{\omega^2}{\tilde{S}^2}\right) \tag{4.8}$$

and

$$Q = J\left(1 - \frac{\tilde{N}^2}{\omega^2}\right), \tag{4.9}$$

where ω is the angular frequency at which the coupling is to be calculated.

The local radial wavenumber in the asymptotic approximation can be written as $k_r^2 = -PQ/r^2$. The boundaries of the evanescent zone, r_1 and r_2, are defined by the zeros of $P(r)$ and $Q(r)$ respectively (note that r_1 and r_2 are switched in Pinçon et al. 2020 compared to Takata 2016a and the Takata order is used in this work):

$$P(r = r_1) = 0 \Leftrightarrow \tilde{S}(r_1) = \omega \tag{4.10}$$

and

$$Q(r = r_2) = 0 \Leftrightarrow \tilde{N}(r_2) = \omega. \tag{4.11}$$

Due to J, the new turning points could differ from those in the Cowling approximation, in particular in the inner regions. Figure 4.1 shows a propagation diagram of a $1\mathrm{M}_{\odot}$ star in the RGB. It shows how $\tilde{N}$ behaves as S_ℓ and how $\tilde{S}$ behaves as N in the core of the star and behave like their non-reduced counterparts in the outer regions. J can also slightly modify the location of the intermediate evanescent zone, as can be seen in the same figure.

The resonance condition for dipole mixed modes obtained in Takata (2016a) for the case of very narrow evanescent zones, has the same functional shape as that from Shibahashi (1979) in the framework of the Cowling approximation with a large evanescent zone. The phases in the p- and g-mode cavities (Θ_p, Θ_g) may differ from those in previous works (Takata 2016a; Pinçon et al. 2019), but more important for the present work is the new expression for the transmission coefficient T, and hence X. The new X of Takata (2016a) contains a term that includes the properties of stratification in the evanescent zone via the $\tilde{N}$ and $\tilde{S}$ gradients, in addition to the integral of the radial wavenumber in the evanescent zone. Thus, this approximation shows the dependence of the transmission rate on the properties of the stellar structure in the region above the hydrogen-burning shell.

Pinçon et al. (2020) studied the ability to extract information about properties of the evanescent zone (radial extent and density stratification) from the coupling coefficient q, observed in subgiants and RGB stars. To follow an analytical approach, they adopted simplified structure models in which $\tilde{N}$ and $\tilde{S}$ follow power-laws. They follow the same power-law when the evanescent zone has a radiative stratification ($\mathrm{d}\ln\tilde{N}/\mathrm{d}\ln r = \mathrm{d}\ln\tilde{S}/\mathrm{d}\ln r = \beta$). When the evanescent zone has a convective stratification, $\tilde{S}$ follows a power law whilst $\tilde{N}$ is 0.

4.2.2 Computation of the coupling coefficient q using stellar models: approach and limitations

In this work we numerically compute the coupling coefficient, q, following the weak and strong approximations in stellar models from the end of the main sequence to the end of central helium-burning. We cover different masses and chemical compositions, since these parameters affect both the radial extent and stratification of the corresponding evanescent zones.

We follow the approach described in Takata (2016a), which is summarized in Appendix D.1 of Pinçon et al. (2020), for the solution of the oscillation problem in the evanescent zone. First, a new spatial variable is defined by

$$s = \ln\left(\frac{r}{r_0}\right), \tag{4.12}$$

where

$$r_0 = \sqrt{r_1 r_2}. \tag{4.13}$$

In this new reference system the centre of the evanescent zone r_0 becomes $s = 0$, and the boundaries of the evanescent zone r_1 and r_2 in terms of s then become $s = s_0$ and $s = -s_0$ respectively, where

$$s_0 = (\ln r_1 - \ln r_2)/2. \tag{4.14}$$

Both $s = 0$ and r_0 refer to the same location in the star in different coordinate systems, and s_0 can be negative.

Using equation (61) of Takata (2016a), the expression for X in the coupling coefficient is:

$$X = \frac{1}{\pi}\int_{-|s_0|}^{|s_0|} \kappa(s)\sqrt{{s_0}^2 - s^2}\, ds + \frac{\mathcal{G}^2_{s=0}}{2\kappa_{s=0}} = \frac{I}{\pi} + \frac{\mathcal{G}^2_{s=0}}{2\kappa_{s=0}}. \tag{4.15}$$

The first term is equivalent to that in Equation (4.4), which is the integral of the wavenumber in the evanescent zone, with

$$\kappa = \sqrt{\frac{PQ}{{s_0}^2 - s^2}}, \tag{4.16}$$

and the second term is the stratification term, with $\mathcal{G}_{s=0}$ related to the gradients of $\tilde{N}$ and $\tilde{S}$ at the centre of the evanescent zone:

$$\mathcal{G} = \frac{1}{4}\frac{\mathrm{d}}{\mathrm{d}s}\left[\ln\left(\frac{P}{Q}\frac{s+s_0}{s_0-s}\right)\right] - \frac{1}{2}\left(\mathcal{V} - \mathcal{A} - J\right), \tag{4.17}$$

where

$$\mathcal{V} = \frac{2J}{\tilde{S}^2}\frac{g}{r} \tag{4.18}$$

and

$$\mathcal{A} = J\frac{\tilde{N}^2 r}{g}. \tag{4.19}$$

Hence, using the detailed structure of stellar models over the course of their evolution, we compute the coupling coefficient at frequencies close to the central value of their expected oscillation domain ($\omega = 2\pi\nu_{\max}$). The coupling coefficient q, and its dependence on ω, if any, determines the properties of the dipole oscillation spectra for different stellar parameters. The coupling coefficient q is defined as:

$$q = \frac{1 - \sqrt{1 - e^{-2\pi X}}}{1 + \sqrt{1 - e^{-2\pi X}}}. \tag{4.20}$$

Since this work is mainly numerical in nature, some approximations made in Takata (2016a) to make the problem more tractable for analytic study can be ignored. One such approximation is carried out when determining X, and if the approximation is skipped, X takes the form of:

$$X = \frac{1}{\pi}\int_{-d_0}^{d_0} \kappa\sqrt{d_0^2 - s^2}\,\mathrm{d}s, \tag{4.21}$$

where

$$d_0^2 = {s_0}^2 + \frac{\mathcal{G}_{s=0}^2}{\kappa_{s=0}^2}. \tag{4.22}$$

However, in practice the effect this approximation has on the calculated coupling during core helium-burning is negligible (typically a relative change of less than 1% in q). As such, we use the definition of X described in Equation (4.15).

There are three main limitations which give rise to problems when numerically determining the coupling coefficient:

(1) There is no prescription for intermediate coupling, which typically occurs when the evanescent zone transitions from being fully radiative to fully convective (Pinçon et al. 2019, 2020).

(2) Glitches, or sharp changes, in the structure where the asymptotic approximation becomes questionable.

(3) There are multiple evanescent zones.

Figure 4.2 shows a propagation diagram of an RGB star which shows a spike in the Brunt-Väisälä frequency below the convective envelope left by the deepening convective envelope due to the first dredge-up. This model exhibits all three limitations: 1) the evanescent zone is transitioning from being entirely located in the radiative region above the hydrogen-burning shell, to being located entirely in the convective envelope (Type-a and Type-b in Pinçon et al. (2020) respectively), 2) there is a spike in $\tilde{N}$ at around 0.4 $R_\odot$, and 3) there are two evanescent zones separated by this spike in $\tilde{N}$.

The issue which arises due to limitation 1 when calculating the strong coupling, is the following: when the centre of the evanescent zone crosses the convective envelope boundary, the large change in the slope of $\tilde{N}$ as seen in Figure 4.2 (and therefore Q) causes $\mathcal{G}$ to change abruptly as $Q \simeq J$ on the convective side of the boundary and therefore $\mathrm{d}\ln Q/\mathrm{d}s \simeq 0$. As $\mathcal{G}$ is only evaluated at $s = 0$ due to the assumption of a thin evanescent zone, this can cause q to vary rapidly even though there is only a negligible difference between the position corresponding to $s = 0$ being convective or radiative.

Limitation 2 is encountered when the rapid variation of $\tilde{N}$ due to the spike with respect to k invalidates the asymptotic approximation used, as the JWKB approximation is no longer usable because the local wavelength of the oscillation is of similar scale to the width of the spike. Additionally, as the frequency ν_q drops below the trough of the $\tilde{S}$ bump to ν'_q, the size of the evanescent zone increases abruptly, causing a discontinuity in q. This increase in s_0 would, counter-intuitively,

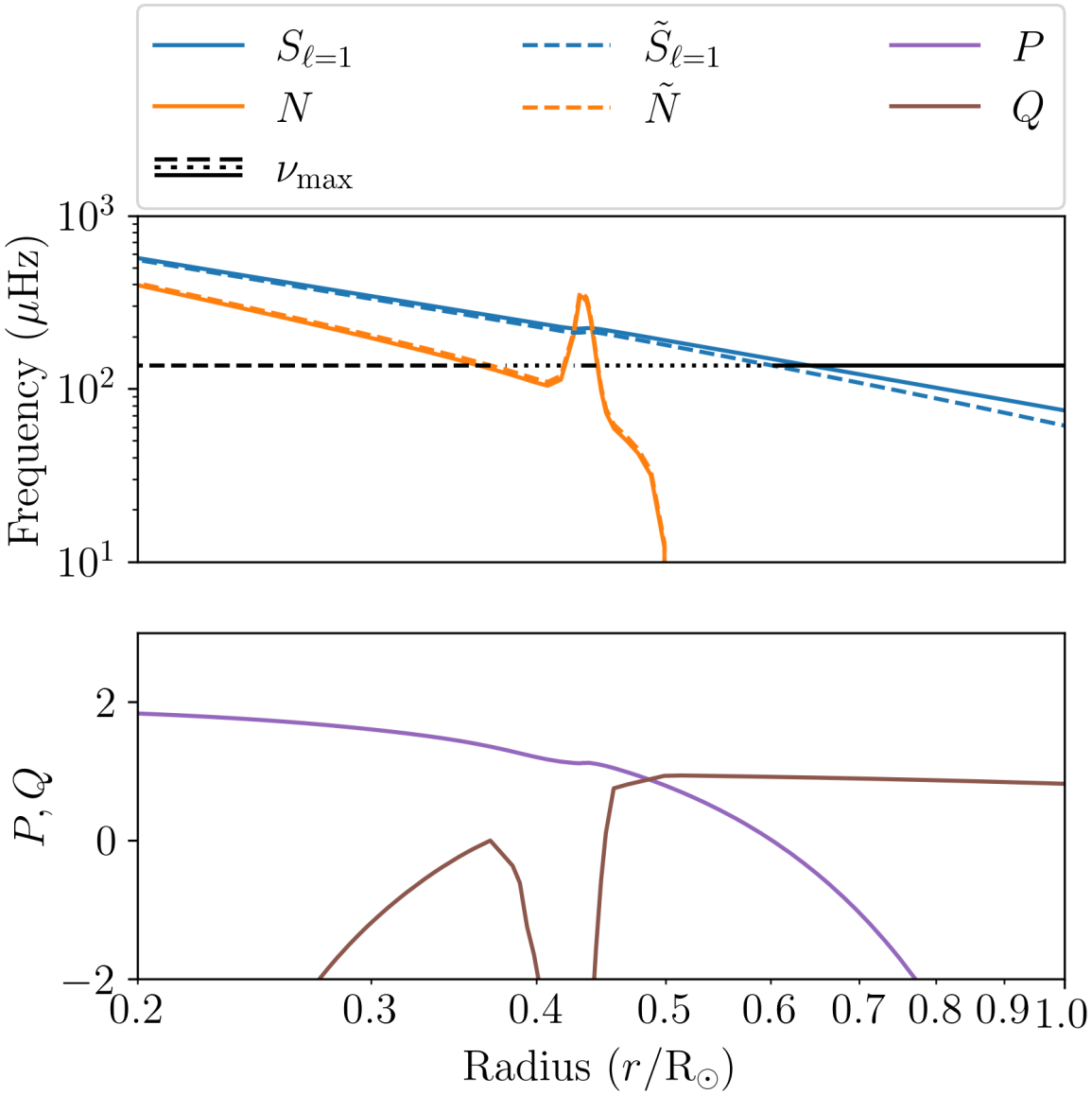

Figure 4.2: Similar to Figure 4.1 but zoomed in around the evanescent zone and showcasing an example where the strong-coupling prescription is not valid. This model is 150 Myr earlier in the RGB than the propagation diagram shown in Figure 4.1.

increase q as the increase in I due to the larger integration domain is surpassed by a decrease in $\mathcal{G}^2$. It is possible to split the gradient part of $\mathcal{G}$ into three parts:

$$\frac{\mathrm{d}}{\mathrm{d}s}\left[\ln\left(\frac{P}{Q}\frac{s+s_0}{s_0-s}\right)\right] = \frac{\mathrm{d}\ln P}{\mathrm{d}s} - \frac{\mathrm{d}\ln Q}{\mathrm{d}s} + \frac{\mathrm{d}}{\mathrm{d}s}\ln\left(\frac{s+s_0}{s_0-s}\right). \tag{4.23}$$

The first two terms (as well as $\mathcal{V}-\mathcal{A}-J$) at $s=0$ remain almost constant as $\nu_q \simeq \nu'_q$ and $\mathrm{d}\ln\tilde{S}/\mathrm{d}s \simeq \mathrm{d}\ln\tilde{N}/\mathrm{d}s \simeq$ constant (e.g. Pinçon et al. 2020). The change in r_0 is relatively small as $\Delta r_0 \simeq r_0(\sqrt{r'_1/r_1}-1)$, assuming $r_2 \simeq r'_2$. However, the third term evaluates to $2/s_0$ at $s=0$, which decreases quickly as s_0 grows.

Finally, limitation 3 can be encountered in two different ways. The first way is when the spike in the Brunt-Väisälä frequency is above the main evanescent zone and ν_q is slightly larger than the reduced Lamb frequency (green line) at the spike (e.g. $\nu_q \sim 30\,\mu$Hz in Figure 4.2). This creates a small secondary evanescent zone which breaks the assumption that there is only one evanescent zone. The second way is when the $\tilde{N}$ spike is inside the main evanescent zone which causes it to be split in two (e.g. Jiang et al. 2022). This breaks Takata's assumption that there is only one sign change for both P and Q in the region around the evanescent zone. It is unclear what the limits of this evanescent zone should be. Additionally, we should take into account the problem of coupling when more propagation cavities exist (as for instance in Deheuvels & Belkacem 2018, where the study is done in the asymptotic and weak-coupling approximation). Work is ongoing to study and resolve this problem and, recently, Pinçon & Takata (2022) have derived the resonance condition for multiple evanescent cavities.

The three limitations discussed above appear at different evolutionary stages. For instance, early in the RGB all three limitations are encountered at approximately the same time. Here, the evanescent zone is transitioning from fully radiative to fully convective (limitation 1). There is also a spike in $\tilde{N}$ due to the composition change caused by the deepening convective envelope (limitation 2), and this spike splits the evanescent zone as $\nu_{\max}$ decreases due to the envelope's expansion (limitation 3). On the other hand, during the RC, limitation 3 is encountered and limitation 1 oc-

curs when $\nu \lesssim \nu_{\max} - 2\Delta\nu$. In the RC we neglect the effect of limitation 3 as the second evanescent zone is due to the convective core (e.g. Figure 4.9C) and far from the evanescent zone of interest. However, the effects of limitation 1 need to be taken into account. More details and examples of these limitations are described in Section 4.3.

As there is currently no approximation available for coupling in the intermediate regime (limitation 1), we use the strong prescription when the evanescent zone is less than 20% convective in terms of s and Takata's weak prescription when it is more than 80% convective in s. We define this fraction of the evanescent zone which is convective ($f_{\rm CZ}$) as:

$$f_{\rm CZ} = \frac{|s_0| - s_{\rm bCZ}}{2|s_0|} \tag{4.24}$$

where $s_{\rm bCZ}$ is the location of the bottom of the convective envelope in terms of s and is defined as:

$$s_{\rm bCZ} = \ln\left(\frac{r_{\rm bCZ}}{r_0}\right). \tag{4.25}$$

If $0.2 < f_{\rm CZ} < 0.8$ or the spike in $\tilde{N}$ is in the evanescent zone we do not compute the coupling coefficient because it is not valid and therefore we leave it undefined. The final coupling equation becomes:

$$q = \begin{cases} q_s = \dfrac{1 - \sqrt{1 - e^{-2\pi X}}}{1 + \sqrt{1 - e^{-2\pi X}}} & f_{\rm CZ} \leq 0.2, \\ q_w = \dfrac{1}{4}\exp(-2I) & f_{\rm CZ} \geq 0.8, \\ \text{undefined} & \text{otherwise.} \end{cases} \tag{4.26}$$

where X and I are defined in Equation (4.15). For the weak coupling we use X defined by Takata (2016a), which includes the perturbation to the gravitational potential. These limits on $f_{\rm CZ}$ are arbitrary and the computed q when $0 < f_{\rm CZ} < 1$ should be used qualitatively. Nevertheless, the resulting behaviour of Equation (4.26) is similar to observations (Figure 4.11) and that in Jiang et al. (2022) as this results in the use of the weak-coupling prescription when $q \lesssim 0.12$. However, due to the inclusion in our models of overshooting below the convective envelope, we cannot compute the coupling in the transition regime as the glitch has a finite width, and therefore cannot compare our modelled coupling coefficients directly to Jiang et al. (2022).

Table 4.1: Summary of applicability of coupling prescriptions. Type-a and type-b evanescent zones are defined following Pinçon et al. (2019).

Type	Prescription	Evanescent zone properties	Evolutionary phases
Weak	Shibahashi (1979)	Type-b, large, convective	RGB, AGB
Weak	Takata (2016a)	Type-b, large, convective	RGB, AGB
Strong	Takata (2016a)	Type-a, small, radiative	SGB, RC
Strong	Parallel	Type-a, small, radiative	SGB, RC
Strong	Non-parallel	Type-a, small, radiative	SGB, RC
Intermediate	–	Partially radiative and convective	E-RGB, He-flashes, E-AGB

For reference we present the domains of applicability of our various prescriptions described in Table 4.1. We also include two additional approximations to the strong regime, which are described in more detail in Section 4.3.5. The strong parallel case assumes $\tilde{S}$ and $\tilde{N}$ both have the same power-law in r, and the strong non-parallel case assumes they both have different power-laws in r. Given all the assumptions, one should be careful when quantitatively comparing modelled coupling coefficients with observations. However, taking these limitations into account gives us grounds to explore how coupling depends on stellar properties.

We have implemented the above equations in the stellar evolution code `MESA` v11701 (Paxton et al. 2011, 2013, 2015, 2018, 2019) and the implementation details can be found in Section 4.2.3. A small grid of models was run to explore the behaviour of q in different conditions. Table 4.2 shows some of our key model parameters. Buldgen et al. (2023) showed that high $(Z/X)_{\rm surf}$ of e.g. Grevesse & Sauval (1998) are disfavoured due to helioseismic constraints. We therefore calibrate our initial metallicity using $(Z/X)_{\rm surf} = 0.0178$ from (Serenelli et al. 2009). The initial metallicity, helium abundance, and mixing-length parameter are calibrated on the Sun, so that a 1 $M_\odot$ model has $(Z/X)_{\rm surf} = 0.0178$ (Serenelli et al. 2009), $\log_{10}(L/L_\odot) = 0 \pm 10^{-5}$, and $\log_{10}(R/R_\odot) = 0 \pm 10^{-5}$ at the Solar age of $4.567 \pm 5 \times 10^{-3}$ Gyr (Connelly et al. 2012).

Table 4.2: Key parameters used in the simulations.

Parameter	Symbol	Values
Mass	m_i	0.7, 1.0, 1.5, 2.3, 3.0
Metallicity	[Fe/H]	-1.0, -0.5, 0.0, 0.25, 0.4
Solar initial metallicity	$Z_\odot$	0.0145
Solar initial helium abundance	$Y_\odot$	0.263
Mixing-length parameter	$\alpha_{\rm MLT}$	1.702
Enrichment law	$\frac{\Delta Y}{\Delta Z}$	1.007
Undershooting	$f_{\rm US}$	0.02
Overshooting	$\alpha_{\rm OS,CHeB}$	0.5

4.2.3 Calculation of q in MESA

As we are interested in the behaviour of the coupling coefficient q as a star evolves, the Takata prescription for strong coupling has been implemented in MESA. The calculation in MESA is done in several steps and is structured as follows:

(1) Calculate J, $\mathcal{A}$ and $\mathcal{V}$ in the star (Equations (4.7), (4.19), and (4.18)), where J is the perturbation to the gravitational potential, and $\mathcal{A}$ and $\mathcal{V}$ are variables used in the oscillation equations and depend on N and S respectively.

(2) Calculate the angular frequency, ω, of the frequencies at which the coupling is to be calculated and then for each angular frequency ω do the following:

(3) Calculate P and Q (Equations (4.8) and (4.9)).

(4) Find the initial estimate of the evanescent zone boundaries, r_1 and r_2, using P and Q respectively.

(5) Smooth P and Q as a function of s (Equation 4.27) fully inside and a few points outside the evanescent zone.

(6) Find the final evanescent zone boundaries, r_1 and r_2, using the smoothed P and Q respectively from step 5.

(7) Calculate X (Equation 4.15) and evaluate q (Equation 4.20).

Steps 1–3 are straightforward calculations and steps 4–7 are explained in more detail below. In steps 4 and 6, the edges of the evanescent zones are found by searching for the zeros of P and Q. As `MESA` is cell based we search for where the signs of P and Q change, and then linearly interpolate to find r_1 and r_2. However, as $\tilde{N}$ becomes large at the surface (e.g. Figure 4.1), the outer 10% by radius is not considered when searching for these zeros. As we are interested in the evanescent zone between the convective envelope and radiative core we only search for zeros above the area where the maximum hydrogen-burning rate takes place. This is above the centre of the star during the MS or above the hydrogen-burning shell in later evolutionary phases.

In step 5, using Equations (4.8) and (4.9), P and Q are evaluated and smoothed. The smoothing is done around and inside the evanescent zone, but not in the convective zone. The smoothing is done in two steps. First, a weighted moving average is taken around the central point as follows:

$$P_k = \frac{w_2 P_{k-1} + P_k + w_1 P_{k+1}}{1 + w_1 + w_2}, \tag{4.27}$$

where k is the cell index, and w_1 and w_2 are the weights above and below the central point respectively and are defined by

$$w_1 = \frac{s_{k-1} - s_k}{s_{k-1} - s_{k+1}} \quad \text{and} \quad w_2 = \frac{s_k - s_{k+1}}{s_{k-1} - s_{k+1}}, \tag{4.28}$$

and

$$s_k = \ln\left(\frac{r_k}{\sqrt{r_1 r_2}}\right). \tag{4.29}$$

The same is done for Q. Second, a quadratic is fit to the points $k-2$, $k-1$, and $k+1$ and evaluated at k, which becomes the new value y_{new} for all the points to be smoothed. The new value is only accepted if $\min(y_{k-2}, y_{k-1}, y_{k+1}) \leq y_{\text{new}} \leq \max(y_{k-2}, y_{k-1}, y_{k+1})$. Additionally, when smoothing

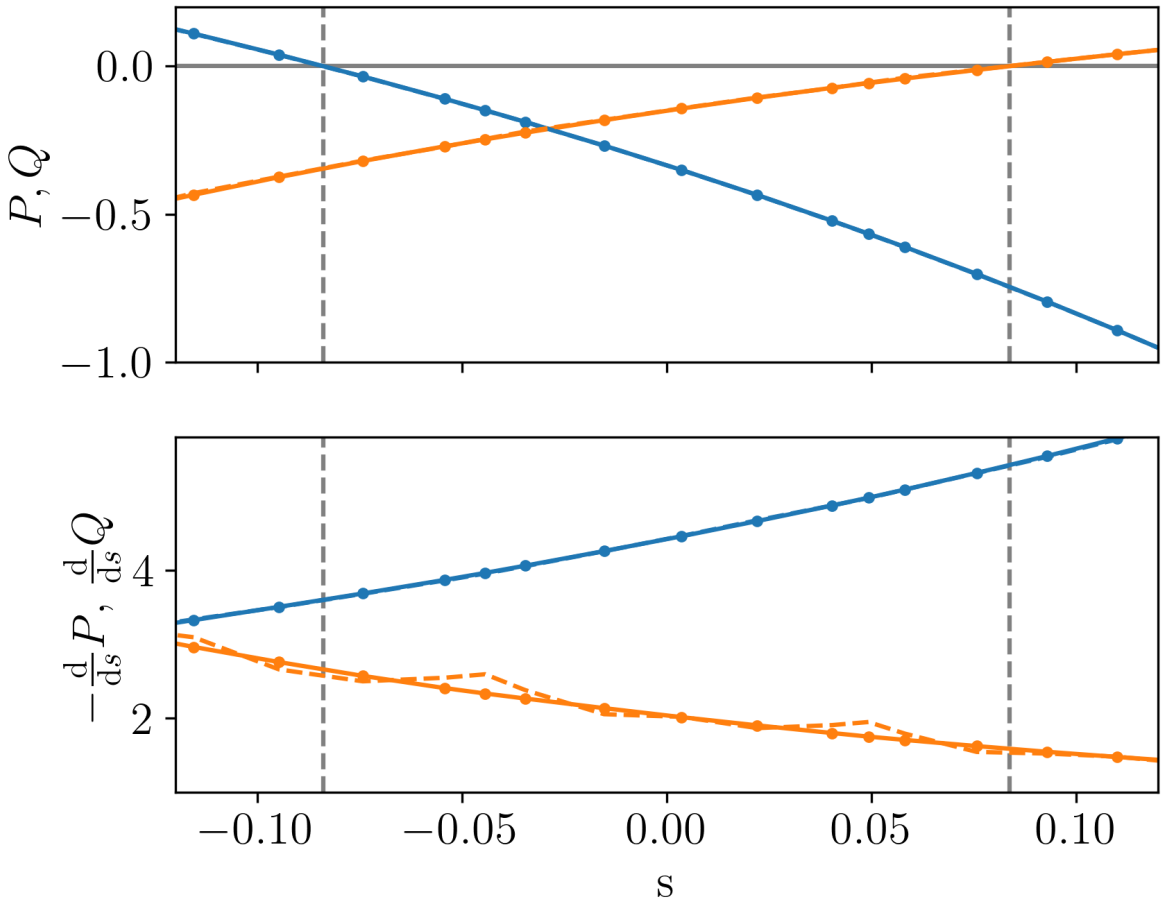

Figure 4.3: Before (dashed) and after (solid with points) smoothing of P (blue) and Q (orange) in the top panel and their gradients in the bottom panel. The vertical grey dashed lines show $\pm s_0$.

Q, $y_{\mathrm{new}} = \min(y_{\mathrm{new}}, 1)$ is included in the fit. This procedure is then repeated for points $k-1$, $k+1$, and $k+2$. This pair of interpolations is repeated 5 times. Figure 4.3 shows the result of this smoothing process, where the solid lines with points show the smoothed quantities, and the dashed lines show the raw quantities. In the top panel the smoothed and unsmoothed P and Q overlap, and in the bottom panel the smoothed and unsmoothed $\mathrm{d}P/\mathrm{d}s$ also overlap. However, $-\mathrm{d}Q/\mathrm{d}s$ shows a good improvement in smoothness.

In step 7 the calculation of X (Equation 4.15) is split into two components, an integral

part and a gradient part. The integral part is calculated first, which is done in two steps. First, a numerical integral is done using the composite Simpson's rule. This works well with relatively large evanescent zones. However, when the evanescent zone is narrow and contains only a few cells, the value returned is dominated by noise as the mesh does not resolve $\sqrt{PQ}$. As a work-around, we construct a polynomial from 3 points. From the way that P and Q are defined we know that $P(s_0) = 0$ and $Q(-s_0) = 0$. We use $P(0) = P_0$ and $Q(0) = Q_0$, and $P(-s_0) = P_1$ and $Q(s_0) = Q_1$. This allows us to construct the following equations for P and Q:

$$P(s_0) = a_2 {s_0}^2 + a_1 s_0 + a_0 = 0, \tag{4.30}$$

$$P(0) = a_0 = P_0, \tag{4.31}$$

$$P(-s_0) = a_2 {s_0}^2 - a_1 s_0 + a_0 = P_1, \tag{4.32}$$

and

$$Q(s_0) = a_2 {s_0}^2 + a_1 s_0 + a_0 = Q_1, \tag{4.33}$$

$$Q(0) = a_0 = Q_0, \tag{4.34}$$

$$Q(-s_0) = a_2 {s_0}^2 - a_1 s_0 + a_0 = 0. \tag{4.35}$$

Solving for the polynomial coefficients for P gives:

$$a_2 = \frac{P_1 - 2P_0}{2{s_0}^2}, \tag{4.36}$$

$$a_1 = \frac{-P_1}{2s_0}, \tag{4.37}$$

$$a_0 = P_0 \tag{4.38}$$

and for Q:

$$a_2 = \frac{Q_1 - 2Q_0}{2{s_0}^2}, \tag{4.39}$$

$$a_1 = \frac{Q_1}{2s_0}, \tag{4.40}$$

$$a_0 = Q_0. \tag{4.41}$$

P_0, P_1, Q_0, and Q_1 are found by interpolating using three mesh points on either side of the point of interest using the algorithm described by Fornberg (1988), and the implementation by Bjorn & Čertík (2021). Nominally this is an algorithm for the calculation of weights in finite difference formulas for arbitrarily spaced grids, however, in the spacial case of approximating the zeroth derivative, it provides a fast procedure for polynomial interpolation.

The integral in Equation (4.15) is then performed using the composite Simpson's rule with 20 sub-intervals. The numerical integral is used when either of the following empirically determined conditions are true:

(1) the evanescent zone is partially convective and there are at least six meshpoints in the evanescent zone, or

(2) the mean absolute difference between the quadratic fit of P and Q and the values of P and Q at each meshpoint in the evanescent zone is greater than 5% and there are at least six meshpoints in the evanescent zone.

If neither condition is true, then the quadratic approximation is used. The first condition ensures that the large or partially convective case is avoided when using the quadratic approximation as Q is not approximated well by a quadratic. The second condition avoids using the quadratic approximation in case of a bad fit. Using these thresholds for switching between the quadratic approximation and the numerical integral does not result in noticeable jumps when transitioning between the two. However, using these thresholds does result in a reduction of noise due to the low number of meshpoints. Figure 4.4 shows the resulting polynomials for P, Q, and the integrand $\sqrt{PQ}$ in Equation (4.15). The resulting equations for P and Q work well and can easily be integrated even though there are only four meshpoints inside the evanescent zone. Comparing this method to a trapezium integration when there are between 6 and 20 meshpoints available, the integrals are consistent with each other to within 3%. As fewer meshpoints become available the difference between the two

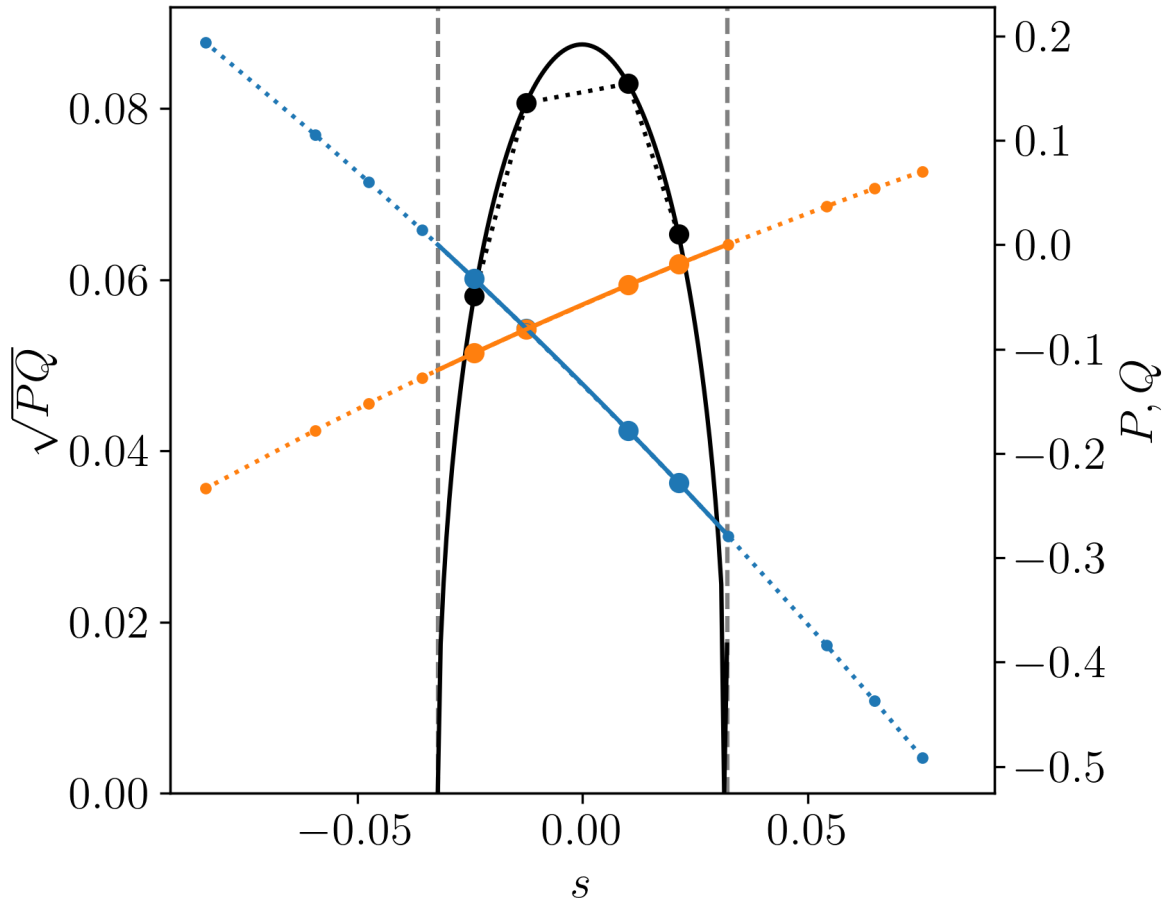

Figure 4.4: P, Q, and $\sqrt{PQ}$ are shown as blue, orange, and black lines respectively. Solid lines show values calculated using the quadratic fit, and dotted lines show values using linear interpolation. The coloured circles show values at mesh points, with small circles being outside the evanescent zone and large circles inside. The vertical grey dashed lines show $\pm s_0$.

methods grows significantly, as shown in Figure 4.5. The trapezium integration uses the meshpoints in the evanescent zone as well as two additional points at $s = \pm s_0$, where $\sqrt{PQ} = 0$. When the number of meshpoints in the evanescent zone is less than three the trapezium integration is dominated by noise, and when there are zero meshpoints in the evanescent zone the trapezium integral cannot be computed. However, when any part of the evanescent zone is convective, P and Q are no longer well approximated by a quadratic.

The calculation of the strong-coupling coefficient using the Takata prescription is sensitive to the gradient term when the evanescent zone is small ($|s_0| \lesssim 0.1$) as $\frac{I}{\pi} \ll \frac{\mathcal{G}^2_{s=0}}{2\kappa_{s=0}}$ in this regime. The gradient part of the $\mathcal{G}$ term defined in Equation (4.17) can be split in two parts:

$$\frac{\mathrm{d}}{\mathrm{d}s}\left[\ln\left(\frac{P}{Q}\frac{s+s_0}{s_0-s}\right)\right] = \frac{\mathrm{d}}{\mathrm{d}s}\ln\left(\frac{P}{s_0-s}\right) - \frac{\mathrm{d}}{\mathrm{d}s}\ln\left(\frac{Q}{s+s_0}\right). \tag{4.42}$$

To accurately evaluate these gradient components at $s = 0$ a cubic polynomial is fit to the mesh around $s = 0$. However, there are some difficulties when simply fitting this cubic directly to the points around $s = 0$. The first issue is that the behaviour of the points around $s = s_0$ for P and $s = -s_0$ for Q introduces noise because both the numerator and the denominator approach 0 as s goes to s_0 for P and s goes to $-s_0$ for Q. This issue is avoided by cutting out the problematic points and inserting a point at $\pm s_0$ using de l'Hôpital's rule, which states that indeterminate forms of $f(x)/g(x)$ such as 0/0 or ∞/∞ can be determined by evaluating the limit of the quotient of the derivatives $f'(x)/g'(x)$. The second issue is that the point where $s = 0$ moves from one cell to another during the evolution of the star. This, in turn, causes jumps in the polynomial coefficients, which in turn cause jumps in q. To avoid these issues, we remesh the points we fit to have an exponential spacing with endpoints between $s = \pm s_0/2$ or $s = \pm 0.05$, whichever is greater. This results in the following points in s:

$$s_i = i\Delta s \exp\left(\frac{\left\lfloor \frac{n}{2} \right\rfloor - |i|}{\frac{1}{2}\left\lfloor \frac{n}{2} \right\rfloor}\right) \tag{4.43}$$

where

$$\Delta s = \frac{-\max(|s_0|, 0.05)}{n} \tag{4.44}$$

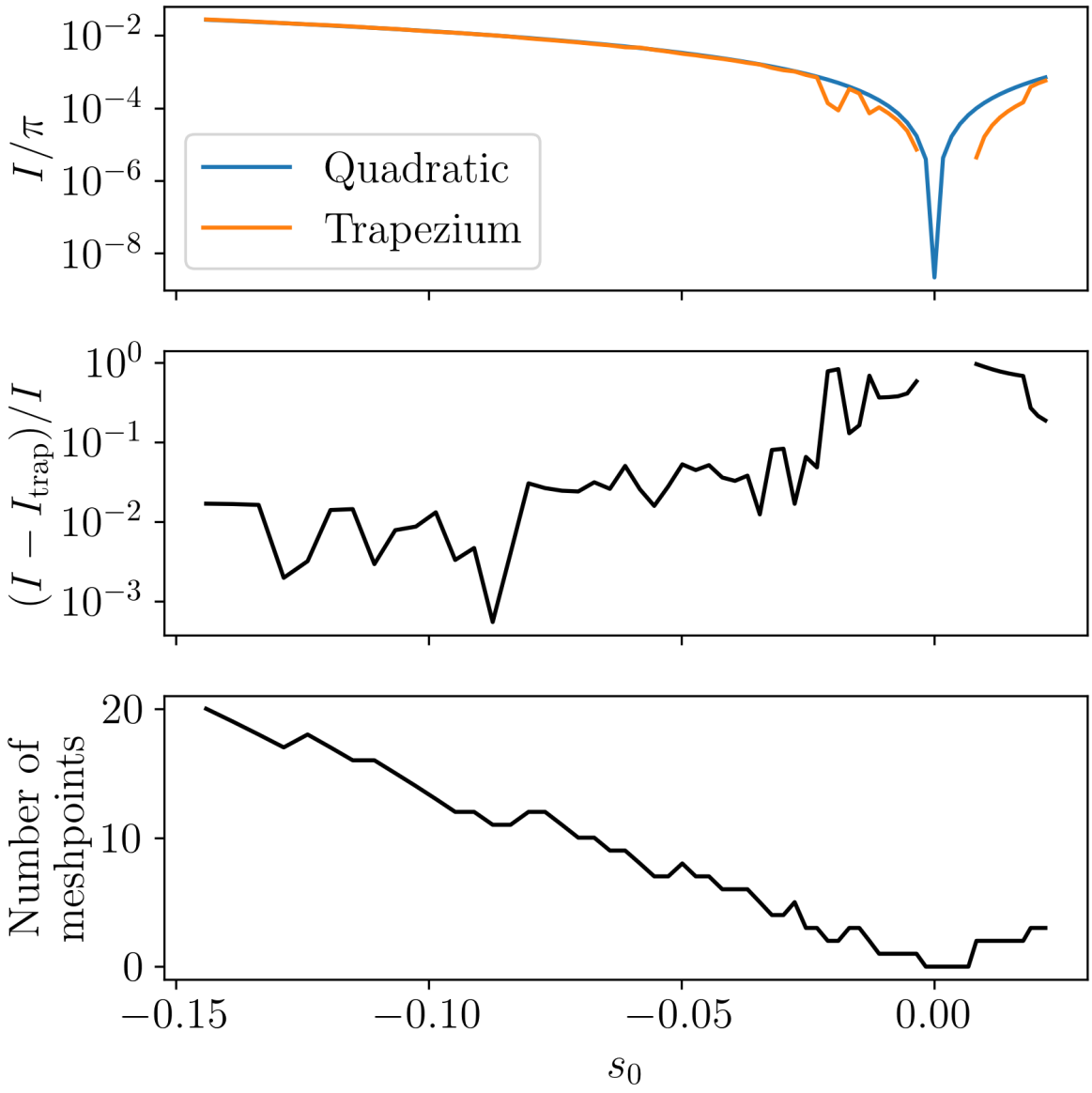

Figure 4.5: The top panel shows the integral component of X, I/π, as a function of s_0 of a 1 $M_\odot$ Solar metallicity star in the SGB. The quadratic approximation is shown in blue and the trapezium integration in orange. The middle panel shows the fractional difference between the quadratic approximation and the trapezium integration. The bottom panel shows the number of meshpoints in the evanescent zone.

and

$$i \in -\left\lfloor \frac{n}{2} \right\rfloor \ldots \left\lfloor \frac{n}{2} \right\rfloor \tag{4.45}$$

and n is the number of points to remesh to and is set to $n = 11$.

A cubic polynomial is fitted to the resulting mesh using LAPACK's `dgels` method (Anderson et al. 1999), which solves a real linear system of equations, giving us the best fitting polynomial coefficients $a_{k,P}$ and $a_{k,Q}$. Finally, to calculate the values for the gradient components we use the following equations:

$$\frac{\mathrm{d}}{\mathrm{d}s} \ln\left(\frac{P}{s_0 - s}\right) = \frac{a_{0,P}}{P_0/s_0}, \tag{4.46}$$

$$\frac{\mathrm{d}}{\mathrm{d}s} \ln\left(\frac{Q}{s + s_0}\right) = \frac{a_{0,Q}}{Q_0/s_0}, \tag{4.47}$$

where P_0 and Q_0 are the value of P and Q at $s = 0$ calculated during the fit for the integral part. Figure 4.6 shows how the fitted cubic performs. The cubic polynomial approximates the gradient around $s = 0$ well whilst also being resilient against changes in which meshpoints are used to fit the cubic.

The methods for finding the polynomial coefficients for the integral and gradient terms of Equation (4.15) are different as they require different properties. In the integral term, it is required that one of the zeros of P and Q coincides with one of the zeros of the quadratic used to fit them, as we are interested in the behaviour near $P = 0$ and $Q = 0$ in the evanescent zone. However, this is not the case when calculating the gradient. When evaluating the gradient we are interested in the behaviour at $s = 0$. Therefore, the fact that the zeros do not coincide exactly has no effect when determining the gradient term. A second, more qualitative reason for not using the integral component's method for evaluating the gradient term, is that it would introduce significant oscillations in $\mathcal{G}$ around crossings of r_1 and r_2.

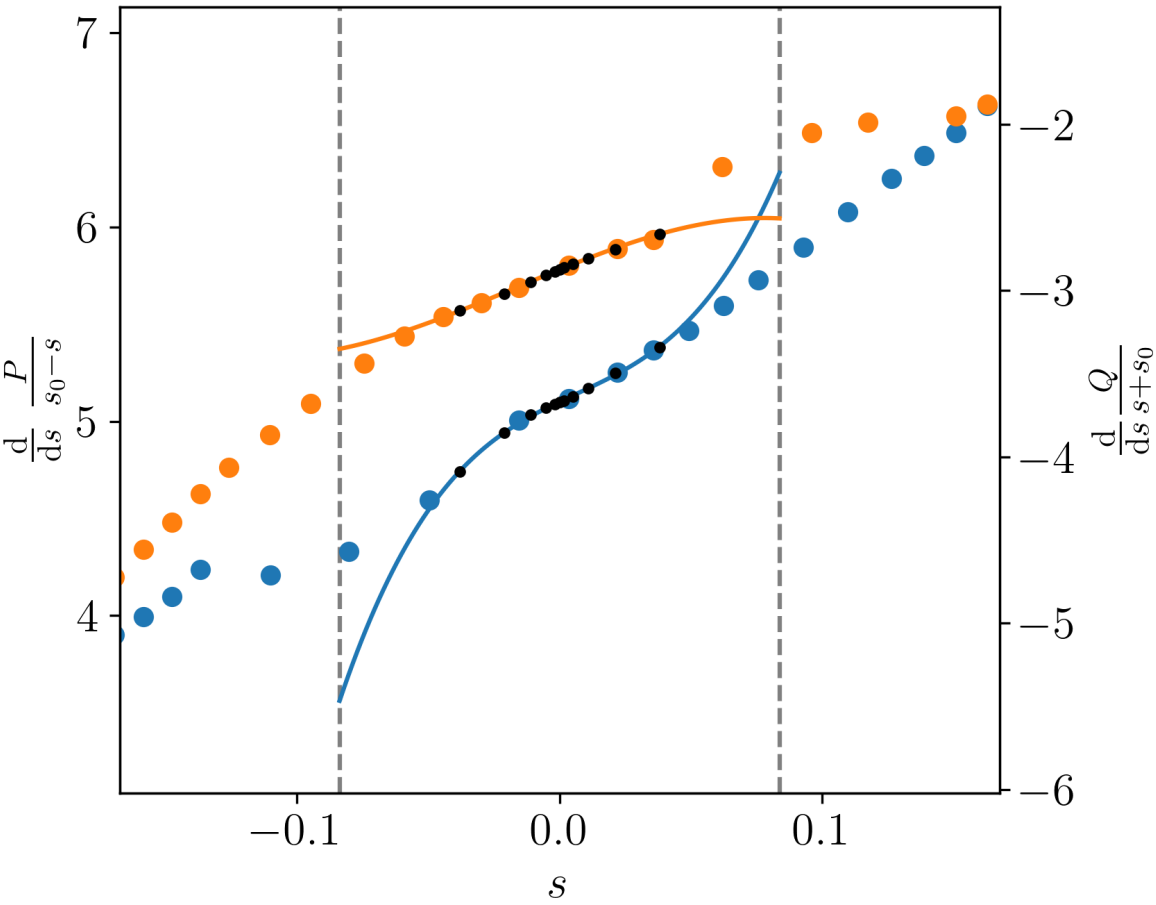

Figure 4.6: $\frac{\mathrm{d}}{\mathrm{d}s}\left(\frac{P}{s_0-s}\right)$ is shown in blue, and $\frac{\mathrm{d}}{\mathrm{d}s}\left(\frac{Q}{s+s_0}\right)$ is shown in orange. Large coloured dots are the calculated gradient after inserting the point using de l'Hôpital's rule. The small black dots are the remeshed points, and the solid lines show the fitted cubic. The vertical grey dashed lines show $\pm s_0$.

4.3 Results

Next, we describe how the coupling coefficient, computed as outlined in Section 4.2, varies with key model properties and how these predictions compare with observational constraints.

4.3.1 Evolutionary state

First, we look at how the coupling between the p- and g-mode cavities changes in different evolutionary phases for a modelled star of a given mass and initial chemical composition.

We consider models as being in the Core Helium-Burning (CHeB) phase if they satisfy the following three conditions. They:

(1) have a convective core,

(2) have a central hydrogen mass fraction less than 10^{-6}, and

(3) have a central helium mass fraction greater than 10^{-6}.

Among these CHeB models we select those with a central helium mass fraction between $0.95 \times Y_{\rm C,max}$ and 0.1, where $Y_{\rm c,max}$ is the maximum central helium mass fraction reached during evolution before CHeB. This additional constraint is included so that the portion of the evolutionary track used in the HRD lies mainly in the same area as the RC (and the secondary clump in the more massive models). Figure 4.7 shows the placement in the HRD of evolutionary tracks between 0.7 and $3 M_\odot$ with Solar metallicity during CHeB and with the RC highlighted in red.

We consider four models (A-D) during the evolution of a 1 $M_\odot$ Solar metallicity star:

(A) RGB at the effective temperature of the RC.

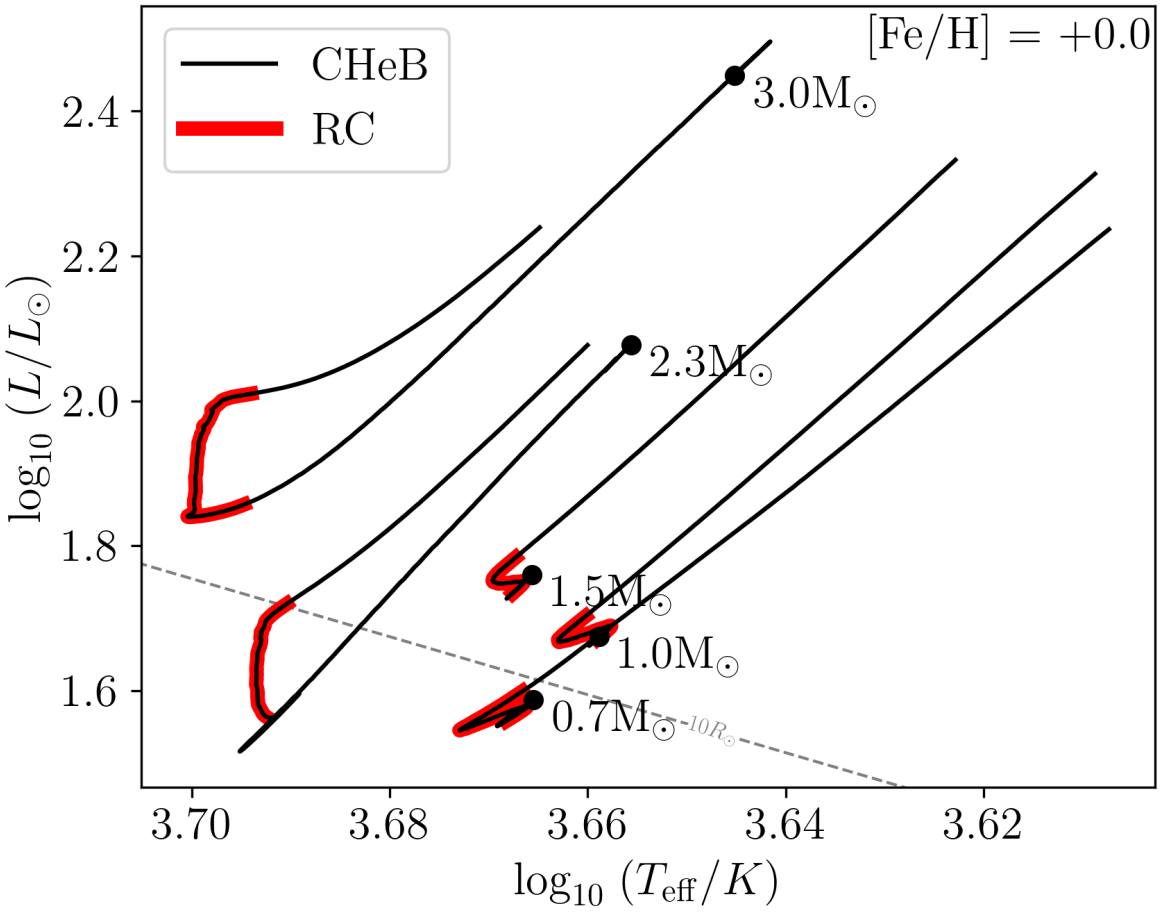

Figure 4.7: Tracks in the HRD of five 0.7–3$M_\odot$ stars with [Fe/H] = 0 during core helium-burning (CHeB). The RC phase is highlighted in red. The black dots indicate the onset of CHeB.

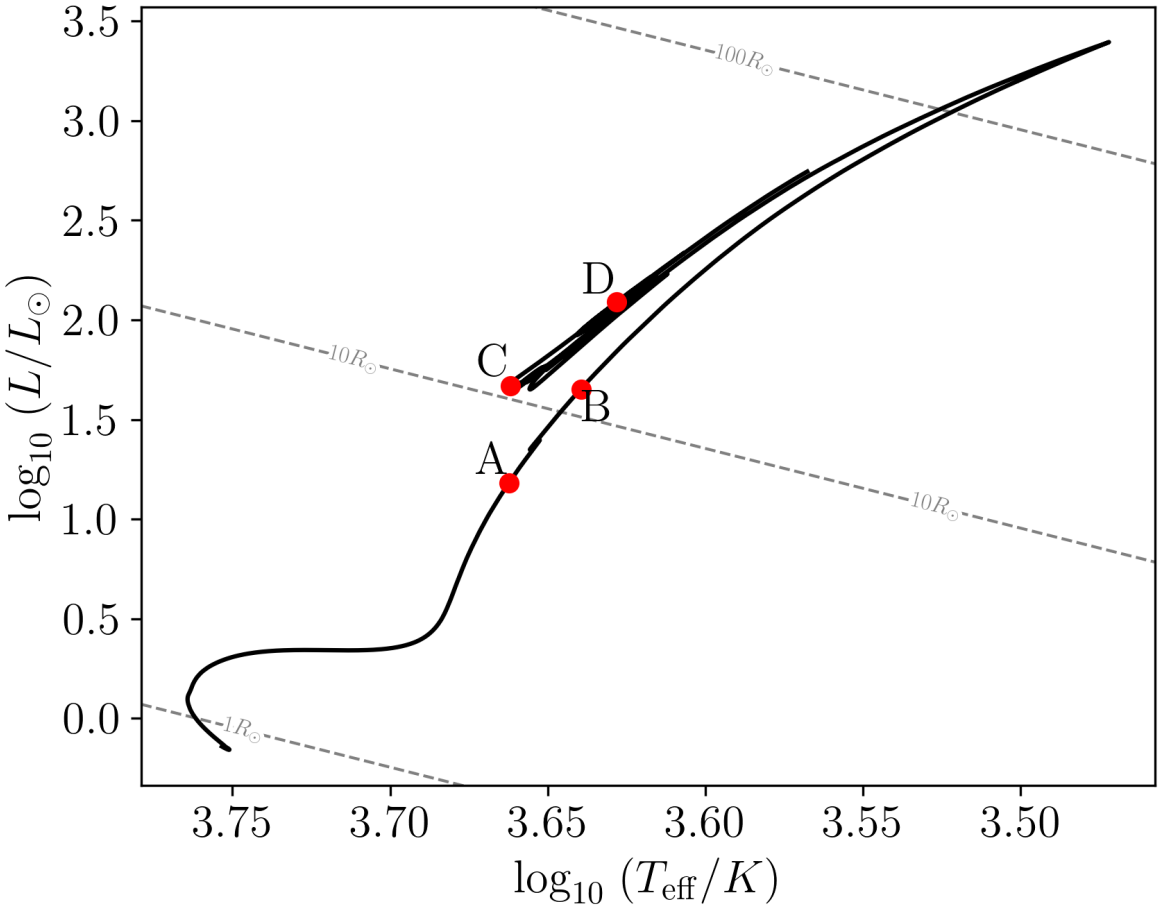

Figure 4.8: Locations of models A–D in the HRD for a $1M_\odot$ [Fe/H] = 0 star.

(B) RGB at the luminosity of the RC.

(C) Middle of core helium-burning (CHeB) in terms of time (at $Y_C = 0.52$).

(D) Early-AGB at the effective temperature of model B (degenerate CO core with shell helium-burning).

Figure 4.8 shows the location of these models in the HRD as red points.

Figure 4.9 shows the propagation diagrams of models A–D. Models A, B, and D have type-b evanescent zones and therefore we use the weak-coupling prescription from Takata (2016a)

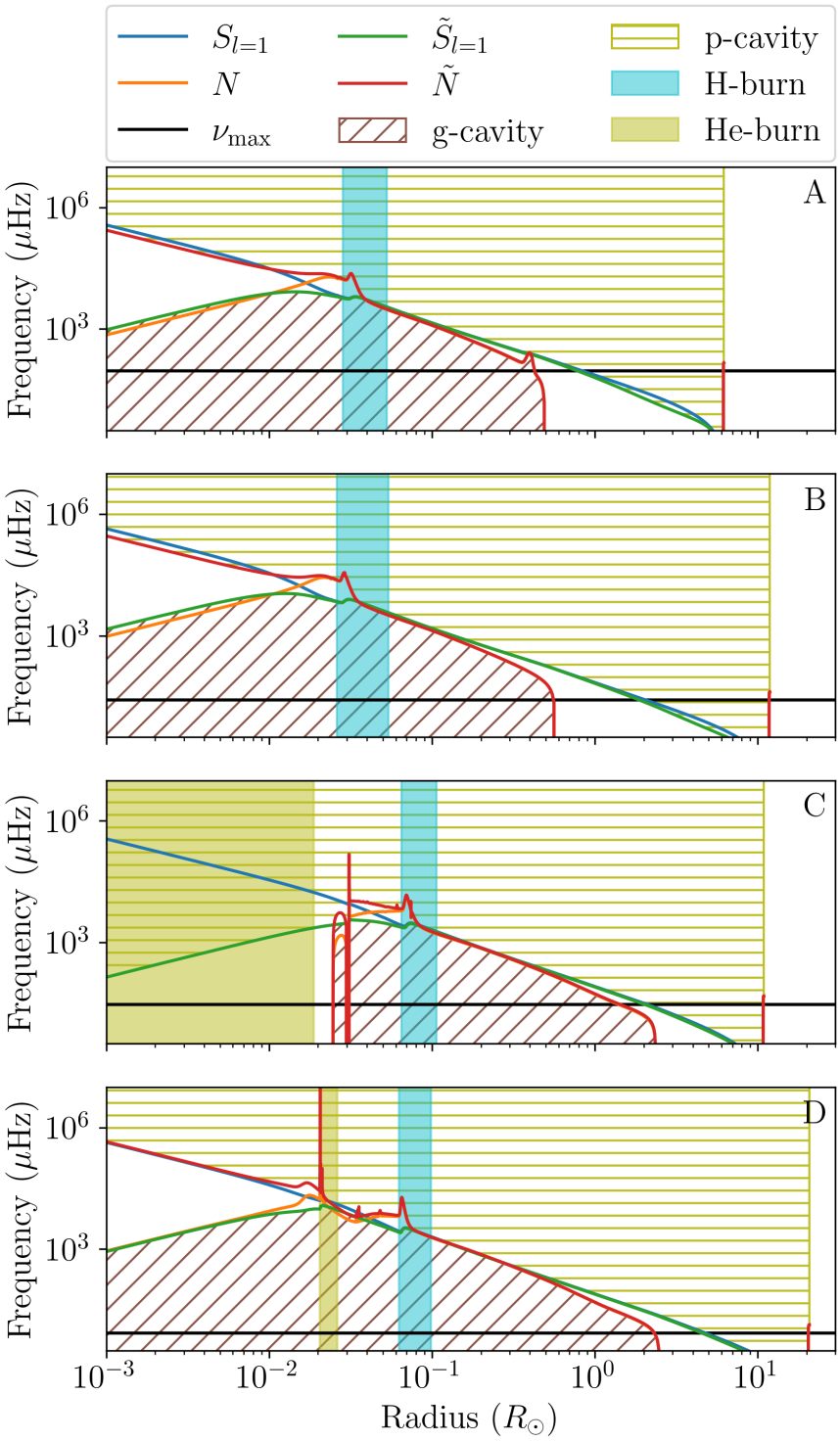

Figure 4.9: Propagation diagrams of models A–D. The Lamb (S) and reduced Lamb ($\tilde{S}$) frequencies are shown as blue and green lines, the Brunt-Väisälä (N) and reduced Brunt-Väisälä ($\tilde{N}$) frequencies are shown as orange and red lines. $\nu_{\max}$ is shown as a black line.

described in Table 4.1 in Section 4.2.2. We use the strong-coupling prescription for model C. The Kippenhahn diagram in Figure 4.10 shows the coupling in the various evolutionary phases from the SGB onward with the locations of models A–D shown along the top. During the SGB, the star is in the strong-coupling regime (solid black line in Figure 4.10) as the evanescent zone is fully radiative (type-a evanescent zone, following Pinçon et al. 2019 and Table 4.1). As the star evolves along the RGB, it encounters the glitch in $\tilde{N}$ below the convective envelope and also enters the transition regime (the gap between the solid and dashed black lines). The star continues up the RGB and its evanescent zone becomes type-b. Therefore, the coupling is in the weak regime (dashed black lines) and decreases as the star evolves further. When the evanescent zone is of type-b, its bottom edge closely follows the bottom of the convective envelope. As the star continues up the RGB, we encounter models A and B (top two panels in Figure 4.9), which are structurally similar. However, model A has not yet gone through the RGB-bump (RGBb) whilst model B has. In the coupling, the RGBb is also visible as a bump in the coupling coefficient (middle of the RGB in Figure 4.10). This bump occurs for the same reason as the RGBb: the hydrogen-burning shell encounters the composition gradient left behind by the first dredge-up. This causes the bottom of the convective envelope to recede, increasing r_2 whilst leaving r_1 relatively untouched, therefore reducing the size of the evanescent zone. The hydrogen-burning shell is visible as the blue shaded region at around 3×10^{-2} $R_\odot$ in Figure 4.9 A and B, and at around $0.2 M_\odot$ in Figure 4.10. Model A has a coupling coefficient of 0.091, whilst the coupling coefficient of model B is around a fifth of model A, at 0.016. This difference is due to the increase in size of the evanescent zone, with $r_1 - r_2 = 0.34$ $R_\odot$ in model A and $r_1 - r_2 = 1.32$ $R_\odot$ in model B. Additionally, the star has almost doubled in size expanding from 6.2 $R_\odot$ in model A to 11.9 $R_\odot$ in model B.

Once CHeB has started, the hydrogen-burning shell has advanced to around 6×10^{-2} $R_\odot$ (0.48 $M_\odot$) and the evanescent zone is of type-a as seen in panel C of Figure 4.9 and in Figure 4.10. The evanescent zone is just below the convective envelope and stays there until the end of the RC phase. This is in contrast to models A and B where the evanescent zone is almost entirely (model

A) or entirely (model B) contained in the convective envelope. Therefore, the density distribution leads to the evanescent zone being smaller than in models A and B, resulting in a stronger coupling of approximately 0.26.

Between the end of the RC phase and the end of CHeB, helium in the convective core is exhausted. The central regions of the star start to contract as the support from helium-burning decreases and the envelope expands. This in turn leads to the convective envelope driving deeper into the star and as a consequence the convective boundary enters the evanescent zone again.

During the early-AGB (model D) the hydrogen-burning shell is at 0.51 $M_\odot$. Helium burning in the star takes place in a shell located at approximately 0.25 $M_\odot$, following a contraction of the central regions. This contraction leads to a structure with a density contrast comparable to that of an RGB star of similar $T_{\rm eff}$. The coupling in this phase is weak with a coefficient of 0.05–0.10. The evanescent zone during this phase is of type-b and starts, as in model B, just inside the lower boundary of the convective envelope.

Figure 4.11 shows the coupling coefficient versus $\Delta\nu$ for a $1M_\odot$ star with Solar metallicity. We define an average $\Delta\nu$ by taking the weighted mean of $\Delta\nu(\nu)$ around $\nu_{\rm max}$ for $\ell = 0$ modes computed using `gyre`. The weights are calculated using the power-spectrum density envelope described in Mosser et al. (2012) and adopted in, e.g., Rodrigues et al. (2017). The four evolutionary snapshots, models A–D, described above are shown as red dots. The RC is clearly visible as the high-q concentration of black dots at $\Delta\nu \sim 4$ μHz. The large spread in coupling coefficients inferred from the observed spectra compared to the model values becomes apparent and is likely due to the effect that buoyancy glitches have on deriving q (Vrard et al. 2016; Mosser et al. 2017, 2018). The observed coupling during the ascent up the RGB is shown by the black squares. The computed weak coupling underestimates the strength of the observed coupling as shown in Figure 4.11. However, very small values of q were penalized when these values were determined (§3.4 in Mosser et al. 2017) and this may explain the lack of observed q below around 0.05. Additionally,

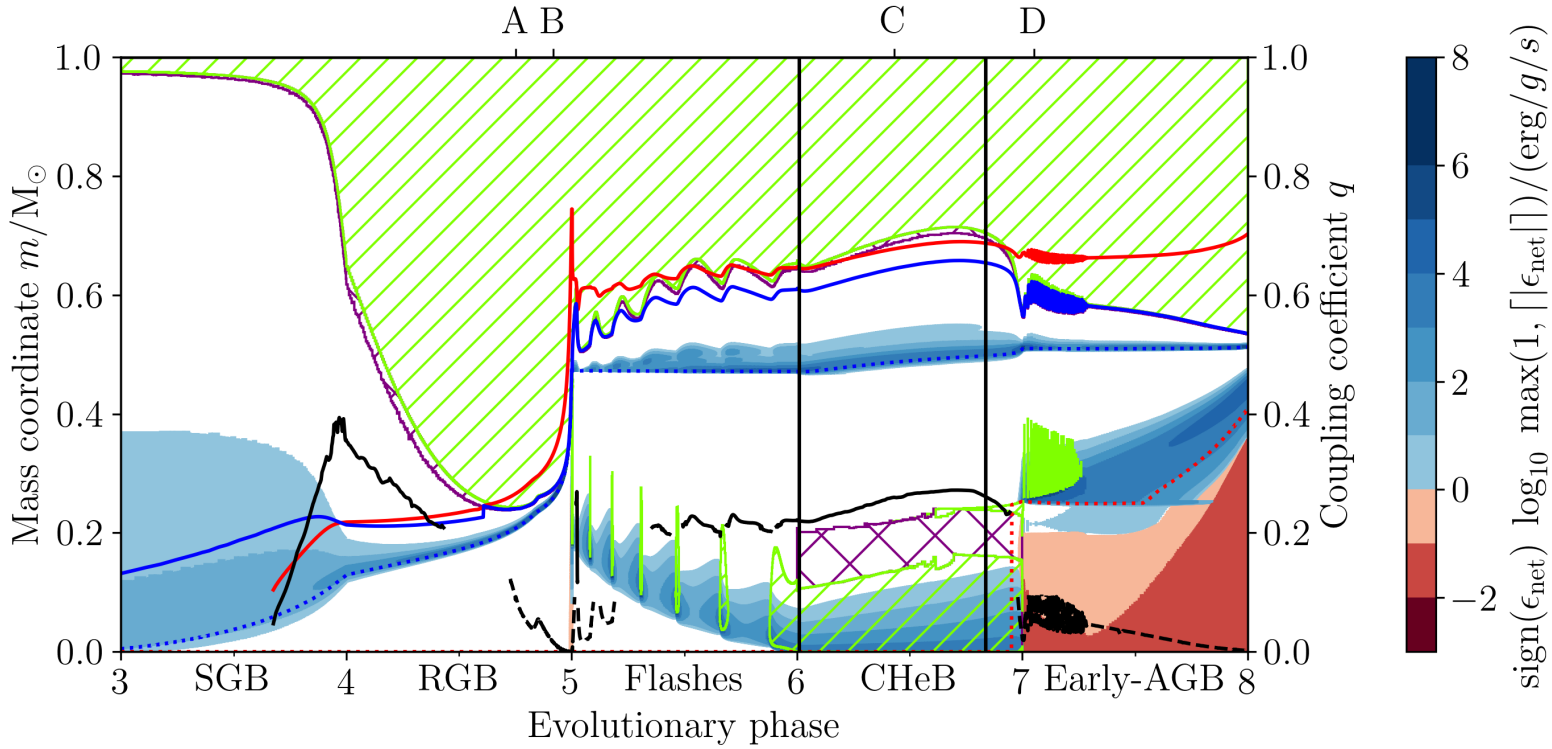

Figure 4.10: Kippenhahn diagram of a 1 $M_\odot$ star with Solar metallicity. The x-axis shows the stellar age with different scales between evolutionary phases. The SGB is shown from 3–4, the ascent up the RGB from 4–5, the helium flashes from 5–6, CHeB from 6–7, and early-AGB from 7–8. Convection is shown by the green //-hashed regions. Convective overshoot is shown by the purple cross-hashed region. The colour scale shows the net nuclear energy generation rate. The blue dashed line shows the boundary between the helium core and hydrogen envelope. The red dashed line shows the boundary between the helium core and the CO core. Strong coupling is shown as a solid black line and weak coupling as a dashed black line. The boundaries of the evanescent zone, r_1 and r_2, are shown as the red and blue lines respectively. The two vertical black lines in the CHeB phase show the start and end of the RC. The locations of models A–D are shown along the top.

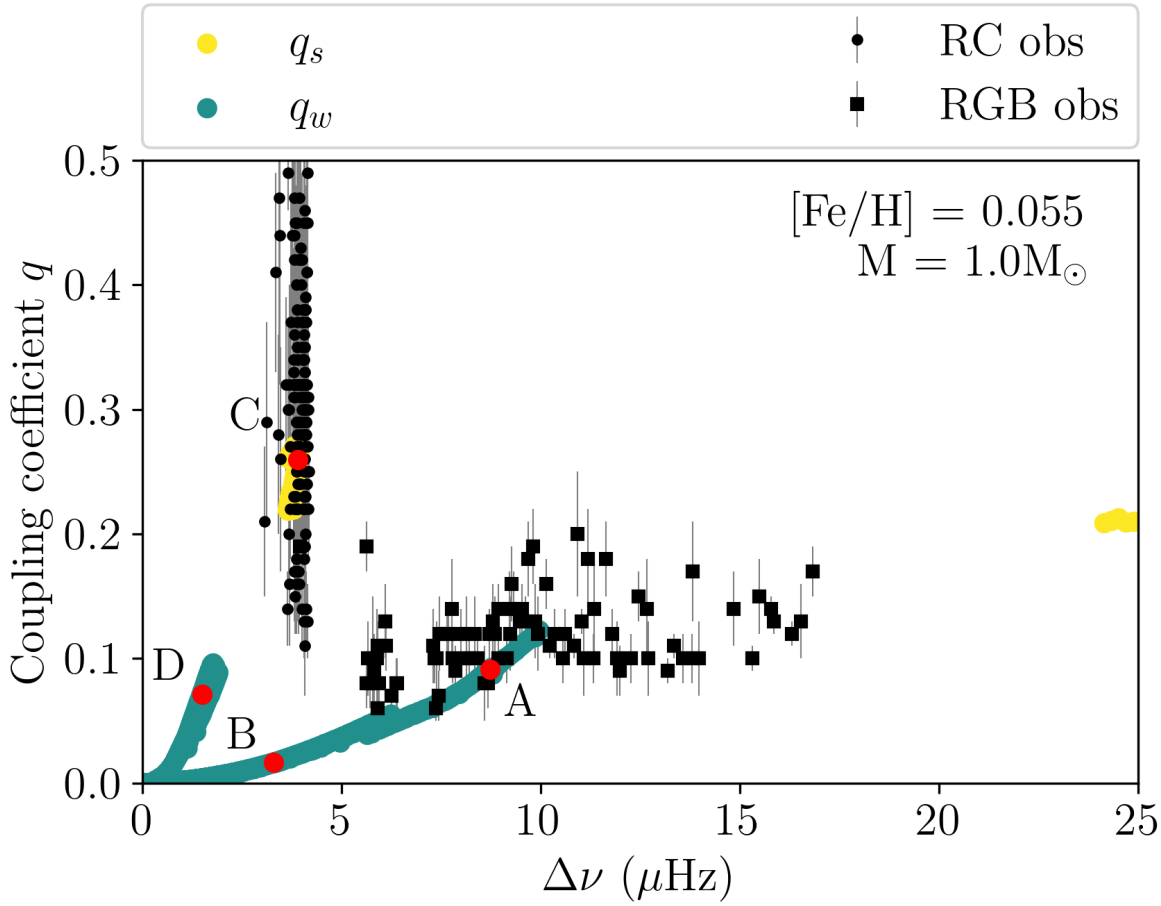

Figure 4.11: Track of a 1 $M_\odot$ star with Solar metallicity showing the coupling coefficient q as a function of the large frequency separation $\Delta\nu$. Yellow points indicate strong coupling, cyan points indicate weak coupling. Observed coupling and $\Delta\nu$ (Vrard et al. 2016; Mosser et al. 2017) in stars with masses between 0.9$M_\odot$ and 1.1$M_\odot$ and metallicities between -0.125 and 0.125 are shown as black dots and squares, with dots having $\Delta\Pi_1 \leq 130$ s and squares $\Delta\Pi_1 > 130$ s. The red points show the locations of models A–D.

the absence of modelled coupling between $10 \lesssim \Delta\nu/\mu\text{Hz} \lesssim 24$ is visible due to the limitations in the coupling prescriptions described in 4.2.2, namely the star being in the transition regime and splitting of the evanescent zone due to the spike in $\tilde{N}$.

4.3.2 Dependence on oscillation frequency

Up to now, we have only looked at q when $\nu_q = \nu_{\max}$. However, stars with SLO have a frequency spectrum with a Gaussian-like power envelope, characterized by $\sigma = 0.66\ \nu_{\max}^{0.88}$ (Mosser et al. 2012). A 1 $M_\odot$ Solar metallicity star at both the RGBb and RC has $\sigma \simeq 1.5\Delta\nu$. Therefore, it is necessary to study how q changes as a function of ν_q for a given model. Jiang et al. (2020) found that the coupling coefficient increases as a function of mode frequency ν_q in the RGB for a given model. Our models show similar behaviour, although our models include undershooting below the convective envelope, and therefore alter the behaviour of the propagation cavity. Their tabulated coupling coefficients also generally fall in the intermediate regime for which a valid approximation of the coupling is not available yet. Figure 4.12 shows the coupling and coupling gradient in our model as a function of $\nu_{\max}$ in a 1 $M_\odot$ Solar metallicity star. There are three different regions apparent in the bottom panel. The first is from approximately 100–80 μHz, then from 80–60 μHz, and finally below 60 μHz. The first and third regions are due to the same effect, where the size of the evanescent zone quickly becomes smaller at higher frequencies because $\tilde{N}$ is steeper than $\tilde{S}$ (panels A and B in Figure 4.9). In the 80–60 μHz region $\langle \mathrm{d}q/\,\mathrm{d}\nu_q \rangle$ is almost constant as $\tilde{N}$ is not as steep as in panels A and B in Figure 4.9. This behaviour may provide a method by which the amount of undershooting can be measured in future work. Larger undershooting reduces the height of the $\tilde{N}$ spike and widens the spike, reducing the spread in $\langle \mathrm{d}q/\,\mathrm{d}\nu_q \rangle$. Larger undershooting also increases the size of the undershooting zone, decreasing the change in slope of $\tilde{N}$ and therefore also reducing the spread in $\langle \mathrm{d}q/\,\mathrm{d}\nu_q \rangle$. These three regions are seen in all our models with masses of 0.7, 1.0, and 1.5 $M_\odot$.

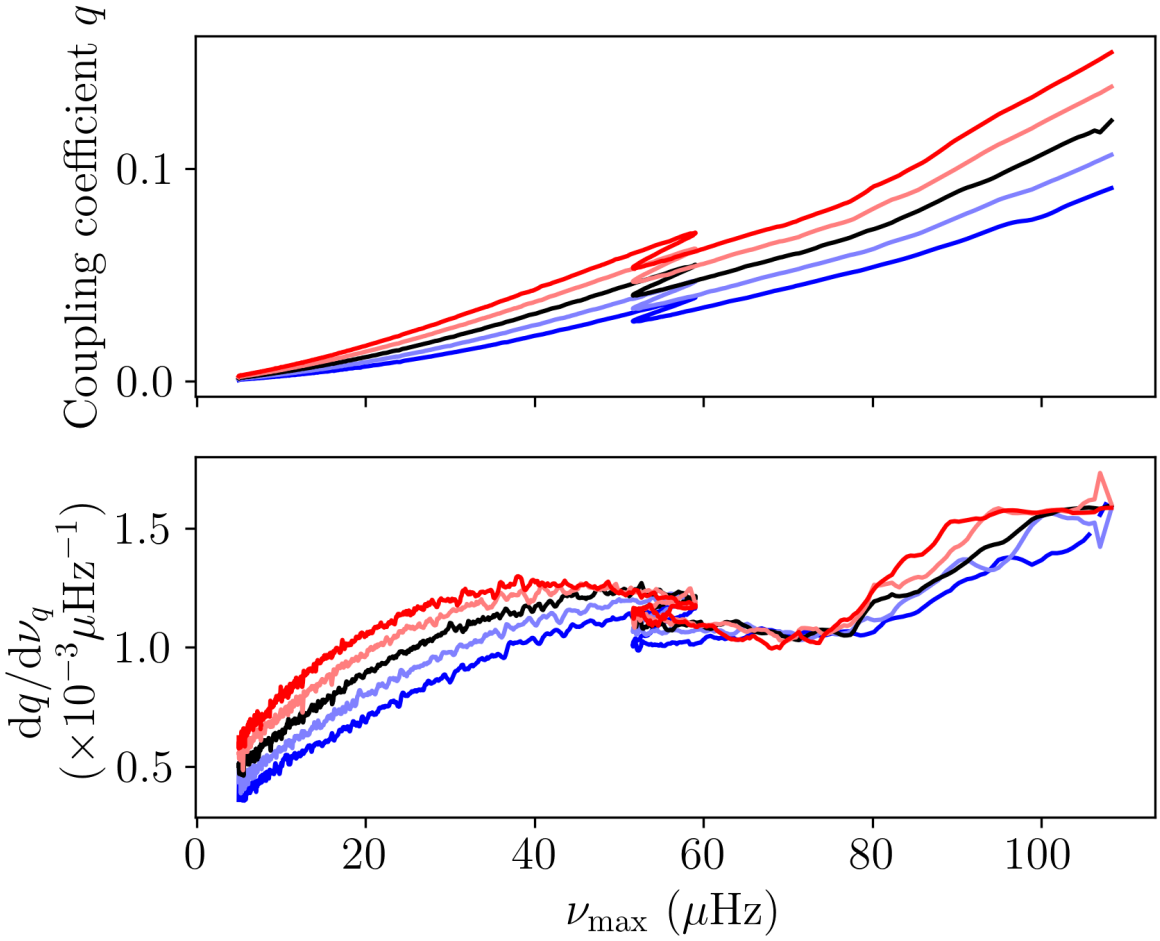

Figure 4.12: The coupling (top) and coupling gradient (bottom) as a function of ν_{max} in a 1 $\mathrm{M}_{\odot}$ star with Solar metallicity. The black line in each panel shows the values at ν_{max}. The red line in each panel shows the values at $\nu_{\mathrm{max}} + 2\Delta\nu$, light red at $\nu_{\mathrm{max}} + \Delta\nu$, light blue at $\nu_{\mathrm{max}} - 2\Delta\nu$, and blue at $\nu_{\mathrm{max}} - 2\Delta\nu$.

Table 4.3 shows the mean coupling coefficient $\langle q \rangle$ at $\nu_{\max}$, mean coupling gradient $\langle \mathrm{d}q/\mathrm{d}\nu_q \rangle$, mean $\nu_{\max}$, and mean $\Delta\nu$ for models during the temporary drop in L in the RGBb. This ensures that $f_{\mathrm{CZ}} \simeq 0$ and that using the weak coupling approximation is valid. We define the mean coupling gradient as:

$$\left\langle \frac{\mathrm{d}q}{\mathrm{d}\nu_q} \right\rangle = \frac{1}{\tau_{\mathrm{RGBb}}} \int_{\mathrm{RGBb}} \frac{q(\nu_{\max} + \Delta\nu) - q(\nu_{\max} - \Delta\nu)}{2\Delta\nu} \, \mathrm{d}t, \tag{4.48}$$

where we define the integration domain as the star being in the RGB with an increasing effective temperature. Within one $\Delta\nu$ frequency interval, there can be a difference of between 10–20% in q. This variation of q, due to different ν_q, should be taken into account when determining q from observations. We also find that before the RGB bump $\langle \mathrm{d}q/\mathrm{d}\nu_q \rangle$ does not vary much as a function of ν_q as seen by the constant $\langle \mathrm{d}q/\mathrm{d}\nu_q \rangle$ in the bottom panel of Figure 4.12 in the 60–80 μHz region. However, after the bump this is no longer the case as all models have steeper $\langle \mathrm{d}q/\mathrm{d}\nu_q \rangle$ at higher ν_q with $\langle \mathrm{d}^2q/\mathrm{d}\nu_q^2 \rangle \simeq 10 - 100 \times 10^{-6}$ $\mu\mathrm{Hz}^{-2}$ at around half the bump's $\nu_{\max}$.

Figure 4.13 shows how the coupling, central helium mass fraction, and the mode frequency vary in a $1\mathrm{M}_\odot$ star with [Fe/H] = 0 in the RC. Table 4.4 shows the mean $\langle \mathrm{d}q/\mathrm{d}\nu_q \rangle$ when the central helium abundance is between $0.4 \leq Y_{\mathrm{C}} \leq 0.6$. We see that there is also a dependence of q on ν_q in RC stars. The relative effect of these type-a evanescent zones is not as strong as in the RGB as one $\Delta\nu$ only results in a change in q of 1–10%. Table 4.4 also shows that our models with masses of $1\mathrm{M}_\odot$ have negative $\langle \mathrm{d}q/\mathrm{d}\nu_q \rangle$. When this is the case, $\tilde{S}$ and $\tilde{N}$ converge increasing r, i.e. the evanescent zone becomes smaller at lower ν_q, and vice versa when $\langle \mathrm{d}q/\mathrm{d}\nu_q \rangle$ is positive. However, below around 20 μHz the star enters the intermediate-coupling regime (dotted dark blue line in the middle panel of Figure 4.13). This is less than the minimum expected observable frequency which in this case is around 1.5 $\Delta\nu$ below $\nu_{\max}$. By numerically calculating the modes' eigenfunctions and inertiae with `gyre`, it becomes apparent that the coupling of these low frequency cases broadly follows the behaviour of the coupling calculated at other frequencies. During evolution in the RC, the strength of the coupling increases as the star consumes helium in the RC (bottom panel of Figure 4.13). Figure 4.14 shows a propagation diagram of a $1\mathrm{M}_\odot$ star in the RC with a central

Table 4.3: Table of the modelled mean coupling coefficient $\langle q \rangle$ and mean coupling coefficient gradient $\langle \mathrm{d}q/\mathrm{d}\nu_q \rangle$ at $\nu_{\max}$ during the RGBb descent.

Mass ($M_\odot$)	Initial [Fe/H]	$\langle q \rangle$	$\langle \mathrm{d}q/\mathrm{d}\nu_q \rangle$ ($\times 10^{-3} \mu\mathrm{Hz}^{-1}$)	$\nu_{\max}$ (μHz)	$\Delta\nu$ (μHz)
0.70	-1.00	0.033	2.00 ± 0.02	23.5	3.55
1.00	-1.00	0.030	2.14 ± 0.09	19.6	2.83
1.50	-1.00	0.028	2.32 ± 0.09	16.3	2.23
0.70	-0.50	0.039	1.43 ± 0.03	39.6	5.17
1.00	-0.50	0.036	1.58 ± 0.06	32.1	4.05
1.50	-0.50	0.034	1.76 ± 0.04	26.1	3.14
0.70	0.00	0.053	1.03 ± 0.02	71.3	7.91
1.00	0.00	0.047	1.17 ± 0.03	55.0	5.98
1.50	0.00	0.042	1.31 ± 0.02	42.7	4.48
0.70	0.25	0.061	0.88 ± 0.01	93.3	9.60
1.00	0.25	0.052	1.01 ± 0.03	68.9	7.02
1.50	0.25	0.045	1.15 ± 0.03	52.2	5.17
0.70	0.40	0.065	0.81 ± 0.01	105.6	10.47
1.00	0.40	0.055	0.95 ± 0.01	76.4	7.55
1.50	0.40	0.047	1.09 ± 0.01	56.8	5.48

Table 4.4: As Table 4.3 for stellar models during the middle of the RC and taking the mean over $0.4 \leq Y_C \leq 0.6$.

Mass ($M_\odot$)	Initial [Fe/H]	$\langle q \rangle$	$\langle \mathrm{d}q/\mathrm{d}\nu_q \rangle$ ($\times 10^{-3} \mu\mathrm{Hz}^{-1}$)	$\nu_{\max}$ (μHz)	$\Delta\nu$ (μHz)
0.70	-1.00	0.706	1.09 ± 0.77	39.8	5.56
1.00	-1.00	0.466	-12.06 ± 1.28	33.3	4.36
1.50	-1.00	0.449	-4.95 ± 1.22	38.3	4.39
2.30	-1.00	0.569	2.95 ± 0.55	43.6	4.49
3.00	-1.00	0.462	4.60 ± 0.56	44.1	4.56
0.70	-0.50	0.527	7.60 ± 0.45	32.8	4.66
1.00	-0.50	0.315	-4.32 ± 0.59	30.5	3.98
1.50	-0.50	0.262	3.18 ± 0.23	38.9	4.33
2.30	-0.50	0.351	-2.69 ± 0.59	71.7	6.29
3.00	-0.50	0.703	-0.41 ± 2.67	34.5	3.46
0.70	0.00	0.424	1.86 ± 0.13	29.9	4.20
1.00	0.00	0.261	-2.24 ± 0.36	29.7	3.79
1.50	0.00	0.195	1.73 ± 0.34	39.3	4.26
2.30	0.00	0.199	0.72 ± 0.26	91.2	7.34
3.00	0.00	0.246	-0.69 ± 0.31	63.5	5.26
0.70	0.25	0.361	-1.87 ± 0.48	29.7	4.13
1.00	0.25	0.219	-2.69 ± 0.29	29.8	3.76
1.50	0.25	0.173	0.84 ± 0.12	39.6	4.22
2.30	0.25	0.178	0.68 ± 0.25	81.0	6.61
3.00	0.25	0.192	0.38 ± 0.22	72.6	5.74
0.70	0.40	0.319	-1.38 ± 0.25	29.6	4.07
1.00	0.40	0.200	-3.22 ± 0.22	29.5	3.70
1.50	0.40	0.161	0.57 ± 0.14	39.1	4.16
2.30	0.40	0.165	0.49 ± 0.10	80.1	6.51
3.00	0.40	0.177	0.43 ± 0.27	72.9	5.71

helium mass fraction of around 0.5. The elements on the plot are the same as in Figure 4.1,but with the inclusion of the additional frequencies in steps of $\Delta\nu$ at which the coupling is calculated as red ($+\Delta\nu$, $+2\Delta\nu$) and blue ($-\Delta\nu$, $-2\Delta\nu$) horizontal lines. The centre of each evanescent zone, r_0, is shown as a vertical dashed line of the same colour. The evanescent zones with $\nu_q \geq \nu_{\max} - \Delta\nu$ are radiative, whilst the evanescent zone with $\nu_q = \nu_{\max} - 2\Delta\nu$ is approximately 5% convective in terms of s.

4.3.3 Dependence on mass and metallicity, and comparison with observations

To compare our models with observations, we use the Mosser et al. (2017) catalogue, which contains the measured coupling coefficients q of over 5000 red giant stars. There are four main potential sources of systematic biases in the procedure to estimate q from observations. They are acoustic glitches, buoyancy glitches, rotational splitting, and assuming that q is not a function of ν_q. For spectroscopic parameters and uncertainties we use SDSS-DR14 (Abolfathi et al. 2018). Finally, we use the full set of inferred masses from Miglio et al. (2021) including stars with less reliable age estimates. The stars common in these three data sets which have inferred masses available and have non-zero uncertainties in q are used, resulting in just under 2500 stars in the final data set.

Figure 4.15 shows the modelled mean coupling in the red clump as square markers and the observed coupling as coloured dots. The colour scale represents the coupling coefficient. A typical observational uncertainty of q is around 20%. The coloured regions in between the modelled markers show the weighted mean of the coupling of all observed stars inside that region. The x-axis shows the observed [Fe/H] of these stars and the y-axis is the inferred mass from Miglio et al. (2021). To select RC stars, we use only stars with $\Delta P > 130$ s. This cut in ΔP is made because there is a clear separation in the $\Delta\nu$-ΔP plane for all stars in the sample of observed stars. In the

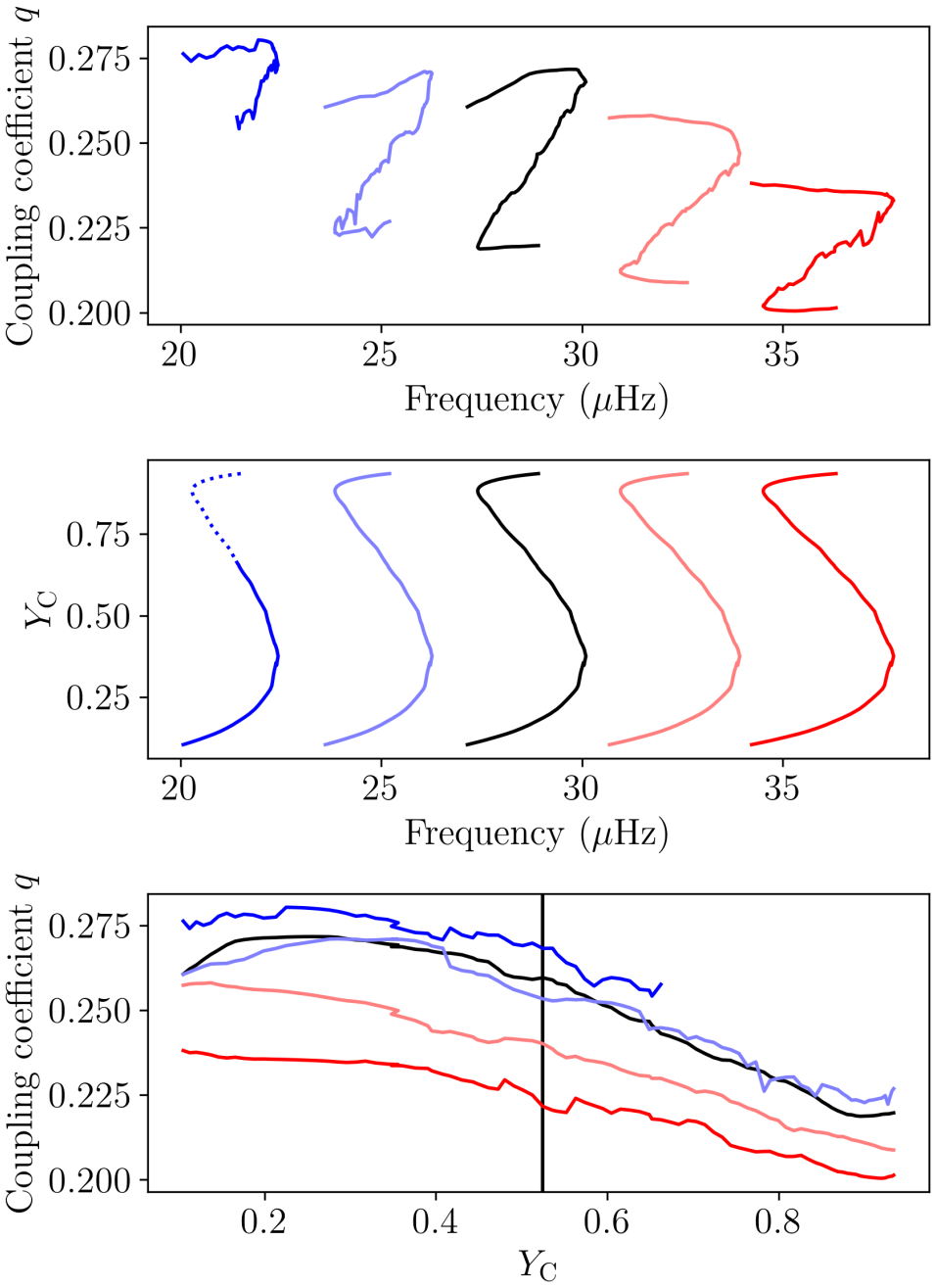

Figure 4.13: The strong-coupling coefficients as a function of frequency in the RC (top), the central helium mass fraction Y_C as a function of frequency (middle), and the coupling coefficient as a function of central helium mass fraction (bottom). The black line corresponds to $\nu_q = \nu_{max}$, the coloured lines correspond to ν_q offset from ν_{max} in steps of $\Delta\nu$. The dotted line in the middle panel represents when the coupling is in the intermediate case.

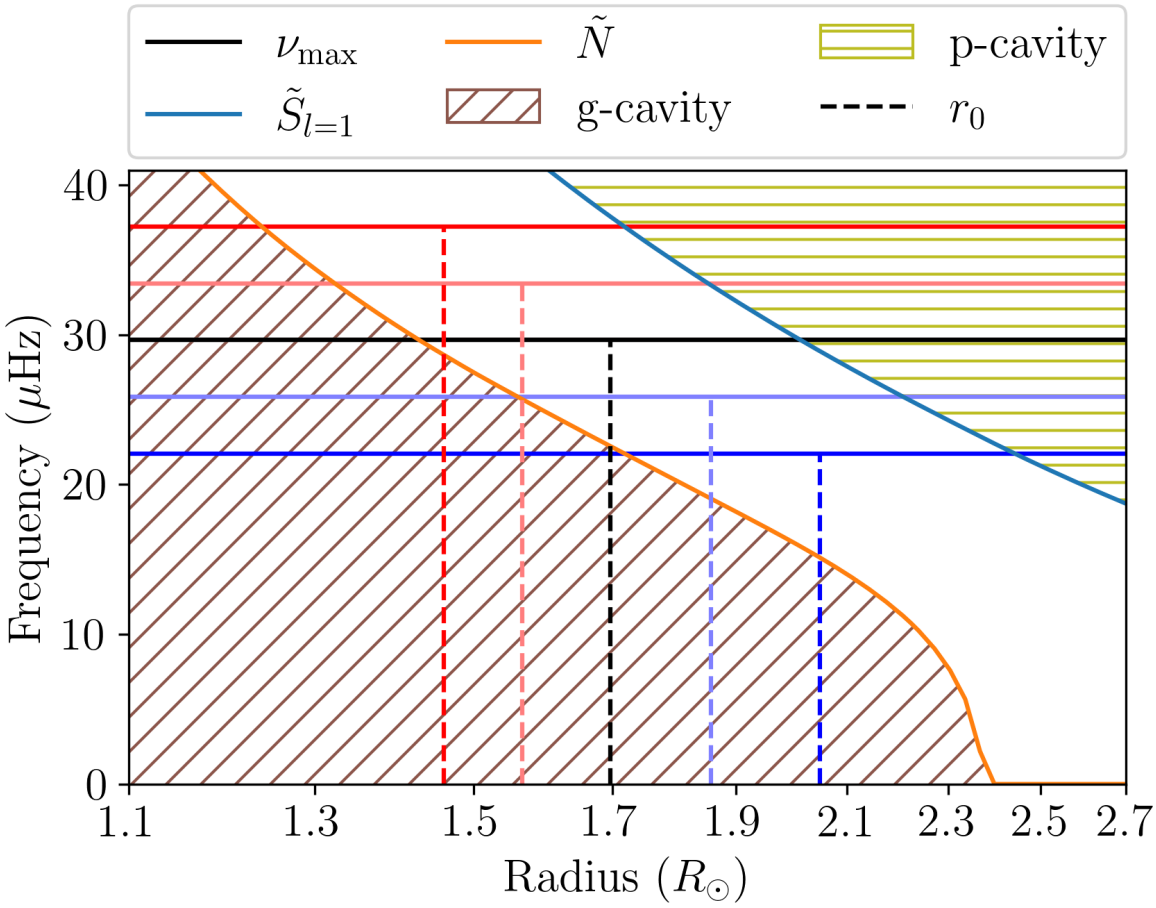

Figure 4.14: Propagation diagram of a $1M_\odot$ Solar metallicity star in the RC with $Y_C \simeq 0.5$. The black horizontal line corresponds to $\nu_q = \nu_{\max}$, and the coloured horizontal lines correspond to ν_q offset from $\nu_{\max}$ in steps of $\Delta\nu$. The vertical dashed lines correspond to r_0 ($s = 0$) at the respective frequency.

RC, we see that the observed stars are concentrated in the lower-mass, higher-metallicity region. Figure 4.15 further shows that there are hardly any observed stars in the top left and bottom right regions of the plot. This lack of stars is expected from Galactic chemical evolution i.e. a lack of young (more massive) metal-poor stars and old (less massive) metal-rich stars.

The observed data anti-correlate between mass and coupling with stronger coupling coefficients being more prevalent at lower masses and lower metallicities. Above around 2.3 $M_\odot$ the coupling coefficient increases with mass. RC stars which fall into high-mass low-metallicity and low-mass high-metallicity regions, are good candidates for further investigation into whether they have had any binary interactions in their past, as high-mass low-metallicity RC stars would be too old to currently exist and not enough time has elapsed for low-mass high-metallicity stars to enter the RC when assuming single stellar evolution.

Figure 4.16 shows coupling coefficient q vs. large frequency separation $\Delta\nu$ for models and observations of RC stars. In general, our models agree for the bulk of observed q with observations being on average 1.5-σ away from a model when taking the quadratic mean. The modelled masses cover the range in observed $\Delta\nu$. However, there are some cases where the observed q lies far away from a corresponding model, e.g. the group of points with low q at a $\Delta\nu$ of around 4 μHz and the $\Delta\nu$ of the 0.7 $M_\odot$ modelled star for [Fe/H] = −0.5 or the more massive stars for [Fe/H] = 0.25.

Figure 4.17 shows the mean coupling in the RC (Section 4.2.2) as a function of initial mass at different metallicities of modelled stars and the observed coupling and metallicity of RC stars. The mean coupling in the RC is defined as:

$$\bar{q}_{\mathrm{RC}} = \frac{\int_{\mathrm{RC}} q \, \mathrm{d}t}{\tau_{\mathrm{RC}}}, \tag{4.49}$$

where τ_{RC} is the lifetime in the RC and the integral is taken over the time spent in the RC. The mean RC coupling is strongest at lower masses and increases when $M \gtrsim 2$ $M_\odot$. The observed coupling coefficients follow this trend as well, with decreasing q at low masses and increasing q at high masses.

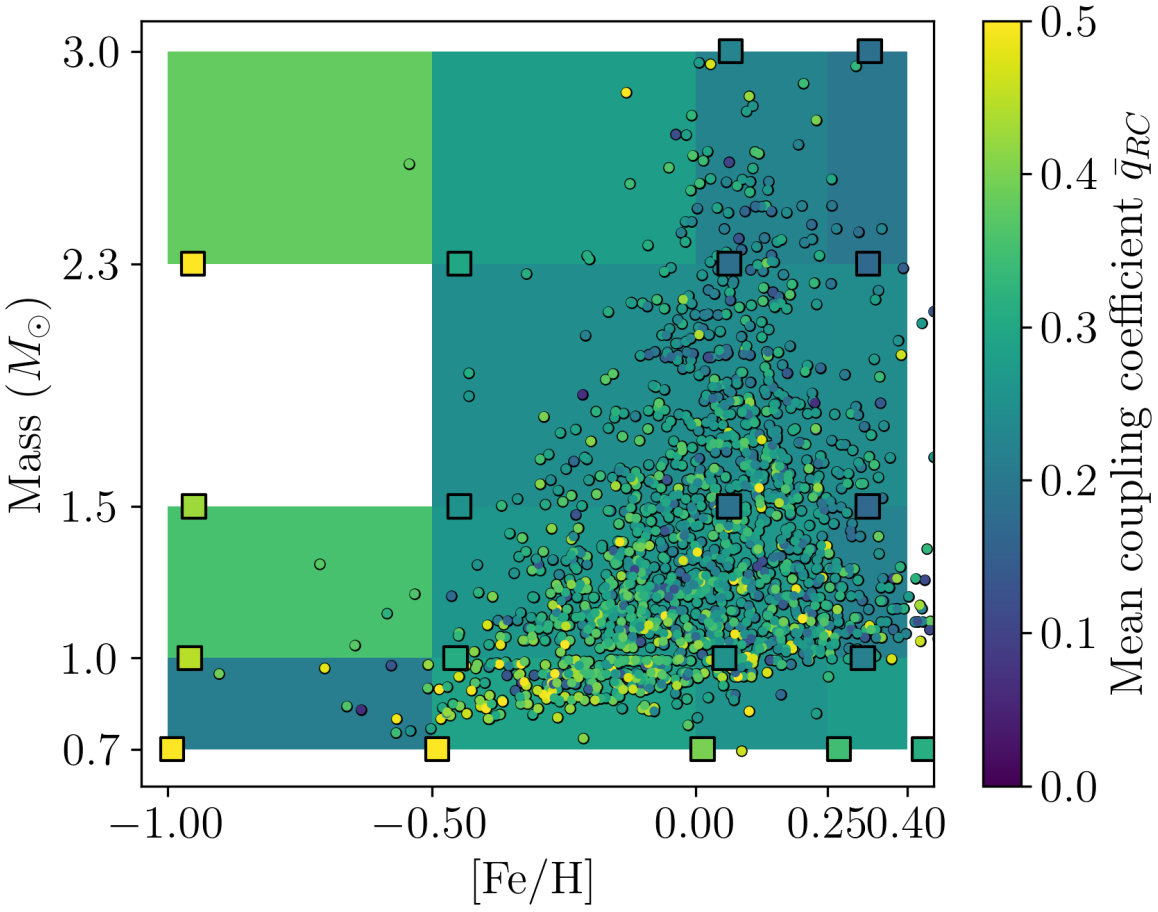

Figure 4.15: Modelled masses and [Fe/H] are shown as coloured squares with black outlines where the colour scale shows the mean coupling in the RC. Observed masses, [Fe/H], and q are shown as dots. The binned weighted mean coupling between models is shown as the shaded rectangles.

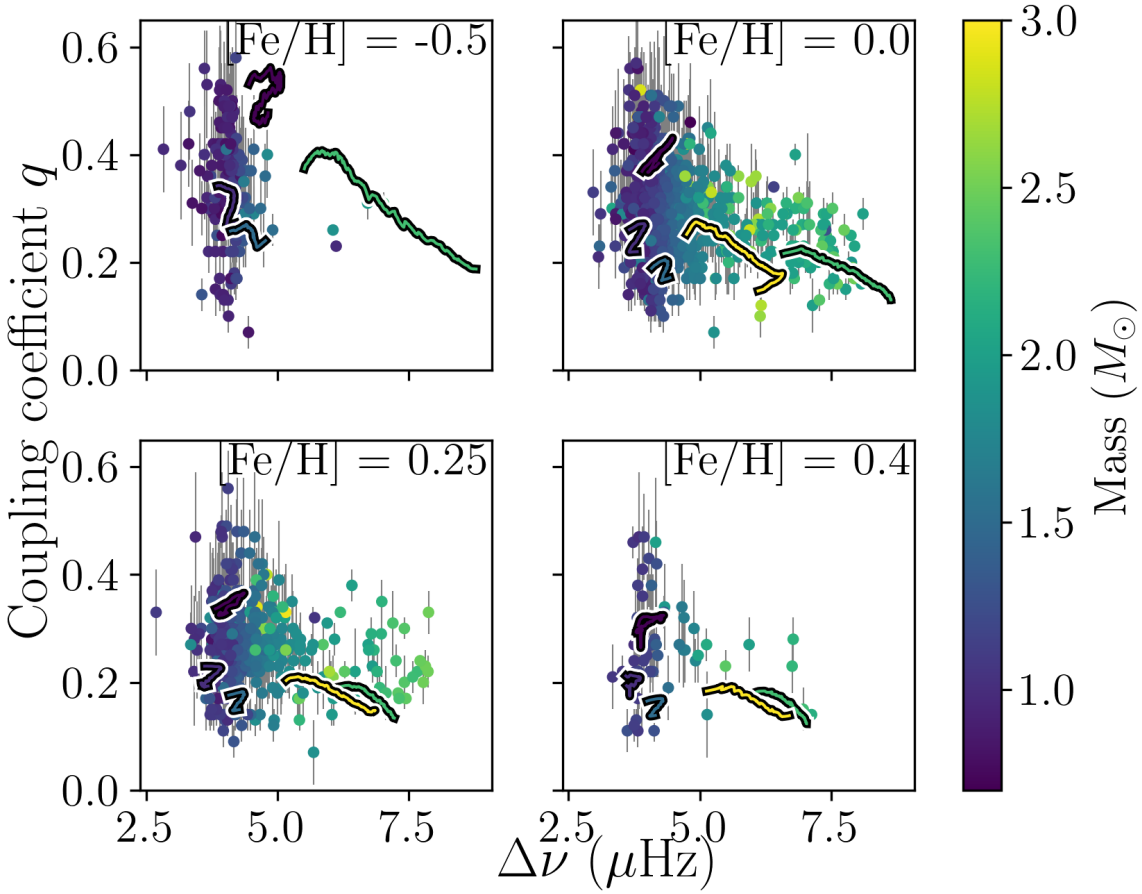

Figure 4.16: Coupling coefficient (q) versus large frequency separation ($\Delta\nu$) in the RC. The colour scale shows the stellar mass. The points are observed coupling and $\Delta\nu$ and the tracks are from modelled stars. From left to right, top to bottom, the model [Fe/H] are -0.5, 0.0, 0.25, and 0.4. Similarly, the ranges for the observed [Fe/H] are -0.75 ≤ [Fe/H] ≤ -0.25, -0.25 ≤ [Fe/H] ≤ 0.125, 0.125 ≤ [Fe/H] ≤ 0.325, 0.325 ≤ [Fe/H].

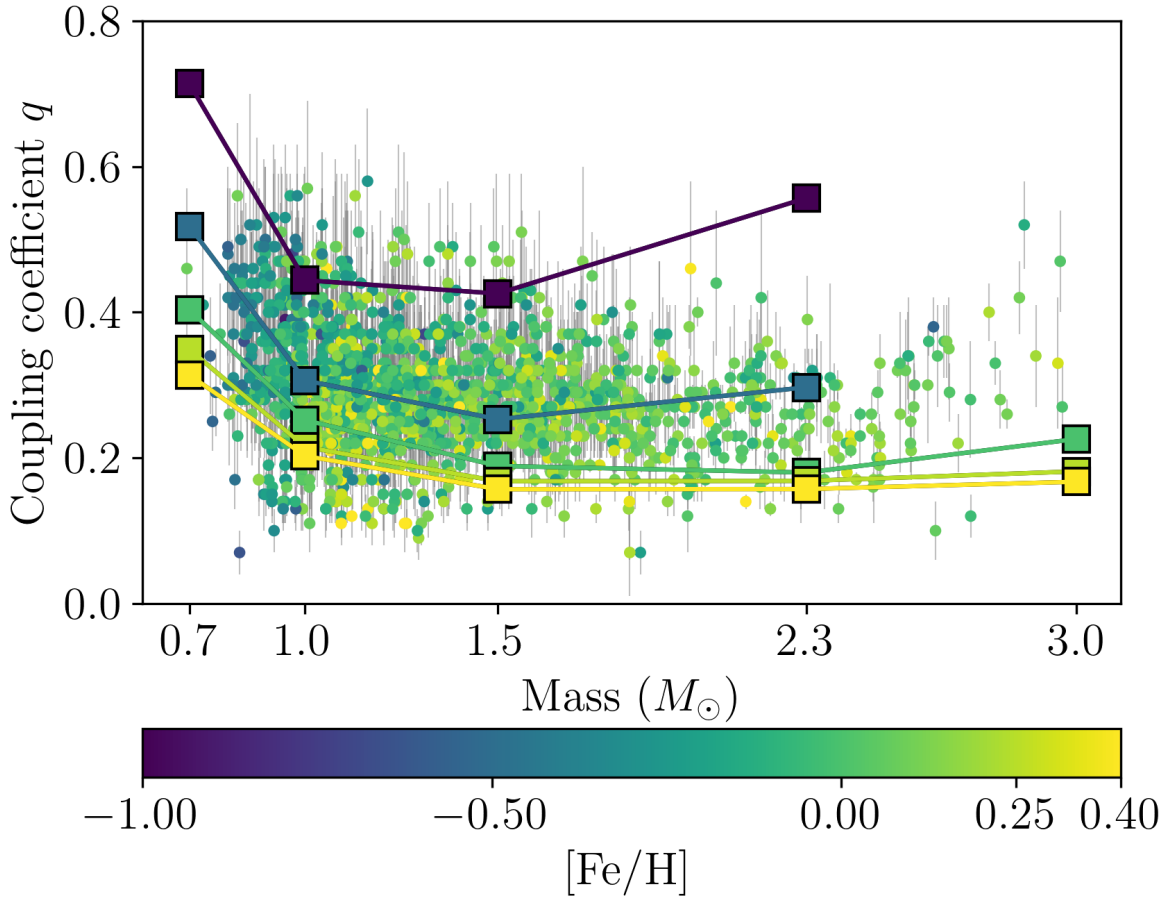

Figure 4.17: Modelled mean coupling in the RC as a function of initial mass at different initial metallicities are shown as squares. Each set of models with the same [Fe/H] is connected by a solid line. Observed masses and q are shown as dots.

Table 4.5: Parameters of the fits to observed [Fe/H] and q as well as the mean mass of stars in each group.

Phase		$\langle M \rangle$	m	b	$\ln \epsilon$
	($M_\odot$)	($M_\odot$)			
RC	< 1.8	1.09 ± 0.22	$-0.093^{+0.011}_{-0.011}$	$0.281^{+0.002}_{-0.002}$	$-2.853^{+0.033}_{-0.033}$
	≥ 1.8	2.01 ± 0.26	$-0.083^{+0.030}_{-0.029}$	$0.257^{+0.005}_{-0.004}$	$-2.940^{+0.061}_{-0.061}$
RGB		1.14 ± 0.14	$-0.019^{+0.005}_{-0.005}$	$0.122^{+0.001}_{-0.001}$	$-3.867^{+0.046}_{-0.047}$

Table 4.6: Parameters of fits to [Fe/H] and q of our RC models.

Phase	Mass	m	b
	($M_\odot$)		
RC	0.7	-0.214 ± 0.009	0.404 ± 0.002
	1.0	-0.124 ± 0.008	0.258 ± 0.001
	1.5	-0.113 ± 0.014	0.197 ± 0.003
	2.3	-0.087 ± 0.050	0.190 ± 0.009
	3.0	-0.167 ± 0.006	0.237 ± 0.001

To determine the dependence of q on [Fe/H] we split the observations into three groups and fit a linear model with Gaussian intrinsic scatter with variance ϵ^2 given by

$$q = m[\text{Fe/H}] + b + \mathcal{N}(0, \epsilon^2). \tag{4.50}$$

This model is fit to each group using flat priors in $\arctan(m)$, b, and $\ln \epsilon$ with `emcee` (Foreman-Mackey et al. 2013), a Markov Chain Monte Carlo (MCMC) ensemble sampler. These groups are RGB stars ($\Delta P < 130$ s), RC stars with masses $M < 1.8$ $M_\odot$ and RC stars with masses $M \geq 1.8$ $M_\odot$. These groups contain 816, 1403, and 276 stars respectively. Figure 4.18 shows the stellar mass distributions of these groups. The mean masses of stars in each group are 1.14 ± 0.06 $M_\odot$, 1.09 ± 0.11 $M_\odot$, and 2.01 ± 0.13 $M_\odot$ respectively. Figures 4.19, 4.20, and 4.21 show corner plots (e.g. Foreman-Mackey 2016) with the posterior distributions of the fitted parameters in the lower triangle and their marginalized posterior distributions along the diagonal panels. The best fitting parameters for each group are given in Table 4.5.

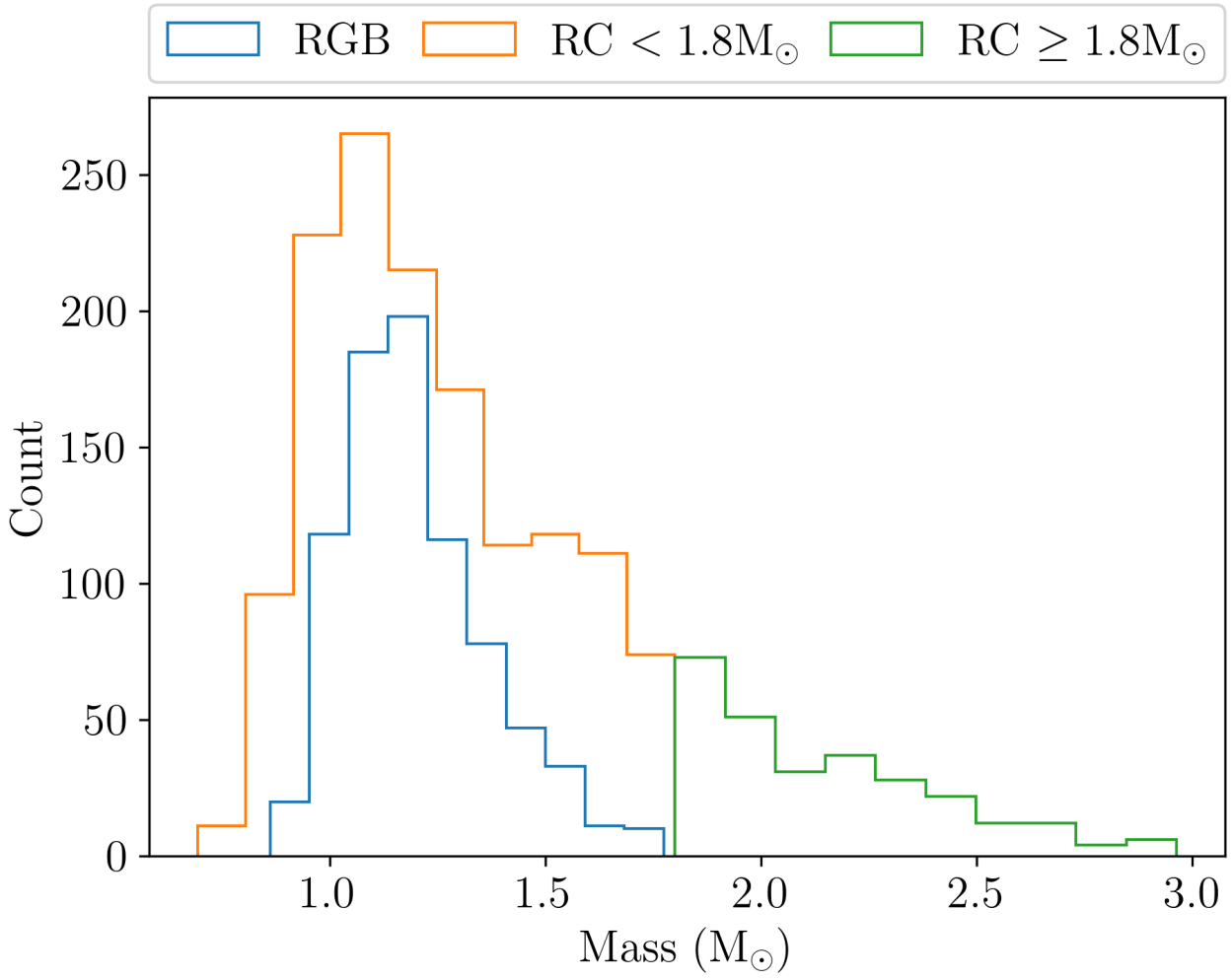

Figure 4.18: Stellar mass distribution of RGB stars (blue), RC stars with masses $M < 1.8\,\mathrm{M}_\odot$ (orange), and RC stars with masses $M \geq 1.8\,\mathrm{M}_\odot$ (green).

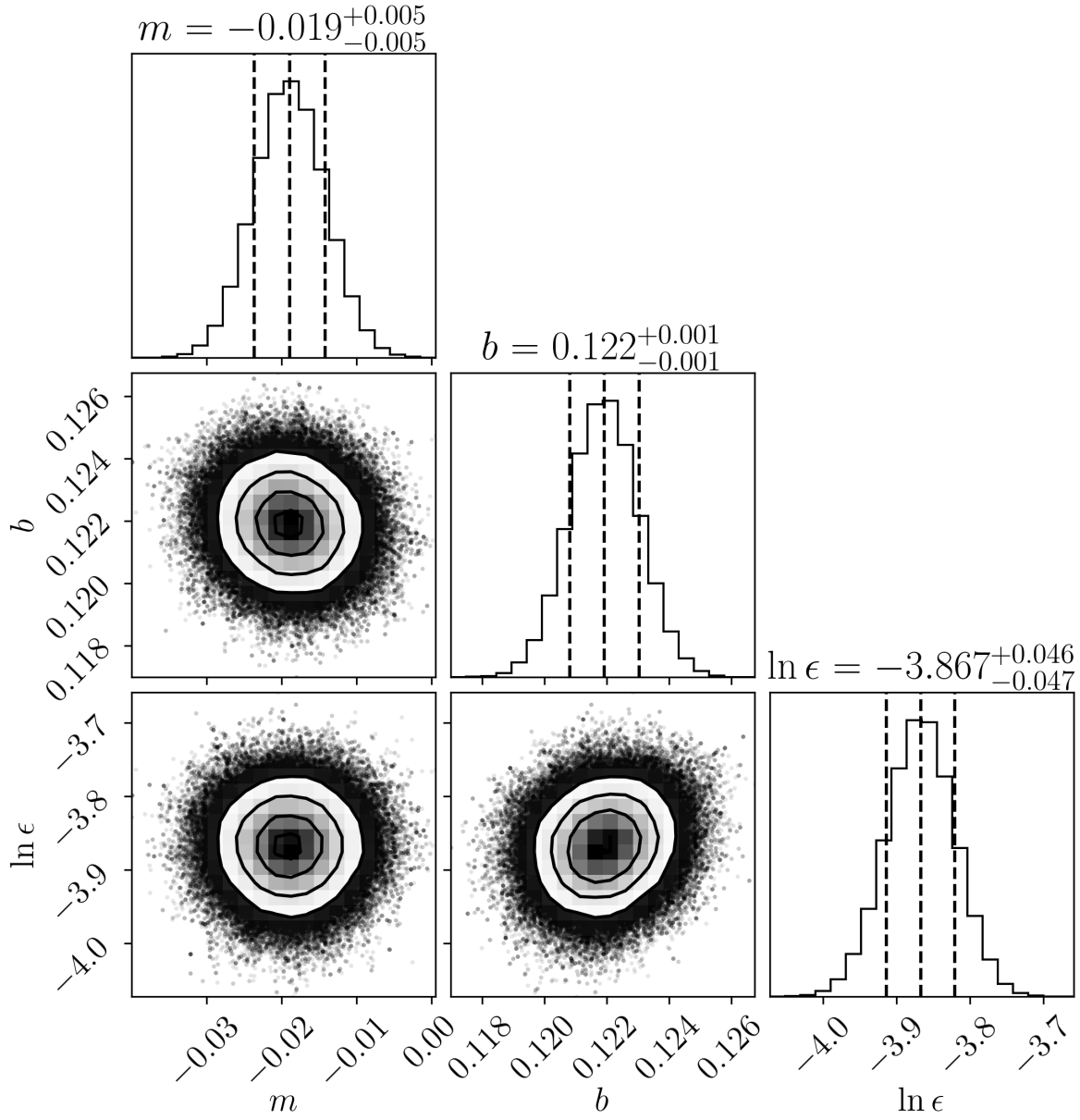

Figure 4.19: Corner plot of the slope m, y-intercept b, and intrinsic scatter ϵ posterior distributions from the RGB fit. The marginalized posterior distributions are shown in the panels in the diagonal with the 16th, 50th, and 84th percentiles shown as vertical dashed lines. The other panels show the 2-d histogram of the joint posterior distributions.

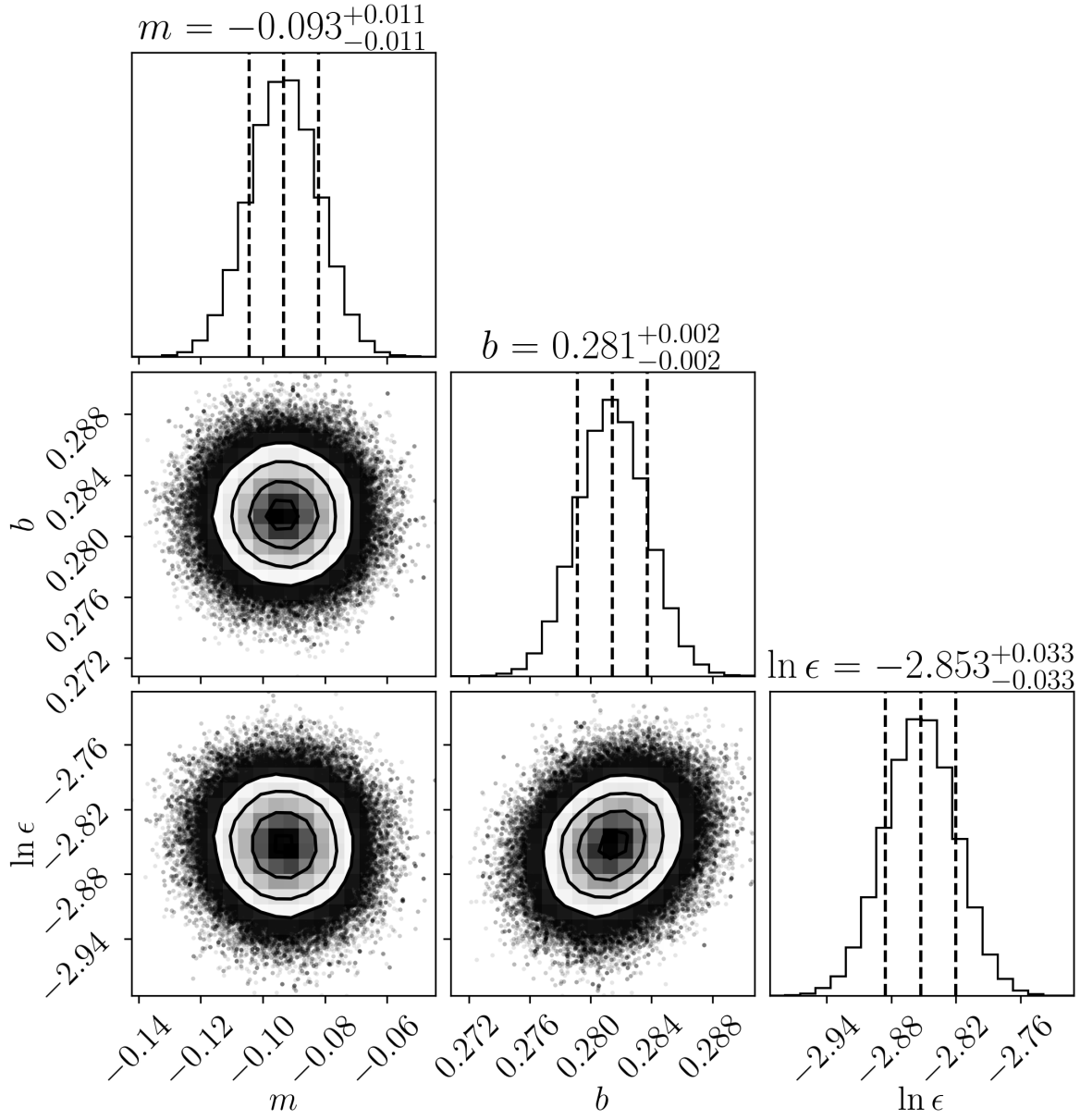

Figure 4.20: As Figure 4.19 but for RC with masses $M < 1.8$ $M_\odot$.

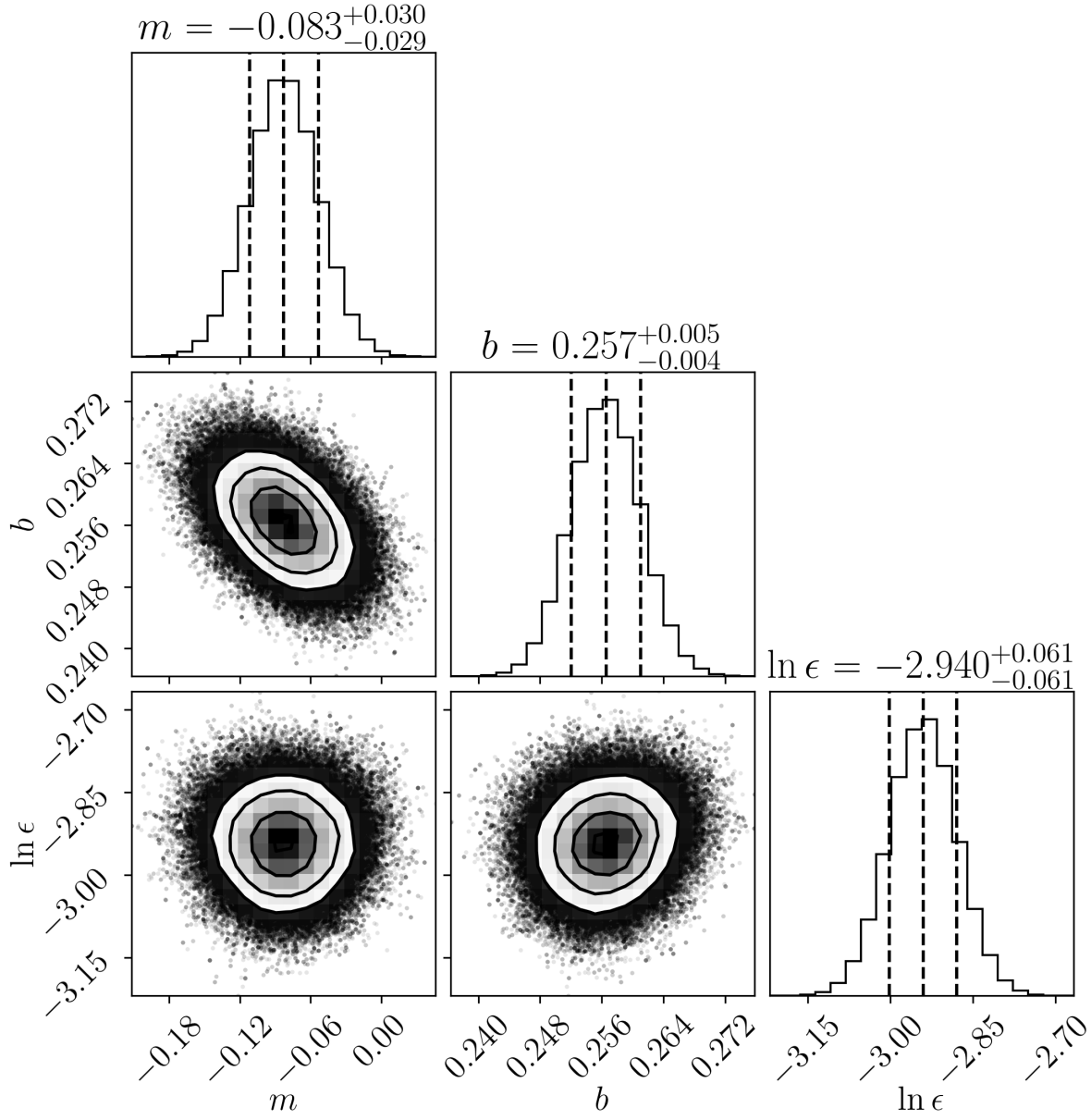

Figure 4.21: As Figure 4.19 but for RC with masses $M \geq 1.8$ $M_{\odot}$.

Figures 4.22, 4.23, and 4.24 show normalized 2-d Kernel Density Estimates (KDE) of observed [Fe/H] and q of RGB stars, RC stars with masses $M < 1.8$ $M_\odot$, and RC stars with masses $M \geq 1.8$ $M_\odot$ respectively. The kernel of each observation is a 2-d Gaussian with the observed uncertainties being the bandwidths in each direction. In Figures 4.23 and 4.24, modelled stars are overlaid as squares with different initial masses labelled by colour. A linear fit to these points is shown by the solid lines. The parameters of these fits are shown in Table 4.6. For RC stars the model slopes are consistent with each other, implying no dependence on mass of the slope. This is likely due to the lack of stars with masses around 3 $M_\odot$, as seen in Figure 4.18. In the lower mass RC case the modelled slope is steeper than the observed slopes, but is consistent to within 2.3-σ. The slope of the higher mass RC case is consistent with observations. For RGB stars the fits to modelled coupling are excluded as a large portion of the models would be in the transition regime between strong and weak coupling. However, qualitatively they still show a similar dependence on [Fe/H]. The y-intercepts are significantly different between the modelled and observed coupling when neglecting the intrinsic scatter. However, including the intrinsic scatter and treating it as an additional uncertainty on b resolves this difference. When comparing the observed and modelled q, modelled q tends to be underestimated (Ong & Gehan 2023; Kuszlewicz et al. 2023, and e.g. Figure 4.11). Additionally, there are systematics which are unaccounted for as the modelled coupling coefficient and the observed coupling coefficient are determined through different methods.

The main reason for the dependence of coupling on metallicity is that metallicity affects the density contrast between the helium core and the convective envelope. Figure 4.25 shows this strong relationship between the contrast and the coupling in these models. To first order, this relationship between density contrast and coupling is the main component driving the changes in the coupling. The mean helium-core density ($\bar{\rho}_{\rm He}$) remains approximately constant throughout the RC, which leaves the changes in the mean convective envelope density ($\bar{\rho}_{\rm CE}$) to drive the changes in density contrast. Changes in the convective envelope caused by different metallicities can be seen in Figure 4.26. It shows part of a propagation diagram of a 1 $M_\odot$ star, at various metallicities

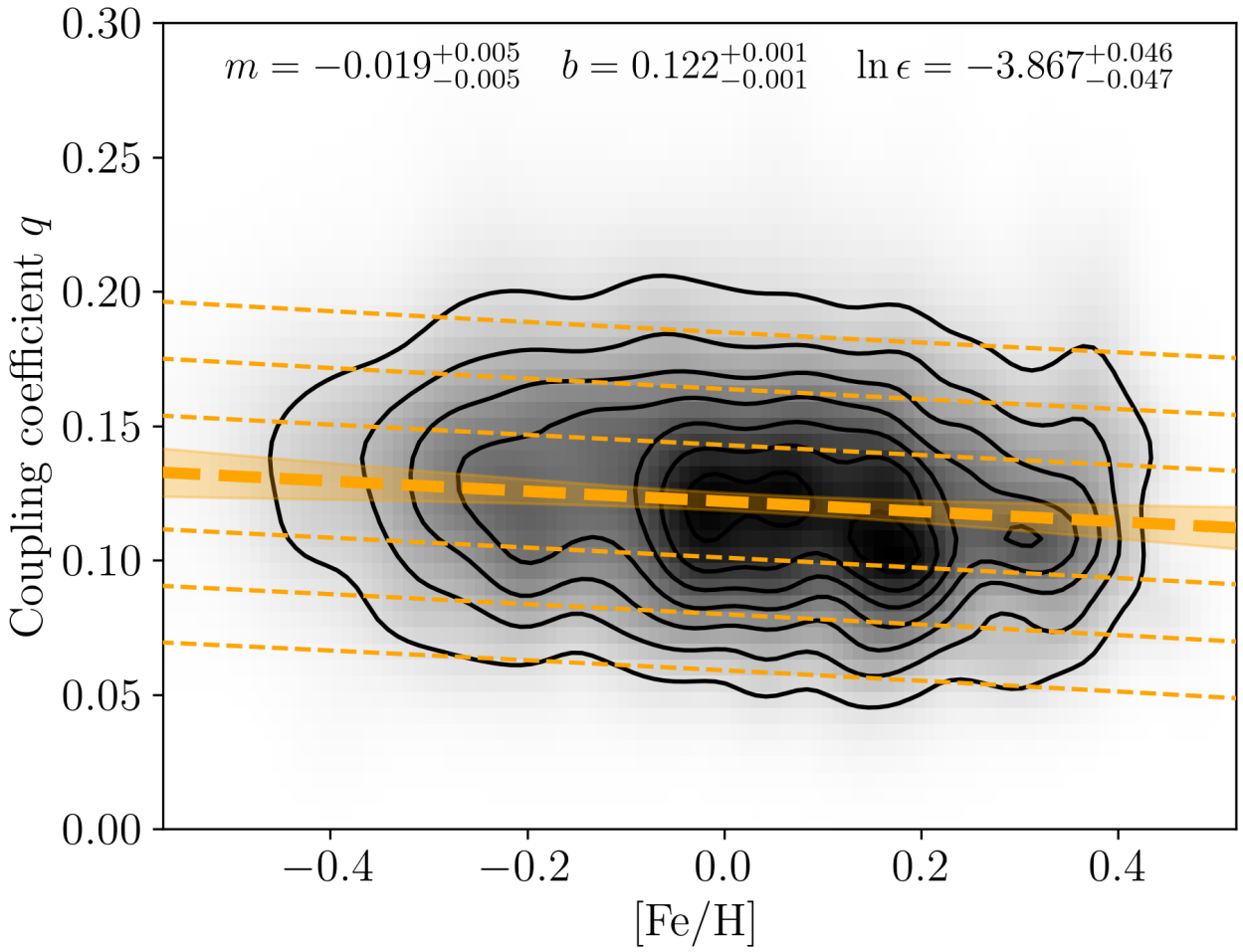

Figure 4.22: A Kernel Density Estimate (KDE) of observed [Fe/H] and q for RGB stars with $\Delta P < 130$ s. The thick orange dashed line shows the fit to the observed data, with the parameters of the fit shown at the top of the panel and Table 4.5. The orange shaded region shows the 3-σ confidence interval on m and b, whilst the thin orange dashed lines show the maximum-likelihood intrinsic relation in steps of 1-σ.

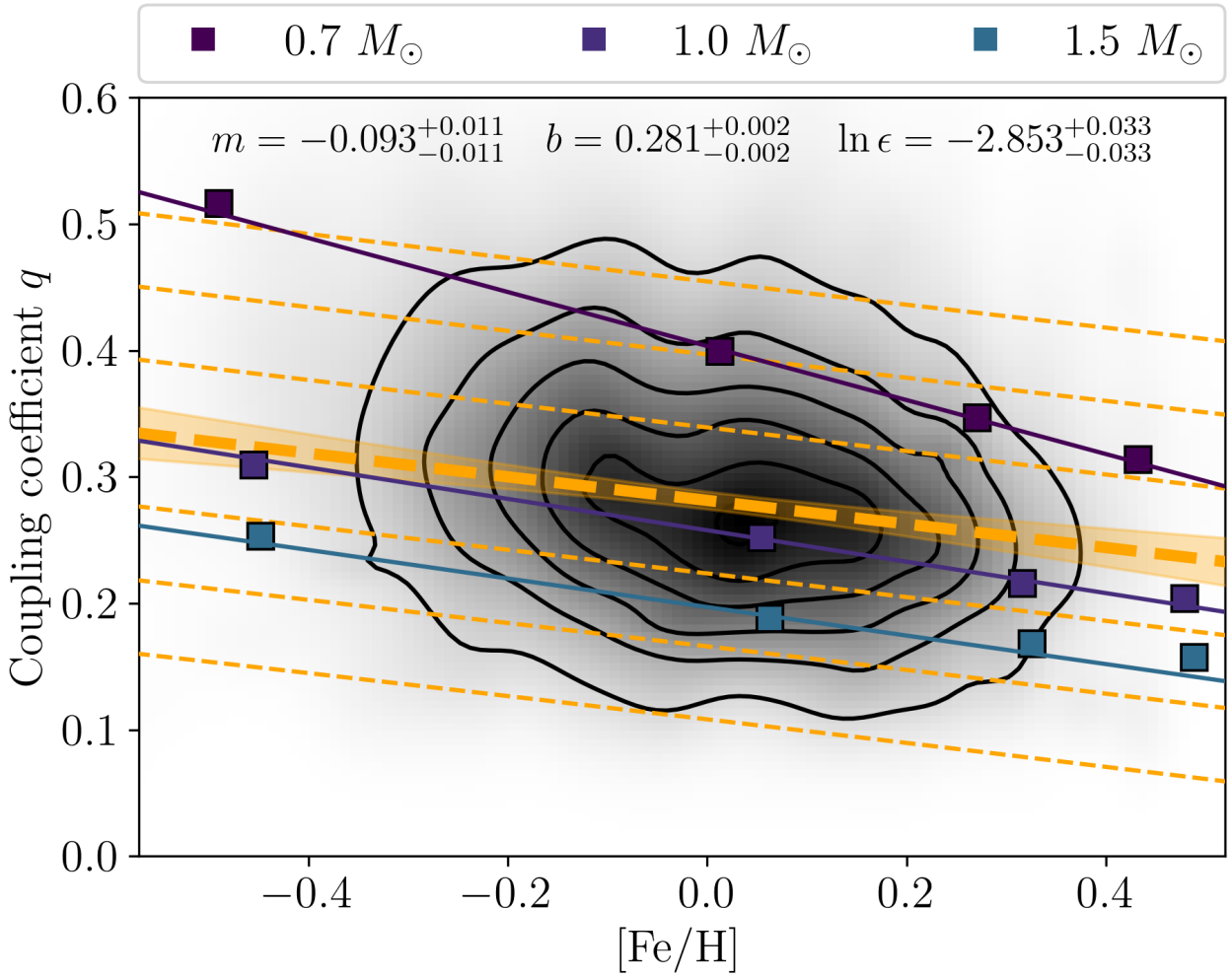

Figure 4.23: As Figure 4.22 but for RC stars with masses $M < 1.8$ $M_\odot$. Modelled [Fe/H] and q are shown for different masses as coloured squares. The solid coloured lines show the fits to our RGB models. The parameters of these fits are shown in Table 4.6.

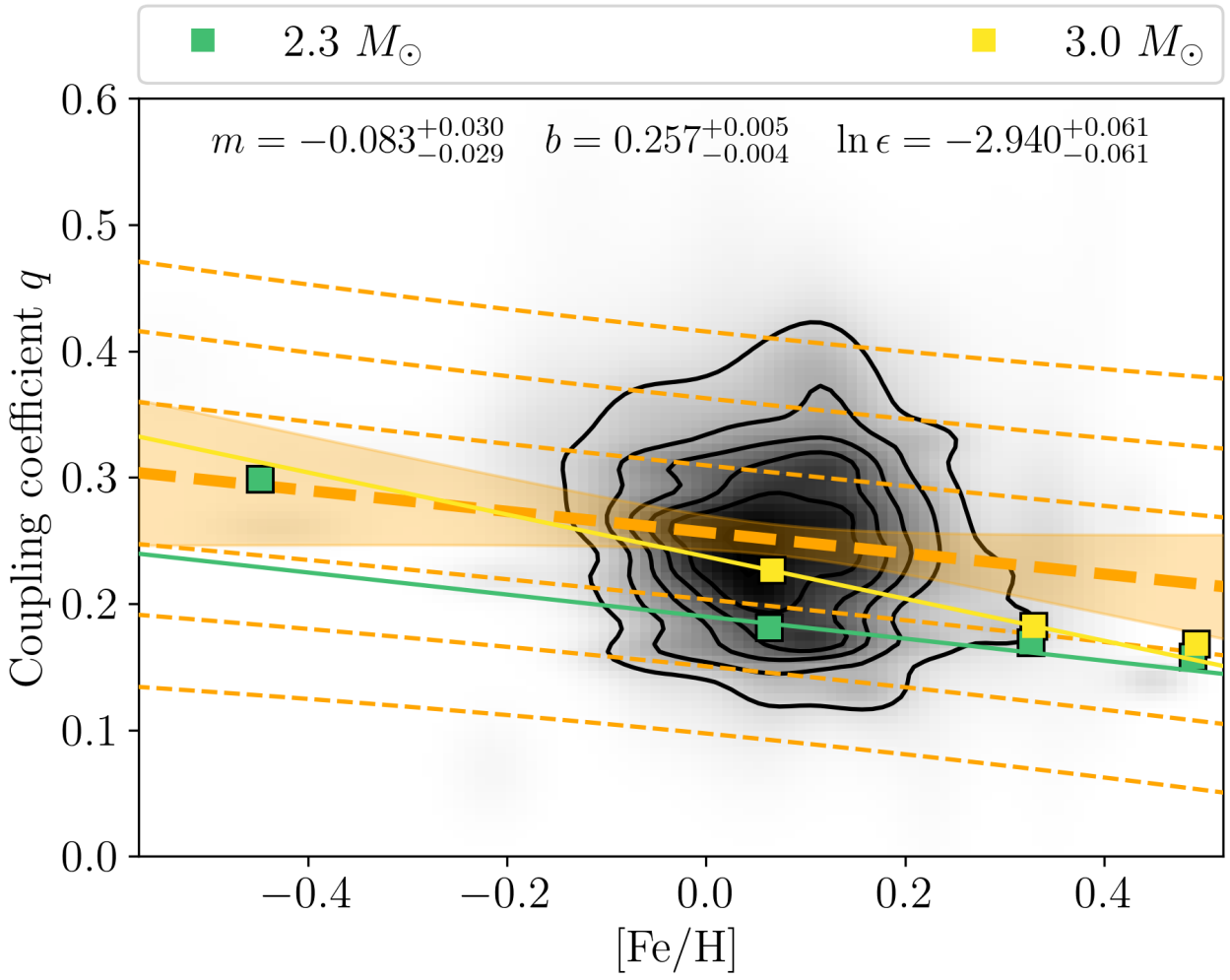

Figure 4.24: As Figure 4.23 but for RC stars with masses $M \geq 1.8$ $M_\odot$.

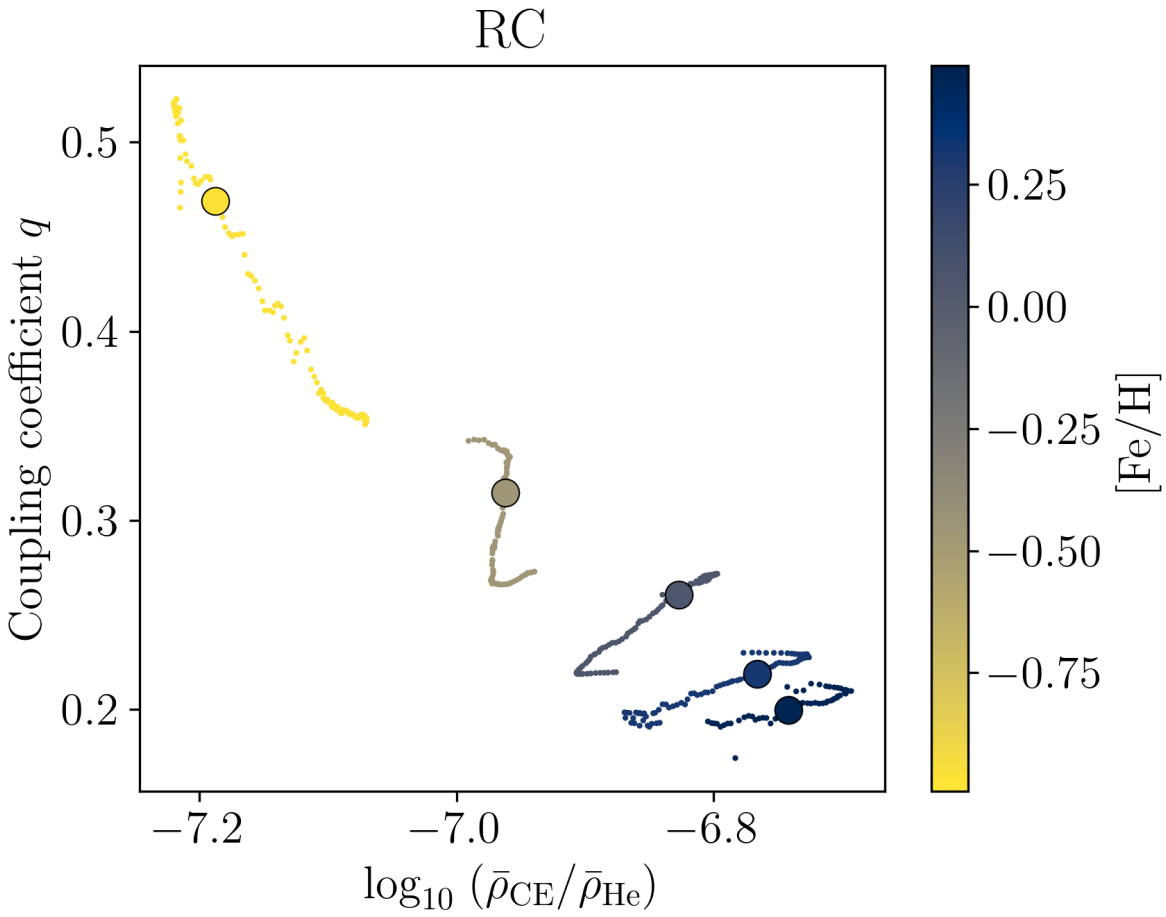

Figure 4.25: Coupling coefficient q versus the logarithm of the ratio of the mean convective envelope density ($\bar{\rho}_{\rm CE}$) to the mean helium core density ($\bar{\rho}_{\rm He}$) in $1 M_\odot$ stars. The large dots show the coupling and density contrast around $Y_{\rm c} = 0.5$. The colour scale shows the [Fe/H].

in the RC, when the central helium mass fraction is approximately 0.5. The size of the evanescent zone is smaller in low-metallicity stars and as metallicity increases, the upper boundary moves outwards, whilst the inner boundary moves toward the centre of the star but at a slower rate. As the metallicity increases, so does the opacity. This both inflates the star and gives it a deeper convective envelope.

Figure 4.27 is similar to Figure 4.26 but shows the propagation diagram as a function of mass coordinate instead of radius. The location of the evanescent zone moves deeper into the star as the metallicity increases and as the convective envelope becomes more massive, going from a mass coordinate of 0.8 $M_\odot$ to around 0.6 $M_\odot$ at the highest metallicity. These two effects, shown in Figures 4.26 and 4.27, account for the relationship between density contrast and coupling seen in Figure 4.25.

The combination of the relationships in Figures 4.15, 4.17, 4.22, 4.23, 4.24, and 4.25 shows that the coupling coefficient is an indirect probe to the depth of the convective envelope. A shallower convective envelope leads to a stronger density contrast, hence to a larger coupling.

4.3.4 Effect of helium abundance on coupling

An additional test was performed to determine how helium abundance affects q. We do this by varying the initial helium abundance of the Solar analogue model by ±0.02. This results in $Y_{\rm init}$ of 0.243, 0.263, and 0.283, and keeping $Z_{\rm init}$ constant at 0.01448, for a 1 $M_\odot$ mass with [Fe/H] = 0. Figure 4.28 shows the HRDs of these three tracks where the helium flashes are removed for clarity. During the MS, SGB, and RGB the helium-rich model (red) is the hottest and the helium-poor (blue) the coolest. This is due to helium-rich mixtures having lower opacities compared to helium-poor mixtures, which increases the efficiency of radiative energy transport. The helium-rich RGBb is slightly hotter by just 0.0006 dex and more luminous by 0.06 dex compared to the default $Y_{\rm init}$,

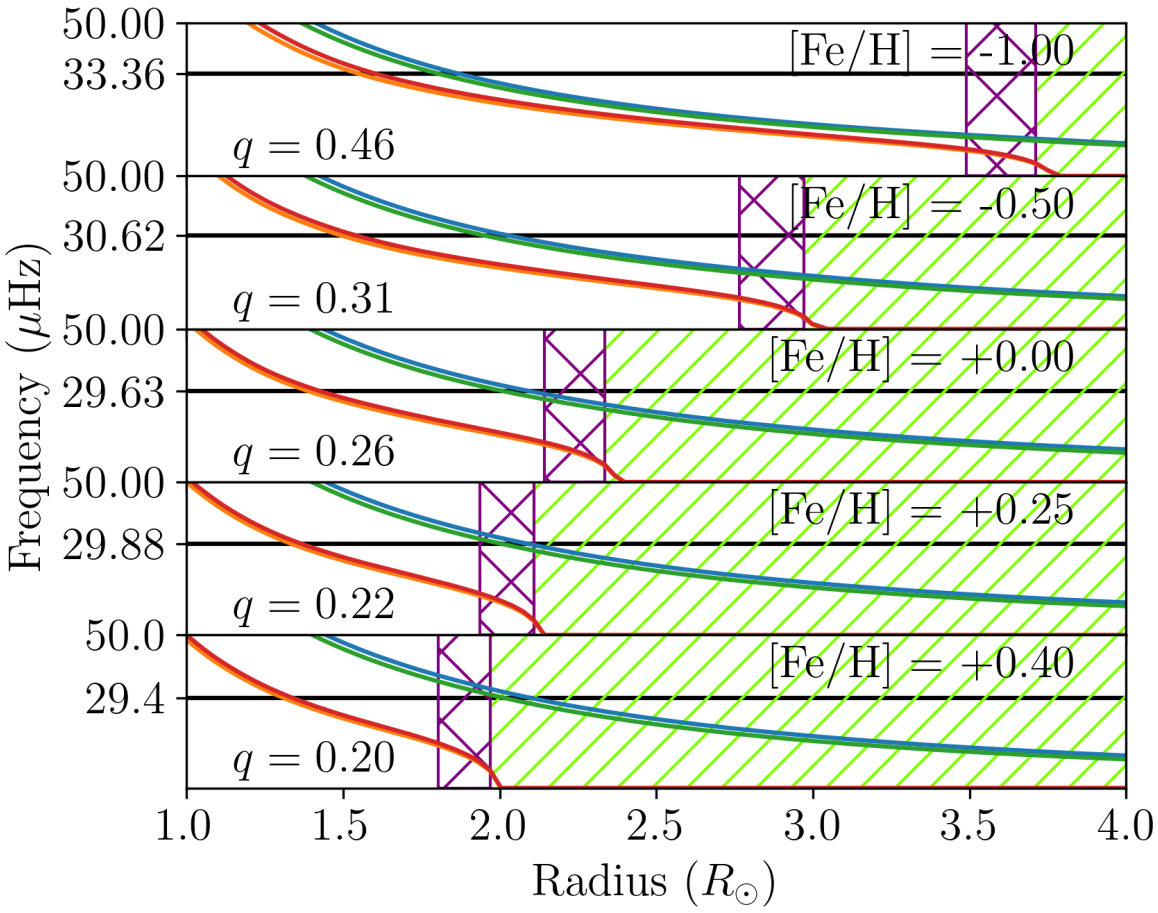

Figure 4.26: Propagation diagrams of 1 $M_\odot$ RC models with $Y_C \simeq 0.5$ showing the Lamb (S) and reduced Lamb ($\tilde{S}$) frequencies as blue and green lines respectively. The Brunt-Väisälä (N) and reduced Brunt-Väisälä ($\tilde{N}$) frequencies are shown as orange and red lines respectively. $\nu_{\max}$ is shown as a horizontal black line. The green hashed regions show where the star is undergoing convection, and the purple cross-hashed region shows where convective overshoot is occurring.

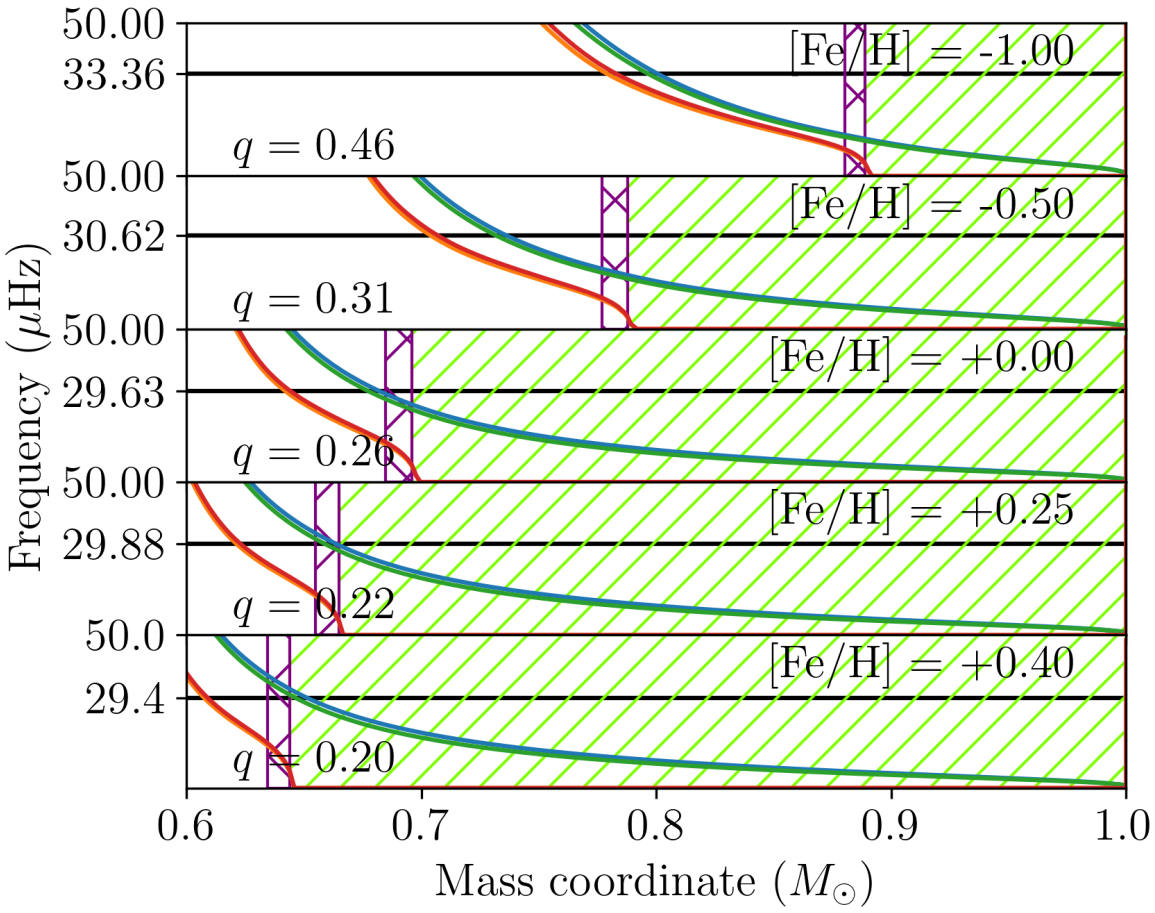

Figure 4.27: Same as Figure 4.26 but as a function of mass.

Table 4.7: Summary of the changes in q due to varying the initial helium abundance. The values of the SGB and RGBb are the maximum q reached during that phase, and for the RC it is the mean.

	Coupling q		
Evolutionary Phase	low $Y_{\rm init}$	default $Y_{\rm init}$	high $Y_{\rm init}$
SGB	0.385	0.399	0.459
RGBb	0.060	0.055	0.050
RC	0.238	0.252	0.258

whilst the helium-poor RGBb is 0.0007 dex cooler and 0.05 dex less luminous. Finally, the RC is at approximately the same effective temperature (differing by 0.0007 dex), whilst the helium-rich RC is 0.04 dex more luminous and the helium-poor RC is 0.04 dex less luminous.

Figure 4.29 shows three Kippenhahn diagrams with $Y_{\rm init}$ increasing from top to bottom. Table 4.7 shows the observed general effects on the coupling caused by the changes in initial helium abundance. Figure 4.29 and Table 4.7 show that during the SGB q is correlated with the initial helium abundance, during the RGB it is anti-correlated, and during the RC it is correlated again with $Y_{\rm init}$. However, many of these changes are likely caused by the change in $\nu_{\rm max}$ due to the increased $T_{\rm eff}$ due to a higher helium abundance. For example, qualitatively, in the RC all three modelled stars have approximately the same q of 0.22 when $\nu_q \simeq 30\,\mu$Hz and a central helium mass fraction of around 0.5. However, the range q takes when comparing similar frequencies during the RC is larger for helium-rich models.

During the ascent up the RGB and RGBb, the helium-rich core mass is correlated with the helium abundance at a given effective temperature with $\Delta m_{\rm He} \simeq 0.1\Delta Y_{\rm init}$. The location of the RGBb in our models is separated mainly by luminosity, with the helium-poor model being the faintest at around 21 $L_\odot$, the default model at around 23 $L_\odot$, and the helium-rich model at around 27 $L_\odot$. These different luminosities in the RGBb are due to the hydrogen-burning shell reaching the chemical discontinuity left by the first dredge-up later in the helium-rich models than in the helium-poor models. This is due to the convective envelope not plunging as deep as in the helium-poor

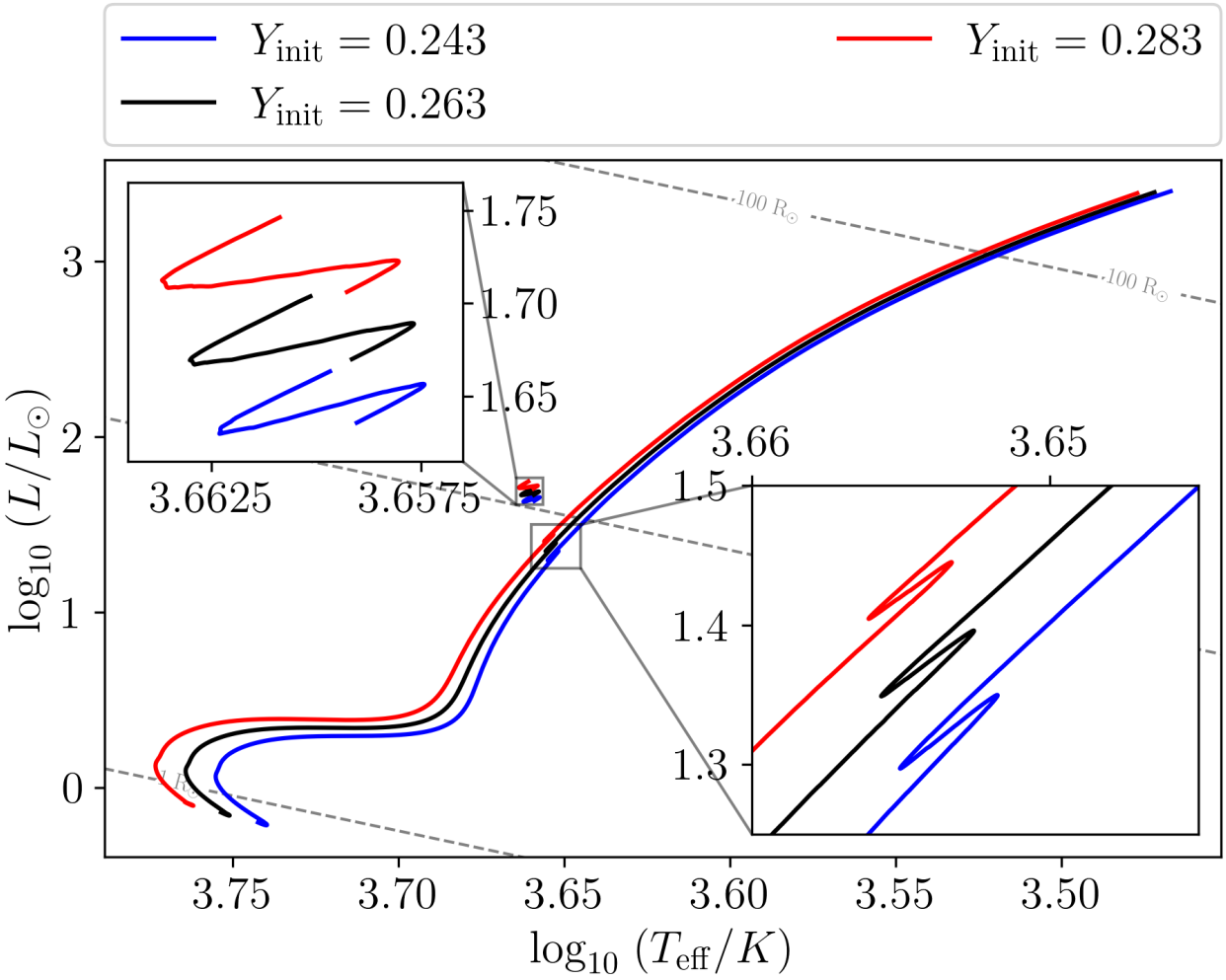

Figure 4.28: HRD tracks of modelled 1 $M_\odot$ stars with initial helium abundances $Y_{\rm init}$ of 0.243 (blue), 0.263 (black), and 0.283 (red) . The helium flashes are removed for clarity. The upper left inset zooms in on the RC, and the lower right inset zooms in on the RGBb.

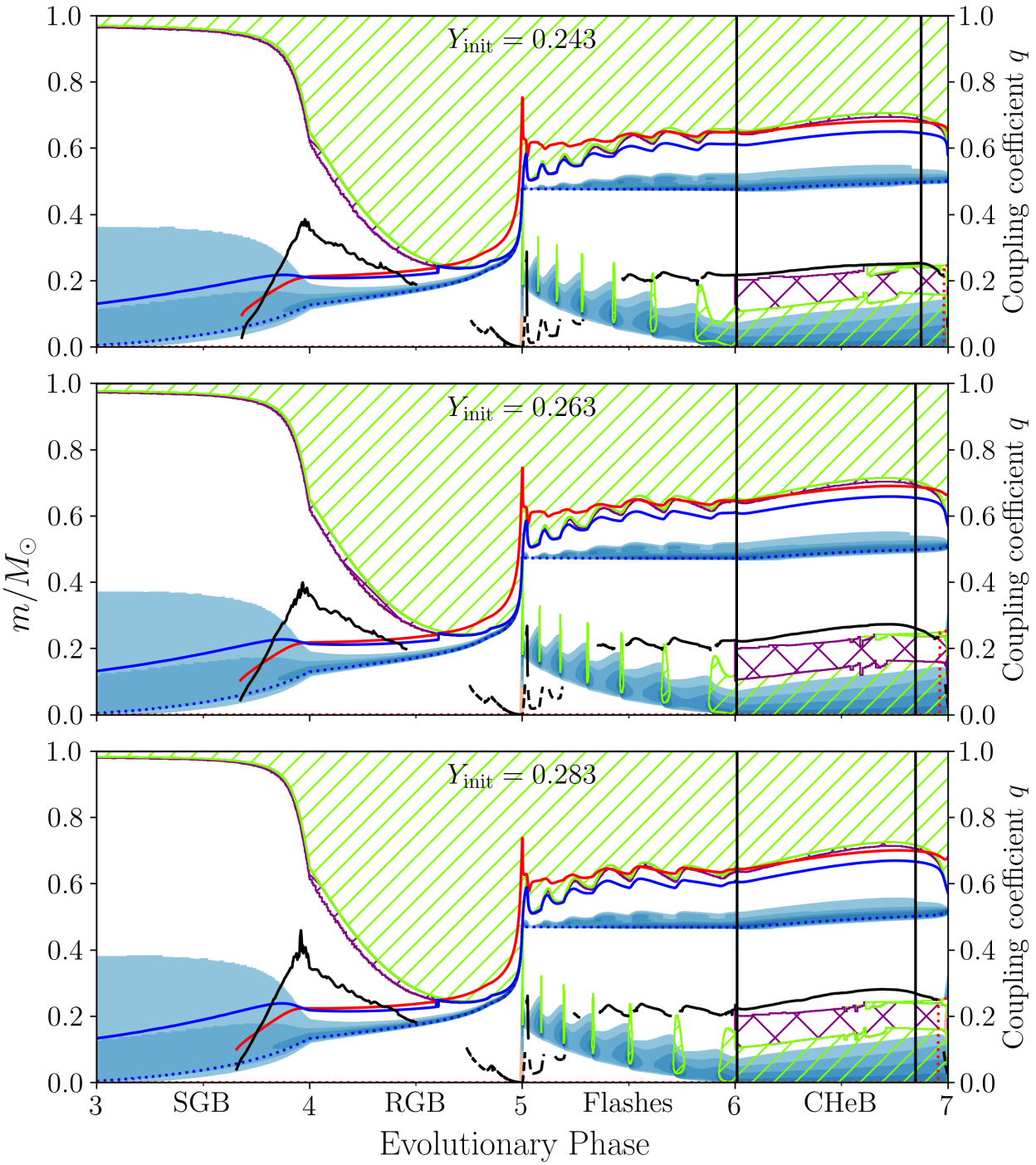

Figure 4.29: Kippenhahn diagrams of a 1 $M_\odot$ star with initial helium abundances of 0.243, 0.263, and 0.283 in the top, middle, and bottom panels respectively. The middle panel is the same as Figure 4.10.

cases as the opacity of the envelope decreases as the helium abundance increases. The luminosity at the tip of the RGB decreases only slightly with increasing $Y_{\rm init}$ (2510 $L_\odot$ vs. 2450 $L_\odot$), and the helium-core mass at the tip is largest in the helium-poor model at 0.476 $M_\odot$ and smallest in the helium-rich model at 0.469 $M_\odot$. During the RC, the helium-poor model has the lowest luminosity of around 44 $L_\odot$ whilst the helium-rich model has a luminosity of around 52 $L_\odot$ with the $T_{\rm eff}$ of the three cases differing by approximately 10 K during this phase.

4.3.5 Verification of the strong, parallel, and non-parallel coupling prescriptions

In this section we explore the effect of using different approximations when numerically calculating the coupling coefficient.

As illustrated in Pinçon et al. (2019) and described in Appendix 3 of Takata (2016a), the strong-coupling prescription can also be approximated by assuming $\tilde{S}$ and $\tilde{N}$ are parallel and follow a power-law. This simplifies the calculation of $\mathcal{G}$ somewhat. In this case Equation (4.17) can be replaced by the following equation:

$$\mathcal{G} = -\beta\left(\frac{\alpha}{1-\alpha} + \frac{1}{\ln\alpha}\right) - \frac{1}{2}\left(\mathcal{V} - \mathcal{A} - J\right), \tag{4.51}$$

where

$$\beta \equiv -\left(\frac{\mathrm{d}\ln\tilde{S}}{\mathrm{d}\ln r}\right)_{r_0}, \tag{4.52}$$

and

$$\alpha = \left(\frac{r_2}{r_1}\right)^{\beta}. \tag{4.53}$$

This method of calculating the gradient term is referred to as the parallel approximation in this work.

As an additional test, we remove the assumption from the parallel approximation that $\tilde{N}$

and $\tilde{S}$ are parallel, but still follow power-laws, which results in the following equation for $\mathcal{G}$.

$$\mathcal{G} = -\beta_S \left(\frac{\alpha_P^\gamma \gamma - \alpha_P \left(\alpha_P^\gamma \gamma + \alpha_P^\gamma - 1 \right)}{2 \left(\alpha_P - 1 \right) \left(\alpha_P^\gamma - 1 \right)} + \frac{1}{\ln \alpha_P} \right) - \frac{1}{2} \left(\mathcal{V} - \mathcal{A} - J \right), \tag{4.54}$$

where

$$\gamma = \frac{\beta_{\tilde{N}}}{\beta_{\tilde{S}}} \tag{4.55}$$

and

$$\alpha_P = \left(\frac{r_2}{r_1} \right)^{\beta_{\tilde{S}}}. \tag{4.56}$$

Equation (4.54) reduces to Equation (4.51) when $\tilde{N}$ and $\tilde{S}$ are parallel, i.e. when $\gamma = 1$. We refer to this as the non-parallel approximation.

We quantitatively compare the coupling computed following these different assumptions early on in the RGB and SGB, as well as during the RC. Figure 4.30 shows the modelled coupling coefficient computed using the Takata prescription, parallel approximation, and non-parallel approximation as a function of $\nu_{\max}$ during the SGB and early RGB of a 1 $M_\odot$ Solar metallicity star in the top panel, and the fractional error in the bottom panel. We stop at $\nu_{\max} = 300$ μHz as below this frequency the Takata prescription encounters the limitations described in Section 4.2.2 and is therefore not valid. During the SGB ($\nu_{\max} \gtrsim 1000$ μHz) both the parallel and non-parallel approximations overestimate q, with the parallel approximation overestimating by 10–200% and the non-parallel approximation overestimating by 20–50%, as seen in the bottom panel of Figure 4.30. On the RGB below $\nu_{\max}$ of 800 μHz the non-parallel approximation outperforms the parallel approximation with a typical error of approximately 5%, whereas the parallel approximation has typical errors of 5–15%. However, the Takata prescription is more sensitive to numerical noise in $\mathcal{G}$ when the evanescent zone is very thin and its boundaries cross (i.e. $r_1 \approx r_2$), resulting in a typical uncertainty of around 3% during the SGB and early RGB.

Similar to Figure 4.30, the top panel in Figure 4.31 shows the modelled coupling coefficient computed using the Takata prescription, parallel approximation, and non-parallel approximation

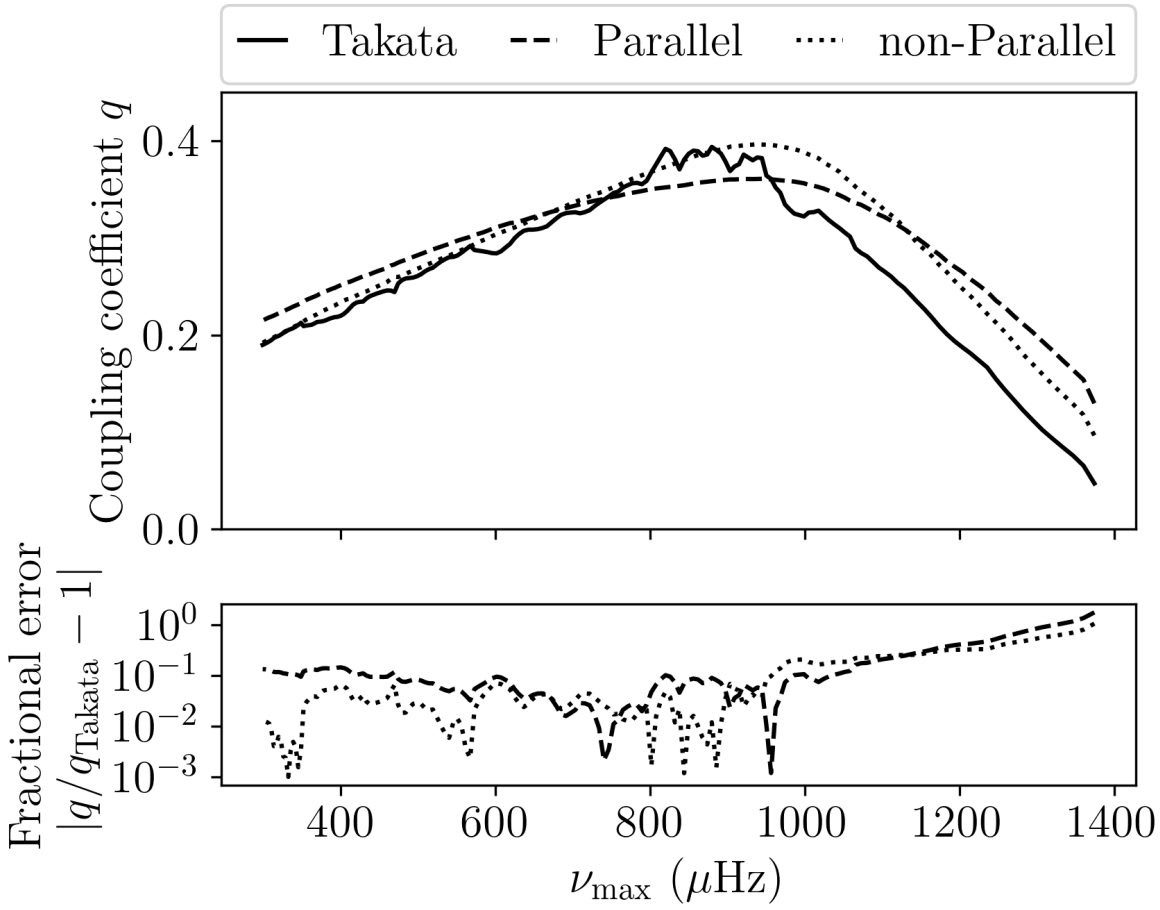

Figure 4.30: The top panel shows the modelled coupling coefficient q during the SGB and early RGB of a 1 $M_\odot$ Solar metallicity star as a function of $\nu_{\rm max}$ computed using using the Takata prescription as a solid black line, the parallel approximation as a dashed black line, and the non-parallel approximation as a dotted black line. The bottom panel shows the fractional error between the Takata prescription and the parallel or non-parallel as the dashed and dotted black lines respectively.

of a 1 $M_\odot$ Solar metallicity star in the RC. The bottom panel shows the fractional error compared to the Takata prescription. Both the parallel and non-parallel approximations underestimate the coupling coefficient in the RC. However, the parallel approximation performs better as its error is typically around 5%, whereas the non-parallel approximation underestimates q by 8–14%. In this case, the non-parallel approximation performs worse than the parallel approximation as the evanescent zone is near the bottom of the convective envelope. In this region $\tilde{N}$ steepens and it is not well described by a single power-law as $\beta_{\tilde{N}}$ increases, as seen in Figure 4.32. This increasing $\beta_{\tilde{N}}$ causes $Q(s = 0)$ to be overestimated, which makes the $\mathrm{d}\ln Q/\mathrm{d}s$ part of $\mathcal{G}$ to be too small (Equation 4.23), increasing $\mathcal{G}$ and therefore decreasing q. During the SGB and early-RGB the evanescent zone is far from the bottom of the convective envelope (e.g. Figure 4.10). This means that $\tilde{N}$ is well approximated by a power-law with a constant exponent and does not encounter this issue.

4.4 Summary and prospects

In this chapter we established through detailed stellar modelling that the coupling coefficient describing the interaction between p- and g-modes depends on stellar global parameters, evolutionary stage, and structural properties. Crucially, we have checked against observations the formulation by Takata (2016a) in RC stars. Our main conclusions are as follows:

- We have shown that both mass and metallicity play a significant role in mixed-mode coupling in the RC. They both affect the density contrast between the core and envelope, and thus affect the depth of the convective envelope, and therefore also determine the location and size of the evanescent zone. Additionally, as shown in Figures 4.22, 4.23, and 4.24, there is an anti-correlation between metallicity and coupling in both the RGB and in the RC. We also find that coupling decreases as a function of mass in low-mass models, and increases as

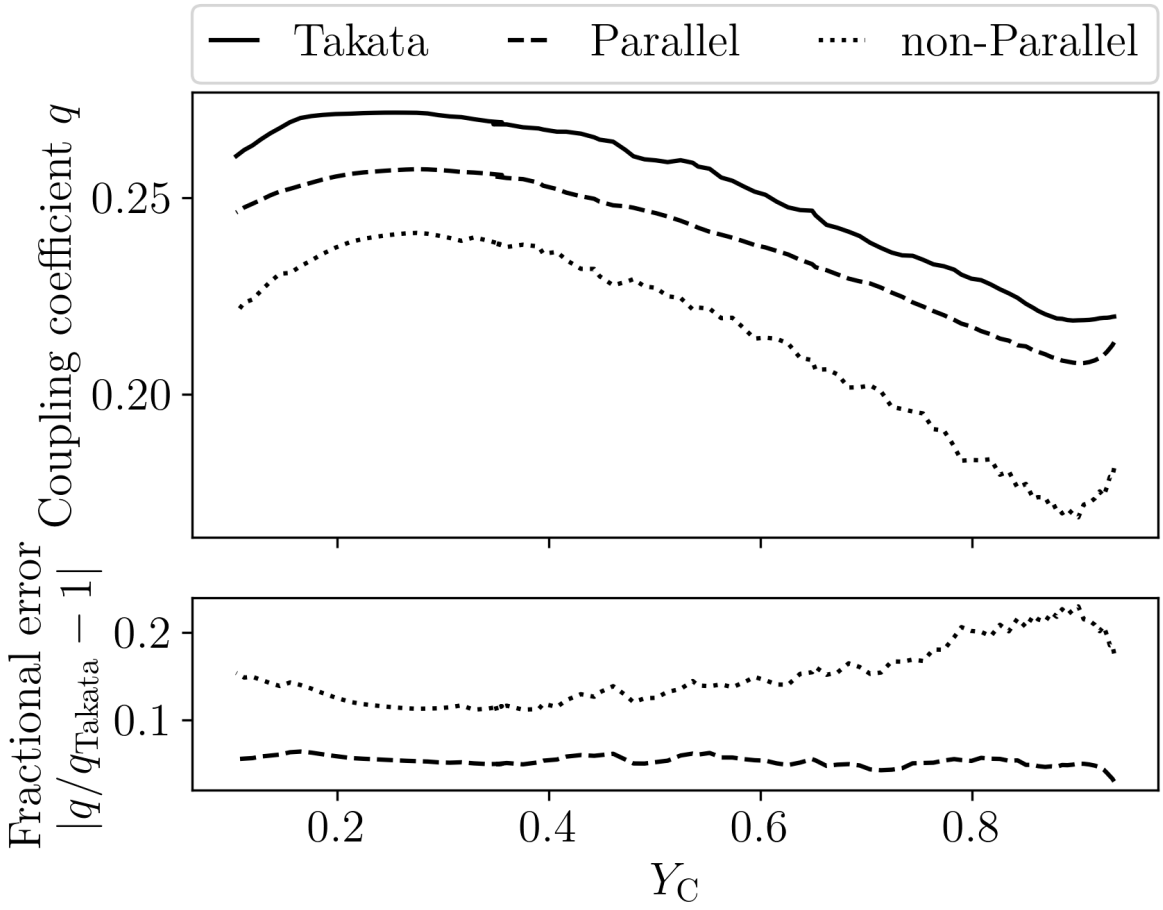

Figure 4.31: The top panel shows the modelled coupling coefficient q during the RC of a 1 $M_\odot$ Solar metallicity star as a function of the central helium mass fraction $Y_{\rm C}$ computed using using the Takata prescription as a solid black line, the parallel approximation as a dashed black line, and the non-parallel approximation as a dotted black line. The bottom panel shows the fractional difference between the Takata prescription and the parallel or non-parallel as the dashed and dotted black lines respectively.

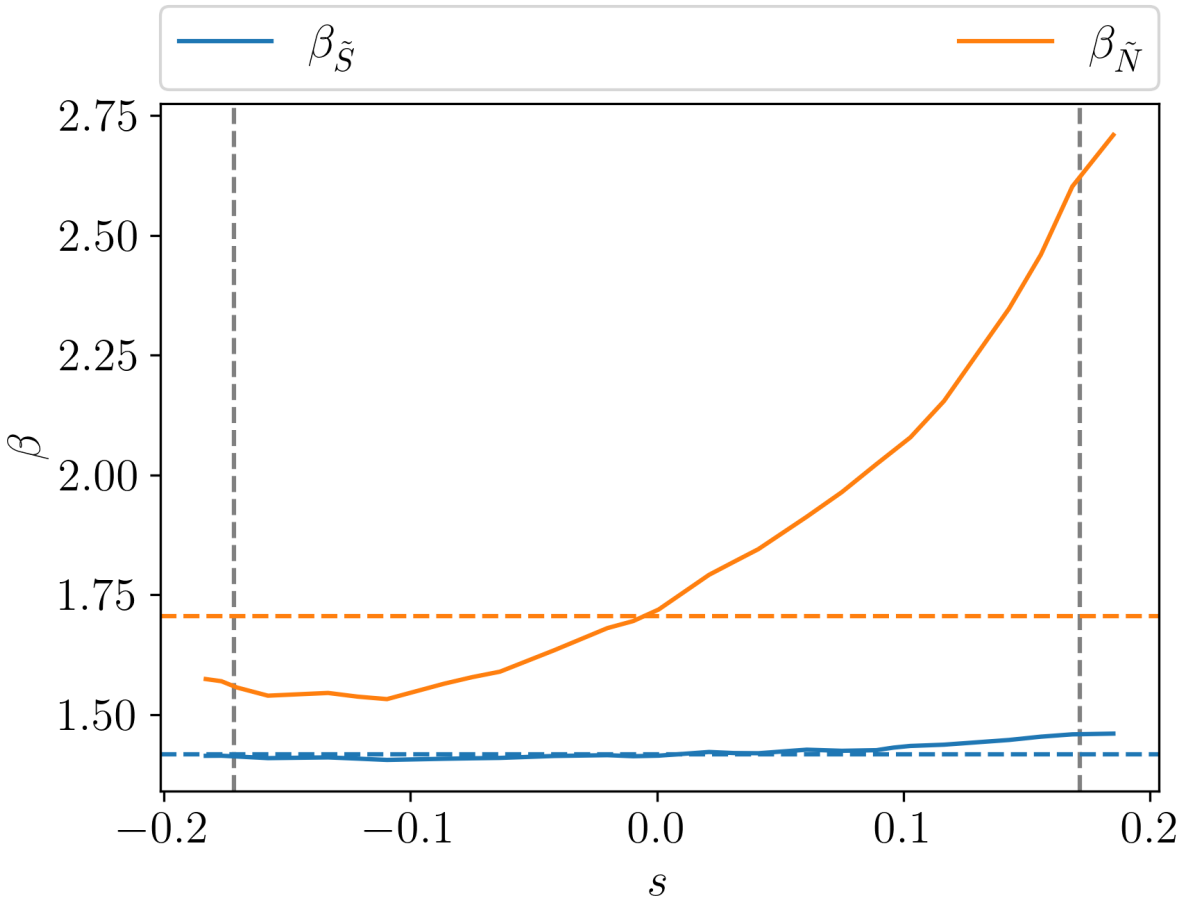

Figure 4.32: Power-law exponents $\beta_{\tilde{S}}$ and $\beta_{\tilde{N}}$ as a function of s in a 1 $M_\odot$ Solar metallicity RC star are shown as solid blue and orange lines respectively. The values of $\beta_{\tilde{S}}$ and $\beta_{\tilde{N}}$ used in the power-laws are shown as the horizontal dashed blue and orange lines respectively. The vertical grey dashed lines show the boundaries of the evanescent zone, $\pm s_0$.

a function of mass for high-mass models.

- These model-predicted trends in [Fe/H] and q (Figures 4.22, 4.23, and 4.24) agree with observations, with $q = -0.093^{+0.011}_{-0.011}$[Fe/H] + $0.281^{+0.002}_{-0.002}$ + $\mathcal{N}(0, 3.33^{+0.22}_{-0.22} \times 10^{-3})$ in RC stars with masses below 1.8 $M_\odot$, $q = -0.083^{+0.030}_{-0.029}$[Fe/H]+$0.257^{+0.005}_{-0.004}$+$\mathcal{N}(0, 2.80^{+0.34}_{-0.34}\times10^{-3})$ in RC stars with masses above 1.8 $M_\odot$, and $q = -0.019^{+0.005}_{-0.005}$[Fe/H] + $0.122^{+0.001}_{-0.001}$ + $\mathcal{N}(0, 4.38^{+0.40}_{-0.41} \times 10^{-4})$ in RGB stars. However, a note of caution should be given about the possible presence of glitches, which may affect the determination of the mean period spacings, which in turn may affect coupling coefficients (Vrard et al. 2016; Mosser et al. 2017). Additionally, for modelled stars, there is some ambiguity about what value q has in the transition regime between the strong and weak cases as there is no coupling prescription for the intermediate regime, e.g. during the RGB.

- We find the coupling coefficient to be frequency dependent (Jiang et al. 2020, in the RGB). When coupling is determined the frequency dependence is neglected (Mosser et al. 2017). The frequency dependence of q could be a source of error when determining the observed coupling. The frequency dependence is particularly strong in the RGB (panels A and B in Figure 4.9). Within one $\Delta\nu$ frequency interval, there can be a difference of between 10–20% in q. This variation in q due to different ν_q should be taken into account when determining q from observations, and when comparing to model predictions.

- The sensitivity of the coupling coefficient with frequency opens up the possibility for a detailed mapping of the evanescent zone. We have presented a possible method to measure undershooting through the spread in $\langle \mathrm{d}q/\mathrm{d}\nu_q \rangle$ in the RGB as larger undershooting would reduce the size of the $\tilde{N}$ spike causing it to widen and become lower in amplitude, reducing the spread in $\langle \mathrm{d}q/\mathrm{d}\nu_q \rangle$.

- We have also introduced an additional approximation to calculate the gradient term for the coupling based on the work done by Takata (2016a) and Pinçon et al. (2019) and the fact that

the Brunt-Väisälä and Lamb frequencies are not parallel. This works well in type-a evanescent zones on the early RGB with errors of around 5% using the non-parallel approximation compared to 10% when using the parallel approximation.

- The determined minimum coupling coefficients in the data set are around 0.05. It is not clear if this minimum is intrinsic to observed stars or whether this is an artefact caused by the limitations of the method to obtain coupling from observations. Our models show that coupling coefficients of less than 0.05 are possible, but that limitations in the method for determining q make it too difficult to determine such small coupling coefficients from observations.

The relationship between the coupling coefficient and the internal structure of stars highlighted in this work provides a foundation for further study in which one can also potentially identify structures with non-standard core-mass to envelope-mass ratios. This in turn is a way to identify a signature of the effect of mass transfer.

Chapter Five

Mixed-mode coupling in the red clump: II. Parametric mass transfer/merger models

This chapter is a reformatted version of van Rossem et al. (in prep.) of which I am to be first author and will be submitted to A&A. I completed all the work, with detailed discussions with Andrea Miglio and Josefina Montalbán.

This work explores whether we can discriminate between stars of similar mass but with different core-to-envelope ratios. We approximate stars which have undergone mass transfer or mergers and have non-standard helium-core masses in comparison to their total mass using parametric models with various helium core masses. We find that the inferred masses and radii using the seismic scaling relations are up to 15% and 10% smaller respectively in the lower-mass models ($\lesssim 2$ $M_\odot$). Including luminosity in the scaling relations and using reference frequencies derived from the model grid eliminates this deviation in all models of the grid. We investigate the potential seismic signatures of mass transfer or mergers by looking at the large frequency separation, frequency of maximum oscillation power, period spacing, and mixed mode coupling. We show that our single stellar evolution models can reproduce the vast majority of the data, and suggest a prescription of overshooting during the core-helium burning phase to fit the range of observed

period spacing. Finally, we search for stars which have atypical observables and investigate them in more detail.

5.1 Introduction

Research into mixed-mode coupling in the red clump is needed for robust inferences to be made about the deep interior of stars (Bedding et al. 2011; Bossini et al. 2017, Chapter 4). The rigorous application of realistic simulation models to understand the diagnostic potential of mixed-mode coupling is essential to advance the understanding of stellar interiors. This work follows up the groundwork done in Chapter 4, and focuses on stars in the red clump (RC). Chapter 4 studied the information provided by mixed modes in standard stellar structures. Here we investigate whether mixed modes can be used as signatures of non-standard structures, e.g. originating from binaries which have transferred mass or merged. We study the effect that parametrically varying the helium-core mass has on various stellar properties, setting aside whether the combination of helium-core mass and total mass are realistically achievable through binary interactions. We aim to understand how the helium-core mass of a star affects its evolution.

Stars below approximately 1.8 $M_\odot$ which have evolved as single stars have relatively narrow range of helium-core masses depending on their total mass (Girardi 2016, and references therein). They ignite helium in the core with helium-core masses of around 0.48 $M_\odot$ (more details in Section 2.1.1.7). Stars in the red clump with masses below around 1.8 $M_\odot$, depending on metallicity (Chiosi et al. 1992), all ignite helium under degenerate conditions in a shell in the helium core. As stars become more massive, the helium core masses at which the core ignites decreases to around 0.35 $M_\odot$ in a 2.2 $M_\odot$ star because the strength of the degeneracy in the core decreases. Above 2.2 $M_\odot$, the helium core mass is approximately 20% of the total mass (Chiosi et al. 1992; Girardi 2016, Section 2.1.1.7).

Stars which have undergone binary interactions may have had a significant change to their structure take place due to undergoing mass transfer or merging with their companion. This may cause the post-interaction remnant to have a helium-core mass fraction which deviates from the expected range for a given stellar mass. Being able to characterise stars such as these helps better understand the mass transfer and merger process. It also helps to identify such stars amongst field stars, which may pollute samples used in Galactic archaeology (e.g. Miglio et al. 2021).

This chapter is structured as follows. In Section 5.2 we describe the construction of parametric Mass Transfer/Merger (MT/MG) analogues. In Section 5.3 we describe the differences in the structure of parametric models, and crucially, in the seismic properties between Single Stellar Evolution (SSE) models and parametric models. We then compare these models to observations. Finally, in Section 5.4 we discuss the implications of this work and conclude.

5.2 Method

In this section we first describe the observational data, their sources, cuts we make when using them. We then describe how we compute our grid of SSE and parametric MT/MG analogue models.

5.2.1 Observational data

The observational data used to compare our stellar evolutionary models to, are based on the catalogues by Vrard et al. (2016) and Mosser et al. (2017), providing the period spacing and coupling. We select only the stars with `alias` = 0, and `method` = 2 in Table 2 of Vrard et al. (2016) when the values between the two catalogues differ by less than 5%. We do this because it eliminates stars that have different solutions for the period spacing in these two catalogues. In Vrard et al.

Table 5.1: Median fractional uncertainties of observations. [a] The median uncertainty for [Fe/H] is shown in dex.

Observable	Median fractional uncertainty
$T_{\rm eff}$	1.05×10^{-2}
L	4.03×10^{-2}
$\nu_{\rm max}$	1.81×10^{-2}
$\langle \Delta\nu \rangle$	7.28×10^{-3}
ΔP	1.13×10^{-2}
q	2.16×10^{-1}
[Fe/H]	7.09×10^{-3} [a]

(2016), the `alias` flag is 1 if ΔP likely is an alias, otherwise it is 0. The `method` flag is 2 if the two implementations used to determine ΔP in Vrard et al. (2016) agree. This is separate from the additional constraint we impose where both the Vrard et al. (2016) and the Mosser et al. (2017) period spacings differ by less than 5%. To select only RC stars we limit our selection to stars with $\Delta P > 120$ s (Bedding et al. 2011). For the coupling we use data from Mosser et al. (2017) as there are no uncertainties available for the coupling in the Vrard et al. (2016) catalogue. Abdurro'uf et al. (2022) provides spectroscopic data, and we use stars with $-0.09 \leq$ [Fe/H] ≤ 0.21. We take this cut in [Fe/H] so that the observed [Fe/H] are close to our model [Fe/H] of approximately 0.06, reducing the spread in our observables, leaving 1029 in our sample. Yu et al. (2018) provides $\langle \Delta\nu \rangle$ and $\nu_{\rm max}$. Finally, Willett et al. (2023) provide luminosities based on *Gaia* (Gaia Collaboration et al. 2016) parallaxes using the Lindegren et al. (2021) zero-point correction and the crossmatching between Abdurro'uf et al. (2022), Yu et al. (2018), and Lindegren et al. (2021). Table 5.1 shows the median fractional uncertainties of these quantities for reference.

Table 5.2: Summary of the parameters varied for the SSE grid.

Parameter	Symbol	Unit	Values
Initial mass	m_i	$M_\odot$	1.0, 1.2, 1.4, 1.6, 1.8, 1.9, 2.0, 2.1, 2.2, 2.3, 2.5, 2.7, 3.0
Mixing-length parameter	$\alpha_{\rm mlt}$		1.8, 1.9
Main sequence exponential overshooting	$f_{\rm OV,H}$		0.000, 0.005, 0.010, 0.015
Initial Z	$Z_{\rm init}$		0.01448
Initial Y	$Y_{\rm init}$		0.26317

5.2.2 Single stellar evolution grid

In this section we describe how we compute our grid of SSE models. To create a grid of SSE which fits the observed data we vary the mixing-length parameter $\alpha_{\rm mlt}$ and the main-sequence exponential Overshooting (OS) parameter $f_{\rm OV,H}$. $\alpha_{\rm mlt}$ determines how efficiently convection can transport energy, with larger $\alpha_{\rm mlt}$ resulting in hotter and more compact stars. In stars with convective cores during the main sequence, higher $f_{\rm OV,H}$ results in more massive helium-cores due to increased mixing above the convective core. This higher helium-core mass at a given stellar mass results in the transition between degenerate and non-degenerate core-helium ignition occurring at lower stellar masses. We also use a modified version of the penetrative convective overshooting scheme from Bossini et al. (2017), which is described in Section 5.2.2.1. We use the same definition of modelled RC stars as in Chapter 4, where we select only models with convective cores and central-helium mass-fractions between $0.95 \times Y_{\rm C,max}$ and 0.1, where $Y_{\rm C,max}$ is the maximum central helium mass fraction reached during evolution.

To determine which combination of $\alpha_{\rm mlt}$ and $f_{\rm OV,H}$ best fit the observations we run a grid of SSE models. We then compare between the observed and modelled ΔP, $T_{\rm eff}$, $\nu_{\rm max}$, and $\langle\Delta\nu\rangle$ to find the best combination of $\alpha_{\rm mlt}$ and $f_{\rm OV,H}$. We then use this combination of parameters in our MT/MG grid. The grid is summarized in Table 5.2.

5.2.2.1 Modified core overshooting

To model the mixing in radiative regions surrounding the helium-burning core, we use a modified version of the penetrative overshooting scheme described in Bossini et al. (2017), where the overshooting region has an adiabatic temperature gradient. The overshooting scheme is modified by increasing the helium-core overshooting parameter, $\alpha_{\rm OV,He}$, as the helium is depleted in the core. This is done so that our SSE models reproduce the observed range of ΔP of approximately 230–330 s for stars with $M \lesssim 1.8$ M$_\odot$, which modelled stars using the unmodified penetrative overshooting are unable to do (e.g. Bossini et al. 2017). Spruit (2015) showed that there is a maximum rate at which helium can be ingested into a convective core, and this growing $\alpha_{\rm OV,He}$ results in a growth rate of the well-mixed region similar to that described in Spruit (2015) of the order of 10^{-2} M$_\odot$ Myr^{-1}. The modification takes on the following form by changing $\alpha_{\rm OV,He}$:

$$\alpha_{\rm OV,He,scaled} = \begin{cases} 0, & Y_{\rm C,off} \leq Y_{\rm C}, \\ \alpha_{\rm OV,He} \frac{Y_{\rm C,off} - Y_{\rm C}}{Y_{\rm C,off} - Y_{\rm C,on}}, & Y_{\rm C,off} < Y_{\rm C} \leq Y_{\rm C,on}, \text{and} \\ \alpha_{\rm OV,He}, & Y_{\rm C} < Y_{\rm C,on}, \end{cases} \tag{5.1}$$

where $Y_{\rm C}$ is the central-helium mass fraction, $Y_{\rm C,off}$ is the central-helium mass fraction above which overshooting is fully switched off, $Y_{\rm C,on}$ where overshooting is fully switched on, and $\alpha_{\rm OV,He}$ is the step-overshooting parameter. We use $Y_{\rm C,off} = 0.9$, $Y_{\rm C,on} = 0.2$, and $\alpha_{\rm OV,He} = 0.85$. This value of $\alpha_{\rm OV,He}$ is close to the value adopted in Bossini et al. (2017) of 0.5. The result of using this modified overshooting is described in Section 5.3.1 and in Figures 5.5 and 5.6. $Y_{\rm C,off}$ approximately corresponds to the time when the mass coordinates of the convective core and convective envelope no longer change due to the ignition of the core. Whilst $Y_{\rm C,on}$ corresponds to time when the ^{12}C$(\alpha,\gamma)^{16}$O reaction rate exceeds the triple-α reaction in the core. We stress that the aim of this modified core overshooting is to create SSE models which fit the observed data, and we do not discuss the physical nature of this mixing recipe.

5.2.3 Parametric MT/MG analogue grid

To test how different helium-core masses affect the seismic signature of stars, we create models with varying initial helium-core masses and total masses. We focus on the helium-core mass and its effects. Models are generated with the `MESA` code (Paxton et al. 2011, 2013, 2015, 2018, 2019, version 11701). We use the `relax_composition_filename` option which allows an arbitrary composition profile to be evolved. Unless stated otherwise, we use the same `MESA` settings as in Chapter 4.

Parametric models are used to create initial stellar models with arbitrary combinations of helium-core mass and total mass. These initial stellar models are then evolved using `MESA`. Comparing our parametric models to observations, potentially allows the identification of stars which have undergone non-standard evolution. The parametric models used in this study are constructed using three key parameters. The first parameter is the helium-core mass fraction $f_{\rm He}$, which is defined as

$$f_{\rm He} = M_{\rm He}/M_{\star}, \tag{5.2}$$

where $M_{\rm He}$ is the helium-core mass, and $M_{\star}$ is the stellar mass. The other two parameters describe the core-to-envelope transition region between the helium core and the hydrogen envelope. The core-to-envelope transition region is important as modelling it correctly, improves both the accuracy of our stellar models and reduces the likelihood of `MESA` being unable to converge on a solution. The core and envelope compositions are determined, using a 1 $M_{\odot}$ model with initial compositions calibrated on the Sun. The core composition ($X_{\rm core}$) is the mean composition of the core of the star close to the tip of the RGB where the core is effectively hydrogen free. The envelope composition ($X_{\rm env}$) is taken to be the mean composition where the hydrogen mass fraction is greater than 0.7. These initial mean compositions for our parametric models are shown in Table 5.3. We then create a composition profile using the helium-core mass fraction and these mean core and envelope compositions. We use a two-sided clipped sigmoid function in the core-to-envelope

Table 5.3: Logarithmic mean core and envelope mass fractions used to create the narrow and wide core-to-envelope transition regions in the composition profiles.

Isotope	Core (dex)	Envelope (dex)
H-1	-23.2250	-0.1504
H-2	-20.6499	-16.6525
He-3	-36.5732	-2.8619
He-4	-0.0064	-0.5575
Li-7	-21.7875	-16.0745
Be-7	-31.9197	-10.5862
B-8	-61.1485	-19.0299
C-12	-3.5066	-2.6620
N-14	-2.0745	-2.9465
O-16	-3.0382	-2.2148
Ne-20	-2.8572	-2.8737
Mg-24	-2.4355	-2.4513

transition region between the helium core and the envelope, with different scaling parameters on each side of the centre of the transition region. The shape of this core-to-envelope transition region is different for single stars which undergo the helium flash. Single stars which have undergone the helium flash have a narrower transition between the core and envelope whilst more massive stars, which quiescently ignite helium, have a wider core-to-envelope transition region. To approximate both a more massive star which is stripped, and a less massive star which gains mass, we model both a wide core-to-envelope transition region and a narrow core-to-envelope transition region for each combination of $f_{\rm He}$ and stellar mass. We thus use the following expression:

$$X_i(x) = X_{i,\rm env} + (X_{i,\rm core} - X_{i,\rm env})\, f_{\rm sigm}(x), \tag{5.3}$$

where X_i is the composition of species i, and x is defined as:

$$x = 1 - \frac{m}{M_\star}, \tag{5.4}$$

Table 5.4: Parameters used to create the narrow and wide core-to-envelope transition regions in the composition profiles.

	$k_{\rm clip}$	σ_l	σ_r
narrow	4	3.6×10^{-5}	3.2×10^{-5}
wide	1	3.0×10^{-4}	1.2×10^{-2}

where m is the mass coordinate, $M_\star$ the total mass of the star, and $f_{\rm sigm}$ is a sigmoid function,

$$f_{\rm sigm} = \frac{1}{1 + \exp(-\frac{x - x_0}{\sigma})}, \tag{5.5}$$

where

$$x_0 = 1 - f_{\rm He}, \tag{5.6}$$

and σ is a scaling factor for the width of the sigmoid function, with $\sigma = \sigma_l$ when $x < x_0$ and $\sigma = \sigma_l$ when $x \geq x_0$. When clipping, we scale $f_{\rm sigm}$ in the following way:

$$f_{\rm sigm,scaled} = \left[f_{\rm sigm}(x) - \frac{1}{2} \right] \left(1 + 2e^{-k_{\rm clip}} \right) + \frac{1}{2}, \tag{5.7}$$

and we clip it to ensure it is between 0 and 1:

$$f_{\rm sigm,clip} = \begin{cases} 0, & f_{\rm sigm,scaled} \leq 0, \\ f_{\rm sigm,scaled}, & 0 < f_{\rm sigm,scaled} \leq 1, \text{ and} \\ 1, & 1 < f_{\rm sigm,scaled}. \end{cases} \tag{5.8}$$

Table 5.4 shows the parameters used to create the narrow and wide core-to-envelope transition regions.

We closely reproduce a 1 $M_\odot$ RGB tip star using a helium-core mass of 0.472 $M_\odot$ and using the narrow composition profile. This helium-core mass is equal to that of a 1 $M_\odot$ star at the start of the core helium-burning phase. The top panel of Figure 5.1 shows the mean molecular mass (μ) profile of a 1 $M_\odot$ Single Stellar Evolution (SSE) model assuming a fully ionized gas (Equation 3.58) at the tip of the RGB. The fractional difference in μ between the RGB-tip SSE model and

Table 5.5: RMS fractional difference of $T_{\rm eff}$, L, $\nu_{\rm max}$, $\langle\Delta\nu\rangle$, ΔP, and coupling coefficient q between a 1 $M_\odot$ SSE star and a parametric star with the same helium-core mass.

Observable	RMS fractional difference
$T_{\rm eff}$	1.16×10^{-4}
L	2.20×10^{-3}
$\nu_{\rm max}$	1.16×10^{-2}
$\langle\Delta\nu\rangle$	9.17×10^{-3}
ΔP	2.13×10^{-2}
q	1.31×10^{-2}

the initial parametric model is shown in the bottom panel. In the envelope the fractional difference in μ between the SSE and parametric model is of order 10^{-7}. In the core the fractional difference in μ is between 2–3$\times10^{-4}$. In the transition region at around 0.47 $M_\odot$ the difference is up to 0.4. However, once shell hydrogen-burning starts in the parametric star, the difference in the transition region reduces to around 0.02. When using this method with the same helium-core mass and same total mass as a SSE star, we are able to closely reproduce the behaviour of $T_{\rm eff}$, L, $\nu_{\rm max}$, $\langle\Delta\nu\rangle$, ΔP, and coupling coefficient q in the RC, as shown in Figure 5.2. Figure 5.2 shows $T_{\rm eff}$, L, $\nu_{\rm max}$, $\langle\Delta\nu\rangle$, ΔP, and q of the 1 $M_\odot$ SSE star and the parametric star in the RC. Root Mean Square (RMS) fractional differences between the two modelled stars are shown in Table 5.5.

Based on the results from the SSE grid, described in Section 5.3.1, we create a grid of parametric models with the properties described in Table 5.6 and the method described in this section.

5.2.4 Mean large frequency separation $\langle\Delta\nu\rangle$

We use the stellar oscillation code `gyre` (Townsend & Teitler 2013; Townsend et al. 2018) to calculate mode frequencies in our models. We then calculate the average large frequency separation

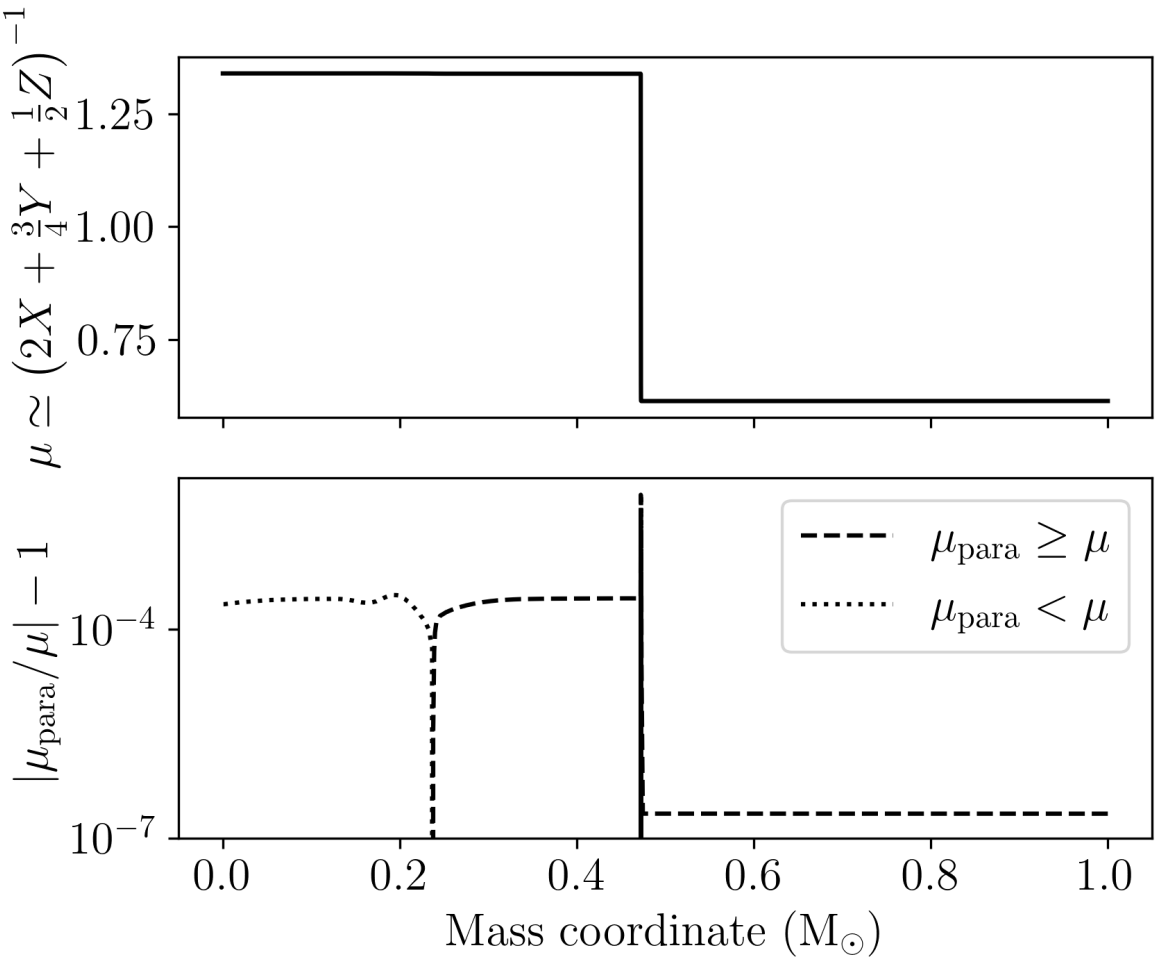

Figure 5.1: Mean molecular mass μ profile assuming a fully ionized gas (Equation 3.58) of a 1 $M_\odot$ SSE model at the tip of the RGB is shown in the top panel. The bottom panel shows the fractional difference between the SSE model μ and the initial parametric model μ. The fractional difference is shown as a dashed line when $\mu_{\rm para} \geq \mu$, and as a dotted line when $\mu_{\rm para} < \mu$.

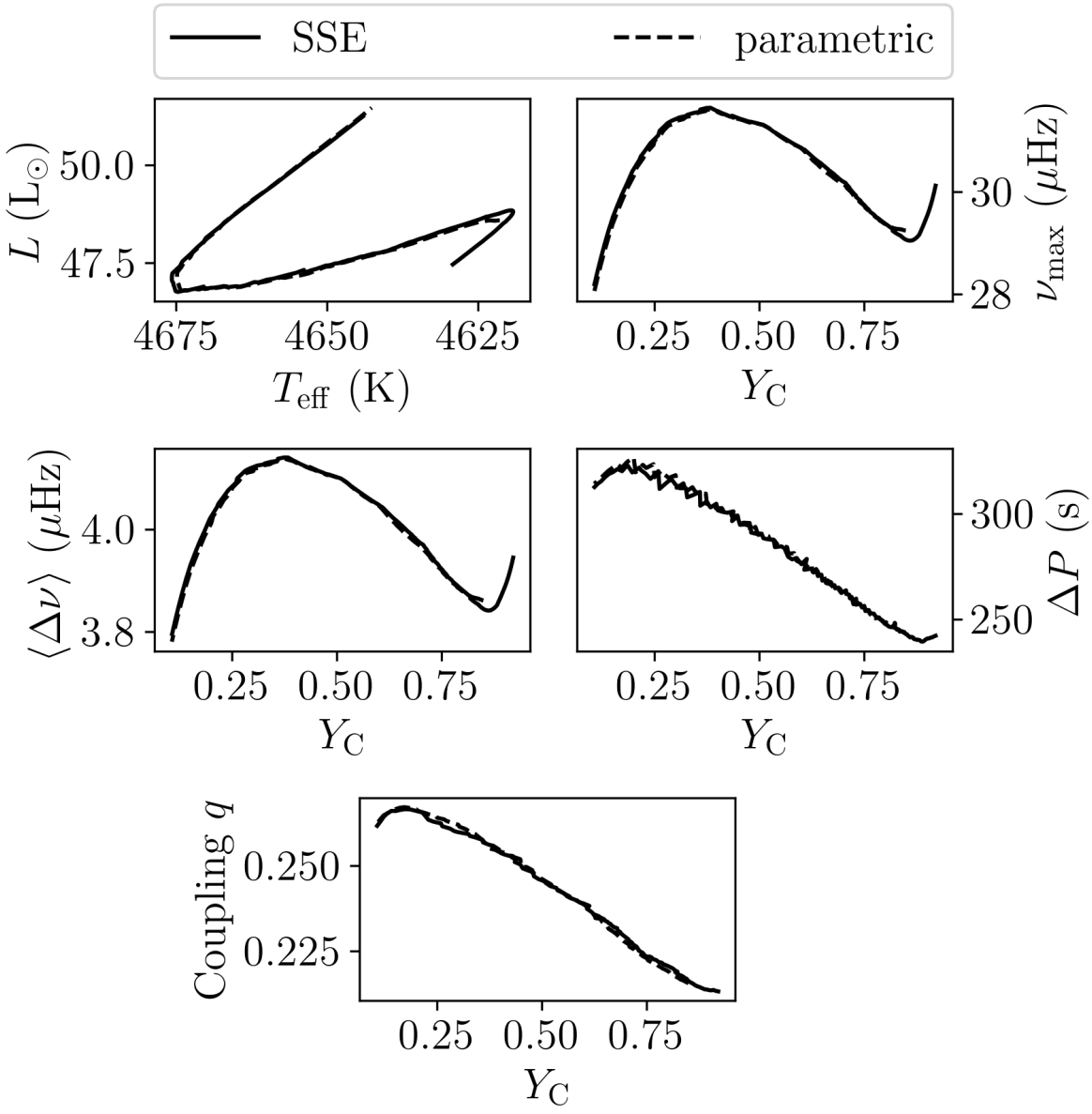

Figure 5.2: $T_{\rm eff}$, L, $\nu_{\rm max}$, $\langle\Delta\nu\rangle$, ΔP, and coupling coefficient q of a 1 $M_\odot$ SSE star and parametric star with the same helium-core mass are shown as a solid black and dashed black line respectively. The tracks in the HRD are shown in the top left panel. $\nu_{\rm max}$, $\langle\Delta\nu\rangle$, ΔP, and coupling coefficient q are shown as a function of the central-helium mass fraction in the top right, middle left, middle right, and bottom panels respectively.

Table 5.6: Summary of the parameters varied for the parametric grid. The parameters for the transition width are varied together as a group.

Parameter	Symbol	Unit	Values
Initial mass	m_i	$M_\odot$	1.0, 1.2, 1.4, 1.6, 1.8, 2.0, 2.2, 2.5, 2.7, 3.0
Helium-core mass	M_{He}	$M_\odot$	0.30, 0.35, 0.40, 0.45, 0.50, 0.55, 0.60
Transition width	$k_{clip}, \sigma_l, \sigma_r$		4, 3.6×10^{-5}, 3.2×10^{-5}, 1, 3.0×10^{-5}, 3.2×10^{-5}

$\langle \Delta\nu_{\texttt{gyre}} \rangle$ from the $\ell = 0$ mode frequencies computed using `gyre` by taking a weighted average of $\Delta\nu_n$ around ν_{max}. The weighting uses the power-spectrum density envelope approximation described in Mosser et al. (2012). This results in the following equation for the mean large frequency separation $\langle \Delta\nu_{\texttt{gyre}} \rangle$:

$$\langle \Delta\nu_{\texttt{gyre}} \rangle = \frac{\sum_n w_n(\nu_{n+1} - \nu_n)}{\sum_n w_n}, \tag{5.9}$$

where the weighting, w_n, is defined as:

$$w_n = \exp\left[-\left(\frac{\nu_n - \nu_{max}}{0.66\nu_{max}^{0.88} / \sqrt{2 \ln 2}} \right)^2 \right]. \tag{5.10}$$

We do not write a `gyre` profile at every timestep in `MESA` due to concerns about storage and computation efficiency. We rescale $\Delta\nu_{sc}$ calculated in `MESA` from the scaling relations, defined as:

$$\Delta\nu_{sc} = \Delta\nu_\odot \left(\frac{M}{M_\odot} \right)^{1/2} \left(\frac{T_{eff}}{T_{eff,\odot}} \right)^3 \left(\frac{L}{L_\odot} \right)^{-3/4}, \tag{5.11}$$

where $\Delta\nu_\odot = 135\ \mu$Hz, using $\langle \Delta\nu_{\texttt{gyre}} \rangle$. This is done by fitting a quadratic to $\langle \Delta\nu_{\texttt{gyre}} \rangle / \Delta\nu_{sc}$ as a function of the central-helium mass fraction Y_C. We then rescale $\Delta\nu_{sc}$ using this polynomial which results in the model $\langle \Delta\nu \rangle$ used in the rest of this work, resulting in the following equation:

$$\langle \Delta\nu \rangle = \Delta\nu_{sc} f(Y_C), \tag{5.12}$$

where $f(Y_C)$ is the quadratic fit to $\langle \Delta\nu_{\texttt{gyre}} \rangle / \Delta\nu_{sc}$.

Figure 5.3 shows how a rescaling using Equations (5.9) and (5.10) affects the model large-frequency separation as a function of central-helium mass fraction. The quadratic fit (Equation 5.12) works well over the range of masses used as shown in Figure 5.3 and also shows that the correction increases as helium is consumed. Varying $\alpha_{\rm mlt}$ or $f_{\rm OV,H}$ causes small ($\lesssim 0.004$) changes in the correction factor. However, each modelled star is corrected individually using $\langle\Delta\nu_{\texttt{gyre}}\rangle$.

5.2.5 Determination of mass and radius

To determine the masses and radii of observed stars and compare them to modelled stars we use the seismic scaling relations which result in the following equations:

$$\frac{M_{\rm seis}}{\rm M_\odot} \simeq \left(\frac{\langle\Delta\nu\rangle}{\Delta\nu_{\rm ref}}\right)^{-4}\left(\frac{\nu_{\rm max}}{\nu_{\rm max,ref}}\right)^{3}\left(\frac{T_{\rm eff}}{\rm T_{eff,ref}}\right)^{3/2}, \tag{5.13}$$

and

$$\frac{R_{\rm seis}}{\rm R_\odot} \simeq \left(\frac{\langle\Delta\nu\rangle}{\Delta\nu_{\rm ref}}\right)^{-2}\left(\frac{\nu_{\rm max}}{\nu_{\rm max,ref}}\right)\left(\frac{T_{\rm eff}}{\rm T_{eff,ref}}\right)^{1/2}. \tag{5.14}$$

Equation (5.13) depends strongly on $\langle\Delta\nu\rangle$. However, stars with the same mass and radius but different internal structures have different $\langle\Delta\nu\rangle$ as $\langle\Delta\nu\rangle \approx \left(2\int_0^R \frac{\mathrm{d}r}{c_{\rm s}}\right)^{-1}$. An alternative to Equation (5.13) can be achieved using the scaling of $\nu_{\rm max}$ with M, R, and $T_{\rm eff}$ and combining it with the blackbody luminosity equation $L \propto R^2 T_{\rm eff}^4$ (e.g. Miglio et al. 2012). This results in the following equation:

$$\frac{M_{\rm seis}}{\rm M_\odot} \simeq \left(\frac{L}{L_\odot}\right)\left(\frac{\nu_{\rm max}}{\nu_{\rm max,ref}}\right)\left(\frac{T_{\rm eff}}{\rm T_{eff,ref}}\right)^{-7/2}, \tag{5.15}$$

which removes the dependence on $\langle\Delta\nu\rangle$. This expression depends only on surface quantities, as $\nu_{\rm max}$ is thought to be closely related to the acoustic cut-off frequency (Brown et al. 1991; Belkacem et al. 2011). Similarly, as we have luminosities using the parallaxes from *Gaia* we use the photospheric radius:

$$\frac{R}{\rm R_\odot} \simeq \left(\frac{L}{L_\odot}\right)^{1/2}\left(\frac{T_{\rm eff}}{\rm T_{eff,ref}}\right)^{-2} \tag{5.16}$$

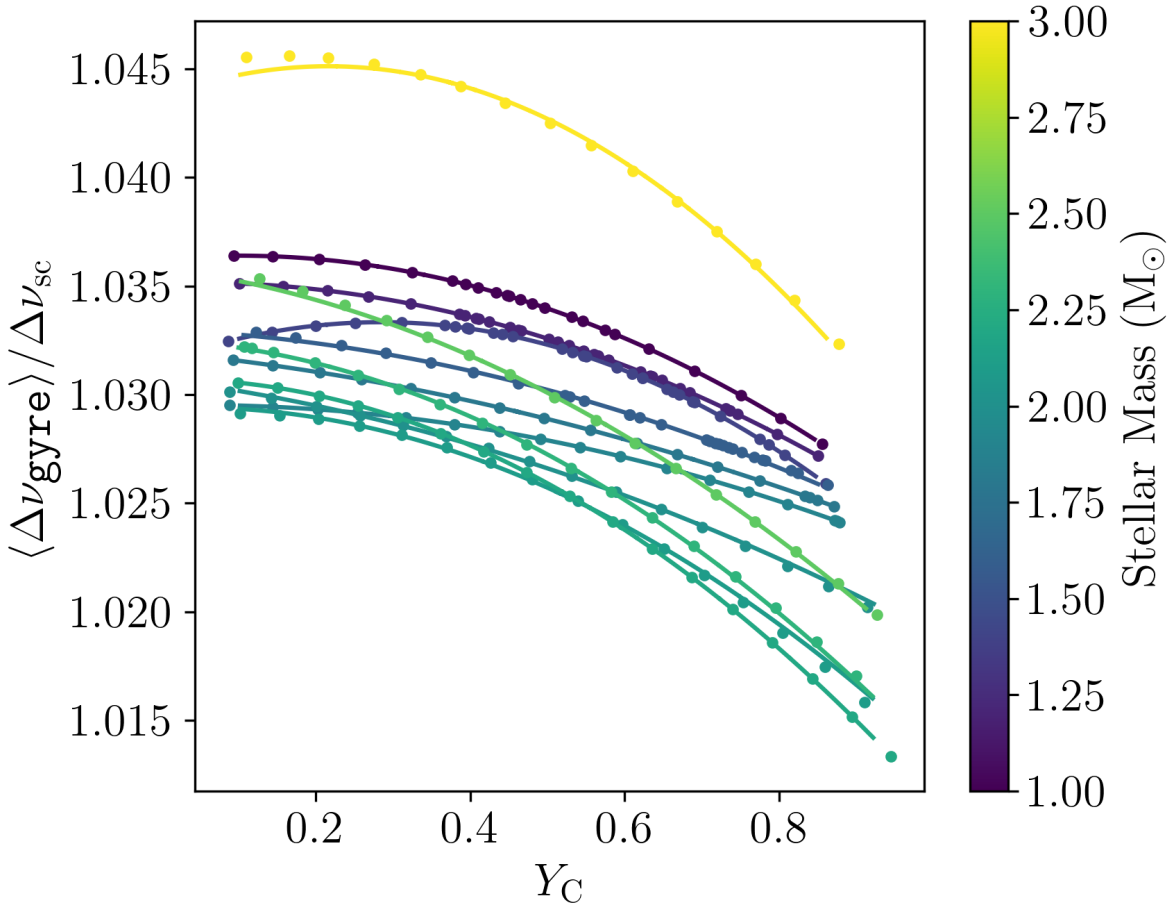

Figure 5.3: Correction factor applied to $\Delta\nu_{\mathrm{sc}}$ as a function of central-helium mass fraction of the $\alpha_{\mathrm{mlt}} = 1.8$ $f_{\mathrm{OV,H}} = 0.010$ SSE models. Dots show the `gyre` values used to compute the quadratic fit, and lines show the fitted quadratic. The colour scale shows the stellar mass.

Table 5.7: Reference values used in Equations (5.15) and (5.16).

Parameter	Model reference values	Solar reference values
$\Delta\nu_{\rm ref}$ (μHz)	139.331 ± 0.105	135.1 ± 0.1
$\nu_{\rm max,ref}$ (μHz)	3100.34 ± 1.41	3090 ± 30
$T_{\rm eff,ref}$ (K)	5776.07 ± 0.75	5777 ± 1

for the radii. Equations (5.15) and (5.16) only depend on surface properties, and in our models they are equal to the mass and photospheric radius respectively. The reference values used in Equations (5.13), (5.14), (5.15) and (5.16) are determined by a least squares fit using the luminosity scaling relation (Equation 5.17) and the model photospheric luminosity, as Equations (5.15) and (5.16) have no $\langle\Delta\nu\rangle$ dependence. This is done using the following equation:

$$\frac{L_{\rm seis}}{\rm L_\odot} = \left(\frac{\langle\Delta\nu\rangle}{\Delta\nu_{\rm ref}}\right)^{-4}\left(\frac{\nu_{\rm max}}{\nu_{\rm max,ref}}\right)^{2}\left(\frac{T_{\rm eff}}{\rm T_{eff,ref}}\right)^{5}. \tag{5.17}$$

We find reference values used in Equations (5.13), (5.14), (5.15) and (5.16) by performing a least squares fit between the luminosity scaling relation using Equation (5.17) and the modelled luminosity. These reference values are only used in the scaling relations for the models. Scaling relations for observations use the Solar $\nu_{\rm max}$ and $\langle\Delta\nu\rangle$ from Huber et al. (2011). This results in the reference values shown in Table 5.7.

Figure 5.4 shows the improvement in our model seismic mass when using Equation (5.15) instead of Equation (5.13). The fractional difference in mass when using Equation (5.13) is up to 7% for stars with masses $M \gtrsim 2$ M$_\odot$, and around 2% for stars with masses $M \lesssim 2$ M$_\odot$. When using Equation (5.15) it is of order 10^{-10}, as replacing L, $\nu_{\rm max}$, and $T_{\rm eff}$ with their scaling relations leaves only M on the right hand side of Equation (5.15). The fractional difference when using Equation (5.13) decreases as the helium-core becomes more massive in all our modelled stars. Whenever we refer to the mass of observed stars, we use the mass inferred using Equation (5.15) and the reference values determined from our modelled stars. The fractional difference in radius when Equation (5.16) instead of Equation (5.14) show the same behaviour as in Figure 5.4 except

that the fractional differences are half that for the mass. This is due to the $\langle\Delta\nu\rangle$ dependence of the seismic mass being $M_{\rm seis} \propto \langle\Delta\nu\rangle^{-4}$ and $R_{\rm seis} \propto \langle\Delta\nu\rangle^{-2}$.

5.3 Results

In this section we present the comparisons between our SSE models, parametric models, and observations. In particular, we look at our SSE models and how they compare to observations. In doing so we identify stars which do not follow standard evolution. As period spacing depends strongly on helium-core mass (Montalbán et al. 2013) during core helium-burning, the period spacing represents a promising indicator of non-standard helium-core masses.

5.3.1 Model input parameter calibration

To determine the best mixing-length parameter $\alpha_{\rm mlt}$ and main-sequence exponential overshooting parameter $f_{\rm OV,H}$ we compare our SSE models to observations using the corrections to $\langle\Delta\nu\rangle$ described in Section 5.2.4 and using modelled ΔP, $T_{\rm eff}$, and $\nu_{\rm max}$. Table 5.2 shows the main parameters of this grid.

We first look at the effect that modified overshooting, described in Section 5.2.2.1, has on our model tracks in the HRD. Figure 5.5 shows an HRD using the modified OS prescription in black and a standard penetrative OS with $\alpha_{\rm OV,He} = 0.5$ in red. It shows that there is little difference in the effective temperatures of our models in the RC, to order of 0.1%. The main difference is that modelled stars with modified OS have minimum luminosities which are 0.5–3% lower and maximum luminosities which are 1–4% higher than the standard overshooting case. This is due to the modified OS models having RC lifetimes of around 15% longer than those with standard OS because the higher maximum $\alpha_{\rm OV,He}$ causes the helium core to grow for longer.

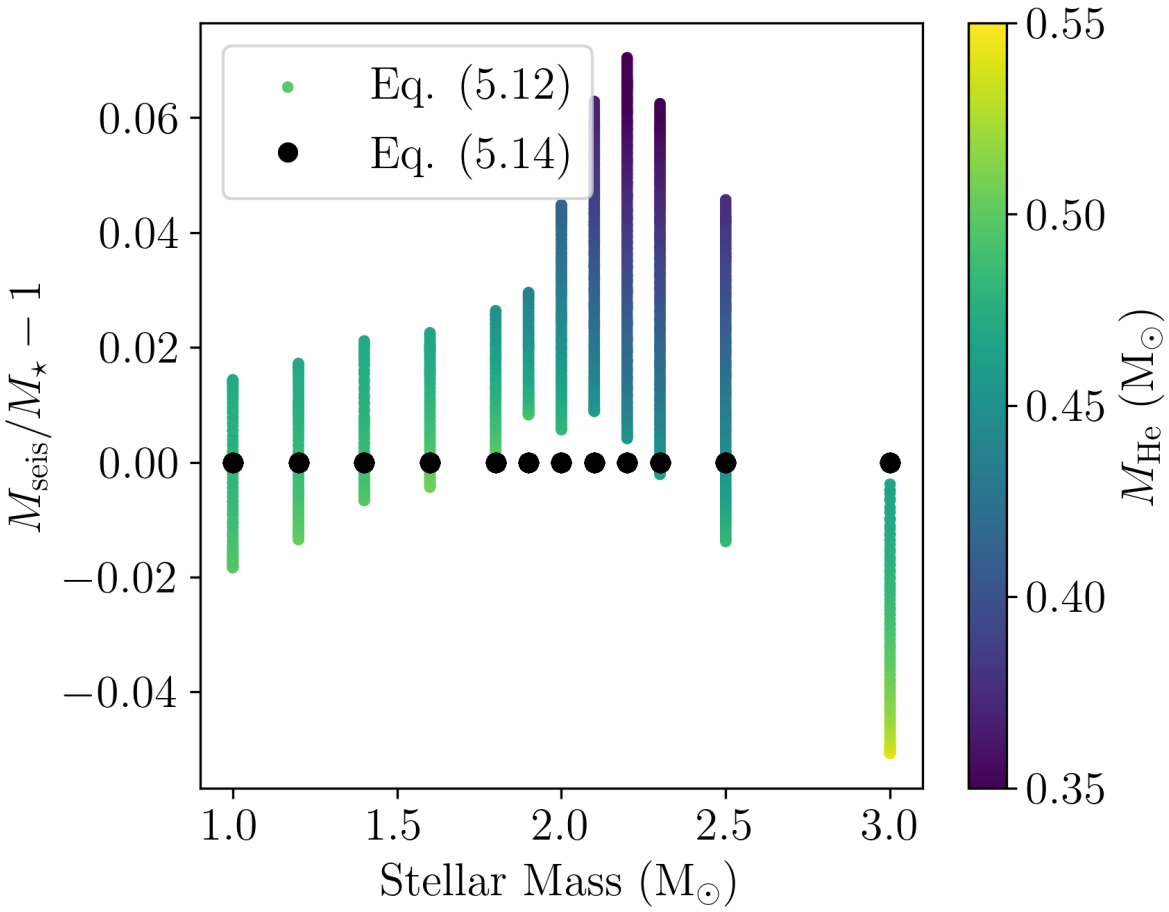

Figure 5.4: Difference in seismic mass compared to model mass in the $\alpha_{\rm mlt}$ =1.8, $f_{\rm OV,H}$ = 0.010 models when using Equation (5.13) is shown as coloured lines, the difference when using Equation (5.15) is shown as black dots. Helium-core mass is shown using the colour scale. Stars evolve from top to bottom. Differences when using Equation (5.15) cannot be seen at the scale of the plot.

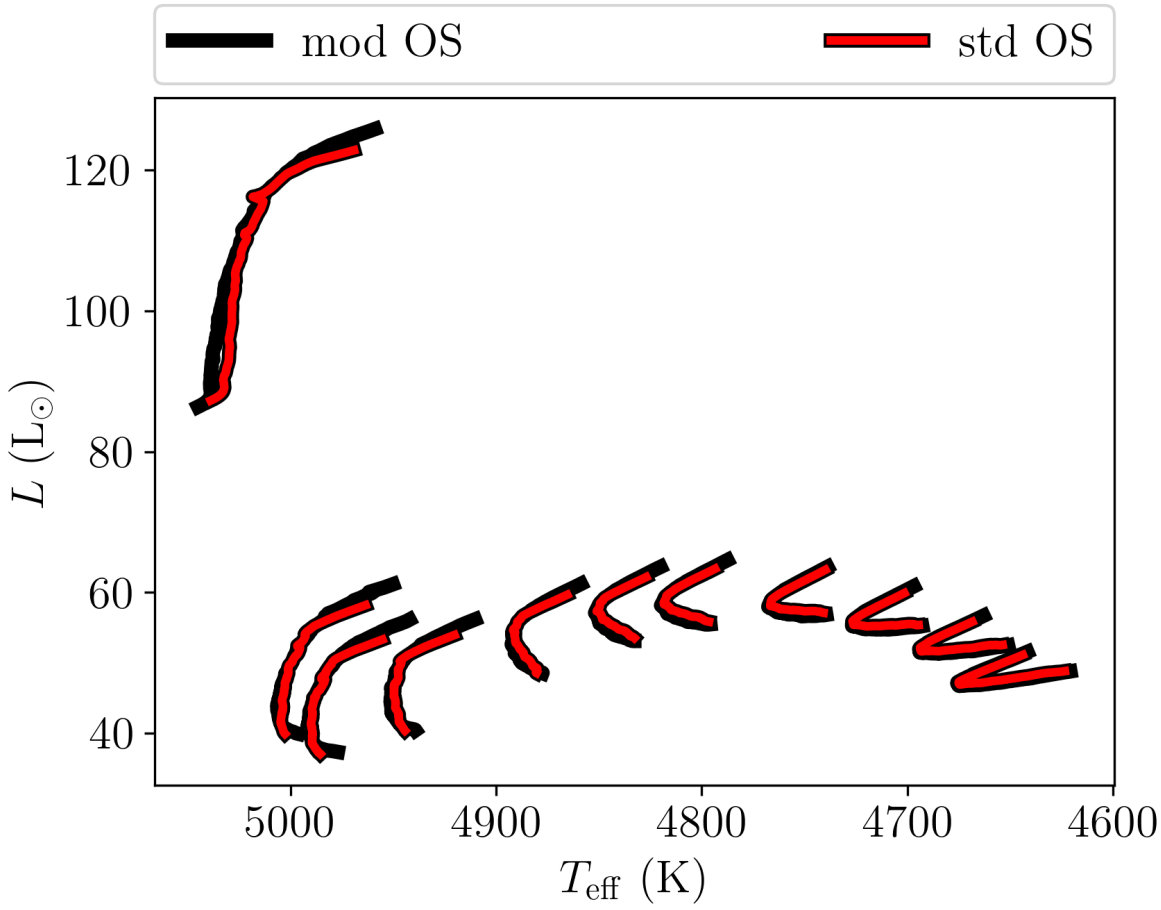

Figure 5.5: HRD tracks comparing the effects of using the modified overshooting described in Equation (5.1) in black and standard penetrative OS in red.

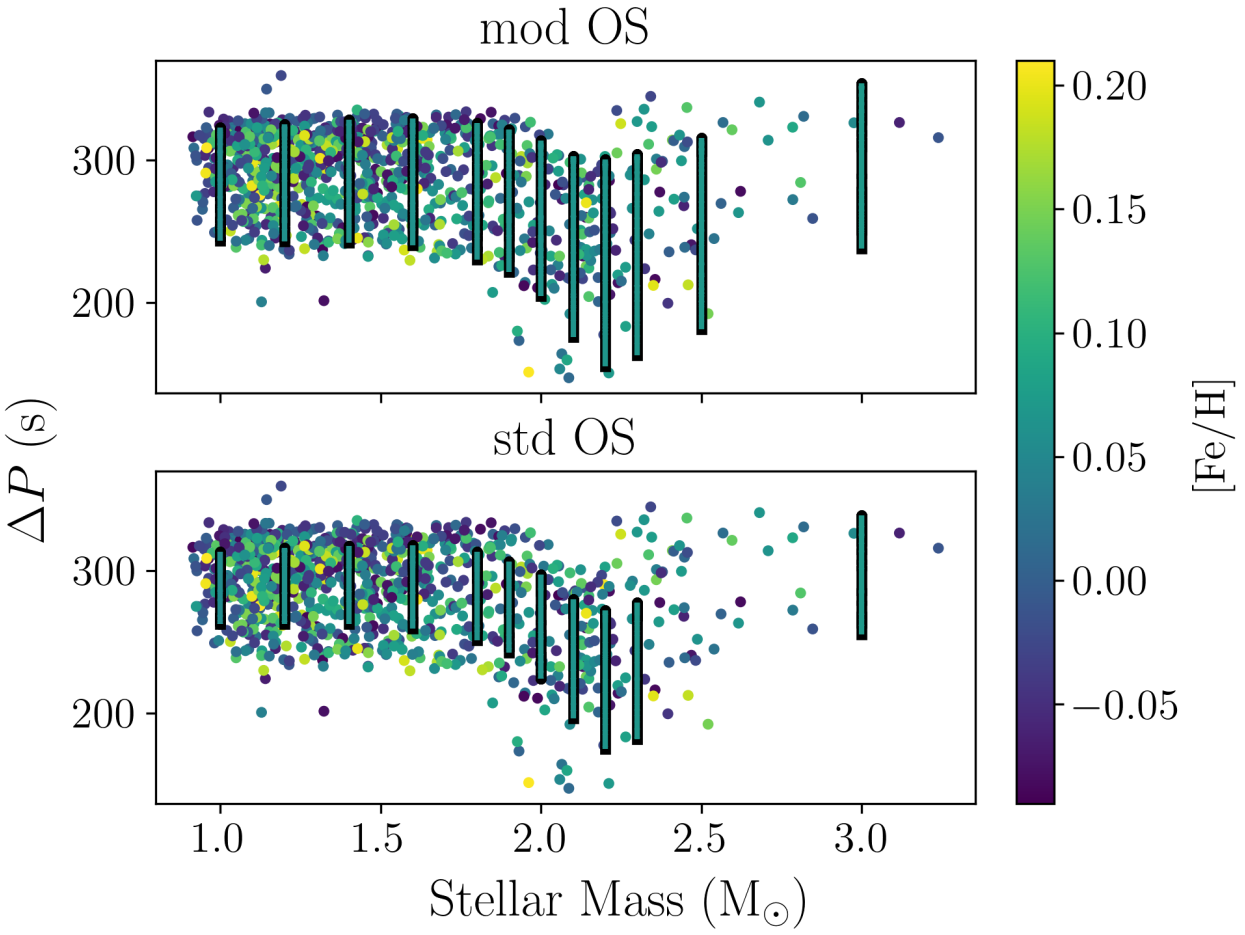

Figure 5.6: Period spacing ΔP as a function of mass comparing the effects of using the modified OS described in Equation (5.1) in the top panel and standard penetrative OS in the bottom panel. Observed stars are shown as coloured dots, and modelled stars as coloured bars.

The biggest difference between our modified and standard OS models is seen in period spacing. Figure 5.6 shows the period spacing as a function of stellar mass. In our modified OS scheme $\alpha_{\rm OV,He}$ increases from 0 to 0.85 as helium is consumed in the core. Our RC models span the full range of observed ΔP, between a minimum of 240 s and a maximum of 340 s, as shown in the top panel of Figure 5.6. In the standard OS case, shown in the bottom panel, our models do not span the full range of observed ΔP. Decreasing $\alpha_{\rm OV,He}$ in the standard OS case causes the modelled ΔP to decrease, exacerbating the issue that the modelled stars do not reach the high observed period spacing of $\gtrsim$ 320 s. On the other hand, increasing $\alpha_{\rm OV,He}$, increases the modelled ΔP and

therefore increases the discrepancy between our models and observations at low-ΔP ($\lesssim$ 260 s). For stars with masses $M \gtrsim 2.5$ M$_\odot$, it is difficult to draw a definitive conclusion on how effective our modified overshooting is because there are only 16 observed stars in this mass range. Also note that there are two observed stars with masses of approximately 1.2 M$_\odot$ which have ΔP of 350–360 s, which is 20–30 s larger than that attained by stars with the modified OS scheme. There are also observed stars with ΔP less than the minimum ΔP of the models. These stars are most likely pre- or post-RC stars as our SSE models only reach these ΔP during those phases. Figure 5.7 shows the ratios of modelled ΔP, L, $\nu_{\rm max}$, $\langle\Delta\nu\rangle$, $T_{\rm eff}$, and $M_{\rm He}$ between the modified overshooting and standard overshooting as a function of mass at the start and end of the RC. When using the modified overshooting scheme, modelled ΔP are 6–10% smaller at the start of the RC and 3–10% larger at the end of the RC. Similarly, modelled luminosities are 0.5–3% lower and 1–4% higher at the start and end of the RC respectively when using the modified overshooting scheme. Both of these observables are correlated with the helium-core mass $M_{\rm He}$, which is 0.5–2% smaller at the start of the RC and 0.1–2% larger at the end of the RC. Modelled $\nu_{\rm max}$ and $\langle\Delta\nu\rangle$ are anti-correlated with $M_{\rm He}$. $\nu_{\rm max}$ is up to 3% larger at the start of the RC and 1–5% smaller at the end of the RC. Similarly, modelled $\langle\Delta\nu\rangle$ is up to 3% larger at the start of the RC and 1–3% smaller at the end of the RC. However, the $\langle\Delta\nu\rangle$ ratio dips to -1% at 2.2 M$_\odot$ at the start of the RC. Finally, the modelled $T_{\rm eff}$ at the start of the RC is within around 0.1%, and around 0–0.2% cooler at the end of the RC.

To constrain $f_{\rm OV,H}$ and $\alpha_{\rm mlt}$ we compare ΔP, $T_{\rm eff}$, $\nu_{\rm max}$, and $\langle\Delta\nu\rangle$ of our grid of modelled SSE stars to observations. The mass at which stars transition between degenerate and non-degenerate core helium ignition is visible in the helium-core mass of the star. We vary $f_{\rm OV,H}$, which is the amount of exponential overshooting during the main sequence. Higher $f_{\rm OV,H}$ will result in a more massive helium-core in stars with convective cores during the main sequence due to increased mixing above the convective core. This increase in helium-core mass will cause the transition between degenerate and non-degenerate helium-ignition to occur at a lower stellar mass. As we cannot measure $M_{\rm He}$ directly, we use ΔP as a proxy for $M_{\rm He}$ (Montalbán et al. 2013). We rescale observed

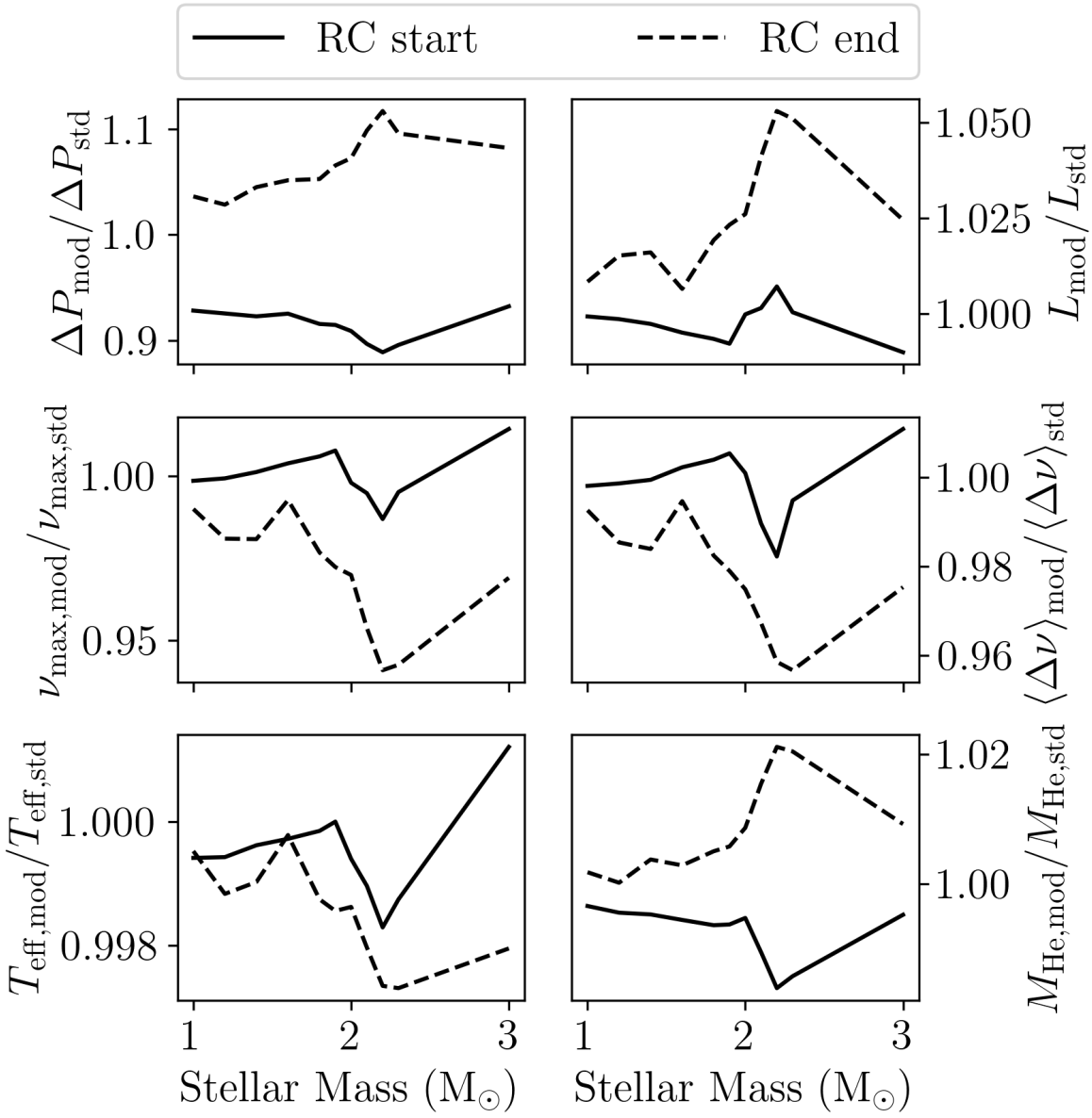

Figure 5.7: Ratios of ΔP, L, $\nu_{\rm max}$, $\langle\Delta\nu\rangle$, $T_{\rm eff}$, and $M_{\rm He}$ between the modified overshooting and standard overshooting as a function of mass from the top left panel to the bottom right panel. The ratios at the start of the RC are shown as solid black lines and the ratios at the end of the RC are shown as dashed black lines.

Table 5.8: RMS of the RMS σ-differences between observed and modelled ΔP, $T_{\rm eff}$, $\nu_{\rm max}$, and $\langle\Delta\nu\rangle$ shown in Figure 5.8.

$f_{\rm OV,H}$	$\alpha_{\rm mlt}$	RMS-σ
0.000	1.8	2.58
0.005	1.8	1.99
0.010	1.8	1.68
0.015	1.8	1.92
0.000	1.9	4.20
0.005	1.9	3.91
0.010	1.9	3.74
0.015	1.9	3.78

$\langle\Delta\nu\rangle$ by $\langle\Delta\nu\rangle_{\rm ref}/\langle\Delta\nu\rangle_{\odot}$, $\nu_{\rm max}$ by $\nu_{\rm max,ref}/\nu_{\rm max,\odot}$, and $T_{\rm eff}$ by $\rm T_{eff,ref}/T_{eff,\odot}$ to bring the observations and models to the same scale. Figure 5.8 shows the comparison between observed and modelled ΔP, $T_{\rm eff}$, $\nu_{\rm max}$, and $\langle\Delta\nu\rangle$. The observed and modelled 5$^{\rm th}$ and 95$^{\rm th}$ percentiles are shown for ΔP and the observed median for $T_{\rm eff}$, $\nu_{\rm max}$, and $\langle\Delta\nu\rangle$ in each mass bin. The modelled percentiles and medians are weighted by the timestep of each model. We find that within our SSE grid, $f_{\rm OV,H} = 0.010$ and $\alpha_{\rm mlt} = 1.8$ best fits the observed ΔP, $T_{\rm eff}$, $\nu_{\rm max}$, and $\langle\Delta\nu\rangle$, with an RMS deviation of 1.68-σ. Table 5.8 shows the RMS σ-difference between the observed and modelled ΔP, $T_{\rm eff}$, $\nu_{\rm max}$, and $\langle\Delta\nu\rangle$ shown in Figure 5.8. Figures 5.9, 5.10, 5.11, and 5.12 show the underlying observations and best fitting set of modelled stars. The switch in behaviour due to degenerate or non-degenerate ignition of the helium core is also visible in $T_{\rm eff}$, $\nu_{\rm max}$, and $\langle\Delta\nu\rangle$, as the break in the slopes coinciding with the minimum ΔP (or $M_{\rm He}$) in each set of modelled stars. $\alpha_{\rm mlt}$ is largely constrained through $T_{\rm eff}$ and to a lesser degree by $\nu_{\rm max}$ and $\langle\Delta\nu\rangle$, as shown in Figure 5.8. Higher $\alpha_{\rm mlt}$ makes energy transport through convection more efficient, resulting in stars which are hotter and smaller. These hotter and smaller stars have $\nu_{\rm max}$ and $\langle\Delta\nu\rangle$ which are higher because $\nu_{\rm max} \propto M_\star/(R_\star^2\sqrt{T_{\rm eff}})$ and $\langle\Delta\nu\rangle \propto \sqrt{M_\star/R_\star^3}$ (Equations 3.61 and 3.63 respectively).

Figure 5.9 shows period spacing vs. mass of observed and modelled stars. The modelled

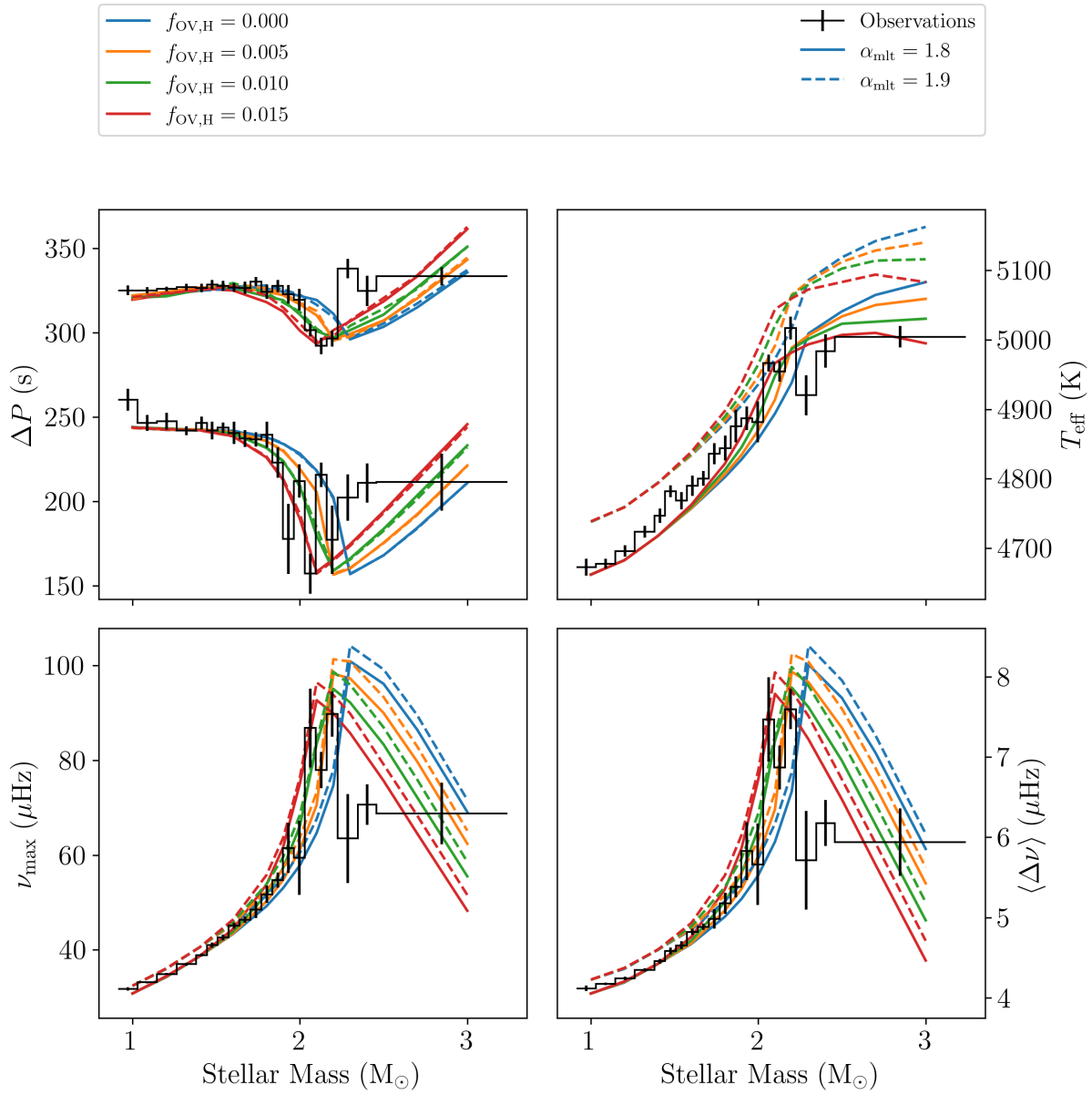

Figure 5.8: Comparison between observed and modelled ΔP, $T_{\rm eff}$, $\nu_{\rm max}$, and $\langle\Delta\nu\rangle$. The observed 5$^{\rm th}$ and 95$^{\rm th}$ percentiles of ΔP in each mass bin and the observed median in each mass bin of $T_{\rm eff}$, $\nu_{\rm max}$, and $\langle\Delta\nu\rangle$ are shown in black in their respective panels. Models with $f_{\rm OV,H} = 0.000, 0.005, 0.010$, and 0.015 are shown in blue, orange, green, and red respectively. Models with $\alpha_{\rm mlt} = 1.8$ are shown as solid coloured lines and models with $\alpha_{\rm mlt} = 1.9$ as dashed coloured lines.

stars use the best fitting $f_{\rm OV,H}$ and $\alpha_{\rm mlt}$ of 0.010 and 1.8 respectively. At around 1.8 $M_\odot$ the period spacing starts to decrease and above 2 $M_\odot$ it increases with mass. Below around 1.8 $M_\odot$, the maximum and minimum period spacing is approximately constant. The exact mass at which this transition occurs depends on the strength of overshooting during the MS, as shown in the top left panel of Figure 5.8, where the minimum ΔP moves to lower masses as $f_{\rm OV,H}$ increases. Figure 5.10 shows effective temperature $T_{\rm eff}$ vs. stellar mass of the observations and the modelled $f_{\rm OV,H} = 0.010$ and $\alpha_{\rm mlt} = 1.8$ stars. The [Fe/H] dependence of $T_{\rm eff}$ is visible as the vertical gradient in colour, with metal-poor stars having higher $T_{\rm eff}$. Figures 5.11 and 5.12 show $\nu_{\rm max}$ and $\langle\Delta\nu\rangle$ as a function of mass respectively. We see that there is an excess of stars with low $\nu_{\rm max}$ and $\langle\Delta\nu\rangle$ for stars with masses $M \gtrsim 2$ $M_\odot$, and that our RC models with these masses do not reach these low frequencies. However, these stars have radii which are larger than that of the modelled RC stars, indicating that they are likely pre- or post-RC stars. Figure 5.13 shows stellar radius as a function of stellar mass of observed stars and modelled SSE stars. The period spacing is shown using the colour scale. A small offset in the x-direction is applied for each model in a track so that the track evolves from left to right. The transition between degenerate and non-degenerate core-helium ignition is visible as a dip in radius at around 2 $M_\odot$. The observed stars with $M \lesssim 2$ $M_\odot$, radii of approximately 14 $R_\odot$ and low-ΔP of around 200 s are likely stars which are either pre- or post-RC stars. These low-ΔP and large radii only occur as stars approach or leave the RC.

5.3.2 Inferred helium-core masses assuming SSE

Montalbán et al. (2013) showed that period spacing ΔP can be used as a proxy for helium-core mass $M_{\rm He}$ in RC stars. However, RC stars reach a maximum ΔP before helium exhaustion at central-helium mass fraction $Y_{\rm C} \approx 0.1 - 0.2$, causing a single ΔP to have two possible helium-core masses during up to 40% of their lifetime when burning helium. Instead of using ΔP, here we use $\Delta P/\nu_{\rm max}$ which is monotonic in the RC as helium is consumed in the core. This is shown in Figure

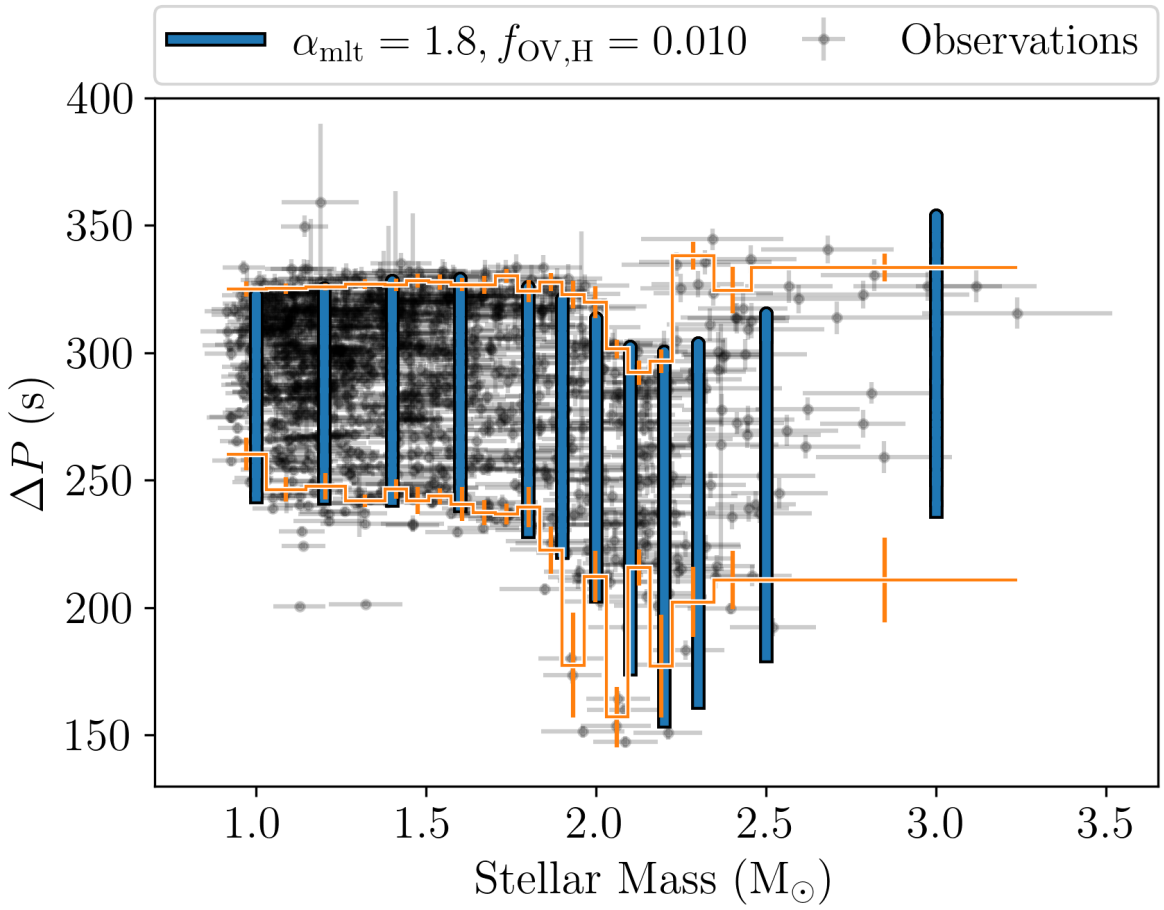

Figure 5.9: Period spacing ΔP as a function of stellar mass of observations (small grey dots) and our models (blue vertical bars). The bottom and top orange lines show the 5$^{\rm th}$ and 95$^{\rm th}$ percentiles of the observed ΔP distribution in each mass bin respectively. The uncertainty on the percentiles is determined through bootstrapping.

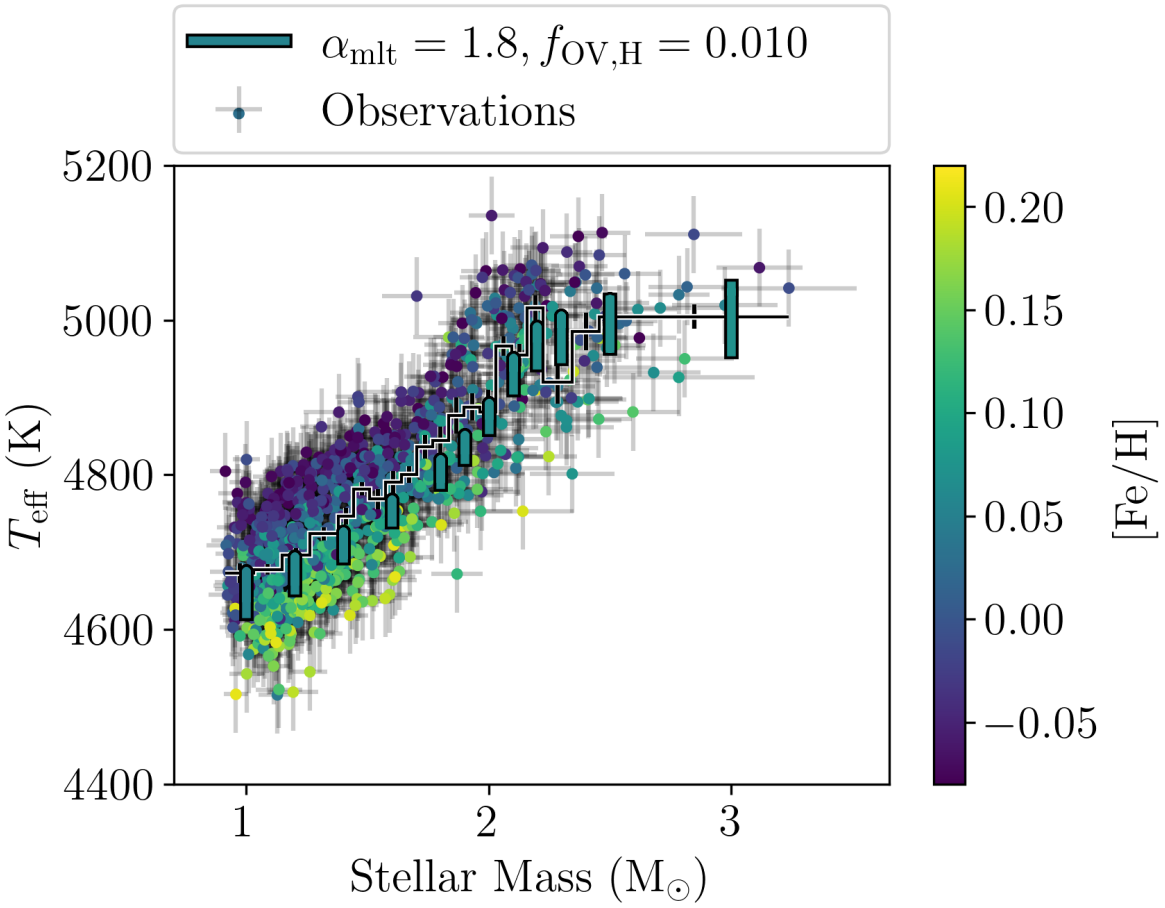

Figure 5.10: Effective temperature $T_{\rm eff}$ as a function of stellar mass of observations (small points) and our models (vertical bars). The colour scaling shows [Fe/H] of observations and surface [Fe/H] of our SSE models. The median effective temperature in each mass bin is shown as the black line with a white outline. The uncertainty on the median is determined through bootstrapping.

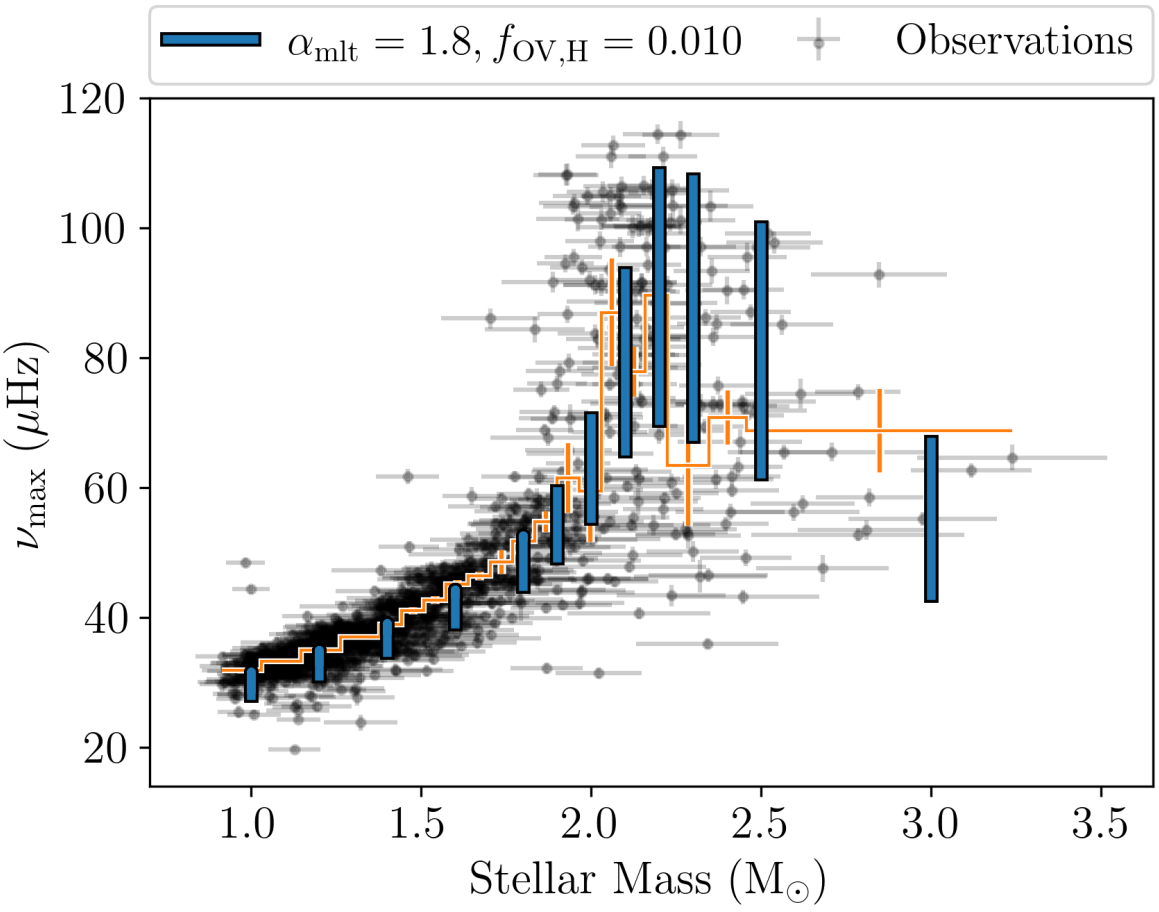

Figure 5.11: $\nu_{\rm max}$ as a function of stellar mass of observations (small points) and our models (blue vertical bars). The median $\nu_{\rm max}$ in each mass bin is shown as the orange line. The uncertainty on the median is determined through bootstrapping.

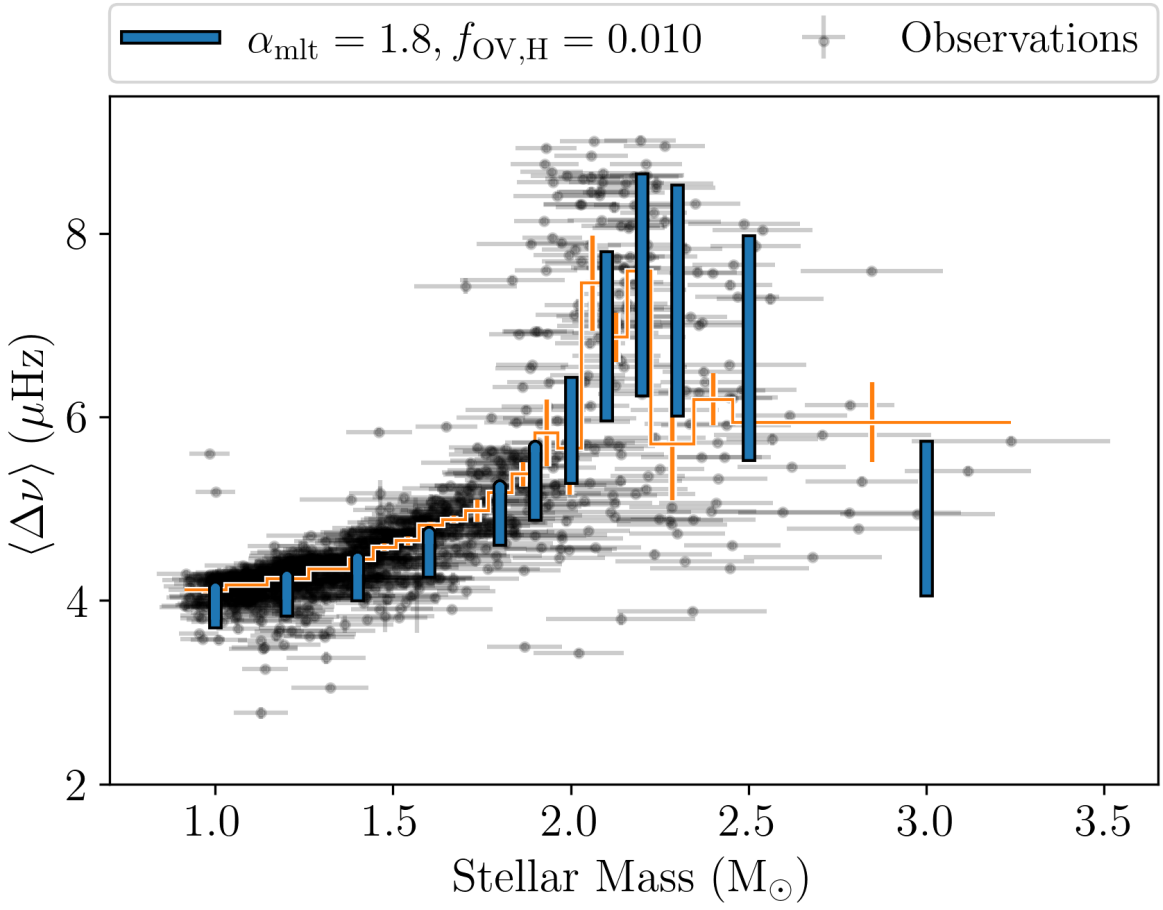

Figure 5.12: $\langle \Delta\nu \rangle$ as a function of stellar mass of observations (small points) and our models (blue vertical bars). The median $\langle \Delta\nu \rangle$ in each mass bin is shown as the orange line. The uncertainty on the median is determined through bootstrapping.

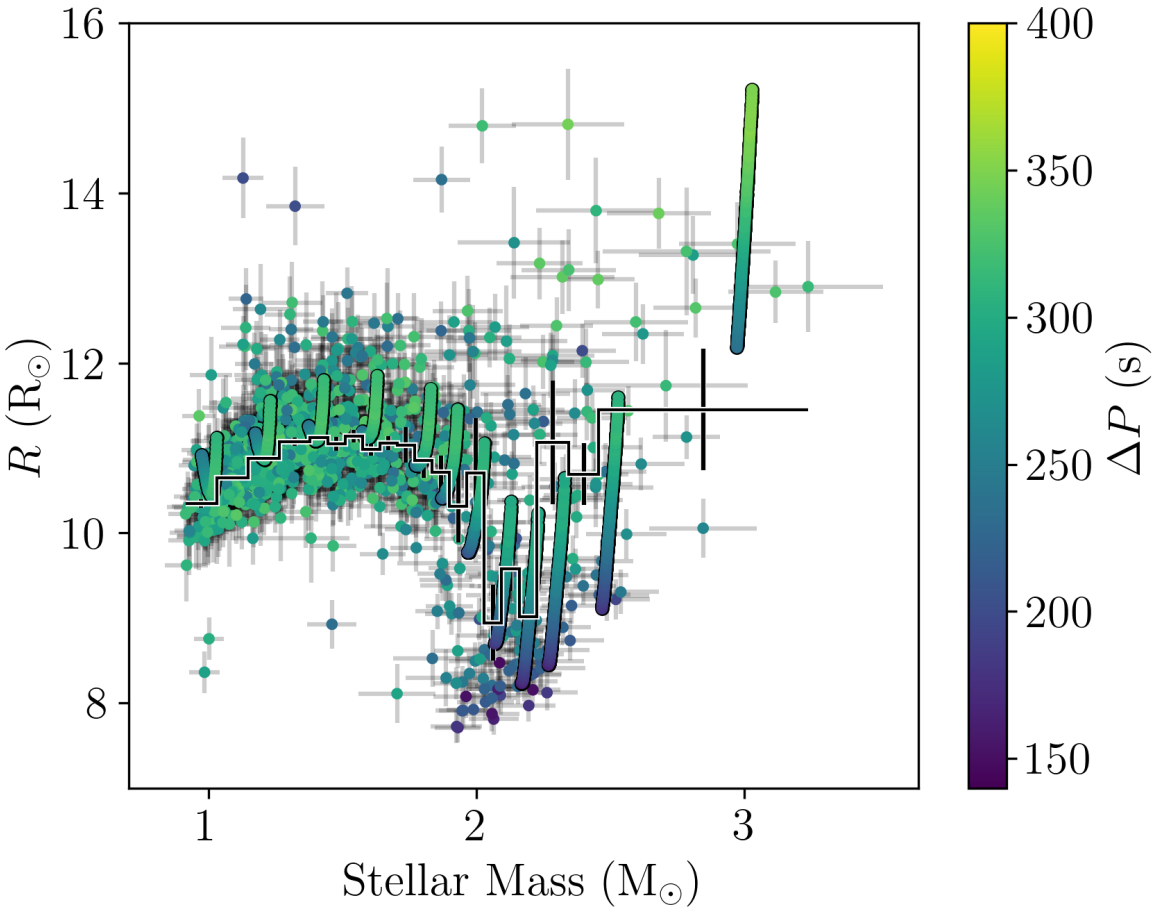

Figure 5.13: Radius as a function of mass of observations (small points) and our SSE models (vertical bars). ΔP is shown using the colour scale. The median radius in each mass bin is shown as a black line with a white outline. The uncertainty on the median is determined through bootstrapping. A small x-offset to each model in a track is applied so that they do not overlap themselves and evolve from left to right.

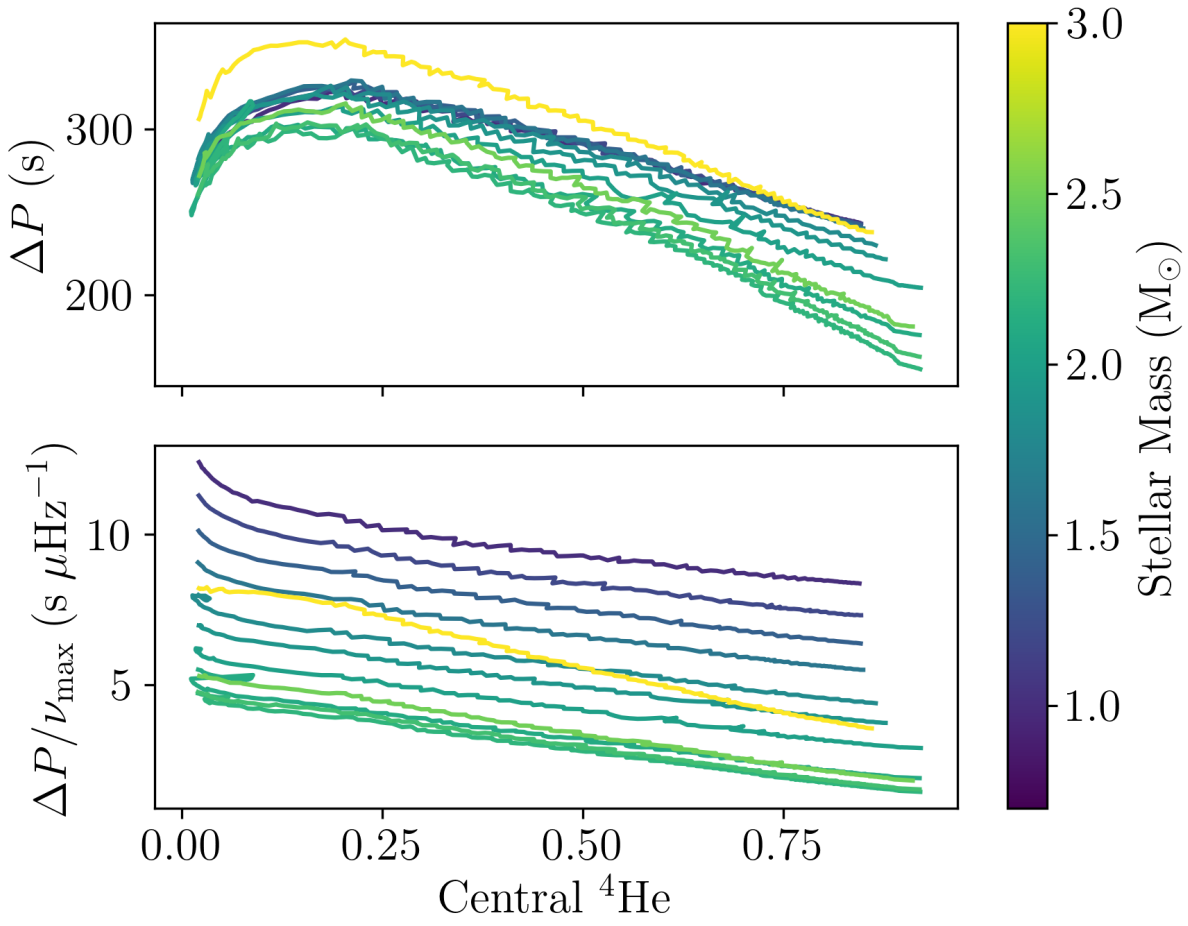

Figure 5.14: ΔP (top) and $\Delta P/\nu_{\rm max}$ (bottom) as a function of central-helium mass fraction $Y_{\rm C}$ of our modelled SSE stars. Stellar mass is shown using the colour scale.

5.14, which shows how ΔP reaches a maximum at $Y_{\rm C} \approx 0.1 - 0.2$ and shows that $\Delta P/\nu_{\rm max}$ is still increasing below this $Y_{\rm C}$.

To infer helium-core masses, we fit a quadratic to each track in the $\log_{10}(\Delta P/\nu_{\rm max})$-$\log_{10} M_{\rm He}$ plane. We then find the coefficients of the quadratic corresponding to a given mass by interpolating between the fitted coefficients. We do this for observed stars which lie within the region covered by the tracks in the M-$\Delta P/\nu_{\rm max}$ plane. This results in $M_{\rm He}$ for 810 RC stars out of the total 1029. Figure 5.15 shows $M_{\rm He}$ as a function of $\Delta P/\nu_{\rm max}$ of our modelled stars and inferred $M_{\rm He}$ of the

observations.

This technique to determine $M_{\rm He}$ is input-model dependent. Performing the same process using the grid of models with standard penetrative OS and selecting RC stars common in both sets of $M_{\rm He}$, gives differences in helium-core mass of up to 2.5%. However, selecting stars in common between the two excludes the high- and low-$\Delta P/\nu_{\rm max}$ stars at a given stellar mass as the range $\Delta P/\nu_{\rm max}$ takes is smaller due to the smaller range in ΔP.

5.3.3 Corrections to $\langle\Delta\nu\rangle$ using `gyre` for parametric stars

To accurately determine $\langle\Delta\nu\rangle$ for our parametric models, we perform the same correction to $\langle\Delta\nu\rangle$ described in Section 5.2.4. Figure 5.17 shows how the correction to $\langle\Delta\nu\rangle$ affects the parametric grids. The correction becomes large, almost 8%, in our models with the most massive helium cores and least massive envelopes. In these core helium-burning models, using only the scaling relation for $\langle\Delta\nu\rangle$ results in an underestimate of around 2–4% in $\langle\Delta\nu\rangle$ in our SSE models and up to 8% in our parametric models. This implies that when comparing the model seismic radius (Equation 5.14) to the model photospheric radius (Equation 5.16) or the model seismic mass (Equation 5.13) to the alternative model seismic mass (Equation 5.15) they would differ by up to 8% and 17%, respectively.

5.3.4 Inferred model mass and model radii

Section 5.2.5 showed that in our SSE models the inferred mass using Equation (5.13) and inferred radius using Equation (5.14) can differ by up to 6% and 3% respectively. Performing the same comparison on our parametric stars shows that this difference increases to up to 15% and 8% respectively. Figures 5.18 and 5.19 show the fractional difference in seismic mass and fractional difference in seismic radius as a function of model mass of our parametric models respectively. Our

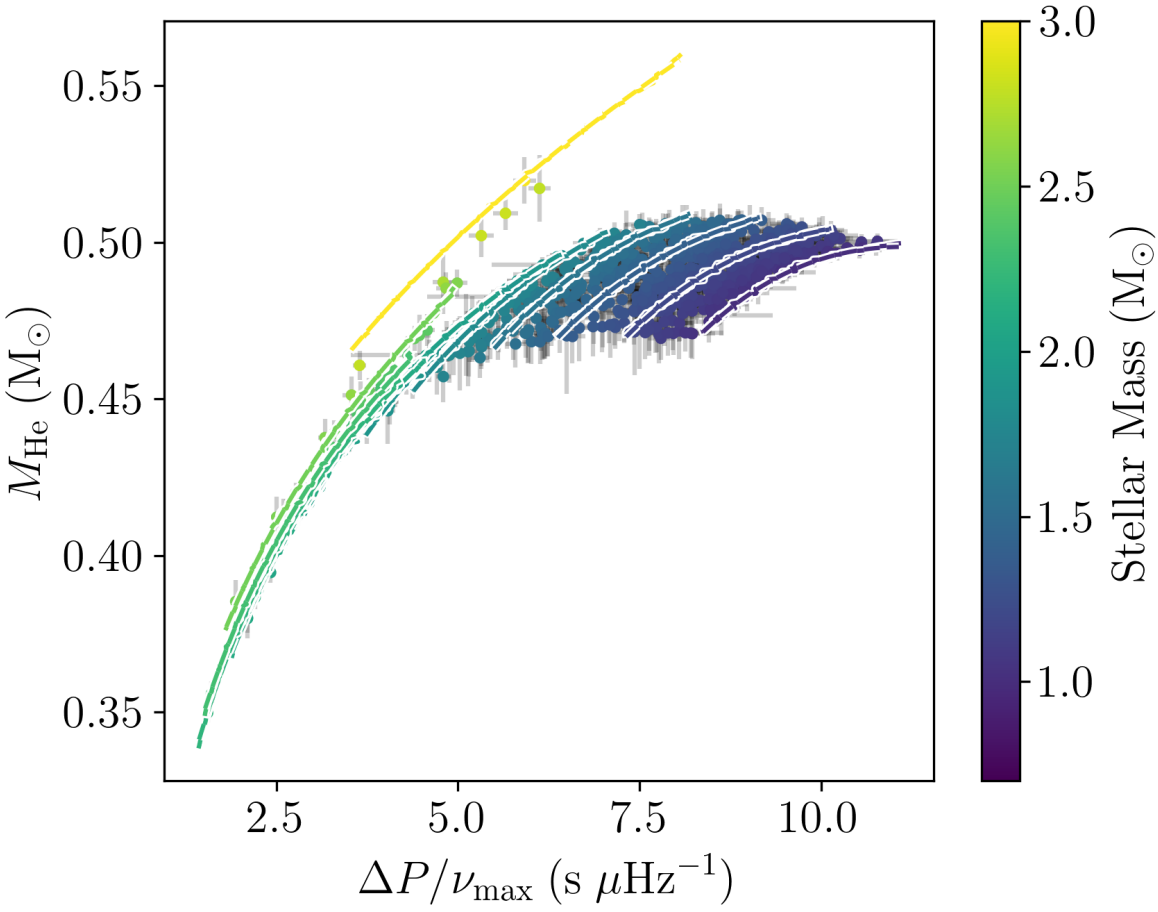

Figure 5.15: Helium-core mass $M_{\rm He}$ as a function of $\Delta P/\nu_{\rm max}$. Stellar mass is shown using the colour scale. Stars evolve up and towards the right. Model tracks are shown as lines and observations as dots.

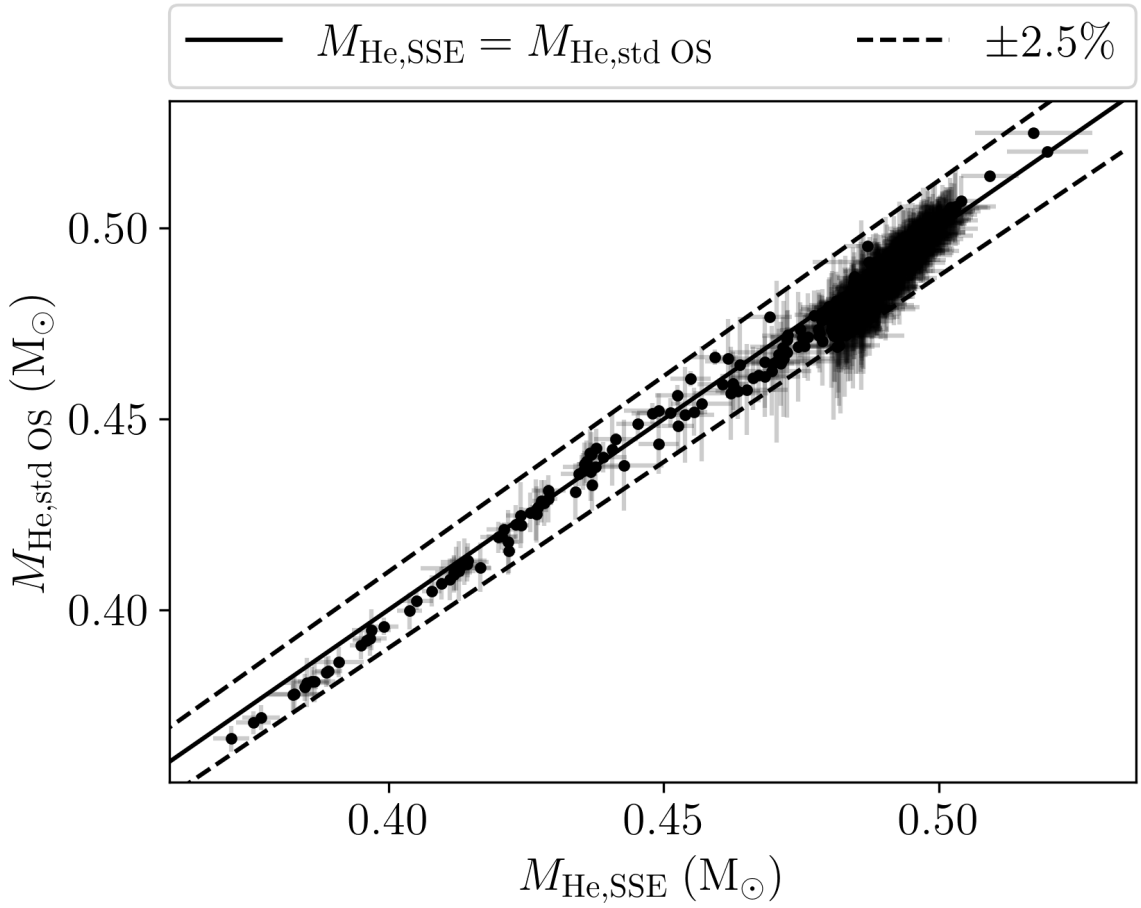

Figure 5.16: Helium-core masses using the best fitting SSE grid $M_{\rm He,SSE}$ against helium-core masses using the standard penetrative OS grid $M_{\rm He,stdOS}$ are shown as black dots. The solid black line shows $M_{\rm He,stdOS} = M_{\rm He,SSE}$, the dashed black lines show a ±2.5% difference between the two helium-core mass determinations.

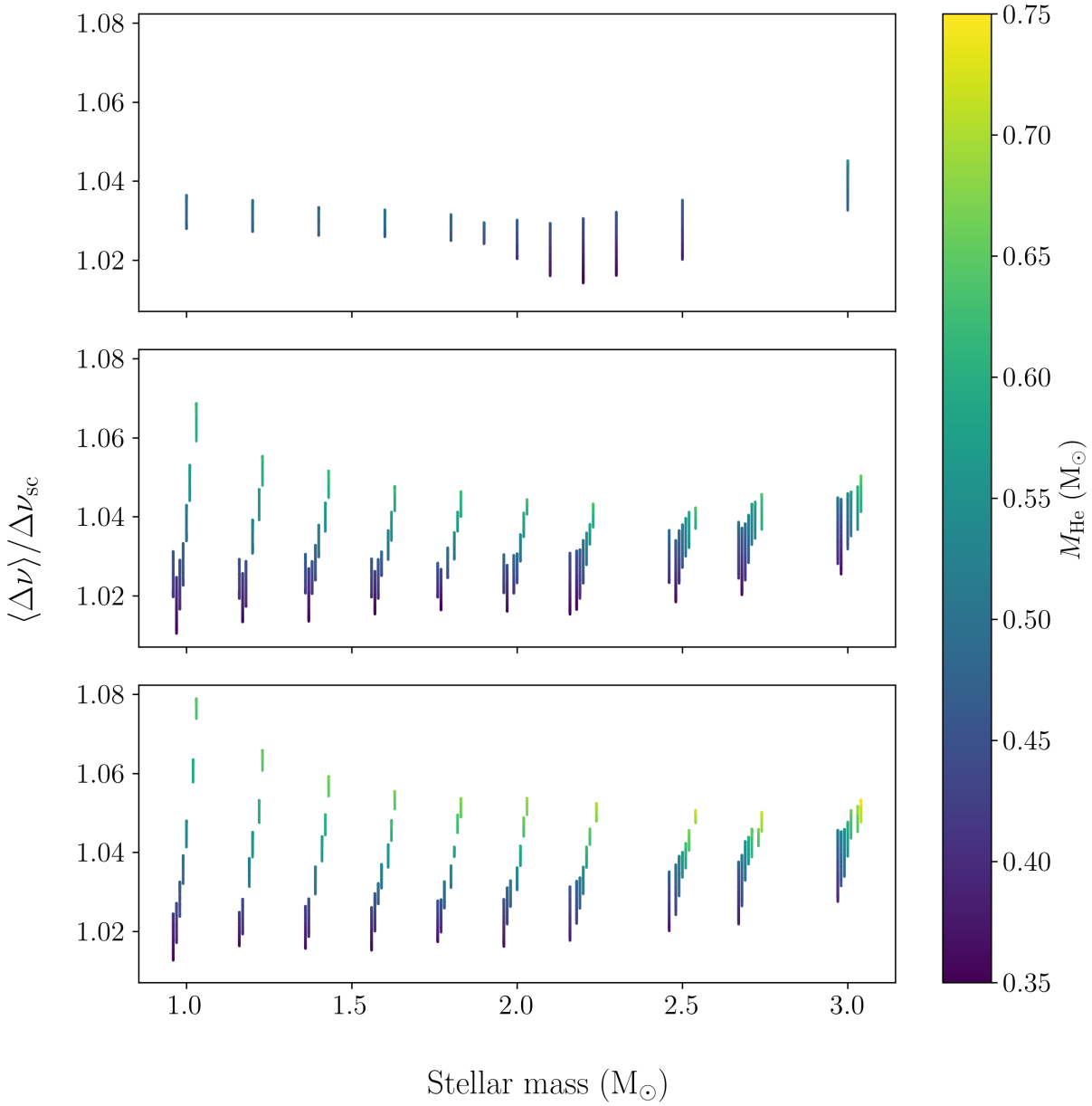

Figure 5.17: Correction factor of $\langle\Delta\nu\rangle$ for our $\alpha_{\rm mlt}$ =1.8 $f_{\rm ov,H}$ = 0.010 SSE models (top) and the narrow and wide parametric grids (middle and bottom). The helium-core mass $M_{\rm He}$ is shown using the colour scale. A small offset in the x-direction is applied to each parametric model track for clarity.

parametric models have fractional differences that are anti-correlated with their helium-core mass. Models with helium cores more massive than their corresponding SSE models have inferred masses and radii which are up to 15% and 10% smaller respectively in the low-mass cases, and around 5% smaller in both mass and radius in the higher mass cases. In the lower-mass models ($\lesssim 2$ M$_\odot$) with helium cores less massive than the corresponding SSE models, the inferred masses and radii are up to 8% and 4% too large, respectively. Therefore, even when including a correction factor like that in Miglio et al. (2012), Rodrigues et al. (2017), or Section 5.2.4, modelled stars with non-standard structures still result in incorrect inferred masses and radii when using Equations (5.13) and (5.14) for the mass and radius respectively. This implies that the masses and radii inferred for observed stars with non-standard structures are incorrect when using these equations.

5.3.5 Comparisons between SSE and parametric MT/MG models

In this subsection, we compare SSE and parametric MT/MG models. As we are interested in stars which have undergone non-standard evolution, we want to determine the difference in observables compared to SSE models. We use the same internal physics in both sets of models but we vary the initial helium-core mass and core-to-envelope transition width in our parametric models. The difference between the narrow and wide parametric models during CHeB is that the wide models have more massive helium cores for the same initial helium-core mass. By the time that the centre of the star has reached the conditions necessary for ignition, the hydrogen-burning shell has advanced enough to largely eliminate differences between the wide and narrow composition profiles.

We first look at the behaviour of helium-core masses of our parametric stars. Figure 5.20 shows model mass vs helium-core mass during core helium-burning. $M_{\rm He}$ in our narrow parametric models with initial $M_{\rm He} \geq 0.35$ M$_\odot$ increases by less than 0.013 M$_\odot$ before entering the RC phase. However, the parametric models with initial $M_{\rm He} = 0.30$ M$_\odot$ gain around 0.09–0.13 M$_\odot$, except for the 2.2 M$_\odot$ which gains 0.04 M$_\odot$. The initial structure of these parametric models is more

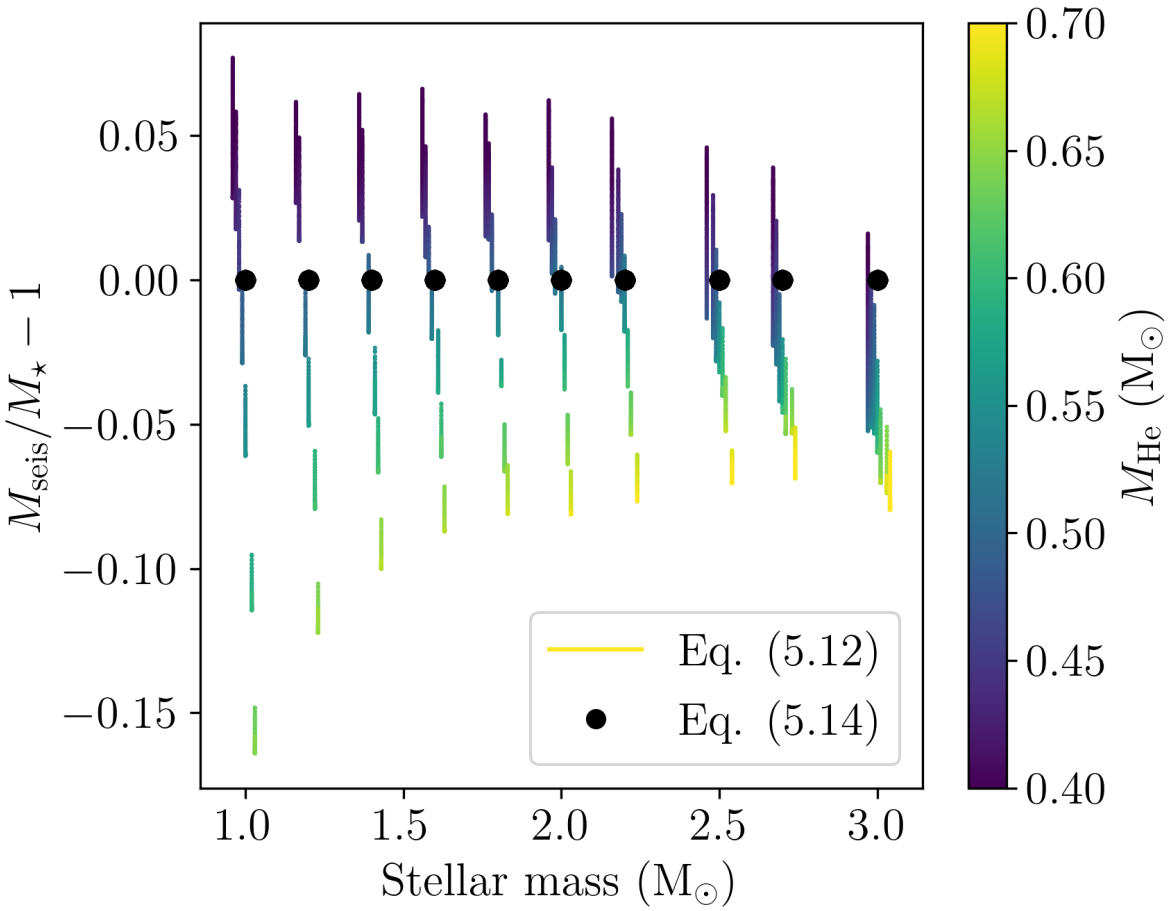

Figure 5.18: Fractional difference in seismic mass compared to model mass of our parametric models using Equation (5.15) is shown as coloured lines or Equation (5.13) as black dots. The helium-core mass $M_{\rm He}$ is shown using the colour scale. A small offset in the x-direction is applied to each model track for clarity. Differences when using Equation (5.15) cannot be seen at the scale of the plot.

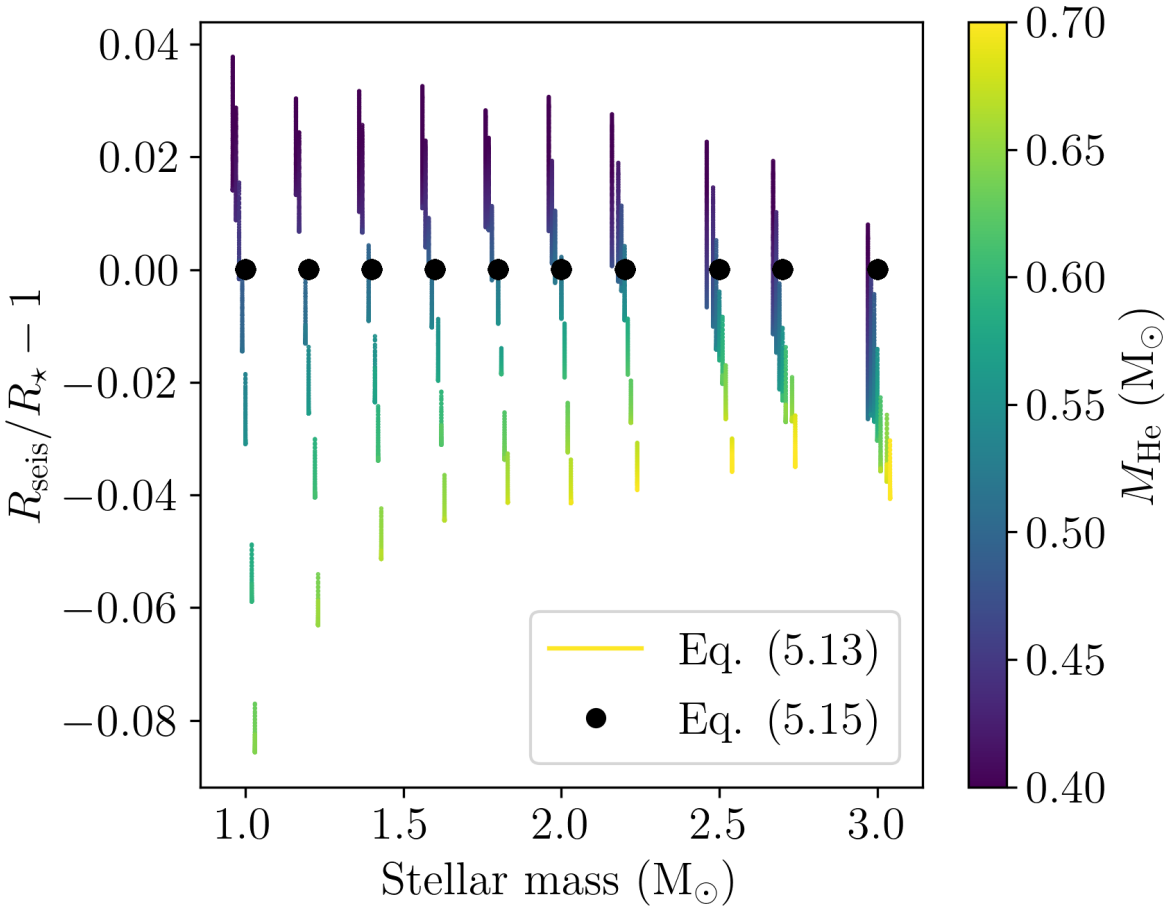

Figure 5.19: As Figure 5.18 but showing the fractional difference in radius using Equations (5.14) and (5.16). Differences when using Equation (5.16) cannot be seen at the scale of the plot.

RGB-like, with $M_{\rm He}$ not massive enough to start helium burning. This causes them to first ascend the RGB and grow their helium cores before ignition. Our wide parametric models have smaller increases in their core masses, increasing from 0.02 $M_\odot$ in the 1 $M_\odot$ models to 0.07 $M_\odot$ in the 3 $M_\odot$ models.

The behaviour of helium-core masses of the parametric MT/MG models is also seen in ΔP of these models. Figure 5.21 shows stellar mass vs. period spacing of our SSE and parametric grids. We see two different behaviours around the transition at approximately 2 $M_\odot$. Stars more massive than this threshold ignite helium in non-degenerate conditions, and therefore their helium-core masses are proportional to their total mass. Stars less massive than this threshold ignite helium in degenerate conditions with a constant helium-core mass independent of their total mass. Our single-star models cover the majority of observed stars, as shown in Figure 5.9. However, there are some stars which have period spacings which fall outside the range covered by our models; for example, the observations of stars with period spacing longer than approximately 350 s and those with period spacings of around 200 s with masses $M \lesssim 1.5$ $M_\odot$, as shown in the top panel of Figure 5.21. These high-ΔP stars, with $\Delta P \gtrsim 350$ s, are candidates for having had a binary interaction in their past, and the low-ΔP stars, with $\Delta P \lesssim 200$s, are stars which are most likely to be pre- or post-RC stars. Stars which have had binary interactions and also have period spacings in the range covered by single stellar models require an additional method to differentiate them from their single stellar evolution counterparts. Both narrow and wide parametric model grids have minimum and maximum period spacings which span almost the whole range of observed ΔP. However, in both cases, stars with $\Delta P \lesssim 200$s in the transition regime with masses 1.8 $M_\odot \lesssim M \lesssim 2.2$ $M_\odot$ are not covered by our parametric models. This is because these stars are most likely pre- or post-RC stars.

The HRDs shown in Figure 5.22, show that our SSE models follow the behaviour of observations. Observed stars with $T_{\rm eff}$ higher than around 5000 K have lower [Fe/H] than our models and therefore it is not unexpected that our models do not reach these temperatures. This is shown

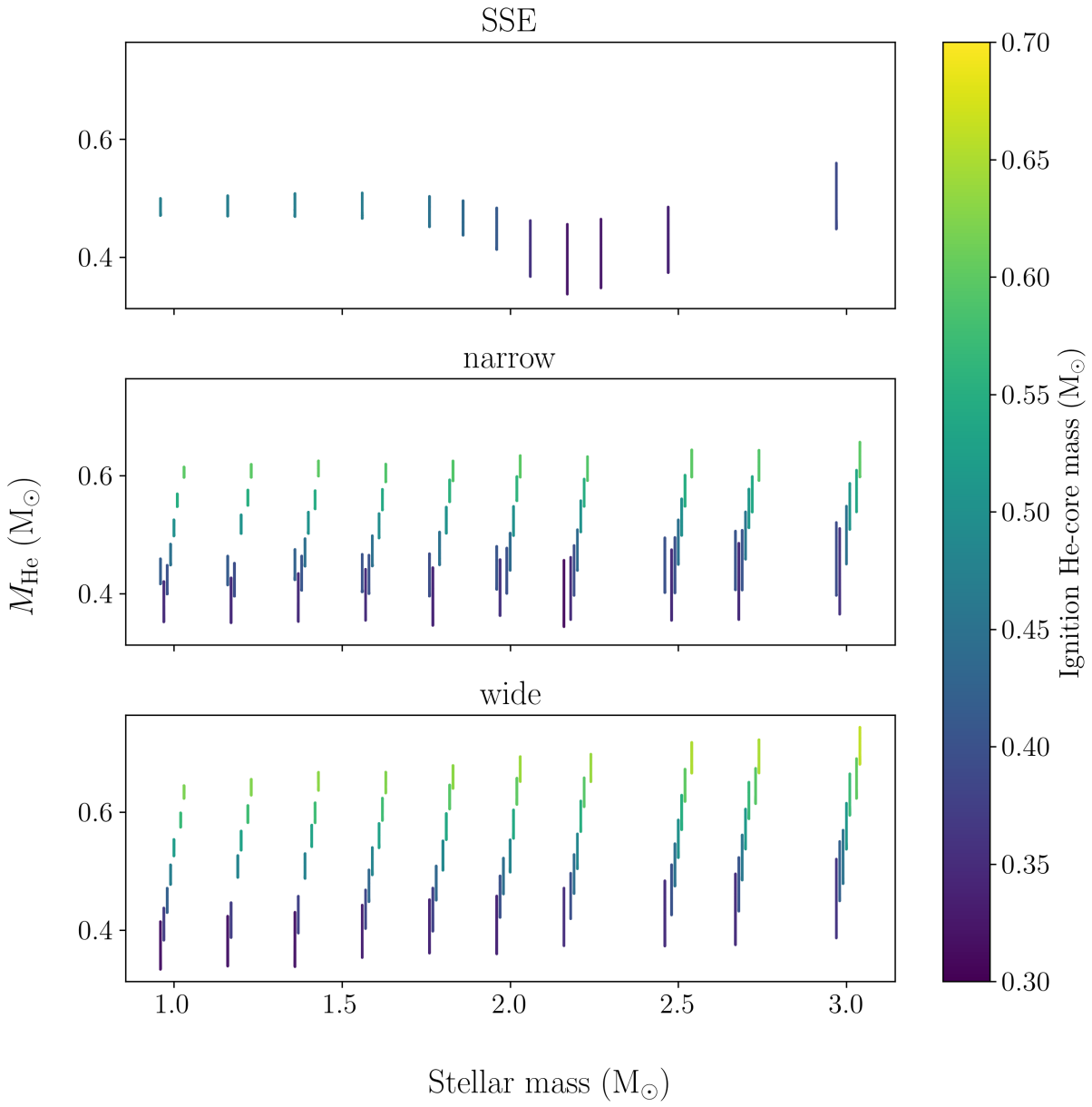

Figure 5.20: Helium-core mass as a function of stellar mass. The core mass at which helium starts to burn quiescently is shown on the colour scale. A small offset in the x-direction is applied to each model track for the narrow and wide parametric grids.

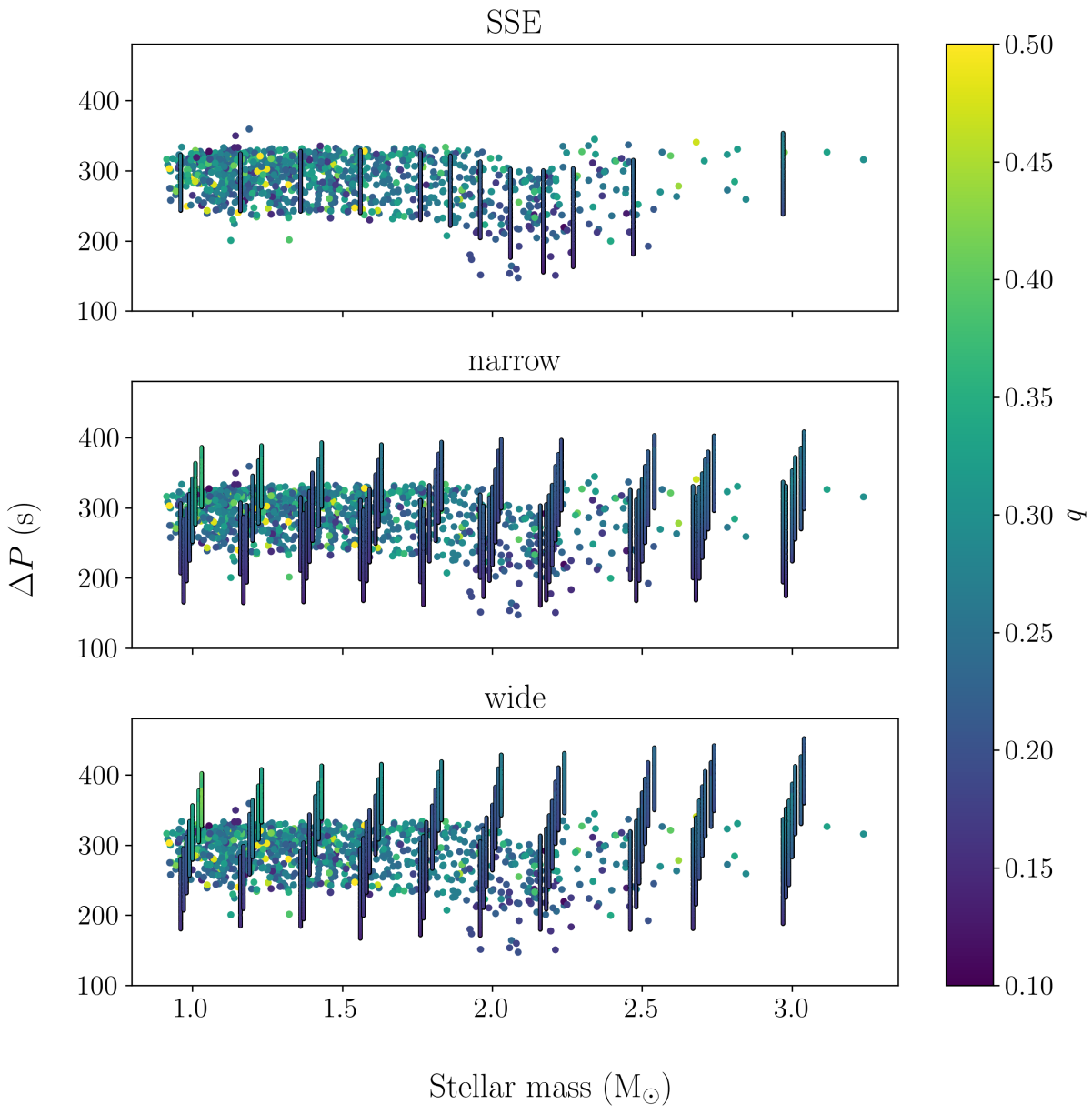

Figure 5.21: Observed and modelled period spacing as a function of stellar mass. SSE models are shown in the top panel and the parametric models in the bottom two panels. Observations are shown as coloured dots. Our models are shown as coloured vertical bars. The coupling is shown as the colour scale. A small offset in the x-direction is applied to each model track for the narrow and wide parametric grids.

in Figure 5.10, where only a limited number of stars are observed with $T_{\rm eff} > 5000$ K and they are all more metal-poor than our models. Similarly, stars with $T_{\rm eff} < 4600$ K are more metal-rich than our models. Our parametric models span a large range in luminosity from 25–250 $L_\odot$, reflecting the large range in helium-core masses, as shown in the bottom two panels. Models with initial helium-core masses of 0.6 $M_\odot$ have helium cores which are more massive than their SSE counterparts, as seen in Figure 5.20. This results in the helium-core luminosity being brighter, as $L_{\rm He} \propto M_{\rm He}^4$ (e.g. Salaris & Cassisi 2005).

Density contrast is a crucial parameter in determining the strength of mixed-mode coupling. Figure 5.23 shows density contrast, $\rho_{\rm CZ}/\rho_{\rm He}$, as a function of stellar mass. In our SSE models, there is a clear distinction in the behaviour of $\rho_{\rm CZ}/\rho_{\rm He}$ above and below the transition mass of $M \approx 2.1$ $M_\odot$ (e.g. Figure 5.9 also shows the transition mass). Below it $\rho_{\rm CZ}/\rho_{\rm He}$ increases with increasing mass, whilst above it $\rho_{\rm CZ}/\rho_{\rm He}$ decreases with increasing mass. The $\rho_{\rm CZ}/\rho_{\rm He}$ increase is due to the mass of the hydrogen envelope increases and the helium-core mass and stellar radius remain constant (Figures 5.20 and 5.13). This increases $\rho_{\rm CZ}$ whilst keeping $\rho_{\rm He}$ approximately constant. Similarly, in more massive stars $\rho_{\rm He}$ remains approximately constant (within a factor $\sim$ 2), but $\rho_{\rm CZ}$ decreases with increasing mass as the stellar radius is no longer constant with increasing mass (Figure 5.13). In our parametric models this is still the case, as stellar radius is a function of helium-core mass. Our wide parametric models reach stronger $\rho_{\rm CZ}/\rho_{\rm He}$ compared with our narrow parametric models as the wide parametric models have more massive helium cores.

Figure 5.24 shows q as a function of $\rho_{\rm CZ}/\rho_{\rm He}$ in our SSE models in the top panel and parametric models in the middle and bottom panels. Individual tracks with helium-core mass fraction $f_{\rm He} \lesssim 0.2$ $M_\odot$ have q and $\rho_{\rm CZ}/\rho_{\rm He}$ which are anti-correlated, and correlated when $f_{\rm He} \gtrsim 0.2$. When looking at all models together, q and $\rho_{\rm CZ}/\rho_{\rm He}$ are anti-correlated. In stars with masses below 1.8 $M_\odot$, these evolutionary effects indicate that q is correlated with $\rho_{\rm CZ}/\rho_{\rm He}$ as a given star evolves, whilst in stars with masses above the transition mass q is anti-correlated with $\rho_{\rm CZ}/\rho_{\rm He}$. Therefore, it is possible to use q to probe $\rho_{\rm CZ}/\rho_{\rm He}$. Our parametric models reach a stronger $\rho_{\rm CZ}/\rho_{\rm He}$ of around

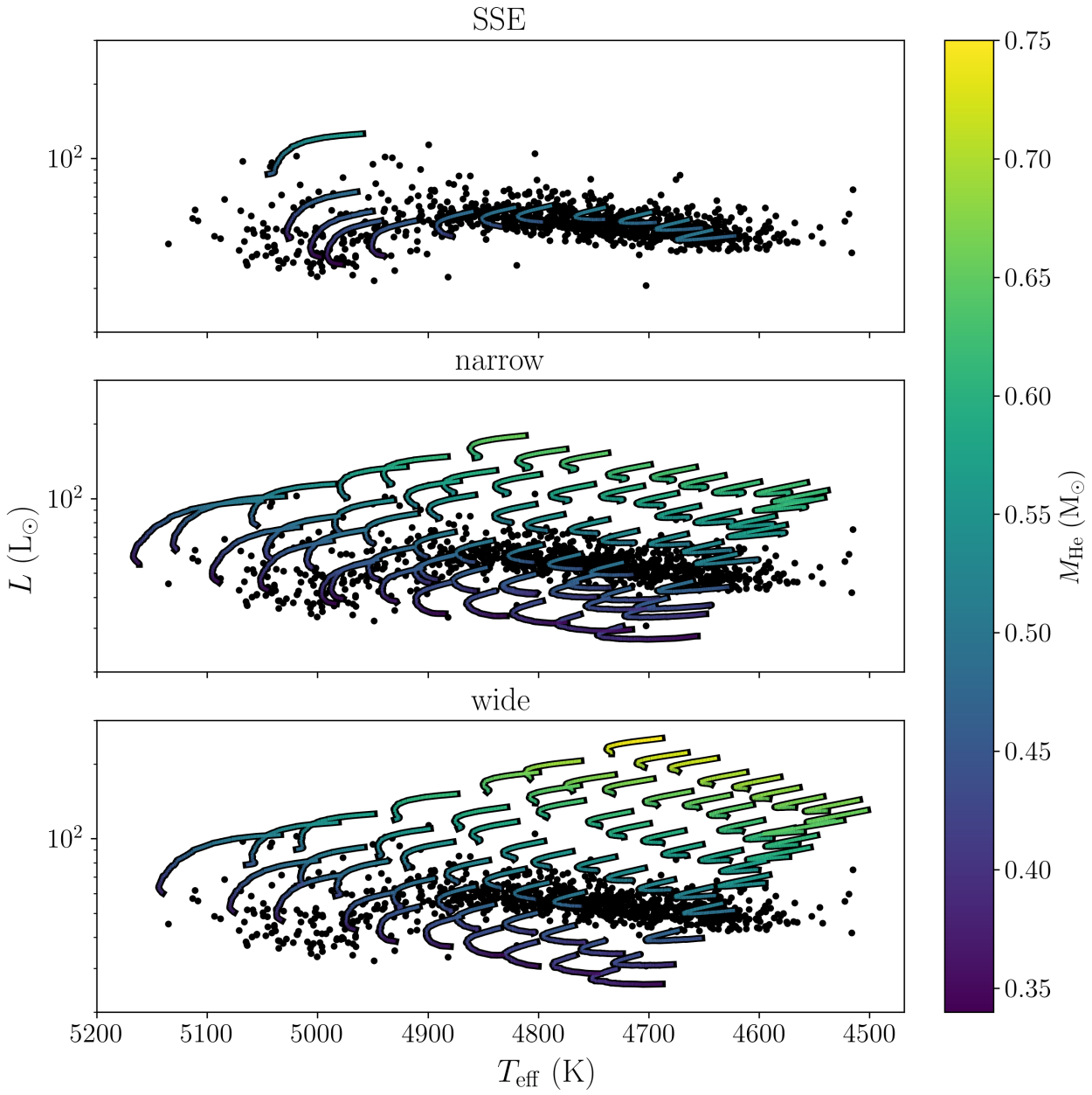

Figure 5.22: Tracks in the HRD of our SSE (top panel) and narrow and wide parametric stars (middle and bottom panels). The small black dots show the observations. The modelled tracks are shown as the coloured tracks. The helium-core mass of the models is shown using the colour scale.

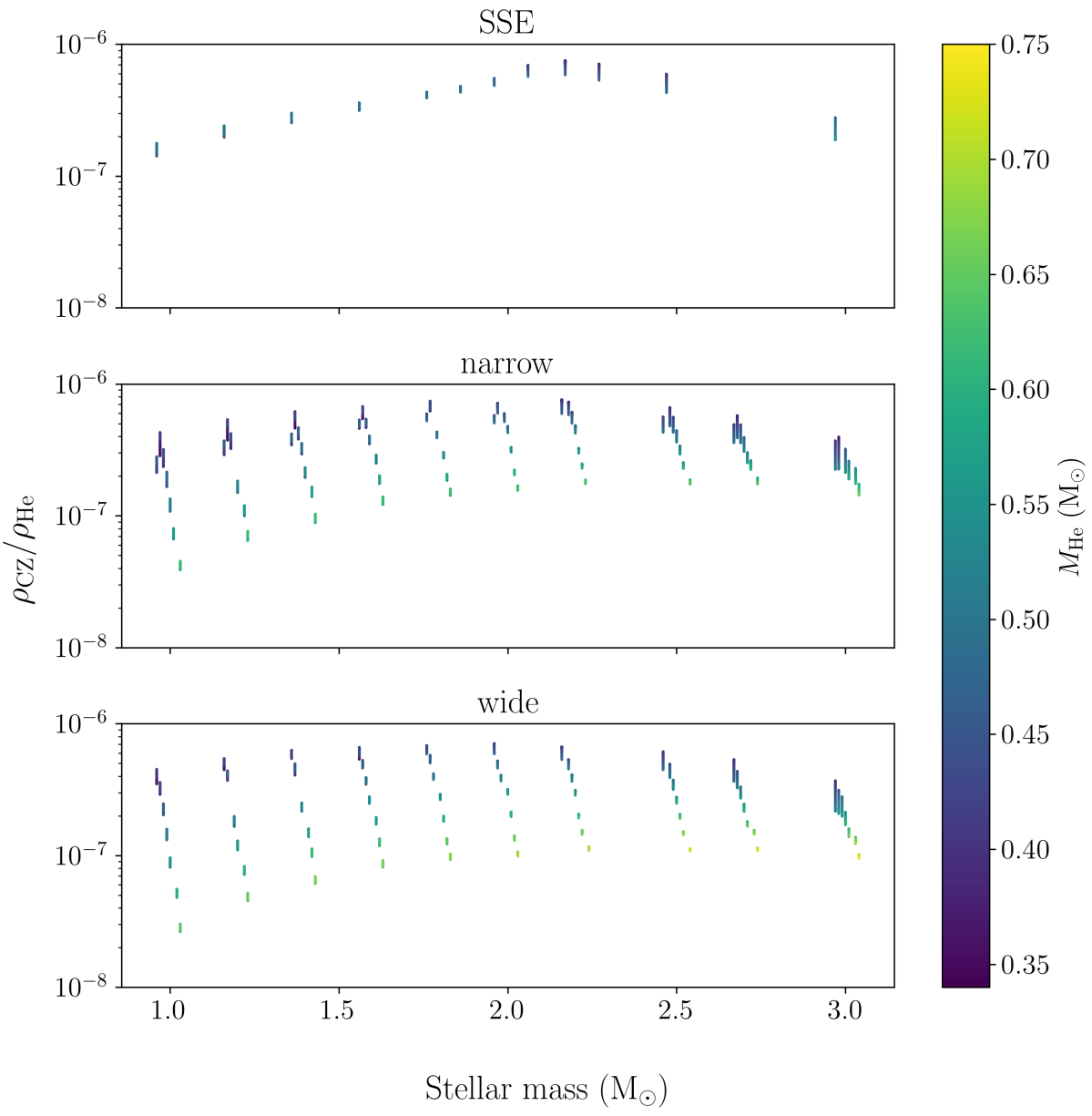

Figure 5.23: Density contrast ρ_{CZ}/ρ_{He} as a function of stellar mass. SSE models are shown in the top panel. The narrow and wide parametric models are shown in the bottom two panels. The tracks the modelled stars take are shown as the coloured lines. The helium-core mass is shown as the colour scale. A small offset in the x-direction is applied to each model track for the narrow and wide parametric grids.

3×10^{-8} than the SSE models due to their more massive helium cores. This is because of their higher helium-core mass fraction $f_{\rm He}$ of up to 0.65 that is reached in our parametric models. Therefore, observed stars with strong coupling fall outside the regime covered by SSE models and thus make good candidates for stars which have undergone non-standard evolution.

Figure 5.25 shows coupling coefficient as a function of stellar mass. In our SSE models coupling is underestimated when compared to observational data. Part of this is due to the range in [Fe/H] used, as q is dependent on metallicity (as discussed in Section 4.3.3). However, this only accounts for part of this discrepancy. Our parametric models with masses $M < 1.8$ M$_\odot$ and helium cores more massive than their SSE counterparts have coupling coefficients which are 30–80% larger than their SSE counterparts. Parametric models with masses $M \geq 1.8$ M$_\odot$ or initial helium-core masses less than or equal to their SSE counterparts, have coupling coefficients within 10% of the SSE models. Exception are the 1 M$_\odot$ parametric models with initial helium-core masses of 0.3 and 0.35 M$_\odot$ which have coupling coefficients 20-25% smaller. However, this spread cannot be explained solely by the changes in the density contrast. Figure 5.23 shows that in models with masses greater than 1.8 M$_\odot$ there is a spread in density contrast whilst the coupling takes on a narrow range of values which follow SSE models. Therefore, coupling is more useful to identify lower-mass stars with small hydrogen envelopes (e.g. Matteuzzi et al. 2023).

Using the correlation between ΔP and $M_{\rm He}$, we make an estimate of the minimum-$M_{\rm He}$ that is possible at a given ΔP. Figure 5.26 shows tracks of the helium-core mass as a function of ΔP in our modelled SSE and parametric stars. We fit a quadratic to $M_{\rm He}$ at the maximum-ΔP of each modelled star. This gives us a relation which puts a lower limit on the helium-core mass for stars with $\Delta P \gtrsim 280$ s. This results in the following equation for the minimum helium-core mass:

$$\frac{M_{\rm He,min}}{\rm M_\odot} = 8.8357\times10^{-7}\left(\frac{\Delta P}{\rm s}\right)^2 + 1.2023\times10^{-3}\left(\frac{\Delta P}{\rm s}\right) - 3.5264\times10^{-3}. \tag{5.18}$$

There are two stars with an anomalously high minimum $M_{\rm He}$ for their inferred mass, namely KIC4275220 and KIC6047033. These stars are the two observations with $\Delta P \gtrsim 350$ s in Figures

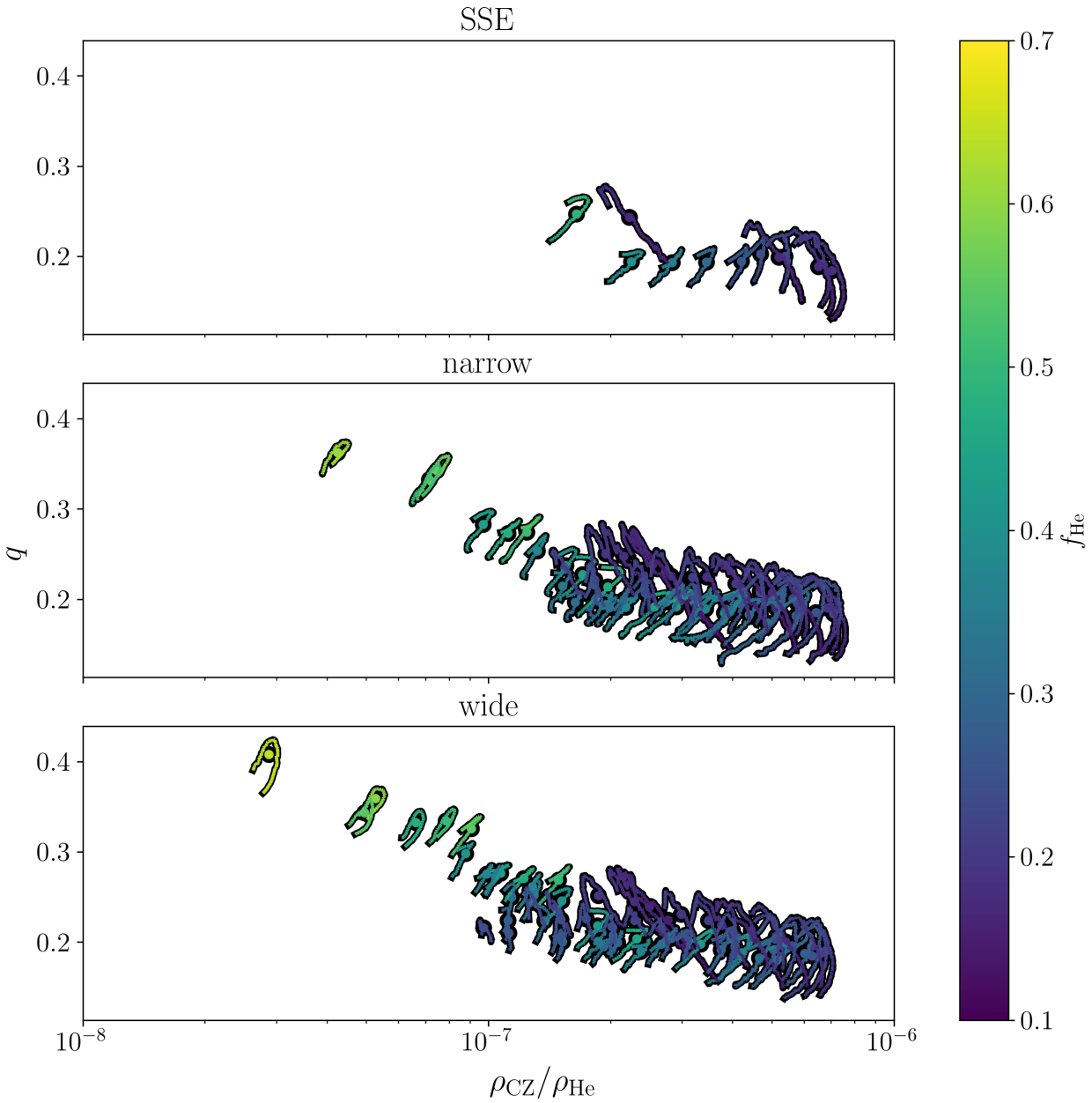

Figure 5.24: Coupling q as a function of density contrast ρ_{CZ}/ρ_{He}. SSE models are shown in the top panel, and the narrow and wide parametric models are shown in the bottom two panels. The tracks the modelled stars take are shown as the coloured lines, median q and ρ_{CZ}/ρ_{He} as shown as coloured dots. The helium-core mass fraction $f_{He} = M_{He}/M$ is shown as the colour scale.

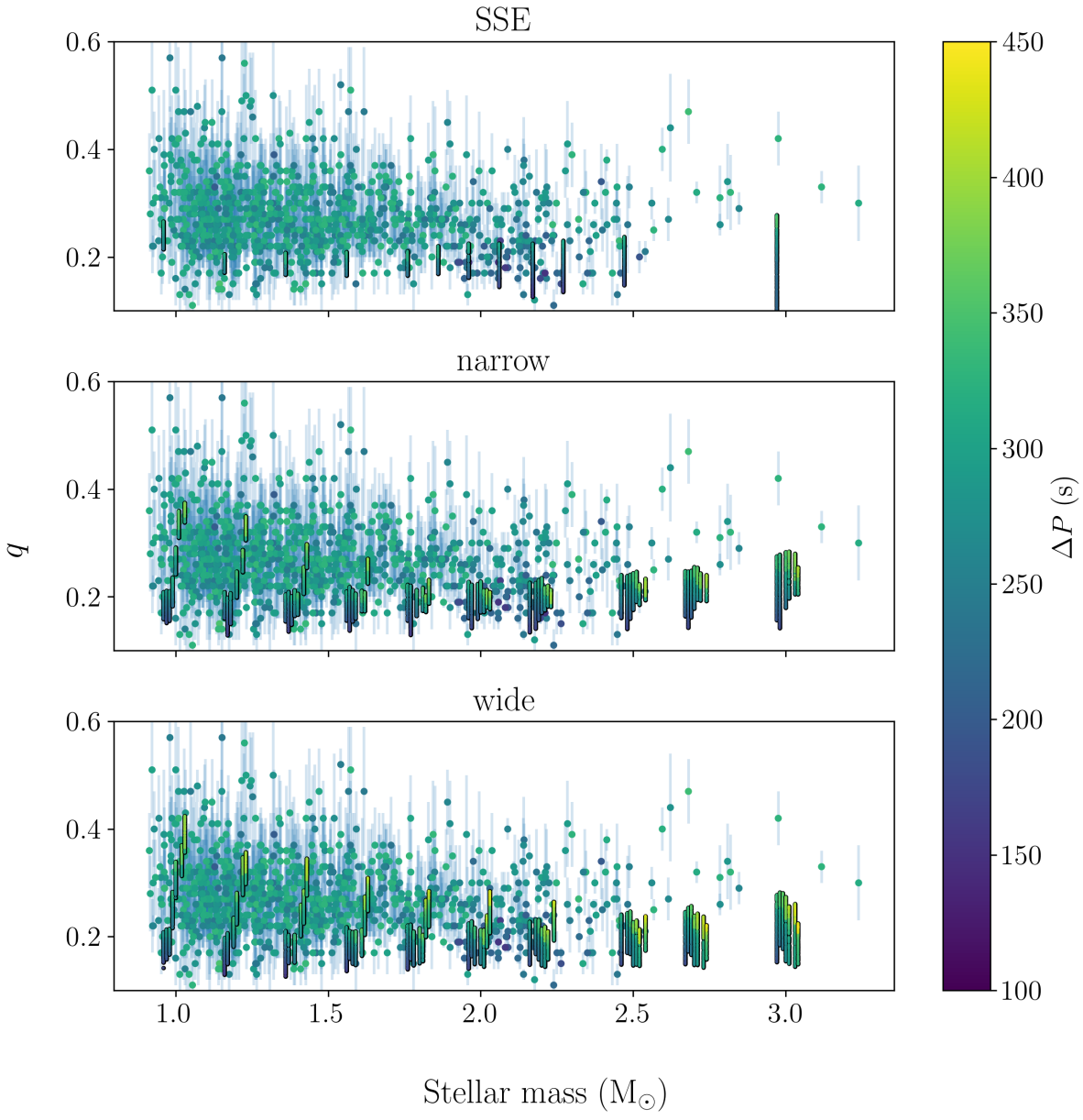

Figure 5.25: Coupling q as a function of stellar mass. SSE models are shown in the top panel and the narrow and wide parametric models are shown in the middle and bottom panels. Modelled stars are shown as vertical coloured bars. Observations are shown as the coloured dots. ΔP is shown using the colour scale. A small offset in the x-direction is applied to each model track for the narrow and wide parametric grids.

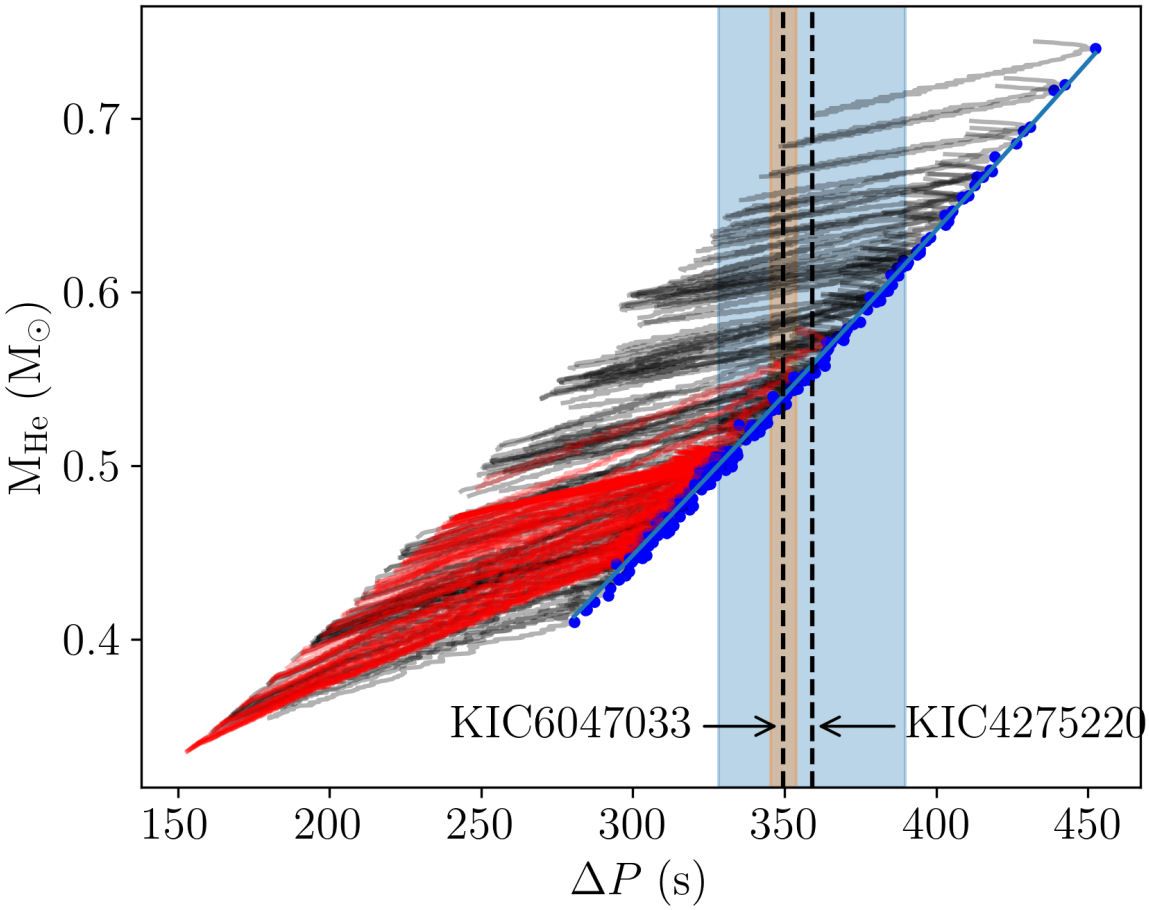

Figure 5.26: Helium-core mass as a function of period spacing for both SSE and parametric grids. Red lines show SSE models and grey lines show the parametric models. The blue points along the right edge show the maximum ΔP of each modelled star. The orange line is the quadratic fit to the maximum ΔP of each modelled star. ΔP of KIC4275220 and KIC6047033 are shown as vertical black dashed lines, the 1-σ errors of these two stars are shown as the blue and orange shaded regions respectively.

Table 5.9: Properties of stars with minimum $M_{\rm He}$ above the maximum $M_{\rm He}$ of a modelled SSE star with a similar mass. The model $M_{\rm He}$ is denoted by a *.

KIC	M ($M_\odot$)	σ_M ($M_\odot$)	[Fe/H]	ΔP (s)	$\sigma_{\Delta P}$ (s)	min $M_{\rm He}$ ($M_\odot$)	$\sigma_{\min M_{\rm He}}$ ($M_\odot$)
4275220	1.19	0.11	-0.03	359.1	30.70	0.542	0.057
6047033	1.14	0.06	-0.01	349.6	4.24	0.525	0.008
Model	1.20		0.06	335.2		0.498	0.501*

5.9. Table 5.9 shows the properties of these two stars. All our SSE models with $M = 1.2$ $M_\odot$ have maximum $M_{\rm He} \simeq 0.502$ $M_\odot$ at their maximum ΔP between 333–338s. The 1.2 $M_\odot$ SSE model included in Table 5.9 uses the same input physics as the parametric models. Our SSE models with total masses similar to KIC4275220 (1.19 ± 0.11 $M_\odot$) and KIC6047033 ($1.14 \pm 0.06 M_\odot$) are unable to reach the high minimum helium-core mass that these two observed stars have, as shown in Figure 5.9. However, they do fall within the range of ΔP of our parametric stars with helium cores more massive than those of SSE stars with the same mass.

5.4 Conclusion

We constructed parametric models using `MESA` which approximate mass transfer or merger models by varying the initial helium-core mass. This allowed us to study the effect that the helium core has on $\langle \Delta\nu \rangle$, ΔP, $T_{\rm eff}$, and $\nu_{\rm max}$. Our conclusions are:

- In SSE models, $\langle \Delta\nu \rangle$ derived from the scaling relations, $\Delta\nu_{\rm sc}$, in the RC is typically 2–5% smaller than that determined through the stellar oscillation code `gyre`, $\langle \Delta\nu_{\texttt{gyre}} \rangle$. In our parametric models, this difference is up to 8%. The correction factor applied to $\Delta\nu_{\rm sc}$ is smallest early on in the RC and grows as helium is depleted in the core. We also find that the correction factor is correlated to helium-core mass. This has direct implications for mass

estimates of stars with over-massive helium-cores. Mass estimates based on $\langle\Delta\nu\rangle$ of these stars can be up to 15% too low for stars with oversized helium cores, around 3% too massive for single stars below the transition mass, and up to 5% too massive for more massive stars.

- When using only the seismic scaling relations (Equations 5.14 and 5.13), inferred masses and radii for modelled stars with non-standard evolution can differ by up to 15% in mass and 10% in radius, and up to 7% in mass and 4% in radius for modelled SSE stars. Including luminosity in the scaling relations for mass and radius (Equations 5.15 and 5.16) should remove this bias, as these equations are assumed be largely insensitive to different internal structure and depend on surface properties only.

- For the ΔP of our models to span the observed range, we modify the penetrative overshooting prescription described in Bossini et al. (2017) by increasing $\alpha_{\rm OV,He}$ from 0 to 0.85 as helium is consumed in the core.

- We introduce a method with which we infer helium-core masses of 810 RC stars with masses between 1 $M_\odot$ and 3 $M_\odot$ by using $\Delta P/\nu_{\rm max}$ and interpolating between our fits to model tracks in $M_{\rm He}$-$\Delta P/\nu_{\rm max}$. This allows us to determine helium-core masses in stars below $Y_{\rm C} \lesssim 0.2$, which have reached their maximum ΔP.

- Our parametric models cover a wide range of helium-core mass and total mass. Once our models are undergoing core helium burning, the difference between the narrow and wide initial composition profiles is only in the total helium-core mass. This difference in helium-core mass is due to hydrogen-shell burning, which advances and removes the different initial composition profiles. Therefore, it is no longer possible to distinguish whether a given helium core had a narrow or wide initial helium composition profile.

- Our parametric models with total masses outside the transition mass ($M \lesssim 1.8$ $M_\odot$ and $M \gtrsim 2.2$ $M_\odot$) cover the range of observed ΔP. Within this range the parametric models are unable to form helium cores with masses below approximately 0.35 $M_\odot$ whilst in the RC

phase. Our SSE models are able to do so as they ignite helium under degenerate conditions in a flash which initiates closer to the centre until there is a single helium flash which becomes the convective core for the 2.1 $M_\odot$ case. Our parametric models work well for helium-core masses above approximately 0.35 $M_\odot$, but are not well suited to simulate helium cores smaller than this as they first ascend the RGB before igniting helium.

- Our parametric models span a large range in ρ_{CZ}/ρ_{He} for each total mass with the spread being larger in lower-mass stars, and a maximum in ρ_{CZ}/ρ_{He} around the transition mass. Larger helium-core masses result in a stronger contrast.

- Coupling is anti-correlated with ρ_{CZ}/ρ_{He}. In stars with masses below the transition mass, q is also anti-correlated with ρ_{CZ}/ρ_{He} during the evolution of an individual model. In the more massive stars q is correlated with ρ_{CZ}/ρ_{He} as the star evolves.

- Coupling in parametric models with masses below the transition mass increases with increasing helium-core mass and decreases with increasing total mass. For masses above the transition mass, larger helium cores increase q to a much lesser degree and q instead increases with increasing mass. Therefore, we expect stars with large helium-core mass fractions to have stronger coupling the lower their total mass is.

- Period spacing is strongly correlated with helium-core mass in our grid of models. The maximum ΔP reached for all models has a sharp boundary, well described by a quadratic, which allows for a minimum helium-core mass at a given ΔP to be found.

- We find two stars, KIC4275220 and KIC6047033 which have minimum helium-core masses that exceed the corresponding SSE model. It is possible that these stars have undergone mass transfer or a merger in their past. However, in KIC4275220 the minimum helium-core mass is still consistent with SSE due to the large error on ΔP. KIC6047033 is a good candidate for further in-depth study to determine its interior structure. Further investigation into stars such as these may help in constraining mass transfer and merger processes.

Chapter Six

Conclusion

Modelling stellar evolution in such a way that all key governing parameters are realistically represented with all the inherent complexity, remains a challenge. Mixed modes enable information about the near-core region of stars to be brought to the surface. In this thesis mixed-mode coupling has been modelled in detail. Modes take on a pressure-mode like characteristic in the outer layers of a star and a gravity-mode like characteristic in the central layers of a star. This work focused on studying the information carried by mixed modes in stars about their cores, and the results are intended to provide a better understanding of mixed-mode coupling in stars undergoing core helium-burning. This work also contributes to the interpretation of mixed-mode coupling of giant stars. The main conclusions from this thesis are:

- Mixed-mode coupling depends directly on mass and metallicity in the RC and RGB. We interpret this behaviour as the effect that mass and metallicity have on the density contrast between the core and envelope, and therefore on the depth of the convective envelope. As a consequence, the depth of the convective envelope determines the location and size of the evanescent zone. Additionally, Figures 4.22, 4.23, and 4.24 show that metallicity and coupling anti-correlate in both the RGB and the RC. The dependence of coupling on mass is illustrated by coupling decreasing in low-mass models and increasing in high-mass models

as mass increases.

- Our model-predicted trends for q as a function of [Fe/H] (Figures 4.22, 4.23, and 4.24) agree with the observed data, and show that there is a strong dependence of q on metallicity in both RC and RGB stars. In RC stars with masses below 1.8 $M_\odot$, $q = -0.093^{+0.011}_{-0.011}[\mathrm{Fe/H}] + 0.281^{+0.002}_{-0.002} + \mathcal{N}(0, 3.33^{+0.22}_{-0.22} \times 10^{-3})$. In RC stars with masses above 1.8 $M_\odot$, $q = -0.083^{+0.030}_{-0.029}[\mathrm{Fe/H}] + 0.257^{+0.005}_{-0.004} + \mathcal{N}(0, 2.80^{+0.34}_{-0.34} \times 10^{-3})$. Whilst in RGB stars $q = -0.019^{+0.005}_{-0.005}[\mathrm{Fe/H}] + 0.122^{+0.001}_{-0.001} + \mathcal{N}(0, 4.38^{+0.40}_{-0.41} \times 10^{-4})$. It should be borne in mind that the measured global q we are comparing with may suffer from systematic effects. For instance, there may be glitches, which are relatively rapid changes in the structure of a star compared to the local mode wavelength. These glitches may affect the determination of mean period spacings, which in turn affects the coupling coefficients (Vrard et al. 2016; Mosser et al. 2017). Additionally, there is some ambiguity about what value q has in the transition regime between the strong- and weak-coupling regimes.

- This work shows the coupling coefficient to be frequency dependent in both the RGB and RC, extending the work of Jiang et al. (2020) in the RGB. The dependence of q on the mode frequency could be a source of error when determining the observed coupling. The frequency dependence of the coupling coefficient is particularly strong in the RGB (panels A and B in Figure 4.9). Within one $\Delta\nu$ frequency interval, there can be a difference of between 10–20% in q. Consequently, this variation of q due to different ν_q should be taken into account when determining q from observations, and when comparing observed q to model predictions.

- The dependence of the coupling coefficient on frequency provides the possibility of detailed mapping of the evanescent zone. This work provides a possible avenue to measure undershooting through the spread in $\langle \mathrm{d}q/\,\mathrm{d}\nu_q \rangle$ in the RGB. Larger undershooting reduces the size of the $\tilde{N}$ spike causing it to widen and become lower in amplitude, thus reducing the spread in $\langle \mathrm{d}q/\,\mathrm{d}\nu_q \rangle$.

- An additional approximation is introduced to calculate the coupling which includes the fact that the Brunt-Väisälä and Lamb frequencies are not parallel and do not follow the same power-law. This approximation works well in type-a evanescent zones, and extends the work by Takata (2016a) and Pinçon et al. (2019).

- The determined minimum coupling coefficients in the data set are approximately 0.05. It is not clear if this minimum is intrinsic to observed stars or whether this is an artefact caused by the limitations of the method used to obtain coupling from observations. Our models show that coupling coefficients of less than 0.05 are possible but that limitations in the method for determining q make it too difficult to determine such small coupling coefficients from observations.

Following the ground work described in Chapter 4, it is possible to apply this approach to models with non-standard internal structures. This is done by creating parametric models with various initial helium-core masses and total masses which approximate stars which have undergone mass transfer or a merger. These parametric models are constructed using the detailed stellar evolution code `MESA`. Based on this approximation it is possible to study the effect of the helium core on various observational parameters such as period spacing, luminosity and coupling. The key conclusions that can be drawn are:

- There is a substantial difference between $\langle \Delta\nu \rangle$ when using the scaling relations or when using `gyre` for both the SSE and parametric models. In SSE models, $\langle \Delta\nu \rangle$ derived from the scaling relations, $\Delta\nu_{\rm sc}$, in the RC is typically 2–5% smaller than that determined through the stellar oscillation code `gyre`, $\langle \Delta\nu_{\texttt{gyre}} \rangle$. In parametric models, this difference is up to 8%. The correction factor applied to $\Delta\nu_{\rm sc}$ is smallest early in the RC and grows as helium is depleted in the core. An additional finding is that the correction factor is also correlated to the helium-core mass. This difference in $\langle \Delta\nu \rangle$ is because RC stars have a different internal structure compared to the Sun, which these scaling relations do not take into account.

- Including luminosity in the scaling relations for mass and radius (Equations 5.15 and 5.16) improves the determined masses and radii. When purely using the seismic scaling relations (Equations 5.13 and 5.14), inferred masses and radii for stars with non-standard evolution can differ by up to 15% and 10% compared to the model mass and radius. Using Equations (5.15) and (5.16) should remove this bias, as these equations are assumed to depend on the surface gravity only, i.e. they are largely insensitive to the different internal structure.

- SSE models with constant overshooting during CHeB are unable to cover the full range of observed ΔP, as stellar models with overshooting at the onset of CHeB have minimum ΔP around 20 s larger than the observed minimum ΔP (Figure 5.6). For ΔP of these SSE models to span the observed range, a modified $\alpha_{\rm OV,He}$ is used, which increases from 0 to 0.85 as helium is consumed in the core.

- We introduce a method with which we infer helium-core masses of 810 RC stars with masses between 1 $M_\odot$ and 3 $M_\odot$ under the assumption that they are SSE stars by using $\Delta P/\nu_{\rm max}$ and interpolating between our fits to SSE model tracks in $M_{\rm He}$-$\Delta P/\nu_{\rm max}$. This allows us to determine helium-core masses in stars with $Y_{\rm C} \lesssim 0.2$, which have reached their maximum ΔP.

- Our parametric models cover a wide range in helium-core mass and total mass. Once these models undergo CHeB, the difference between narrow models, which have a sharp transition between the helium core and hydrogen envelope, and wide models, which have a shallow transition between the helium core and the hydrogen envelope, is only in the total helium-core mass. This difference is because hydrogen-shell burning advances and eliminates the different initial composition profiles. Therefore, the ability to distinguish between whether a helium core initially had a wide or narrow transition is lost.

- Our parametric models span a large range in $\rho_{\rm CZ}/\rho_{\rm He}$ for each stellar mass with the spread being larger in the lower-mass stars. Additionally, our parametric models reach a maximum

in $\rho_{\rm CZ}/\rho_{\rm He}$ around the transition mass of 1.8 $M_\odot \leq M \leq$ 2.2 $M_\odot$. Larger helium-core masses in our parametric models result in a stronger contrast between the mean convective envelope density and the mean helium-core density.

- Coupling is anti-correlated with $\rho_{\rm CZ}/\rho_{\rm He}$ when taking both SSE and parametric models into account. For stars with masses below the transition mass, q is also anti-correlated with $\rho_{\rm CZ}/\rho_{\rm He}$ during the evolution of an individual star. However, for the more massive stars q is correlated with $\rho_{\rm CZ}/\rho_{\rm He}$ as a star evolves.

- Coupling in parametric models with masses below the transition mass, increases with increasing helium-core mass. Coupling in parametric models decreases with increasing total stellar mass below the transition mass. For masses above the transition mass, larger helium cores increase coupling to a much lesser degree and coupling increases with increasing total stellar mass. Therefore, it is expected that stars with large helium-core mass fractions have stronger coupling, the lower their total mass is.

- Period spacing is strongly correlated to helium-core mass. The maximum ΔP reached in all SSE and parametric models has a sharp boundary well described by a quadratic, which allows a minimum helium-core mass to be estimated. This allows limits to be set on where a star can exist in parameter space.

- Two stars, KIC4275220 and KIC6047033 are identified, which have minimum helium-core masses that exceed their corresponding SSE model. However, KIC4275220 is still consistent with SSE due to the large error on ΔP. KIC6047033 is a good candidate for further in-depth study to determine its interior structure. Although it would be relatively straightforward to determine whether a star has lost a lot of mass e.g. sdB stars][]Gotberg2018, the modelling outlined in this thesis provides an avenue for the identification of stars where changes in structure are more subtle.

6.1 Future Work

The work presented in this thesis has opened up an avenue of research to probe the deep interior of stars by taking advantage of mixed-modes' ability to bring information of interior properties to the surface. The work done has also shown potentially interesting areas for future study.

First of all, a more in-depth analysis of $\langle \mathrm{d}q/\,\mathrm{d}\nu_q \rangle$ in the RGB could enable the mapping of the evanescent region. This allows, for example, the amount of undershooting to be measured directly through the spread of $\langle \mathrm{d}q/\,\mathrm{d}\nu_q \rangle$ at different frequencies. This spread is sensitive to the difference in slope between $\tilde{N}$ and $\tilde{S}$, and would be a new method of measuring undershooting. Additionally, including the dependence of q on oscillation frequency would increase the accuracy of measured q.

Two stars, KIC4275220 and KIC6047033, have period spacings and minimum helium-core masses larger than expected when compared to single star models. A more detailed study focussing on these two candidates using the techniques outlined in this thesis could confirm their non-standard evolutionary history.

Mixed-mode coupling may also be an avenue through which the helium abundance of stars can be investigated. In some additional models run with `MESA`, there appears to be a dependence on He, where a higher helium abundance causes a larger coupling during the SGB and RC, and smaller coupling during the RGB and RGBb.

Further investigation into how $\Delta P/\nu_{\max}$ is related to the helium-core mass of stars in the RC may enable model-independent estimations of the helium-core mass of stars. This would assist in placing constraints on mixing in the helium core of helium-burning stars. Additionally it would assist in the identification of stars with non-standard structures.

Finally, re-implementing the calculation for q using a more recent version of `MESA`, which

can take advantage of the `autodiff` module and improvements to the equation of state used by `MESA` (5.3.1 in Jermyn et al. 2022), would likely eliminate or at the very least reduce the need for smoothing Q when calculating $\mathrm{d}P/\mathrm{d}s$ and $\mathrm{d}Q/\mathrm{d}s$.

Appendix One

Python tools and scripts

During the course of this work, a variety of Python tools and scripts were developed to facilitate the running of grids of `MESA` models and exploration of the results of these modelling runs. The Python tools and scripts that have been developed for this thesis are available at https://github.com/waltervrossem. A summary of these tools follows.

A.1 `setup_inlist.py`

The first tool, `setup_inlist.py`, is a flexible and versatile tool that allows for the generation of grids of `MESA` models. It sets up a directory structure where each directory contains all the `MESA` inlists and any additional files for `MESA` to run. It does this by reading in an inlist options file and taking all possible permutations of any lists of parameters. Once all the combinations of parameters for the inlists have been created, the inlists are passed to a finalize function which allows any final adjustments to be made. These final adjusts may depend on any other parameters in the inlists. Some input options require multiple values to be set at once. This is done by treating the multiple inputs as a single parameter when finding the possible permutations. This is called the group unpack method. The group unpack method groups together parameters and treats them as a single parameter when creating individual inlists.

A.1.1 Inlist options

The inlist options file contains the set of parameters for `MESA`. It is a Python file which defines four dictionaries (`OrderedDict` if using a Python version earlier than 3.6) `star_job`, `controls`, `pgstar`, and `master_inlist`. All four contain the same configuration options as the `MESA` inlist files, as well as some additional fields which can be used to pass information to the finalised functions in `setup_inlist.py` using the `non_mesa_key_start` prefix in the dictionary keys. The listing A.1 shows an example `inlist_options` file which creates a grid with three different masses and two different initial metallicities.

Listing A.1: Example options which create a grid.

```
from collections import OrderedDict
import os

inlist_options_path = os.path.abspath(__file__)
non_mesa_key_start = '!PY_KEY_'
star_job = OrderedDict()
controls = OrderedDict()
pgstar = OrderedDict()
master_inlist = OrderedDict()

# --------------------star_job-------------------- #
star_job['type'] = 'star_job'
star_job['filename'] = 'inlist_star'
star_job['group_unpack'] = []

# --------------------controls-------------------- #
controls['type'] = 'controls'
controls['filename'] = 'inlist_controls'
controls['group_unpack'] = []

```

```
controls['initial_mass'] = [1, 1.5, 2]
controls['group_unpack'].append([
{'Z_base':0.01, 'initial_Z':0.01, 'initial_Y':0.24},
{'Z_base':0.02, 'initial_Z':0.02, 'initial_Y':0.23}])

# ---------------------pgstar--------------------- #
pgstar['type'] = 'pgstar'
pgstar['filename'] = 'inlist_pgstar'

# ---------------------master--------------------- #
master_inlist['type'] = 'master'
master_inlist['filename'] = 'inlist'

master_inlist['star_job'] = OrderedDict()
master_inlist['controls'] = OrderedDict()
master_inlist['pgstar'] = OrderedDict()
master_inlist['other'] = OrderedDict()

master_inlist['use_extra_default_inlist'] = []

master_inlist['star_job']['read_extra_star_job_inlist5'] = True
master_inlist['star_job']['extra_star_job_inlist5_name'] = star_job['filename']

master_inlist['controls']['read_extra_controls_inlist5'] = True
master_inlist['controls']['extra_controls_inlist5_name'] = controls['filename']

master_inlist['pgstar']['read_extra_pgstar_inlist5'] = True
master_inlist['pgstar']['extra_pgstar_inlist5_name'] = pgstar['filename']

master_inlist[f'{non_mesa_key_start}_extra_file'] = []

def example_finalize_func_controls(unpacked_controls, unpacked_star_job, key):
```

```
53      # change options as function of MESA input
54      return unpacked_controls
55
56  master_inlist['finalize_funcs'] = {'controls':example_finalize_func_controls}
```

A.2 gyre_driver.py

Similar to `setup_inlist.py`, the `gyre` driver assists with setting up and running `gyre` for a run of `MESA`. It was originally written in `Fortran` by Diego Bossini and Andrea Miglio for use with `gyre` 3.3 and 4.4. I ported the driver to `python` and expanded it for use with `gyre` versions 5 and 6.

The `gyre_driver.py` accepts a list of stellar models and mode degrees for which to compute the eigenfrequencies. It does this by using a base inlist file which is adjusted for each profile. The frequency window over which `gyre_driver.py` searches for eigenfrequencies is set by three parameters which are $\nu_{\max}$, the power spectrum envelope described in Equation (3.62), and an additional user-set constant to adjust the size of this window. This initial search for eigenfrequencies is done for $l = 0$ and the modes which are found are then used as the limits for any subsequent higher degree scans. This results in the following limits for the scan for $l = 0$:

$$\nu_{\text{scan,min}} = \max(10^{-4}\mu\text{Hz}, \nu_{\max} - 2k\sigma) \tag{A.1}$$

$$\nu_{\text{scan,max}} = \nu_{\max} + 2k\sigma, \tag{A.2}$$

where k is a constant passed as an input to the driver and σ is defined in Equation (3.62).

The number of expected orders, based on $\Delta\nu$, in the frequency range for $l = 0$ is:

$$n_{\Delta\nu} = \lceil \frac{\nu_{\text{scan,max}} - \nu_{\text{scan,min}}}{\Delta\nu} \rceil, \tag{A.3}$$

where $\Delta\nu$ is the large frequency separation estimated from the model using the scaling relations. The number of scan points is then taken to be:

$$n_{\rm scan} = 3n_{\Delta\nu}. \tag{A.4}$$

`gyre` is then run for $l = 0$ modes to find the eigenfrequencies which is used for higher degree scans.

For $l \geq 1$ modes, $\nu_{\rm scan,min}$ and $\nu_{\rm scan,max}$ are set by the minimum and maximum mode frequencies found for $l = 0$ modes respectively. Similar to the initial scan, the upper limit to the number of orders expected to be in the frequency range when including the period spacing is:

$$n_{\Delta\Pi_0} = \left\lceil \frac{\nu_{\rm scan,max} - \nu_{\rm scan,min}}{(\nu^{-1}_{\rm scan,min} - \Delta\Pi_0)^{-1} - \nu_{\rm scan,min}} \right\rceil, \tag{A.5}$$

where $\Delta\Pi_0$ is the asymptotic period spacing defined in Equation (3.55). If $n_{\Delta\nu} > n_{\Delta\Pi_0}$, then the following equation is used:

$$n_{\rm scan} = 5n_{\Delta\nu}, \tag{A.6}$$

otherwise the scan is split by order and $n_{\Delta\Pi_0}$ is calculated in each scan window i:

$$n_{{\rm scan},i} = 5\left\lceil \frac{\nu_{{\rm scan,max},i} - \nu_{{\rm scan,min},i}}{(\nu^{-1}_{{\rm scan,min},i} - \Delta\Pi_0)^{-1} - \nu_{{\rm scan,min},i}} \right\rceil. \tag{A.7}$$

A.3 `check_grid.py`

This is a script that checks whether or not a grid has run successfully. For each run of a `MESA` grid, `check_grid.py` reads the out-files which contain `MESA`'s `stdout`. It searches for the termination code that caused `MESA` to stop or for whether an error occurred during the `MESA` run. When reading the history files it only reads the last data row as only this is of interest. It skips the rest, which speeds up the script significantly. It also determines whether the star's core is pre- or post-core H or He exhaustion and displays this information in an easily digestible format. If the grid is run

using the computing cluster job management system `slurm`, it also lists some metadata on the tasks. It is also possible to create a file which can be used to easily restart failed models using the `MESA` photos. Listing A.2 shows the output for a small grid where one model failed before core He exhaustion (pre-CHeX) but after core hydrogen exhaustion (post-CHX) at `model_number` 15769. This script makes it possible to quickly ascertain whether all models in a grid ran successfully, and if any did fail, where and why `MESA` stopped. In the case of this small grid, it was run without `slurm`. If it were, any `slurm`-related error, e.g. running out of allotted walltime or running for a very short period of time, would be shown on line 7.

Listing A.2: Output of `check_grid.py` of a small grid showing that model `0001` failed.

```
1
2  -------------------------------------------
3  termination_code                    count
4  -------------------------------------------
5  xa_central_lower_limit                    8
6  min_timestep_limit                        1
7   └  None                                1
8       └  pre-CHeX                      1
9           └  post-CHX                  1
10 -------------------------------------------
11 0000             post-CHeX 20746 xa_central_lower_limit
12 0001              pre-CHeX 15769 min_timestep_limit
13 0002             post-CHeX 16363 xa_central_lower_limit
14 0003             post-CHeX 15969 xa_central_lower_limit
15 0004             post-CHeX  6964 xa_central_lower_limit
16 0005             post-CHeX  3367 xa_central_lower_limit
17 0006             post-CHeX  3349 xa_central_lower_limit
18 0007             post-CHeX  3170 xa_central_lower_limit
```

```
0008              post-CHeX  3370 xa_central_lower_limit
-------------------------------------------
```

A.4 load_data.py

The load data script contains two classes which allow for easy usage of MESA or gyre data. The first is the MESA data class which reads a MESA history or profile file and only loads the data when it is required. When loading a history file it first checks whether an already processed version of the data file is available and only loads it if it is older than the MESA history or profile file. This increases the speed of loading data as it is not necessary to read and convert all data files from text to a numerical format. When reading text data files the MESA data class reads the header and the first line of data. The header data is stored as a dictionary in the header attribute of the MESA data class. The column names are then extracted from these initial lines read and the data type is inferred using numpy's safe_eval function if the value is not NaN, otherwise it is set as np.float64. Once the column names and data types are known, the rest of the data file is lazily loaded as a record array. This preserves the distinction between floating-point numbers and integers and only loads the data once it is needed. After this initial load, the rows are scrubbed of any duplicate model numbers keeping the most recent. The profile index is also loaded and is used by class methods to allow for convenient look-ups of which profiles correspond to which model numbers and vice versa.

Bibliography

Abdurro'uf, Accetta, K., Aerts, C., et al. 2022, ApJS, 259, 35

Abolfathi, B., Aguado, D. S., Aguilar, G., et al. 2018, ApJS, 235, 42

Aerts, C., Christensen-Dalsgaard, J., & Kurtz, D. W. 2010, Asteroseismology (Springer)

Anders, F., Gispert, P., Ratcliffe, B., et al. 2023, arXiv e-prints, arXiv:2304.08276

Anderson, E., Bai, Z., Bischof, C., et al. 1999, LAPACK Users' Guide, 3rd edn. (Philadelphia, PA: Society for Industrial and Applied Mathematics)

Auvergne, M., Bodin, P., Boisnard, L., et al. 2009, A&A, 506, 411

Baron, F., Monnier, J. D., Pedretti, E., et al. 2012, ApJ, 752, 20

Barrell, J. 1917, Geological Society of America Bulletin, 28, 745

Basu, S. 1997, MNRAS, 288, 572

Basu, S. & Chaplin, W. J. 2018, Asteroseismic Data Analysis. Foundations and Techniques (Princeton University Press)

Beck, P. G. 2013, PhD thesis, Instituut voor Sterrenkunde, KU Leuven, Celestijnenlaan 200D, B-3001 Leuven, Belgium; paul.beck@ster.kuleuven.be

Beck, P. G., Montalban, J., Kallinger, T., et al. 2012, Nature, 481, 55

Bedding, T. R., Huber, D., Stello, D., et al. 2010, ApJ, 713, L176

Bedding, T. R., Mosser, B., Huber, D., et al. 2011, Nature, 471, 608

Belkacem, K., Goupil, M. J., Dupret, M. A., et al. 2011, A&A, 530, A142

Benacquista, M. 2013, An Introduction to the Evolution of Single and Binary Stars (Springer)

Bethe, H. A. 1939, Phys. Rev., 55, 103

Bethe, H. A. & Critchfield, C. L. 1938, Physical Review, 54, 248

Bjorn & Čertík, O. 2021

Borucki, W. J. 2017, Proceedings of the American Philosophical Society, 161, 38

Borucki, W. J., Koch, D., Basri, G., et al. 2010, Science, 327, 977

Bossini, D., Miglio, A., Salaris, M., et al. 2015, MNRAS, 453, 2290

Bossini, D., Miglio, A., Salaris, M., et al. 2017, MNRAS, 469, 4718

Bovy, J., Nidever, D. L., Rix, H.-W., et al. 2014, ApJ, 790, 127

Brogaard, K., Arentoft, T., Jessen-Hansen, J., & Miglio, A. 2021, MNRAS, 507, 496

Brown, T. M., Gilliland, R. L., Noyes, R. W., & Ramsey, L. W. 1991, ApJ, 368, 599

Buldgen, G., Noels, A., Baturin, V. A., et al. 2023, arXiv e-prints, arXiv:2308.13368

Burbidge, E. M., Burbidge, G. R., Fowler, W. A., & Hoyle, F. 1957, Reviews of Modern Physics, 29, 547

Carrier, F., Eggenberger, P., & Bouchy, F. 2005, A&A, 434, 1085

Chandrasekhar, S. 1939, An introduction to the study of stellar structure (The University of Chicago press)

Chaplin, W. J. & Miglio, A. 2013, ARA&A, 51, 353

Chaplin, W. J., Serenelli, A. M., Miglio, A., et al. 2020, Nature Astronomy, 4, 382

Chiappini, C., Anders, F., Rodrigues, T. S., et al. 2015, A&A, 576, L12

Chiosi, C., Bertelli, G., & Bressan, A. 1992, ARA&A, 30, 235

Christensen-Dalsgaard, J. 2014, Lecture Notes on Stellar Oscillations, https://users-phys.au.dk/jcd/oscilnotes/

Christensen-Dalsgaard, J., Gough, D. O., & Thompson, M. J. 1991, ApJ, 378, 413

Connelly, J. N., Bizzarro, M., Krot, A. N., et al. 2012, Science, 338, 651

Cowling, T. G. 1941, MNRAS, 101, 367

Cunha, M. S., Stello, D., Avelino, P. P., Christensen-Dalsgaard, J., & Townsend, R. H. D. 2015, ApJ, 805, 127

Cyburt, R. H., Amthor, A. M., Ferguson, R., et al. 2010, ApJS, 189, 240

Davies, G. R., Chaplin, W. J., Elsworth, Y. P., & Hale, S. J. 2014, Monthly Notices of the Royal Astronomical Society, 441, 3009

Davies, G. R., Lund, M. N., Miglio, A., et al. 2017, A&A, 598, L4

De Marco, O. & Izzard, R. G. 2017, PASA, 34, e001

Degroote, P., Aerts, C., Baglin, A., et al. 2010, Nature, 464, 259

Deheuvels, S. & Belkacem, K. 2018, A&A, 620, A43

Deheuvels, S., Brandão, I., Silva Aguirre, V., et al. 2016, A&A, 589, A93

Deheuvels, S. & Michel, E. 2011, A&A, 535, A91

Di Mauro, M. P. 2016, in Frontier Research in Astrophysics II (FRAPWS2016), 29

Duvall, T. L., J., Dziembowski, W. A., Goode, P. R., et al. 1984, Nature, 310, 22

Duvall, T. L., J. & Harvey, J. W. 1984, Nature, 310, 19

Eddington, A. S. 1920, The Scientific Monthly, 11, 297

Eggenberger, P., Montalbán, J., & Miglio, A. 2012, A&A, 544, L4

Eggleton, P. P. 1983, ApJ, 268, 368

Fitch, W. S. 1976, in Astrophysics and Space Science Library, Vol. 60, IAU Colloq. 29: Multiple Periodic Variable Stars, ed. W. S. Fitch, 167

Foreman-Mackey, D. 2016, The Journal of Open Source Software, 1, 24

Foreman-Mackey, D., Hogg, D. W., Lang, D., & Goodman, J. 2013, PASP, 125, 306

Fornberg, B. 1988, Mathematics of computation, 51, 699

Gabriel, M., Noels, A., Montalbán, J., & Miglio, A. 2014, A&A, 569, A63

Gaia Collaboration, Prusti, T., de Bruijne, J. H. J., et al. 2016, A&A, 595, A1

Gao, S., Liu, C., Zhang, X., et al. 2014, ApJ, 788, L37

Gao, S., Zhao, H., Yang, H., & Gao, R. 2017, MNRAS, 469, L68

García, R. A. & Ballot, J. 2019, Living Reviews in Solar Physics, 16, 4

García, R. A., Turck-Chièze, S., Boumier, P., et al. 2005, A&A, 442, 385

Gehan, C., Mosser, B., Michel, E., Samadi, R., & Kallinger, T. 2018, A&A, 616, A24

Girardi, L. 1999, MNRAS, 308, 818

Girardi, L. 2016, ARA&A, 54, 95

Gough, D. O., Leibacher, J. W., Scherrer, P. H., & Toomre, J. 1996, Science, 272, 1281

Grevesse, N. & Sauval, A. J. 1998, Space Sci. Rev., 85, 161

Hale, S. J., Howe, R., Chaplin, W. J., Davies, G. R., & Elsworth, Y. P. 2016, Sol. Phys., 291, 1

Handberg, R., Brogaard, K., Miglio, A., et al. 2017, MNRAS, 472, 979

Hatt, E., Nielsen, M. B., Chaplin, W. J., et al. 2023, A&A, 669, A67

Hayashi, C. 1966, ARA&A, 4, 171

Haywood, M. 2008, MNRAS, 388, 1175

Hekker, S. & Christensen-Dalsgaard, J. 2017, A&A Rev., 25, 1

Hekker, S., Elsworth, Y., & Angelou, G. C. 2018, A&A, 610, A80

Hekker, S., Kallinger, T., Baudin, F., et al. 2009, A&A, 506, 465

Holmes, A. 1915, Proceedings of the Geologists' Association, 26, 289

Howell, S. B., Sobeck, C., Haas, M., et al. 2014, PASP, 126, 398

Hoyle, F. 1960, MNRAS, 120, 22

Huber, D., Bedding, T. R., Stello, D., et al. 2011, ApJ, 743, 143

Iben, I. 1968, Nature, 220, 143

Iben, Icko, J. 1967, ApJ, 147, 624

Ivanova, N., Justham, S., Chen, X., et al. 2013, A&A Rev., 21, 59

Izzard, R. G., Preece, H., Jofre, P., et al. 2018, MNRAS, 473, 2984

Jermyn, A. S., Bauer, E. B., Schwab, J., et al. 2022, arXiv e-prints, arXiv:2208.03651

Jiang, C., Cunha, M., Christensen-Dalsgaard, J., & Zhang, Q. 2020, MNRAS, 495, 621

Jiang, C., Cunha, M., Christensen-Dalsgaard, J., Zhang, Q. S., & Gizon, L. 2022, MNRAS, 515, 3853

Jofré, P., Jorissen, A., Van Eck, S., et al. 2016, A&A, 595, A60

Kaye, A. B., Handler, G., Krisciunas, K., Poretti, E., & Zerbi, F. M. 1999, PASP, 111, 840

Khan, S., Hall, O. J., Miglio, A., et al. 2018, ApJ, 859, 156

Khan, S., Miglio, A., Mosser, B., et al. 2019, A&A, 628, A35

King, C. R., Da Costa, G. S., & Demarque, P. 1985, ApJ, 299, 674

Kippenhahn, R., Weigert, A., & Weiss, A. 2013, Stellar Structure and Evolution (Springer Berlin)

Kuszlewicz, J. S., Hon, M., & Huber, D. 2023, arXiv e-prints, arXiv:2307.06482

Langer, N. 2012, ARA&A, 50, 107

Leibacher, J. W. & Stein, R. F. 1971, Astrophys. Lett., 7, 191

Leighton, R. B. 1960, in IAU Symposium, Vol. 12, Aerodynamic Phenomena in Stellar Atmospheres, ed. R. N. Thomas, 321–325

Leighton, R. B., Noyes, R. W., & Simon, G. W. 1962, ApJ, 135, 474

Li, Y., Bedding, T. R., Murphy, S. J., et al. 2022, Nature Astronomy, 6, 673

Lindegren, L., Bastian, U., Biermann, M., et al. 2021, A&A, 649, A4

Majewski, S. R., Schiavon, R. P., Frinchaboy, P. M., et al. 2017, AJ, 154, 94

Martig, M., Rix, H.-W., Silva Aguirre, V., et al. 2015, MNRAS, 451, 2230

Matteucci, F., ed. 2001, Astrophysics and Space Science Library, Vol. 253, The chemical evolution of the Galaxy

Matteucci, F. 2021, A&A Rev., 29, 5

Matteuzzi, M., Montalbán, J., Miglio, A., et al. 2023, Red Horizontal Branch stars: an asteroseismic perspective

Mazzitelli, I. & Dantona, F. 1986, ApJ, 308, 706

Miglio, A., Brogaard, K., Stello, D., et al. 2012, MNRAS, 419, 2077

Miglio, A., Chiappini, C., Mackereth, J. T., et al. 2021, A&A, 645, A85

Miglio, A., Montalbán, J., Eggenberger, P., & Noels, A. 2008, Astronomische Nachrichten, 329, 529

Moe, M. & Di Stefano, R. 2017, ApJS, 230, 15

Montalbán, J., Miglio, A., Noels, A., et al. 2013, ApJ, 766, 118

Montalbán, J. & Noels, A. 2013, in European Physical Journal Web of Conferences, Vol. 43, European Physical Journal Web of Conferences, 03002

Mosser, B., Barban, C., Montalbán, J., et al. 2011, A&A, 532, A86

Mosser, B., Benomar, O., Belkacem, K., et al. 2014, A&A, 572, L5

Mosser, B., Elsworth, Y., Hekker, S., et al. 2012, A&A, 537, A30

Mosser, B., Gehan, C., Belkacem, K., et al. 2018, A&A, 618, A109

Mosser, B., Pinçon, C., Belkacem, K., Takata, M., & Vrard, M. 2017, A&A, 607, C2

Mosser, B., Vrard, M., Belkacem, K., Deheuvels, S., & Goupil, M. J. 2015, A&A, 584, A50

Noels, A., Montalbán, J., & Chiappini, C. 2016, Astronomische Nachrichten, 337, 982

Noyes, R. 1990, in The New Solar System, ed. J. K. Beatty & A. Chaikin (Sky Publishing), 23

Ong, J. M. J. & Gehan, C. 2023, ApJ, 946, 92

Owen, J. W. 1957, MNRAS, 117, 384

Paczyński, B. 1971, ARA&A, 9, 183

Paczynski, B. 1976, in IAU Symposium, Vol. 73, Structure and Evolution of Close Binary Systems, ed. P. Eggleton, S. Mitton, & J. Whelan, 75

Pagel, B. E. J. 2009, Nucleosynthesis and Chemical Evolution of Galaxies (Cambridge University Press)

Paxton, B., Bildsten, L., Dotter, A., et al. 2011, ApJS, 192, 3

Paxton, B., Cantiello, M., Arras, P., et al. 2013, ApJS, 208, 4

Paxton, B., Marchant, P., Schwab, J., et al. 2015, ApJS, 220, 15

Paxton, B., Schwab, J., Bauer, E. B., et al. 2018, ApJS, 234, 34

Paxton, B., Smolec, R., Schwab, J., et al. 2019, ApJS, 243, 10

Pedersen, M. G., Aerts, C., Pápics, P. I., & Rogers, T. M. 2018, A&A, 614, A128

Pekeris, C. L. 1938, ApJ, 88, 189

Pinçon, C., Goupil, M. J., & Belkacem, K. 2020, A&A, 634, A68

Pinçon, C. & Takata, M. 2022, A&A, 661, A139

Pinçon, C., Takata, M., & Mosser, B. 2019, A&A, 626, A125

Price-Whelan, A. M. & Goodman, J. 2018, ApJ, 867, 5

Pustylnik, I. 1998, Astronomical and Astrophysical Transactions, 15, 357

Rendle, B. M., Buldgen, G., Miglio, A., et al. 2019, MNRAS, 484, 771

Ricker, G. R., Winn, J. N., Vanderspek, R., et al. 2015, Journal of Astronomical Telescopes, Instruments, and Systems, 1, 014003

Rodrigues, T. S., Bossini, D., Miglio, A., et al. 2017, MNRAS, 467, 1433

Rosdahl, J., Katz, H., Blaizot, J., et al. 2018, MNRAS, 479, 994

Rui, N. Z. & Fuller, J. 2021, MNRAS, 508, 1618

Russell, H. N. 1914, Popular Astronomy, 22, 331

Russell, H. N. 1919, PASP, 31, 205

Salaris, M. & Cassisi, S. 2005, Evolution of Stars and Stellar Populations (Wiley), 400

Salaris, M., Cassisi, S., & Weiss, A. 2002, PASP, 114, 375

Salpeter, E. E. 1952, ApJ, 115, 326

Schönberg, M. & Chandrasekhar, S. 1942, ApJ, 96, 161

Schou, J., Antia, H. M., Basu, S., et al. 1998, ApJ, 505, 390

Serenelli, A. M., Basu, S., Ferguson, J. W., & Asplund, M. 2009, ApJ, 705, L123

Shapley, H. 1919, Nature, 103, 25

Shibahashi, H. 1979, PASJ, 31, 87

Silva Aguirre, V., Bojsen-Hansen, M., Slumstrup, D., et al. 2018, MNRAS, 475, 5487

Solanki, S. K. 2003, A&A Rev., 11, 153

Spruit, H. C. 2015, A&A, 582, L2

Sweigart, A. V., Lattanzio, J. C., Gray, J. P., & Tout, C. A. 2000, in Liege International Astrophysical Colloquia, Vol. 35, Liege International Astrophysical Colloquia, ed. A. Noels, P. Magain, D. Caro, E. Jehin, G. Parmentier, & A. A. Thoul, 529

Takata, M. 2005, PASJ, 57, 375

Takata, M. 2006, PASJ, 58, 893

Takata, M. 2016a, PASJ, 68, 109

Takata, M. 2016b, PASJ, 68, 91

Tassoul, M. 1980, ApJS, 43, 469

Tassoul, M. 1990, ApJ, 358, 313

Thomas, H. C. 1967, ZAp, 67, 420

Thomas, H. C. 1977, ARA&A, 15, 127

Thompson, M. J., Christensen-Dalsgaard, J., Miesch, M. S., & Toomre, J. 2003, ARA&A, 41, 599

Tokovinin, A. 2014a, AJ, 147, 86

Tokovinin, A. 2014b, AJ, 147, 87

Townsend, R. H. D., Goldstein, J., & Zweibel, E. G. 2018, MNRAS, 475, 879

Townsend, R. H. D. & Teitler, S. A. 2013, MNRAS, 435, 3406

Ulrich, R. K. 1970, ApJ, 162, 993

Ulrich, R. K. 1986, ApJ, 306, L37

Unno, W., Osaki, Y., Ando, H., Saio, H., & Shibahashi, H. 1989, Nonradial oscillations of stars (University of Tokyo Press)

Vrard, M., Mosser, B., & Samadi, R. 2016, A&A, 588, A87

Weizsäcker, C. v. 1937, Phys. Zeit., 38, 176

Weizsäcker, C. v. 1938, Phys. Zeit., 39, 633

Willett, E., Miglio, A., Mackereth, J. T., et al. 2023, MNRAS

Yu, J., Huber, D., Bedding, T. R., et al. 2018, ApJS, 236, 42